NANOTECHNOLOGY IN TRADITIONAL MEDICINES AND NATURAL PRODUCTS

EDITED BY: Fang Liu, Ye Tian, Ruibing Wang, Wei Cao and Ruoyu Zhang
PUBLISHED IN: Frontiers in Chemistry

frontiers Research Topics

ISSN 1664-8714
ISBN 978-2-88966-652-2
DOI 10.3389/978-2-88966-652-2

About Frontiers

Frontiers is more than just an open-access publisher of scholarly articles: it is a pioneering approach to the world of academia, radically improving the way scholarly research is managed. The grand vision of Frontiers is a world where all people have an equal opportunity to seek, share and generate knowledge. Frontiers provides immediate and permanent online open access to all its publications, but this alone is not enough to realize our grand goals.

Frontiers Journal Series

The Frontiers Journal Series is a multi-tier and interdisciplinary set of open-access, online journals, promising a paradigm shift from the current review, selection and dissemination processes in academic publishing. All Frontiers journals are driven by researchers for researchers; therefore, they constitute a service to the scholarly community. At the same time, the Frontiers Journal Series operates on a revolutionary invention, the tiered publishing system, initially addressing specific communities of scholars, and gradually climbing up to broader public understanding, thus serving the interests of the lay society, too.

Dedication to Quality

Each Frontiers article is a landmark of the highest quality, thanks to genuinely collaborative interactions between authors and review editors, who include some of the world's best academicians. Research must be certified by peers before entering a stream of knowledge that may eventually reach the public - and shape society; therefore, Frontiers only applies the most rigorous and unbiased reviews.
Frontiers revolutionizes research publishing by freely delivering the most outstanding research, evaluated with no bias from both the academic and social point of view. By applying the most advanced information technologies, Frontiers is catapulting scholarly publishing into a new generation.

What are Frontiers Research Topics?

Frontiers Research Topics are very popular trademarks of the Frontiers Journals Series: they are collections of at least ten articles, all centered on a particular subject. With their unique mix of varied contributions from Original Research to Review Articles, Frontiers Research Topics unify the most influential researchers, the latest key findings and historical advances in a hot research area! Find out more on how to host your own Frontiers Research Topic or contribute to one as an author by contacting the Frontiers Editorial Office: frontiersin.org/about/contact

NANOTECHNOLOGY IN TRADITIONAL MEDICINES AND NATURAL PRODUCTS

Topic Editors:
Fang Liu, Guangzhou University of Chinese Medicine, China
Ye Tian, Nanjing University, China
Ruibing Wang, University of Macau, China
Wei Cao, Northwestern University, United States
Ruoyu Zhang, Qingdao University, China

Citation: Liu, F., Tian, Y., Wang, R., Cao, W., Zhang, R., eds. (2021). Nanotechnology in Traditional Medicines and Natural Products. Lausanne: Frontiers Media SA.
doi: 10.3389/978-2-88966-652-2

Table of Contents

frontiers in Chemistry

EDITORIAL
published: 22 February 2021
doi: 10.3389/fchem.2021.633419

Editorial: Nanotechnology in Traditional Medicines and Natural Products

Ruoyu Zhang[1], Fang Liu[2]*, Ye Tian[3], Wei Cao[4] and Ruibing Wang[5]*

[1]Institute for Chemical Biology and Biosensing, and College of Life Sciences, Qingdao University, Qingdao, China, [2]Institute of Tropical Medicine and Artemisinin Research Center, Guangzhou University of Chinese Medicine, Guangzhou, China, [3]College of Engineering and Applied Sciences, Nanjing University, Nanjing, China, [4]Department of Chemistry, Northwestern University, Evanston, IL, United States, [5]State Key Laboratory of Quality Research in Chinese Medicine, Institute of Chinese Medical Sciences, University of Macau, Taipa, China

Keywords: natural products, traditional nanomedicines, immunotherapy, drug delivery, artemisnins

Editorial on the Research Topic

Nanotechnology in Traditional Medicines and Natural Products

As the most important antimalarial drug, artemisinin has gained worldwide attention, and scientists doing pioneering work in related research field have been awarded Nobel Prize in Physiology or Medicine in 2015. As one example of many cases that natural products play important roles in medical and clinical applications, each year, artemisinins save hundreds of thousands of people's lives around the world. Natural products with medical values include a broad range of substances, which can be obtained directly or extracted from plants, animals, to fungi, yeast, and even minerals. Researchers have spared great efforts to fully exert their potential in promoting health, and preventing and curing diseases. Although with thousands of years of history, traditional medicine remains sort of mysterious and unrevealed due to complex prescription, lack of standard evaluation methods, and effective drug delivery system (Jiang et al., 2010). Even in the well-known example of artemisinin, it takes years' efforts for scientists to find a proper way to fully utilize its antimalarial activity (Tu, 2016). More profound and systematic research work are demanded to push the development of traditional medicine to a new era. In addition, nanotechnology, which benefits modern medicine by versatile formulation and ease of surface modification, offers promising tools for the development of traditional medicines.

This research topic aims to reflect the current progress in natural products and related nanomedicine. The collection includes bioactivity of natural products, nanofabrication, and delivery methods for targeted and controlled release for cancer treatment. Natural products usually suffer poor water solubility, low stability, and lack of targeting capability. To tackle this problem, various nanocarriers are employed for drug delivery. Nanocarriers such as polymeric NPs, liposomes, and biomacromolecules like DNA have good biocompatibility. In this topic, there are some work and reviews that covers the design and fabrications of nanocarriers for drug delivery (Borcan et al.; Li et al.; Xu et al.). Nanocarriers such as mesoporous silica NPs and carbon nanotubes are good scaffolds for drug loading due to their structural advantages (Ma et al., 2019). It is noteworthy that in some cases, the drug carriers may have the functionalities to suppress the unexpected toxicity of a drug. For example, Gao et al. found that when used for anabasine (ANA) loading, a cucurbituril derivative can significantly inhibit the developmental toxicity of ANA on zebra fish. This work is included in this topic (Gao et al.). In addition, additives are used in nanoformulation to activate or improve the drug efficacy. For instance, research has shown that Fe^{2+} is a very important catalyst for artemisinin activation in Fenton-like reaction that generates free radicals and reactive oxygen species (ROS). The finding also promotes the artemisinin-based chemodynamic therapy (CDT) with the assistance of iron-containing

OPEN ACCESS

Edited by:
Nasir Mahmood, RMIT University Melbourne, Australia

Reviewed by:
Syed Shafqat, University of Education Lahore, Pakistan

***Correspondence:**
Ruoyu Zhang
ryzhqd@hotmail.com
Fang Liu
fangliu@gzucm.edu.cn

Received: *25 November 2020*
Accepted: *12 January 2021*
Published: *22 February 2021*

Citation:
Zhang R, Liu F, Tian Y, Cao W and Wang R (2021) Editorial: Nanotechnology in Traditional Medicines and Natural Products. Front. Chem. 9:633419. doi: 10.3389/fchem.2021.633419

nanoformulation. The latest progresses in this research area have been reviewed by Wu et al. and included in this topic (Wu et al.).

Nanotechnology has also benefited the development of traditional medicine by targeted delivery and controlled release. By attaching ligands such as folic acid, hyaluronic acid, cRGD, transferrin, and aptamers, nanoparticles are prone to accumulate in cancer cells through cell internalization processes, hence help reduce the drug dosage and minimize the side effects on normal tissues (Muhamad et al., 2018; Niu et al.). Cell-derived membranes such as cancer cell membranes provide original complex biological entities that are difficult to replicate artificially. These entities not only help avoid body clearance by immune recognition but also allow specific binding with homotypic tumor cells (Harris et al., 2019). Mesoporous silica nanoparticle loading with quercetin (QT) and wrapping in cancer cell membranes have been reported by Huang et al. and included in this topic for enhanced tumor targeting and radiotherapy, which is a good example that biomimetic nanotechnology helps in natural nanomedicine drug delivery (Huang et al.). Many cancer cells are found to have a lower pH and a higher glutathione level; thus, smart responsive nanoformulation has been designed for drug release at target sites upon stimuli such as pH and redox (Jiang et al.). Versatile formulation technology also allows co-delivery of multiple drugs, since multiple active ingredients are usually employed in traditional medicine. It also facilitates the combination of chemotherapy with photothermo- and photodynamic therapy (Chen et al.). Futher details await your reference in this topic for the nanotechnology in traditional medicines and natural products.

Last decades have witnessed the prosperity of immunotherapy in cancer research, which is fundamentally different from traditional chemotherapy or targeted therapy. It activates hosts' own immune systems to fight against cancer cells, avoiding exposure of normal cells and tissues directly to the toxicity of drugs. Mounting evidence has shown the great potential of natural products and their derivatives in cancer immunotherapy (Deng et al., 2020). For example, Liu et al. found a water-soluble polysaccharide isolated from *Polyporus umbellatus* Fries, which has significant immune activity and increases the secretion of inflammatory cytokines. The results show that this polysaccharide may be valuable in bladder cancer treatment (Liu et al.). Other typical examples of natural products with anticancer immunologic activity include polyphenols, cardiotonic steroids, and terpenoids (Deng et al., 2020). We hope the abovementioned content included in this topic is useful for exploring the potential of tradition medicine and natural products in immunotherapy in the future.

Drug delivery by nanocarriers has advantages such as targeted delivery, ease of controlled release, higher stability, and delivery efficiency. Moreover, it makes diagnosis and therapy in-one-go possible, offering chances to relieve patients' pain. Although a wealth of evidence has supported the curative effect of natural product and traditional medicine in disease treatment and cancer therapy, there remain some critical problems and challenges before being widely commercialized. First, most of the research on the nanomedicine of natural product still in the infancy phase of laboratory testing. More work to explore and evaluate their action mechanism and regulation pathway scientifically is needed. In addition, herbal and traditional medicines often adopt complex prescription, which contains more than two active ingredients, making it more difficult to study their curative mechanism. Third, while a plenty of Western nanomedicines such as Doxil, Emend, and Cimzia have been FDA-approved and marketed, there is still a long way to go for traditional medicine and natural products. Standard clinical trials and systematic evaluation are suggested to be established first. More promising results are expected after the merge of the nanomedicine technology and natural products.

AUTHOR CONTRIBUTIONS

RZ drafted the manuscript, and other authors discussed and revised the manuscript.

ACKNOWLEDGMENTS

RZ thanks the National Science Foundation for Young Scientists of China (Grant No. 21904076) and the Research Foundation for talents of Qingdao University. FL thanks the National Natural Science Foundation of China (21807018).

REFERENCES

Deng, L. J., Qi, M., Li, N., Lei, Y. H., Zhang, D. M., and Chen, J. X. (2020). Natural products and their derivatives: promising modulators of tumor immunotherapy. *J. Leukocyte Biol.* 108 (2), 493–508. doi:10.1002/JLB.3MR0320-444R

Harris, J. C., Scully, M. A., and Day, E. S. (2019). Cancer cell membrane-coated nanoparticles for cancer management. *Cancers* 11 (12), 1836. doi:10.3390/cancers11121836

Jiang, Y., David, B., Tu, P., and Barbin, Y. (2010). Recent analytical approaches in quality control of traditional Chinese medicines--a review. *Anal. Chim. Acta* 657 (1), 9–18. doi:10.1016/j.aca.2009.10.024

Ma, Z., Fan, Y., Wu, Y., Kebebe, D., Zhang, B., Lu, P., et al. (2019). Traditional Chinese medicine-combination therapies utilizing nanotechnology-based targeted delivery systems: a new strategy for antitumor treatment. *Int. J. Nanomed.* 14, 2029–2053. doi:10.2147/IJN.S197889

Muhamad, N., Plengsuriyakarn, T., and Na-Bangchang, K. (2018). Application of active targeting nanoparticle delivery system for chemotherapeutic drugs and traditional/herbal medicines in cancer therapy: a systematic review. *Int. J. Nanomed.* 13, 3921–3935. doi:10.2147/IJN.S165210

Tu, Y. (2016). Artemisinin-A gift from traditional Chinese medicine to the world (Nobel lecture). *Angew Chem. Int. Ed.* 55 (35), 10210–10226. doi:10.1002/anie.201601967

Conflict of Interest: The authors declare that the research was conducted in the absence of any commercial or financial relationships that could be construed as a potential conflict of interest.

frontiers in Chemistry

ORIGINAL RESEARCH
published: 28 February 2020
doi: 10.3389/fchem.2020.00134

Supramolecular Nano-Encapsulation of Anabasine Reduced Its Developmental Toxicity in Zebrafish

Yan Gao†, Xue Yang†, Ziyi Wang, Zhangfeng Zhong, Yuanjia Hu and Yitao Wang**

State Key Laboratory of Quality Research in Chinese Medicine, Institute of Chinese Medical Sciences, University of Macau, Macau, China

Anabasine (ANA), a major piperidine alkaloid originally isolated from wild tobacco trees (*Nicotiana glauca*), has been known to induce serious developmental toxicities such as skeletal deformities in livestock and humans. In this study, we thoroughly investigated the supramolecular nano-encapsulations of ANA by an artificial nanocontainer, cucurbit[7]uril (CB[7]), and examined the influences of the nano-encapsulation on ANA's inherent developmental toxicities on a zebrafish model. We have shown that CB[7] formed 1:1 host-guest inclusion complexes with ANA via a relatively high binding strength [K_a of (7.45 ± 0.31) × 10^4 M^{-1}] in an aqueous solution, via UV-vis and ^{1}H nuclear magnetic resonance spectroscopic titrations, as well as isothermal titration calorimetry titration. As a consequence, CB[7] significantly attenuated the developmental toxicity of ANA on zebrafish *in vivo*. In contrast, for a comparative purpose, β-CD didn't exert any influence on the toxicity of ANA due to its weak binding with ANA, which was not even measurable via either spectroscopic methods or ITC titration. This is the first head-to-head comparison of this pair of nanocontainers, CB[7] and β-CD, on their potential roles in influencing the toxicity of guest molecules and the results suggested that CB[7] could become a more promising functional excipient for reducing the inherent toxicities of active pharmaceutical ingredients, particularly alkaloids that may form relatively strong host-guest binding species with the host.

Keywords: supermolecular, anabasine, cucurbit[7]uril, toxicity, zebrafish

OPEN ACCESS

Edited by:
Fang Liu,
Guangzhou University of Chinese Medicine, China

Reviewed by:
Simin Liu,
Wuhan University of Science and Technology, China
Junzhe Lou,
Harvard University, United States

****Correspondence:***
Yuanjia Hu
yuanjiahu@um.edu.mo
Yitao Wang
ytwang@um.edu.mo

†These authors have contributed equally to this work

Specialty section:
This article was submitted to Medicinal and Pharmaceutical Chemistry, a section of the journal Frontiers in Chemistry

Received: *09 January 2020*
Accepted: *13 February 2020*
Published: *28 February 2020*

Citation:
Gao Y, Yang X, Wang Z, Zhong Z, Hu Y and Wang Y (2020) Supramolecular Nano-Encapsulation of Anabasine Reduced Its Developmental Toxicity in Zebrafish. Front. Chem. 8:134. doi: 10.3389/fchem.2020.00134

INTRODUCTION

Anabasine (ANA) (**Figure 1A**), a major piperidine alkaloid originally isolated from wild tobacco trees (*Nicotiana glauca*), has been known to induce serious developmental toxicities, particularly skeletal deformities in livestock (such as goats and swine) and humans (Keeler et al., 1984; Panter et al., 1990; Green et al., 2013a,b). When human beings were presented with poison symptoms after accidental injection of tobacco plant (*N. glauca),* ANA was identified as a crucial substance causing clinical toxicity (Manoguerra and Freeman, 1982; Mellick et al., 1999; Sims et al., 1999; Mizrachi et al., 2000). ANA is a potential nicotinic acetylcholine receptor (nAChR) agonist, existing in tobacco smoke in a trace amount as it is mainly located from the stalks of cultivated tobacco (Jacob et al., 1999; Daly, 2005; Green et al., 2013b). Thus, ANA could be applied as an indicator of smoking (Jacob et al., 1999; Daly, 2005; Green et al., 2013b).

Cucurbit[*n*]uril (CB[*n*], n = 5–8, 10 in particular) is pumpkin-like nano-sized molecule comprised of *n* glycoluril connected by n pairs of methylene bridges (Lagona et al., 2005; Assaf and Nau, 2015). Compared to the well-known cyclodextrins (CDs) family, CB[*n*] family is relatively

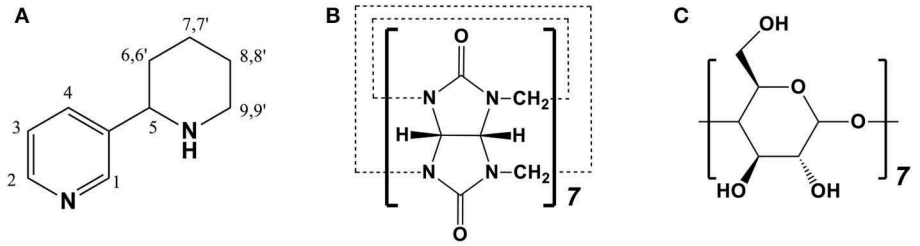

FIGURE 1 | Chemical structures of **(A)** anabasine (ANA), **(B)** cucurbit[7]uril (CB[7]), and **(C)** beta-cyclodextrins (β-CD).

new group of macrocycles, comparable in many ways to CDs (Shetty et al., 2015). In the CB[*n*] family, CB[7] (**Figure 1B**) has caught the most attentions from researchers and has displayed a broad range of potential applications due to its promising biocompatibility, appropriate cavity size, superior molecular recognition ability and moderate solubility in water (Uzunova et al., 2010; Oun et al., 2014; Chen et al., 2015b; Kuok et al., 2017; Yin and Wang, 2018; Zhang et al., 2018). Although CB[7] and β-CD (**Figure 1C**) have rather similar internal cavity volume (279 $Å^3$ vs. 263 $Å^3$), CB[7] has generally higher binding affinities (K_a = 10^4-10^{17} M^{-1}) with a variety of guest species than those of β-CD (K_a = 10^2-10^5 M^{-1}).[13] It has been reported that CB[7] may become an effective pharmaceutical excipient with several benefits (Chen et al., 2015a; Li et al., 2016; Yang et al., 2016, 2017; Huang et al., 2018a; Zhang et al., 2019). For example, it was demonstrated that CB[7] had the promising potential to serve as a taste-masking nanocontainer (Yang et al., 2017). Moreover, Zhang et al. also demonstrated that CB[7] may act as an oral antidote for paraquat poisoning (Zhang et al., 2019).

On the other hand, zebrafish (*Danio rerio*) is a common organism model being used in various biomedical researches. This teleost has high fecundity (200–300 eggs are laid by one adult female fish every week) and rapid *ex utero* development. The early development stages of zebrafish have been well-characterized. As zebrafish's embryo is transparent, the morphologies and internal organs could be well-observed by microscopy without sacrifice (Kimmerl et al., 1995; McGrath and Li, 2008). Thus, zebrafish is an ideal animal model for screening chemical compounds for toxicities. In the present study, we selected natural toxic compound, ANA, as the guest toxic molecule, examined its nano-encapsulation by the synthetic nanocontainer, CB[7], and investigated the possible role of macrocyclic nano-encapsulation in influencing the toxicity of ANA on zebrafish.

MATERIALS AND METHODS

Ethics Statement

The animal experiments and associated experimental protocols were inspected and approved by the Animal Ethics Committee, University of Macau.

Reagents and Instrumentations

Anabasine (ANA) was purchased from Sigma Aldrich (USA), and β-CD was purchased from J&K (Shanghai, China). These chemicals were used without any further purification. CB[7] was prepared based on a published method by Day et al. (2001). Thermo LTQ Orbitrap XL coupled with an ESI/APcl multiprobe was employed to acquire ESI-MS data. Six hundred megahertz NMR (Bruker) spectrometer was employed to collect NMR spectra. A Confocal Imaging System (Olympus DSU) was used to record morphology of zebrafish.

Maintenance of Zebrafish

Zebrafish were originally procured from the ZFIN (Oregon). Zebrafish were kept and maintained at the Zebrafish Aquarium in the Institute of Chinese Medical Sciences, University of Macau. Zebrafish were maintained, bred and selected according to the Zebrafish Handbook, as was previously described (Chen et al., 2015b).

^{1}H NMR Spectroscopy

Solution of ANA (50 μM) was prepared for ^{1}H NMR characterization in D_2O (pD = 7). An deuterated solution of ANA was mixed with different amount of CB[7], 0.6, 1.2, and 2.1 equiv. that of ANA, respectively, without changing the concentration of ANA. These solutions were characterized via ^{1}H NMR spectroscopy (NS = 128 times).

UV-vis Spectroscopy

Two respective aqueous solutions (pH = 7) of ANA (50 μM) and CB[7] (50 μM) were prepared for Job's plot experiment. The samples were prepared by mixing ANA and CB[7] solutions of different volumes to make [CB[7]]/[[ANA] + CB[7]] from 0 to 1.0 at intervals of 0.1. During UV-vis spectroscopic titrations, an aqueous solution of ANA (50 μM) and an aqueous solution of 50 μM ANA and 250 μM CB[7] were prepared (pH = 7). Mixing of the two solutions with different volumes to have [CB[7]]/[ANA] varying from 0 to 5.0 at intervals of 0.5 was conducted and followed by UV-vis absorbance measurements. Same method was employed to prepare β-CD solution for UV-vis spectroscopic titrations with ANA.

ESI-MS Experiment

Aqueous solutions (pH = 7) containing the ANA (50 μM) and 5 equiv. CB[7] (250 μM), and neutral aqueous solution containing ANA (50 μM) and β-CD (1 mM) were prepared. They were subsequently filtered for ESI-MS analysis.

Isothermal Titration Calorimetry (ITC) Experiment

Aqueous solutions of ANA (200 μM) and β-CD (4 mM), ANA (100 μM) and CB[7] (1.5 mM) were prepared, respectively. The four solutions were subsequently degassed by centrifuge (13,000 rpm, 10 min) prior to use for titration. 0.2 mL ANA (200 μM) solution was placed in the sample cell, while 0.04 mL β-CD (4 mM) was placed to syringe for injection. Similarly, ANA (0.2 mL, 100 μM) was the sample cell, and 0.04 mL CB[7] was placed to syringe for injection. The ITC titrations were performed by titrating 19 aliquots (2 μL per drop) of β-CD or CB[7] solutions at room temperature, and the heat evolutions were recorded.

Developmental Toxicity Evaluations of ANA in Zebrafish

Wild type zebrafish embryo was employed as the *in vivo* model to assess the toxicity of ANA in the absence and in the presence of macrocyclic containers. Zebrafish embryos were known to take up chemical species mainly via skin (McGrath and Li, 2008), thus fish were simply incubated in media containing these compounds. The viable hatching rate, survival and morphology of zebrafish embryo were recorded. Zebrafish embryo of 24 hpf were randomly selected and distributed into a 6-well microplate (25–30 embryos/well). To evaluate the developmental toxicity of ANA alone in zebrafish, embryos were incubated in ANA solutions of 4 different concentrations (50, 100, 200, and 300 μM) without CB[7] or β-CD. Of important note, CB[7] was previously investigated to show excellent biocompatibility toward zebrafish embryos in these concentration range (Chen et al., 2015b). Additional experimental groups of embryos were, respectively, incubated in ANA solutions of these 4 different concentrations (50, 100, 200, and 300 μM) with 300 μM CB[7] and 1 mM β-CD (to ensure large excess of β-CD), respectively, for 2 days. At the end of incubation, the number of hatched larvae from each experimental group was recorded and the hatchability rate was analyzed. During the assessment of survival rate, zebrafish embryos (24 hpf) were dechorionated, and the dechorionated embryos were randomly selected and distributed into a 6-well microplate (25–30 embryos/well) and treated with ANA of different concentrations (50, 100, 200, and 300 μM) with or without 300 μM CB[7] or 1 mM β-CD, respectively, for 48 h. Survival rate was recorded by the end of the experiment. In addition, the morphology of zebrafish was measured via an Olympus Confocal Imaging System for further visual assessment.

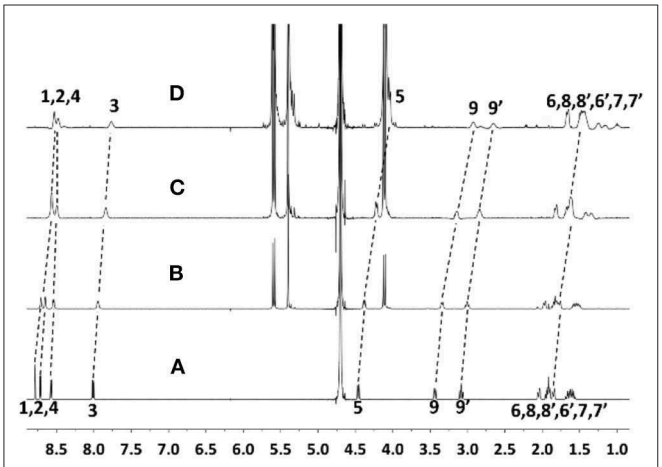

FIGURE 2 | ^{1}H NMR spectra of ANA (50 μM) **(A)** without and with **(B)** 0.6, **(C)** 1.2, and **(D)** 2.1 equiv. CB[7] in D_2O (pD = 7) at room temperature.

RESULTS AND DISCUSSIONS

Encapsulations of ANA by CB[7] and β-CD

The supramolecular nano-encapsulation of ANA by CB[7] was investigated via ^{1}H NMR and UV-Vis spectroscopic titrations and ITC titration. As shown in **Figure 2**, all the protons of ANA exhibited an upfield shift after adding escalating concentration of CB[7], suggesting a full encapsulation of majority of ANA into the nano-cavity of CB[7], as the protons were shielded by the non-poplar cavity. Seilkhanov et al. studied the binding behavior between ANA and β-CD by NMR spectroscopy. Based on their results, ANA forms 1:1 host-guest binding pairs with β-CD with the piperidine fragment being included inside the cavity of CD (Seikhanov et al., 2016).

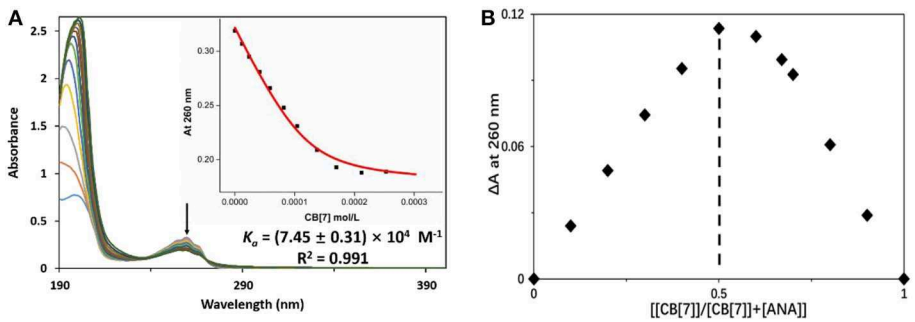

FIGURE 3 | (A) UV-vis measurements of ANA (50 μM) in the presence of increasing concentration of CB[7] (up to 250 μM) in aqueous solution (pH = 7). Inset: the fitting curve of the titration data at 260 nm; **(B)** Job's plot of ANA@CB[7] system (with [ANA]+[CB[7]] = 50 μM) based on a continuous variation titration in aqueous solutions (pH = 7).

UV-vis spectroscopic study was employed to assess the complexation ratio and binding affinity (K_a) between ANA and CB[7] (**Figure 3**). The Job's plot of ANA@CB[7] complex (**Figure 3A**) reached a maximum at 260 nm when [[CB[7]]/[CB[7]] + [ANA]] was 0.5, indicating a 1:1 complexation stoichiometry between ANA and CB[7]. UV-vis spectroscopic titration (**Figure 3B**) of ANA [0.05 mM) with increasing amounts of CB[7] (from 0 to 0.25 mM)] showed a moderate hypochromic shift. The non-linear least-squares fit was used for calculating the binding

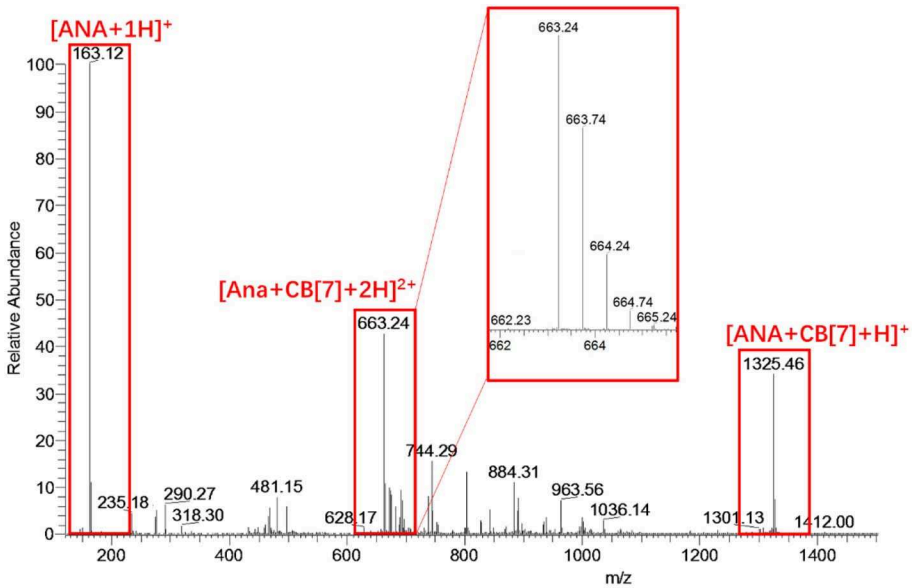

FIGURE 4 | ESI-MS result of an aqueous solution of ANA and CB[7]. The singly-charged peak at m/z = 1325.46 and the doubly-charged peak at m/z = 663.24 suggested a likely 1:1 complexation ratio of ANA@CB[7].

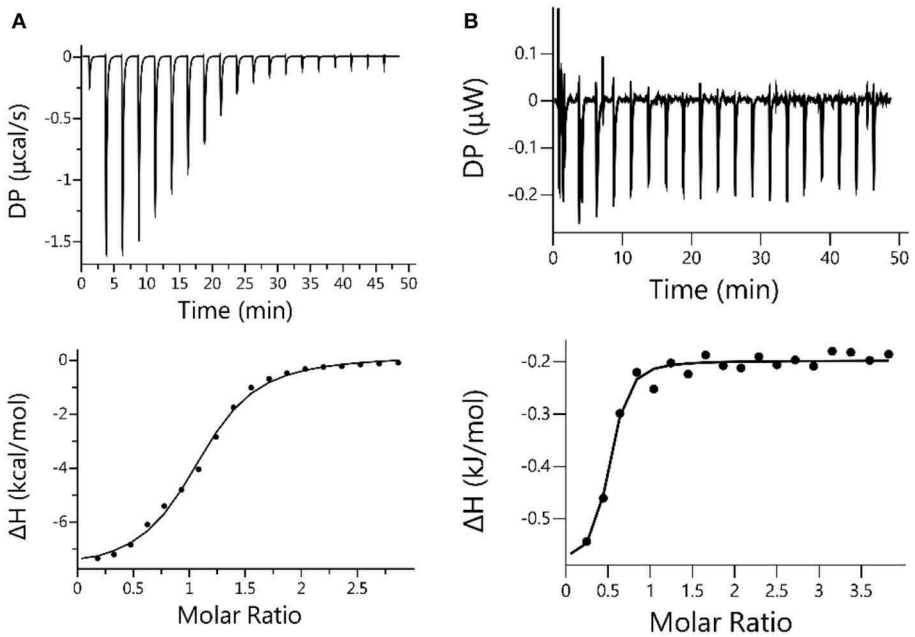

FIGURE 5 | (A) Microcalorimetric measurements of ANA when titrated with CB[7] in water at room temperature. Top: Evolved thermogram during the titration. Bottom: Plot of ΔH against the molar ratio between CB[7] and ANA during the titration, with the best fit by using the "one set of binding sites" binding mode; **(B)** Microcalorimetric measurements of ANA when titrated with β-CD in water at room temperature. Top: Evolved thermogram of during the titration. Bottom: Plot of ΔH against the molar ratio between β-CD and ANA, with the best fit by using the "one set of binding sites" binding mode.

constant, affording a K_a of (7.45 ± 0.31) $\times 10^4$ M^{-1} for ANA@CB[7] pair.

ESI-MS analysis was conducted to further confirm the complexation ratio between ANA and CB[7]. As shown in **Figure 4**, a doubly-charged peak at $m/z = 663.24$ and a singly-charged peak at $m/z = 1325.46$ were observed, corresponding to the $[ANA+CB[7] + 2H]^{2+}$ complex (calculated $m/z = 663.23$) and $[ANA+CB[7]+H]^{1+}$ complex (calculated $m/z = 1325.46$), respectively, confirming the 1:1 complex ratio between ANA and CB[7]. For comparative purpose, ESI-MS analysis of the mixture of ANA and β-CD did not generate any peaks attributed to host-guest complexations, implying that β-CD and ANA binds too weakly in aqueous solutions.

ITC titration was conducted to further verify the relative strong binding between CB[7] and ANA. The result generated $K_a = 1.40 \times 10^5$ M^{-1} shown in **Figure 5A**, consistent with UV-Vis titration results (**Figure 3B**). For a comparative purpose, ITC analysis of the mixture of ANA and β-CD was also conducted, however no meaningful thermal evolvement was observed (**Figure 5B**), suggesting the binding between β-CD and ANA was too weak in aqueous solutions. Collectively, all these results supported that CB[7] formed a relatively stable 1:1 supramolecular complex with ANA with a complexation affinity K_a of (7.45 ± 0.31) $\times 10^4$ M^{-1}, whereas the binding between β-CD and ANA was much weaker.

The Impact of Supramolecular Nano-Encapsulation on ANA's Inherent Developmental Toxicities in Zebrafish

Zebrafish embryos were incubated in different concentrations of ANA with or without CB[7] or β-CD. As was observed in

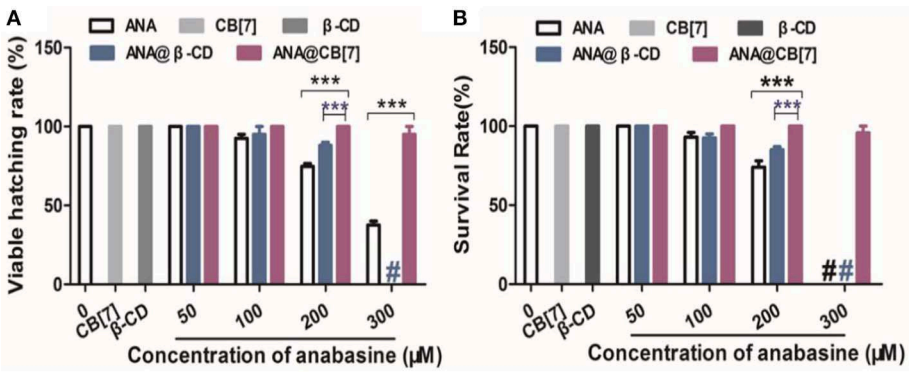

FIGURE 6 | (A) The hatching percentage, and **(B)** survival rate of zebrafish embryos treated with ANA w and w/o CB[7] (300 μM) or β-CD (1 mM), respectively, for 2 days. Data are presented as mean ± S.E.M. ($n = 25$–30). *** *denotes* $P < 0.001$. # denotes that all zebrafish embryos/larva were dead.

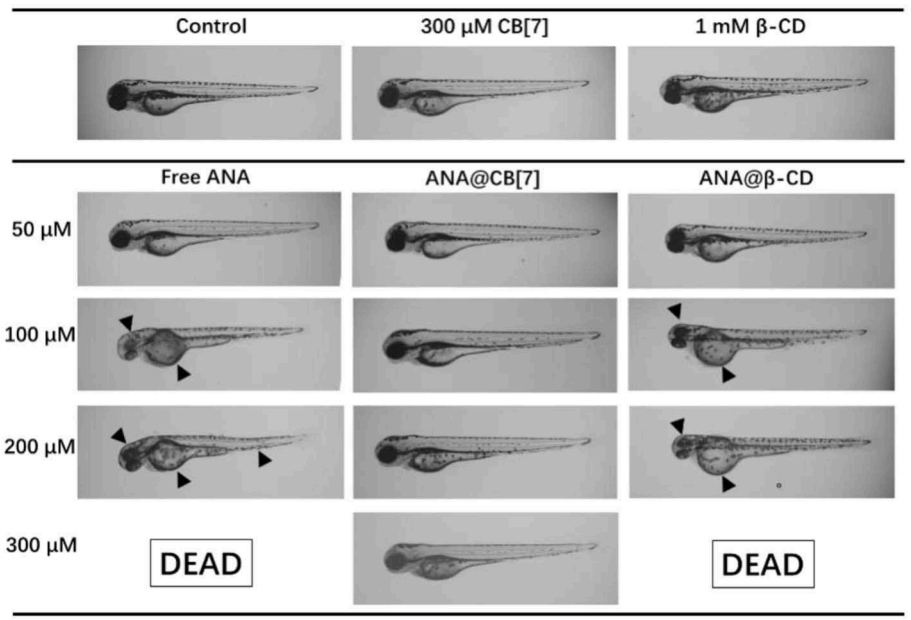

FIGURE 7 | Morphology of representative zebrafish larvae (72 hpf) upon treatment with ANA w and w/o CB[7]/β-CD, respectively, for 48 h. Black arrowheads point to the abnormal morphologies.

Figure 6A, the hatching rate of the fish was decreased with increasing concentrations of ANA, confirming a dose-dependent developmental toxicity of ANA in zebrafish. Embryos incubated with the highest concentration (300 μM) of ANA led to <50% hatching rate. Very interestingly, the hatching rate of embryonic fish incubated with ANA@CB[7] complex exhibited almost the same rate as that of the control group (medium only), suggesting that CB[7] could dramatically alleviate the embryonic developmental toxicity of ANA in fish embryos. Of note, CB[7] alone did not exhibit any signs of toxicity in this study. In contrast, the hatching rate of embryos treated with ANA in the presence of a high concentration of β-CD decreased dramatically with increasing amount of ANA, and the viable hatching rate turned to zero with 300 μM ANA with 1 mM β-CD, which is dramatically lower than that in the free ANA treated group, suggesting that β-CD even somewhat worsened the toxicity of ANA. Similarly, the survival rate of zebrafish treated with free ANA exhibited a dose-dependent manner. In contrast, the survival rate of embryos incubated with ANA@CB[7] complex was maintained the same during 48 h incubation in spite of the increasing doses of ANA. While β-CD showed little effect on the toxicity of ANA in the survival study (**Figure 6B**).

In addition, the developmental morphologies of the fish were further examined. As shown in **Figure 7**, embryo larvae treated with ANA@CB[7] complex displayed normal morphology as well as usual developmental progress, comparable to those in the blank group. In a dramatic contrast, zebrafish larvae treated with free ANA and the mixture of ANA and β-CD both showed obvious developmental malformation, including the malformation of notochord, such as lordosis or cyphosis, yolk deformity, and abnormal head shape. Moreover, with the highest concentration (300 μM) of ANA with and without β-CD, 100% larva were dead. Taken together, CB[7] exhibited significant inhibition effect on the developmental toxicity of ANA whereas β-CD exhibited negligible or even negative effects.

Indeed, several works have previously demonstrated that the CB[*n*]s may alleviate toxicity of guest or included species. For instance, CB[8] played a critical role on formulating a safe, photo-responsive herbicide formulation (Gao et al., 2018). CB[7] was previously reported to inhibit the non-specific teratogenic toxicity of a couple of representative pesticides on a zebrafish model, through a facile supramolecular encapsulation (Yang et al., 2018). In addition, CB[7] was studied for its encapsulation of trazodone (TZ), an anti-depression drug approved by the FDA, but can cause liver damage due to its toxicity (Huang et al., 2018b). CB[7] formed binary host-guest complex with TZ in a relatively strong complexation affinity, and *in vitro* and *in vivo* studies indicated that the hepatotoxicity from TZ were alleviated by CB[7] encapsulation Our present ANA@CB[7] study, as a representative case for guest alkaloid, further supported that CB[7] could become a functional excipient to potentially alleviate undesired toxicities of selected drug or bioactive molecules. And this investigation is the first one to compare the influences of two macrocyclic molecules, CB[7] and β-CD, on the toxicity of a guest species, which may provide new insights on drug's formulations.

CONCLUSIONS

In summary, CB[7] was shown to form a 1:1 stable host-guest complex with a natural alkaloid—ANA, with a relatively high binding affinity. The supramolecular encapsulation exhibited promising inhibitory effects on the developmental toxicity of ANA in zebrafish. In addition, for comparative purpose, β-CD was also investigated in this study, however exhibited negligible effects on the toxicity of ANA. Although β-CD has served as a pharmaceutical excipient for decades, our present study demonstrated that CB[7] might become an important, complementary excipient to β-CD, particularly for reducing undesired toxicity of active compounds such as alkaloids.

DATA AVAILABILITY STATEMENT

The datasets generated for this study are available on request to the corresponding author.

ETHICS STATEMENT

The animal study was reviewed and approved by the Animal Ethics Committee University of Macau.

AUTHOR CONTRIBUTIONS

The project was conceptually designed by YG, YH, and YW. The majority of the experiments were performed by YG and XY, assisted by ZW and ZZ. Data analysis and interpretation were carried out by YG, XY, and YH. The manuscript was prepared by YG, XY, YH, and YW. All authors discussed the results and implications and commented on the manuscript.

FUNDING

This work was financially supported by the Macao Science and Technology Development Fund (FDCT 071/2017/A2 and SKL-QRCM-2020-2022), and the Research Fund of University of Macau (CPG2020-00016-ICMS).

ACKNOWLEDGMENTS

We are also grateful to Prof. Ruibing Wang for technical guidance and helpful discussions.

REFERENCES

Assaf, K. I., and Nau, W. M. (2015). Cucurbiturils: from synthesis to high-affinity binding and catalysis. *Chem. Soc. Rev.* 44, 394–418. doi: 10.1039/C4CS00273C

Chen, H., Chan, J. Y. W., Li, S., Liu, J. J., Wyman, I. W., Lee, S. M. Y., et al. (2015a). *In vivo* reversal of general anesthesia by cucurbit[7]uril with zebrafish models. *RSC Adv.* 5, 63745–63752. doi: 10.1039/C5RA09406B

Chen, H., Chan, J. Y. W., Yang, X., Wyman, I. W., Bardelang, D., Macartney, D. H., et al. (2015b). Developmental and organ-specific toxicity of cucurbit[7]uril: *in vivo* study on zebrafish models. *RSC Adv.* 5, 30067–30074. doi: 10.1039/C5RA04335B

Daly, J. W. (2005). Nictotinic agonists, antagonists, and modulators from natural sources. *Cell. Mol. Neurobiol.* 25, 513–552. doi: 10.1007/s10571-005-3968-4

Day, A., Arnold, A. P., Blanch, R. J., and Snushal, B. (2001). Controlling factors in the synthesis of cucurbituril and its homologues. *J. Org. Chem*. 66, 8094–8100. doi: 10.1021/jo015897c

Gao, C., Huang, Q., Lan, Q., Feng, Y., Tang, F., Hoi, M. P. M., et al. (2018). A user-friendly herbicide derived from photo-responsive supramolecular vesicles. *Nat. Commun.* 9:2967. doi: 10.1038/s41467-018-05437-5

Green, B. T., Lee, S. T., Welch, K. D., and Panter, K. E. (2013a). Plant alkaloids that cause developmental defects through the disruption of cholinergic neurotransmission. *Birth Defects Res. C* 99, 235–246. doi: 10.1002/bdrc.21049

Green, B. T., Welch, K. D., Panter, K. E., and Lee, S. T. (2013b). Plant toxins that affect nicotinic acetylcholine receptors: a review. *Chem. Res. Toxicol.* 26, 1129–1138. doi: 10.1021/tx400166f

Huang, Q., Kuok, K. I., Zhang, X., Yue, X., Lee, S. M., Zhang, J., et al. (2018a). Inhibition of drug-induced seizure development in both zebrafish and mouse models by a synthetic nanoreceptor. *Nanoscale* 10, 10333–10336. doi: 10.1039/C8NR02041H

Huang, Q., Li, S., Yin, H., Wang, C., Lee, S. M. Y., and Wang, R. (2018b). Alleviating the hepatotoxicity of trazodone via supramolecular encapsulation. *Food Chem. Toxicol.* 112, 421–426. doi: 10.1016/j.fct.2017.12.016

Jacob, P., Yu, L., Shulgin, A. T., and Benowitz, N. L. (1999). Minor tobacco alkaloids as biomarkers for tobacco use: comparison of users of cigarettes, smokeless tobacco, cigars, and pipes. *Am. J. Public Health* 89, 731–736. doi: 10.2105/AJPH.89.5.731

Keeler, R. F., Crowe, M. W., and Lambert, E. A. (1984). Teratogenicity in swine of the tobacco alkaloid anabasine isolated from *Nicotiana glauca*. *Teratology* 30, 61–69. doi: 10.1002/tera.1420300109

Kimmerl, C. B., Ballard, W. W., Kimmel, S. R., Ullmann, B., and Schilling, T. F. (1995). Stages of embryonic development of the zebrafish. *Dev. Dyn.* 203, 253–310. doi: 10.1002/aja.1002030302

Kuok, K. L., Li, S., Wyman, I. W., and Wang, R. (2017). Cucurbit[7]uril: an emerging candidate for pharmaceutical excipients. *Ann. N. Y. Acad. Sci.* 1398, 108–119. doi: 10.1111/nyas.13376

Lagona, J., Mukhopadhyay, P., Chakrabarti, S., and Isaacs, L. (2005). The cucurbit[n]uril family. *Angew. Chem. Int. Ed. Engl.* 44, 4844–4870. doi: 10.1002/anie.200460675

Li, S., Chan, J. Y. W., Li, Y., Bardelang, D., Zheng, J., Yew, W. W., et al. (2016). Complexation of clofazimine by macrocyclic cucurbit[7]uril reduced its cardiotoxicity without affecting the antimycobacterial efficacy. *Org. Biomol. Chem.* 14, 7563–7569. doi: 10.1039/C6OB01060A

Manoguerra, A. S., and Freeman, D. (1982). Acute poisoning from the ingestion of *Nicotiana glauca*. *J. Toxicol. Clin. Toxicol.* 19, 861–864. doi: 10.3109/15563658208992520

McGrath, P., and Li, C. Q. (2008). Zebrafish: a predictive model for assessing drug-induced toxicity. *Drug Discov. Today* 13, 394–401. doi: 10.1016/j.drudis.2008.03.002

Mellick, L. B., Makowski, T., Mellick, G. A., and Borger, R. (1999). Neuromuscular blockade after ingestion of tree tobacco (*Nicotiana glauca*). *Ann. Emerg. Med.* 34, 101–104.doi: 10.1016/S0196-0644(99)70280-5

Mizrachi, N., Levy, S., and Goren, Z. (2000). Fatal poisoning from *Nicotiana glauca* leaves: identification of anabasine by gas-chromatography/mass spectrometry. *J. Forensic Sci.* 45, 736–741. doi: 10.1520/JFS14761J

Oun, R., Floriano, R. S., Isaacs, L., Rowan, E. G., and Wheate, N. J. (2014). The *ex vivo* neurotoxic, myotoxic and cardiotoxic activity of cucurbituril-based macrocyclic drug delivery vehicles. *Toxicol. Res.* 3, 447–455. doi: 10.1039/C4TX00082J

Panter, K. E., Bunch, R. F., Keeler, R. F., Sisson, D. V., and Callan, R. J. (1990). Multiple congenital contractures (mcc) and cleft palate induced in goats by ingestion of piperidine alkaloid-containing plants: reduction in fetal movement as the probable cause. *J. Toxicol. Clin. Toxicol.* 28, 69–83. doi: 10.3109/15563659008993477

Seikhanov, T. M., Nurkenov, O. A., Isaeva, A. Z., Nazarenko, L. A., and Seilkhanov, O. T. (2016). Preparation and NMR spectroscopic studies of the supramolecular inclusion complex of anabasine and β-cyclodextrin. *Chem. Nat. Comp.* 52, 1066–1068. doi: 10.1007/s10600-016-1862-6

Shetty, D., Khedkar, J. K., Park, K. M., and Kim, K. (2015). Can we beat the biotin–avidin pair?: cucurbit[7]uril-based ultrahigh affinity host–guest complexes and their applications. *Chem. Soc. Rev.* 44, 8747–8761. doi: 10.1039/C5CS00631G

Sims, D., James, R., and Christensen, T. (1999). Another death due to ingestion of *Nicotiana glauca*. *J. Forensic Sci.* 44, 447–449. doi: 10.1520/JFS14484J

Uzunova, V. D., Cullinane, C., Brix, K., Nau, W. M., and Day, A. I. (2010). Toxicity of cucurbit[7]uril and cucurbit[8]uril: an exploratory *in vitro* and *in vivo* study. *Org. Biomol. Chem.* 8, 2037–2042. doi: 10.1039/b925555a

Yang, X., Li, S., Zhang, Q. W., Zheng, Y., Bardelang, D., Wang, L. H., et al. (2017). Concealing the taste of the Guinness World's most bitter substance by using a synthetic nanocontainer. *Nanoscale* 9, 10606–10609. doi: 10.1039/C7NR03608F

Yang, X., Li, S. K., Lee, M. Y., Wang, L. H., and Wang, R. W. (2018). Constraining the teratogenicity of pesticide pollution by a synthetic nanoreceptor. *Chem. Asian J.* 13, 41–45. doi: 10.1002/asia.201701527

Yang, X., Wang, Z., Niu, Y., Chen, X., Lee, S. M. Y., and Wang, R. (2016). Influence of supramolecular encapsulation of camptothecin by cucurbit[7]uril: reduced toxicity and preserved anti-cancer activity. *Med. Chem. Commun.* 7, 1392–1397 doi: 10.1039/C6MD00239K

Yin, H., and Wang, R. (2018). Applications of cucurbit[n]urils (n=7 or 8) in pharmaceutical sciences and complexation of biomolecules. *Isr. J. Chem.* 58, 188–198. doi: 10.1002/ijch.201700092

Zhang, X., Xu, X., Li, S., Li, L., Zhang, J., and Wang, R. (2019). A synthetic receptor as a specific antidote for paraquat poisoning. *Theranostics.* 9, 633–645. doi: 10.7150/thno.31485

Zhang, X., Xu, X., Li, S., Wang, L.-H., Zhang, J., and Wang, R. (2018). A systematic evaluation of the biocompatibility of cucurbit[7]uril in mice. *Sci Rep.* 8:8819. doi: 10.1038/s41598-018-27206-6

Conflict of Interest: The authors declare that the research was conducted in the absence of any commercial or financial relationships that could be construed as a potential conflict of interest.

frontiers in Chemistry

ORIGINAL RESEARCH
published: 31 March 2020
doi: 10.3389/fchem.2020.00225

Enhanced Tumor Targeting and Radiotherapy by Quercetin Loaded Biomimetic Nanoparticles

Chunyu Huang[1,2†], *Tongkai Chen*[3†], *Daoming Zhu*[2] *and Qinqin Huang*[1*]

[1] *Department of Molecular Pathology, The Second Affiliated Hospital of Zhengzhou University, Zhengzhou, China,* [2] *Key Laboratory of Artificial Micro- and Nano-Structures of Ministry of Education, School of Physics and Technology, Wuhan University, Wuhan, China,* [3] *Science and Technology Innovation Center, Guangzhou University of Chinese Medicine, Guangzhou, China*

In Chinese traditional medicine, quercetin (QT) plays a fundamental role in the treatment of asthma, as an anti-allergen and to lower blood pressure. Recent evidence suggests that QT can improve tumor radiosensitivity through multiple mechanisms. However, poor tumor tissue targeting ability and low water solubility of QT limit its usefulness in the treatment of cancers. Herein, we designed a novel drug delivery system (CQM) consisting of inner QT loaded mesoporous silica nanoparticles (MSNs) and outer cancer cell membranes (CM). The developed nanoplatform had strong anti-cancer effects under X-ray irradiation and good QT loading characteristics. In addition, CQM effectively targeted tumor tissues. Results of *in vitro* and *in vivo* experiments demonstrated that the developed CQM drug delivery system has excellent tumor targeting ability and effectively inhibited tumor growth. Therefore, the CQM platform realized targeted drug delivery and radiotherapy sensitization, which provided a newfangled idea of cancer treatment.

Keywords: cancer cell membrane, quercetin, mesoporous silicon nanoparticles, drug delivery, enhanced radiotherapy

OPEN ACCESS

Edited by:
Ye Tian,
Nanjing University, China

Reviewed by:
Lingmin Zhang,
Guangzhou Medical University, China
Meng Yu,
Southern Medical University, China

****Correspondence:***
Qinqin Huang
qqhuang@zzu.edu.cn

† These authors have contributed equally to this work

Specialty section:
This article was submitted to Nanoscience, a section of the journal Frontiers in Chemistry

Received: *06 February 2020*
Accepted: *09 March 2020*
Published: *31 March 2020*

Citation:
Huang C, Chen T, Zhu D and Huang Q (2020) Enhanced Tumor Targeting and Radiotherapy by Quercetin Loaded Biomimetic Nanoparticles. Front. Chem. 8:225. doi: 10.3389/fchem.2020.00225

INTRODUCTION

In recent years, a number of novel cancer therapies have been developed such as photo thermal therapy (Lin et al., 2017; Yu et al., 2017; Zhou et al., 2018; Cao et al., 2019; Liu et al., 2019; Yang et al., 2019), photodynamic therapy (Song et al., 2015; Sun et al., 2017; Jiang et al., 2018), and chemo dynamic therapy (Zhang et al., 2016, 2019; Ma et al., 2018; Hu et al., 2019; Lei et al., 2019; Li et al., 2019; Xia et al., 2019; Xie Z. et al., 2019), however their adoption has been limited by unstable clinical effects. A traditional treatment for cancer, radiotherapy, has been extensively applied in clinical settings. Radiotherapy promotes the production of reactive oxygen species in tumor tissues, thus promoting tumor cell apoptosis and inhibition of tumor growth (Liu et al., 2015; Song et al., 2016a,c; Du et al., 2017; Lyu et al., 2019). Radiotherapy however, does not discriminate between normal and tumor cells, furthermore a number of tumor types are intrinsically resistant to radiotherapy which has led to a growing need for improved cancer therapies (Fan et al., 2015; Song et al., 2016b, 2017). Therefore, there is an urgent need to develop allergens in radiotherapy to enhance the effectiveness of radiotherapy.

DNA damage responses (DDR), which can reduce cellular death, play a large and necessary role in tumor therapy (Lin et al., 2012). Ataxia telangiectasia mutated (ATM) kinase is a critical DDR element which can mutate and result in an autosomal recessive genetic disease termed

Ataxia Telangiectasia (A-T). Patients who have A-T are extremely sensitive to radiotherapy, and thus are prefect subjects t receiving molecular radiosensitization. Quercetin (QT) is a major flavonoid, a class of secondary metabolic products of plants, which is used as a Chinese traditional medicine (Benkovic et al., 2009) in the treatment of asthma, as an anti-allergen, for lowering blood pressure and in treatment of tumors. Previously, it has been reported that treatment with QT can significantly increase tumor radiosensitivity by inhibiting ATM mediated pathways both *in vitro* and *in vivo*. When used systemically, natural QT is considered a radioprotective agent (Jiang et al., 2018). However, QT has poor tumor targeting ability and low water solubility which limits its systemic use during the treatment of cancers (Ma et al., 2019).

Very recently, the utilization of cellular membranes for surface functionalization of nanomaterials presents a novel method, which offers a unique advantage of a complete copy of the antigenic structure and function from cells to nanoparticles (Fang et al., 2018). Based on this, a series of cell membrane-camouflaged nanoparticles were developed and showed desirable features inherited from source cells. Nanoparticles coated with tumor cell membranes are considered to have good tumor tissue targeting and long circulating ability *in vivo* (Xie W. et al., 2019). However, there has been no research on the application of biomimetic nanoparticles for QT delivery.

In the present study, we designed a novel theranostic system CQM which consisted of a mesoporous silica nanoparticle (MSN) supported QT coated cancer cell membrane (CM) which has prolonged circulation in blood, improved tumor targeting ability, effective drug release capabilities, and strong anti-cancer effects. Mesoporous silica nanoparticles have good drug delivery characteristics due to their large surface area (>1,000 m^2 g^{-1}), high pore volume and tunable pore sizes (2–20 nm) (Ma et al., 2020). In addition, the surface of MSNs is easily loaded with hydrophobic drugs such as QT. Under acidic conditions, QT can be rapidly released from CQM and can therefore be specifically accumulated, and in combination with radiotherapy, can promote cell apoptosis. We investigated the novel theranostic system CQM *in vivo* and *in vitro* and observed that the system possessed outstanding tumor targeting ability and radio sensitivity which promotes tumor apoptosis.

RESULTS AND DISCUSSION

Characterization of CMC NPs

MSN NPs were successfully synthesized and loaded with QT through mechanical mixing. Transmission electron microscopy (TEM) images demonstrated that QT-loaded MSNs measured ∼100 nm in diameter. Cancer cell vesicle (CV)-coated CQM particles had a 6 nm gray outer membrane (**Figure 1A**). Loading of QT and the CV coating were also confirmed using dynamic light scattering (DLS) analysis, SDS-PAGE, and UV-Vis spectrometry. Furthermore, while MSNs (98.5 ± 3.4 nm) and QMs (99.2 ± 4.8 nm) were similar in size, CQM (115.2 ± 6.4 nm)

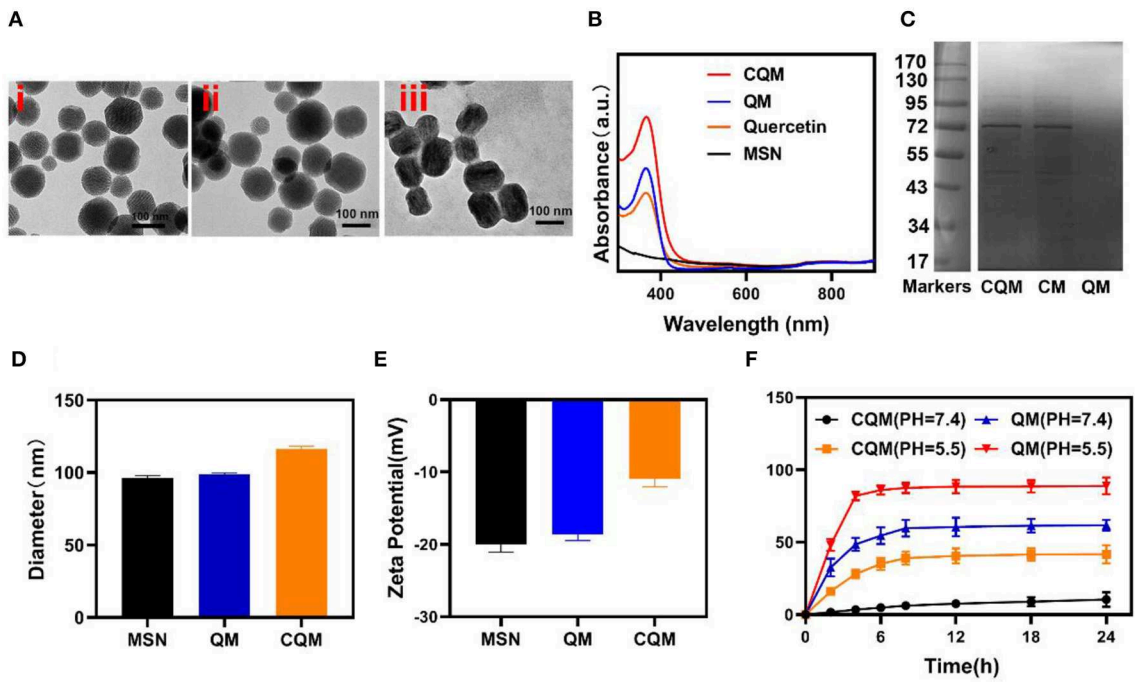

FIGURE 1 | Characterization of CQM nanoparticles. **(A)** TEM image of (i) MSNs, (ii) QM, and (iii) CQM. **(B)** Absorbance spectra of CQM, QM, QT, and MSNs. **(C)** SDS-PAGE protein analysis of CQM, CM, and QM. **(D)** Hydrodynamic diameter and **(E)** Zeta potential of MSN, QM, and CQM. **(F)** QT release profiles under different conditions.

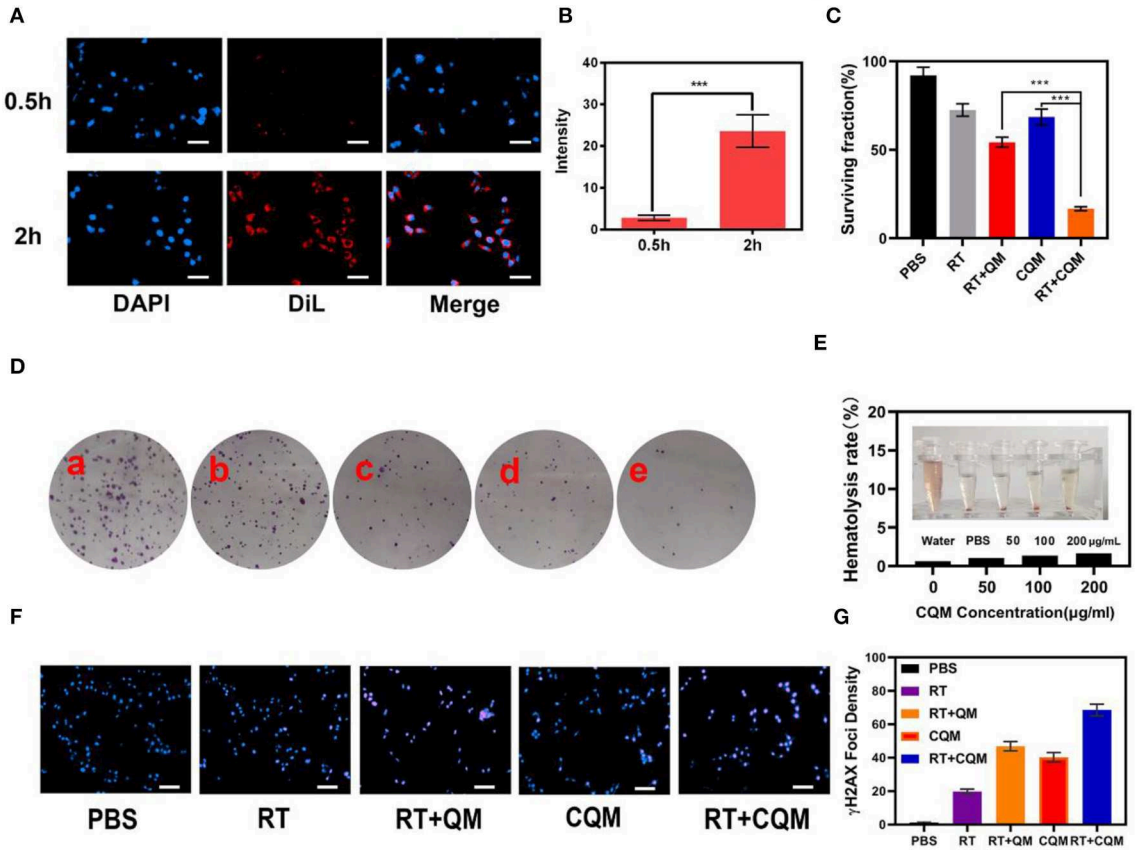

FIGURE 2 | Results of *in vitro* experiments. **(A)** Fluorescence images of 4T1 cells after treatment with CQM across time. Scale bars: 50 μm. **(B)** DiL fluorescence intensity of **(A)** measured using imageJ software. **(C)** Clonogenic 4T1 cell rate of survival when co-incubated with different formulations for 12 h prior to receiving RT or not. Colonies with >50 cells were counted. **(D)** 4T1 cells treated with (a) PBS, (b) RT, (c) CQM, (d) RT+QM, or (e) RT+CQM. The MSN concentration was 200 μg/mL and the irradiation dose was 4 Gy. **(E)** Hemolysis ratio of QM at different CQM concentrations. The inset presents the corresponding hemolysis images. **(F)** Representative fluorescence images of DNA fragmentation and nuclear condensation after different treatments. DAPI and γ-H2AX were used for nuclear visualization and DNA fragmentation, respectively. Scale bars: 50 μm. **(G)** Quantitative analysis of γ-H2AX foci density (γ-H2AX foci/100 μm^{-2}) for n >100 cells in each treatment group. Significant differences among groups as calculated using the Student's *t*-test. ***$P < 0.005$.

were larger than QM, thus indicating successful encapsulation of NPs in membrane vesicles (**Figure 1D**). The Zeta potential of the different particles showed similar trends (**Figure 1E**). In addition, CQM retained significant amounts of CM proteins (**Figure 1C**) and displayed characteristic peaks of QCT near 367 nm (**Figure 1B**). Next, we measured the release of QT from CQM NPs under different conditions. As presented in **Figure 1F**, under acidic conditions, QT was rapidly released from CQM and QM, whereas only small amounts were released under neutral conditions. When compared with QM, the rate of release of QT in CQM was less in acidic or neutral conditions, thus indicating less QT drug leakage.

In vitro Tumor Cells Internalization

Following characterization of CQM nanoparticles, *in vitro* experiments were conducted. As shown in **Figures 2A,B**, fluorescence images of 4T1 cells following treatment with CQM was observed at different time points. CQM fluoresced Dil red and fluorescence intensity increased with incubation time, indicating that CQM is readily accumulated by tumor cells.

In vitro Serum Stability and Enhanced RT

The effect of different NPs on cancer cell colony formation under X-ray irradiation was assessed. As presented in **Figures 2C,D**, non-irradiated PBS treated cells formed numerous and large colonies, which decreased following 4Gy irradiation. It was observed that the cancer cell survival rate differed between the CQM QM groups, thus demonstrating the cancer cell targeting capability of cancer cell membrane coated NPs. Results demonstrate that a combination of CQM and RT resulted in low colony formation and promoted cancer cell apoptosis. Serum stability of CQM in 1,640 medium containing 10% FBS was investigated. **Figure 2E** demonstrates that CQM was stable in blood as it caused low rates of hemolysis at all tested concentrations, thus indicating the stability of CQM in blood. Furthermore, we assessed cell DNA damage of the prepared nanoparticles (**Figures 2F,G**). As demonstrated in **Figure 2G**, no

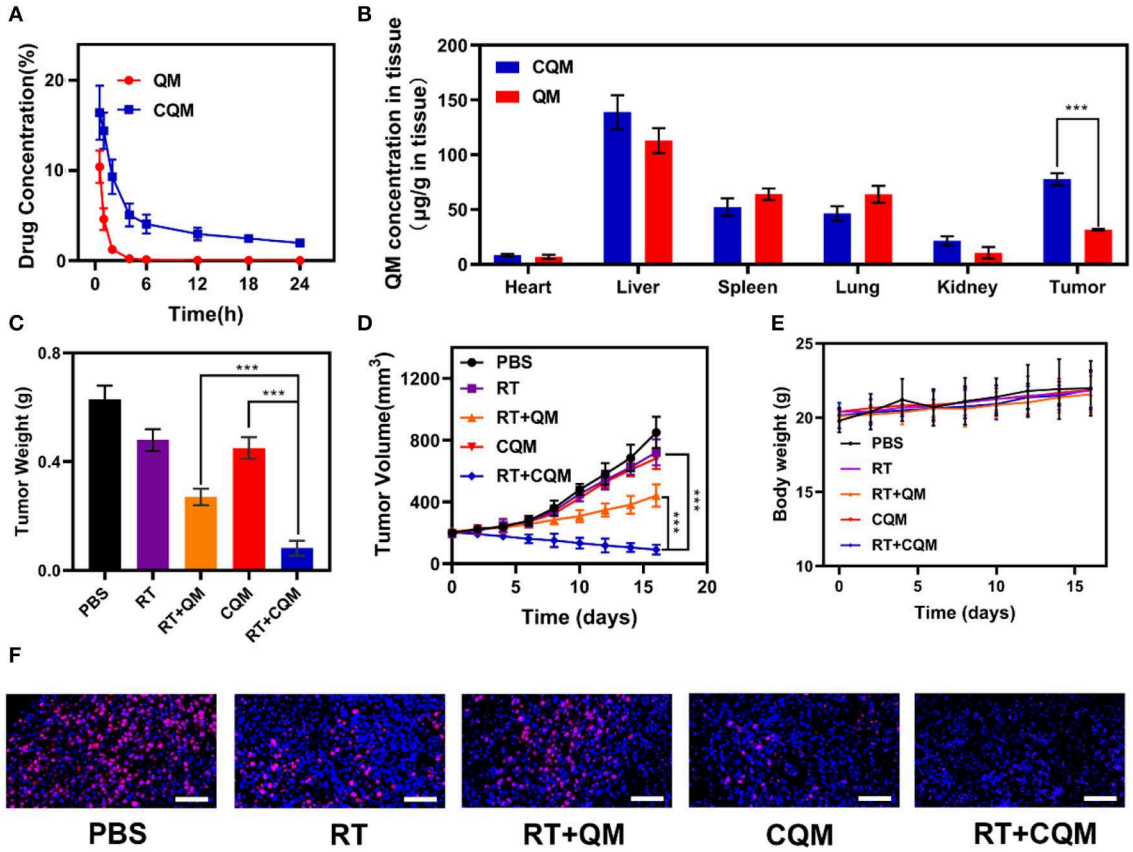

FIGURE 3 | Results of *in vivo* exposures. **(A)** Changes in tumor weight following treatment. **(B)** Change in tumor-volume curves of 4T1 tumor bearing mice after treatments. **(C)** Body weight of 4T1 tumor-bearing mice as recorded every 2 days following treatment. **(D)** Pharmacokinetic behavior of QM and CQM in mice following i.v. administration at doses of 5 mg/kg of MSNs. Data are presented as mean ± SD ($n = 3$). **(E)** Quantitative analysis of QM biodistribution in tissues and tumors of tumor-bearing mice injected with QM or CQM at MSNs dose of 5 mg/kg, respectively. **(F)** Representative Ki-67 stained tumor slice images of mice following treatment. Scale bars: 100 nm. Significant differences among groups as calculated using the Student's *t*-test. $^{***}P < 0.005$.

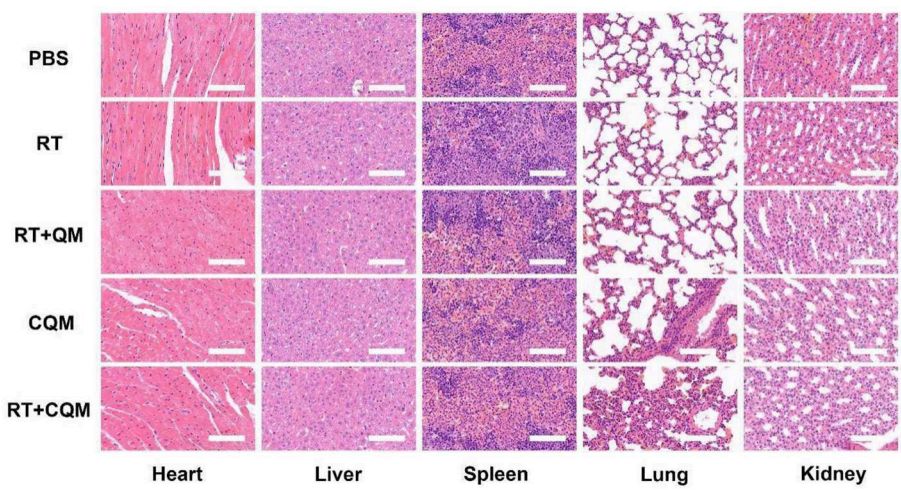

FIGURE 4 | Results of histopathological analysis (H&E stained images) of the major organs; heart, liver, spleen, lung, and kidney, of mice who received various treatments 16 days post-injection under laser irradiation conditions (scale bars: 100 μm).

DNA damage was apparent in the control group and only some cell death was observed in the RT group. Furthermore, the CQM and RT group resulted in significant DNA damage.

In vivo Pharmacokinetics and Biodistribution

In vitro experiments demonstrated that treatment with CQM when combined with radiotherapy resulted in tumor cell apoptosis. Therefore, *in vivo* pharmacokinetic experiments were conducted to investigate the effect of coated cancer membranes on retention in blood. Therefore, SD mice were administered QM and CQM or MSN *via* intravenous (i.v.) injection at doses of 5 mg/kg, respectively (**Figure 3A**). In comparison with the QM group, CQM exhibited enhanced blood retention, suggesting that cancer cell membrane coating prolongs evasion of the immune system MSNs. Next, we investigated biodistribution of QT in QM and CQM groups (**Figure 3B**). In both groups, QT distribution to the heart and kidney was low, while concentrations increased in the tumor and liver 6 h after administration. When compared with the QM group, QT distribution in the CQM group was greater, which further demonstrates the targeting ability of cancer cell membranes.

Antitumor Efficacy *in vivo* and Histological Analysis

In vivo translation potential of developed NPs was investigated. Mice bearing 4T1 tumors were divided into five groups with tumor volumes of approximately 200 mm3 (n = 5 per group): (1) PBS, (2) RT, (3) RT+QM, (4) CQM, or (5) RT+CQM group. Tumor volumes were measured every 2 days using a digital caliper, and tumor weights were calculated. As presented in **Figures 3C,D**, tumor weight of mice treated with PBS increased rapidly throughout the experiments, whereas tumor growth in the QM of the RT group was significantly suppressed. Tumor volume and weight in the CQM of the RT group was significantly suppressed, thus indicating that combination therapy worked best. As demonstrated in **Figure 3E**, the body-weight of all groups developed normally indicating an absence of adverse effects. Following treatment ki-67 staining was conducted (**Figure 3F**), and results demonstrated that CQM + RT effectively inhibited tumor cell proliferation. Furthermore, 16 days after injection, mice were sacrificed and the heart, liver, spleen, lung, and kidney were collected and observed for histological abnormalities. Histopathological analysis of major organs (**Figure 4**) demonstrated that treatment with CQM did not result in noticeable pathological changes when compared with the other treatment groups, highlighting its biocompatibility.

CONCLUSIONS

Overall, a novel drug delivery system (CQM) was designed which was composed of inner QT loaded mesoporous silica nanoparticles (MSNs) and outer cancer cell membranes (CM), which when combined with RT, promoted tumor cell apoptosis. The platform had great tumor targeting ability due to the cancer cell membrane coating. Furthermore, experimental results demonstrated that our system initiated optimal tumor cell apoptosis *in vitro* and inhibited tumor growth *in vivo*. This platform provides the basis for the development of novel radiotherapy sensitization clinical therapies.

DATA AVAILABILITY STATEMENT

The datasets generated for this study are available on request to the corresponding author.

ETHICS STATEMENT

The animal study was reviewed and approved by Institutional Animal Care and Use Committee of Zhengzhou University (Approval number: ZDYWYJY2019018).

AUTHOR CONTRIBUTIONS

All authors listed have made a substantial, direct and intellectual contribution to the work, and approved it for publication.

FUNDING

This work was supported by the National Natural Science Foundation of China (31800085).

REFERENCES

Benkovic, V., Knezevic, A. H., Dikic, D., Lisicic, D., Orsolic, N., Basic, I., et al. (2009). Radioprotective effects of quercetin and ethanolic extract of propolis in gamma-irradiated mice. *Arh. Hig. Rada. Toksikol.* 60, 129–138. doi: 10.2478/10004-1254-60-2009-1908

Cao, Y., Wu, T., Zhang, K., Meng, X., Dai, W., Wang, D., et al. (2019). Engineered exosome-mediated near-infrared-II region V2C quantum dot delivery for nucleus-target low-temperature photothermal therapy. *ACS Nano* 13, 1499–1510. doi: 10.1021/acsnano.8b07224

Du, J., Gu, Z., Yan, L., Yong, Y., Yi, X., Zhang, X., et al. (2017). Poly(Vinylpyrollidone)- and selenocysteine-modified Bi_2 Se_3 nanoparticles enhance radiotherapy efficacy in tumors and promote radioprotection in normal tissues. *Adv. Mater.* 29. doi: 10.1002/adma.201701268

Fan, W., Bu, W., Zhang, Z., Shen, B., Zhang, H., He, Q., et al. (2015). X-ray radiation-controlled NO-release for on-demand depth-independent hypoxic radiosensitization. *Angew. Chem. Int. Ed. Engl.* 54, 14026–14030. doi: 10.1002/anie.201504536

Fang, R. H., Kroll, A. V., Gao, W., and Zhang, L. (2018). Cell membrane coating nanotechnology. *Adv. Mater.* 30:e1706759. doi: 10.1002/adma.201706759

Hu, J. J., Chen, Y., Li, Z. H., Peng, S. Y., Sun, Y., and Zhang, X. Z. (2019). Augment of oxidative damage with enhanced photodynamic process and MTH1 inhibition for tumor therapy. *Nano Lett.* 19, 5568–5576. doi: 10.1021/acs.nanolett.9b02112

Jiang, W., Zhang, H., Wu, J., Zhai, G., Li, Z., Luan, Y., et al. (2018). CuS@MOF-based well-designed quercetin delivery system for chemo-photothermal therapy. *ACS Appl. Mater. Interfaces* 10, 34513–34523. doi: 10.1021/acsami.8b13487

Lei, S., Chen, J., Zeng, K., Wang, M., and Ge, X. (2019). Visual dual chemodynamic/photothermal therapeutic nanoplatform based on superoxide dismutase plus Prussian blue. *Nano Res.* 12, 1071–1082. doi: 10.1007/s12274-019-2348-1

Li, W., Yang, J., Luo, L., Jiang, M., Qin, B., Yin, H., et al. (2019). Targeting photodynamic and photothermal therapy to the endoplasmic reticulum enhances immunogenic cancer cell death. *Nat. Commun.* 10:3349. doi: 10.1038/s41467-019-11269-8

Lin, C., Yu, Y., Zhao, H. G., Yang, A., Yan, H., and Cui, Y. (2012). Combination of quercetin with radiotherapy enhances tumor radiosensitivity *in vitro* and *in vivo*. *Radiother. Oncol.* 104, 395–400. doi: 10.1016/j.radonc.2011.10.023

Lin, H., Gao, S., Dai, C., Chen, Y., and Shi, J. (2017). A two-dimensional biodegradable niobium carbide (MXene) for photothermal tumor eradication in NIR-I and NIR-II biowindows. *J. Am. Chem. Soc.* 139, 16235–16247. doi: 10.1021/jacs.7b07818

Liu, Y., Liu, Y., Bu, W., Xiao, Q., Sun, Y., Zhao, K., et al. (2015). Radiation-/hypoxia-induced solid tumor metastasis and regrowth inhibited by hypoxia-specific upconversion nanoradiosensitizer. *Biomaterials* 49, 1–8. doi: 10.1016/j.biomaterials.2015.01.028

Liu, Y., Zhen, W., Wang, Y., Liu, J., Jin, L., Zhang, T., et al. (2019). Double switch biodegradable porous hollow trinickel monophosphide nanospheres for multimodal imaging guided photothermal therapy. *Nano Lett.* 19, 5093–5101. doi: 10.1021/acs.nanolett.9b01370@@uline@

Lyu, M., Zhu, D., Duo, Y., Li, Y., and Quan, H. (2019). Bimetallic nanodots for tri-modal CT/MRI/PA imaging and hypoxia-resistant thermoradiotherapy in the NIR-II biological windows. *Biomaterials* 233:119656. doi: 10.1016/j.biomaterials.2019.119656

Ma, B., Wang, S., Liu, F., Zhang, S., Duan, J., Li, Z., et al. (2018). Self-assembled copper-amino acid nanoparticles for in situ glutathione "AND" H_2O_2 sequentially triggered chemodynamic therapy. *J. Am. Chem. Soc.* 141, 849–857. doi: 10.1021/jacs.8b08714

Ma, T., Liu, Y., Wu, Q., Luo, L., Cui, Y., Wang, X., et al. (2019). Quercetin-modified metal-organic frameworks for dual sensitization of radiotherapy in tumor tissues by inhibiting the carbonic anhydrase IX. *ACS Nano* 13, 4209–4219. doi: 10.1021/acsnano.8b09221

Ma, W., Zhu, D., Li, J., Chen, X., Xie, W., Jiang, X., et al. (2020). Coating biomimetic nanoparticles with chimeric antigen receptor T cell-membrane provides high specificity for hepatocellular carcinoma photothermal therapy treatment. *Theranostics* 10, 1281–1295. doi: 10.7150/thno.40291

Song, G., Chao, Y., Chen, Y., Liang, C., Yi, X., Yang, G., et al. (2016a). All-in-one theranostic nanoplatform based on hollow taox for chelator-free labeling imaging, drug delivery, and synergistically enhanced radiotherapy. *Adv. Funct. Mater.* 26, 8243–8254. doi: 10.1002/adfm.201603845

Song, G., Chen, Y., Liang, C., Yi, X., Liu, J., Sun, X., et al. (2016b). Catalase-loaded TaOx nanoshells as bio-nanoreactors combining high-Z element and enzyme delivery for enhancing radiotherapy. *Adv. Mater.* 28, 7143–7148. doi: 10.1002/adma.201602111

Song, G., Cheng, L., Chao, Y., Yang, K., and Liu, Z. (2017). Emerging nanotechnology and advanced materials for cancer radiation therapy. *Adv. Mater.* 29. doi: 10.1002/adma.201700996

Song, G., Liang, C., Gong, H., Li, M., Zheng, X., Cheng, L., et al. (2015). Core-shell MnSe@Bi2 Se3 fabricated via a cation exchange method as novel nanotheranostics for multimodal imaging and synergistic thermoradiotherapy. *Adv. Mater.* 27, 6110–6117. doi: 10.1002/adma.201503006

Song, G., Liang, C., Yi, X., Zhao, Q., Cheng, L., Yang, K., et al. (2016c). Perfluorocarbon-loaded hollow Bi2Se3 nanoparticles for timely supply of oxygen under near-infrared light to enhance the radiotherapy of cancer. *Adv. Mater.* 28, 2716–2723. doi: 10.1002/adma.201504617

Sun, H., Su, J., Meng, Q., Yin, Q., Chen, L., Gu, W., et al. (2017). Cancer cell membrane-coated gold nanocages with hyperthermia-triggered drug release and homotypic target inhibit growth and metastasis of breast cancer. *Adv. Funct. Mater.* 27:1604300. doi: 10.1002/adfm.201604300.

Xia, D., Xu, P., Luo, X., Zhu, J., Gu, H., and Huo, D. (2019). Overcoming hypoxia by multistage nanoparticle delivery system to inhibit mitochondrial respiration for photodynamic therapy. *Adv. Funct. Mater.* 29:1807294. doi: 10.1002/adfm.201807294

Xie, W., Deng, W. W., Zan, M., Rao, L., Yu, G. T., Zhu, D. M., et al. (2019). Cancer cell membrane camouflaged nanoparticles to realize starvation therapy together with checkpoint blockades for enhancing cancer therapy. *ACS Nano* 13, 2849–2857. doi: 10.1021/acsnano.8b03788

Xie, Z., Cai, X., Sun, C., Liang, S., Shao, S., Huang, S., et al. (2019). O2-loaded pH-responsive multifunctional nanodrug carrier for overcoming hypoxia and highly efficient chemo-photodynamic cancer therapy. *Chem. Mater.* 31, 483–490. doi: 10.1021/acs.chemmater.8b04321

Yang, J., Xie, R., Feng, L., Liu, B., Lv, R., Li, C., et al. (2019). Hyperthermia and controllable free radical coenhanced synergistic therapy in hypoxia enabled by near-infrared-II light irradiation. *ACS Nano* 13, 13144–13160. doi: 10.1021/acsnano.9b05985

Yu, X., Li, A., Zhao, C., Yang, K., Chen, X., and Li, W. (2017). Ultrasmall semimetal nanoparticles of bismuth for dual-modal computed tomography/photoacoustic imaging and synergistic thermoradiotherapy. *ACS Nano* 11, 3990–4001. doi: 10.1021/acsnano.7b00476

Zhang, C., Bu, W., Ni, D., Zhang, S., Li, Q., Yao, Z., et al. (2016). Synthesis of iron nanometallic glasses and their application in cancer therapy by a localized fenton reaction. *Angew. Chem. Int. Ed. Engl.* 55, 2101–2106. doi: 10.1002/anie.201510031

Zhang, K., Yu, Z., Meng, X., Zhao, W., Shi, Z., Yang, Z., et al. (2019). A Bacteriochlorin-based metal-organic framework nanosheet superoxide radical generator for photoacoustic imaging-guided highly efficient photodynamic therapy. *Adv. Sci.* 6:1900530. doi: 10.1002/advs.201900530

Zhou, J., Jiang, Y., Hou, S., Upputuri, P. K., Wu, D., Li, J., et al. (2018). Compact plasmonic blackbody for cancer theranosis in the near-infrared II window. *ACS Nano* 12, 2643–2651. doi: 10.1021/acsnano.7b08725

Conflict of Interest: The authors declare that the research was conducted in the absence of any commercial or financial relationships that could be construed as a potential conflict of interest.

frontiers in Chemistry

ORIGINAL RESEARCH
published: 07 April 2020
doi: 10.3389/fchem.2020.00251

Injectable Hydrogel for NIR-II Photo-Thermal Tumor Therapy and Dihydroartemisinin-Mediated Chemodynamic Therapy

Danyang Chen[1†], Chuang Chen[2†], Chunyu Huang[1], Tongkai Chen[3] and Zeming Liu[1*]*

[1] Department of Plastic Surgery, Zhongnan Hospital of Wuhan University, Wuhan, China, [2] Department of Breast and Thyroid Surgery, Renmin Hospital of Wuhan University, Wuhan, China, [3] Science and Technology Innovation Center, Guangzhou University of Chinese Medicine, Guangzhou, China

In traditional Chinese medicine, dihydroartemisinin (DHA) is the focus of extensive attention because of its unique activity with Fe^{2+} to produce reactive oxygen species (ROS) and promote apoptosis. In this work, we designed a newfangled ink@hydrogel containing $FeCl_3$, traditional Chinese ink (Hu Kaiwen ink), and agarose hydrogel to create a synergistic activity with DHA in the treatment of cancer. When the system is irradiated under 1,064 nm for a few minutes, the ink in the ink@hydrogel converts the light to heat and hyperthermia causes the reversible hydrolysis of hydrogel. Then, Fe^{3+} quickly diffuses from the hydrogel to the tumor microenvironment and is reduced to Fe^{2+} to break the endoperoxide bridge in pre-injected DHA, which results in the release of free radicals for a potent anticancer action. To our knowledge, this is the first report of a hydrogel tumor therapy system that induces a photo-thermal response in the second near infrared window (NIR-II). *in vivo* experiments also showed a significant effect of DHA-Fe^{2+} in chemodynamic therapy (CDT) and in photo-thermal therapy. This hydrogel platform provided an encouraging idea for synergistic tumor therapy.

Keywords: injectable hydrogel, NIR-II photothemal therapy, dihydroartemisinin, Hu Kaiwen ink, chemodynamic therapy

OPEN ACCESS

Edited by:
Wei Cao,
Northwestern University, United States

Reviewed by:
Yang Mai,
Sun Yat-sen University, China
Junzhe Lou,
Harvard University, United States

****Correspondence:***
Tongkai Chen
chentongkai@gzucm.edu.cn
Zeming Liu
6myt@163.com

[†]These authors have contributed equally to this work

Specialty section:
This article was submitted to Nanoscience, a section of the journal Frontiers in Chemistry

Received: *12 February 2020*
Accepted: *17 March 2020*
Published: *07 April 2020*

Citation:
Chen D, Chen C, Huang C, Chen T and Liu Z (2020) Injectable Hydrogel for NIR-II Photo-Thermal Tumor Therapy and Dihydroartemisinin-Mediated Chemodynamic Therapy. Front. Chem. 8:251. doi: 10.3389/fchem.2020.00251

INTRODUCTION

Cancer is the leading cause of death worldwide and poses a huge threat to human health, even after the recent significant research advances (Li et al., 2017; Wu et al., 2018; Zhang et al., 2019). Recently, new tumor treatments, such as photothermal therapy (PTT) (Chu and Dupuy, 2014; Song et al., 2015; Sun et al., 2017; Yang et al., 2017; Jiang et al., 2018; Zhou et al., 2018; Liu et al., 2019) and chemodynamic therapy (CDT) (Jia et al., 2016), have attracted much attention due to the limited side effects and drug resistance compared with traditional strategies like chemotherapy, surgery, and radiotherapy.

The emerging PTT treatment uses nanoparticles as photo-thermal agents (PTAs) (Sun et al., 2017; Jiang et al., 2018; Cao et al., 2019; Yang et al., 2019) since they have a high absorbance in the near-infrared (NIR) to convert light to thermal energy and induce tumor ablation. PTT causes little damage to the patient and has minimal side effects. It can be used by itself or combined with other therapies like photodynamic therapy (PDT) (Hu et al., 2019; Liang et al., 2019). However, most PTAs have a limited penetration depth since they are only active in the NIR-I window (750–1,000 nm), which reduces their efficiency and clinical performance. Although NIR-II radiation (1,000–1,350 nm) (Lin et al., 2017; Yu et al., 2017; Cao et al., 2019)

has a better maximum permissible exposure (MPE) and a larger penetration depth, there is a lack of PTAs with a strong enough absorption and a high enough photo-thermal conversion efficiency. Therefore, it is necessary to explore PTAs that are active in the NIR-II window for tumor therapy. Traditional Chinese ink like the Hu Kaiwen ink has a good photo-thermal conversion efficiency, a high stability in liquid, and an excellent biocompatibility. It is therefore expected to have a great potential as an NIR-II photo-thermal material (Wang et al., 2017; Ouyang et al., 2019). Recently, light-responsive hydrogel (Xing et al., 2016; Niu et al., 2017; Hou et al., 2018; Qiu et al., 2018; Wu et al., 2019) was introduced as creative and novel drug release vessel for tumor treatment. It has attached much attention and has a great potential for the controlled release of active agents. Furthermore, the drug release rate can be controlled by changing the power density of the incident light and the exposure time to modify the dissolution of the hydrogel. However, the photo-thermal response of hydrogels in the NIR-II spectrum has not yet been studied.

In traditional Chinese medicine, dihydroartemisinin (DHA) and its derivatives have been extensively used as an effective anti-malaria drug since the 1970s (Wang et al., 2016). Recently, they have been studied as alternative tumor therapeutic agents to kill various tumor cells *in vitro* and *in vivo* through the generation of active oxygen radicals via the homolytic cleavage of the weak endoperoxide bridge accelerated by high concentrations of ferrous irons (Wang et al., 2016). However, the insufficient availability of Fe^{2+} in the tumor tissues severely limits the clinical performance and an urgent solution is needed to increase the Fe^{2+} content in the tumor tissues and create a synergetic therapy with DHA.

Herein, we designed a newfangled ink@hydrogel containing $FeCl_3$, traditional Chinese ink (Hu Kaiwen ink), and agarose hydrogel to act synergistically with DHA in the treatment of cancer. When the system is irradiated at 1,064 nm for a few minutes, the ink in the ink@hydrogel converts light to heat and hyperthermia causes the reversible hydrolysis of hydrogel. Then, Fe^{3+} ions diffuse from the hydrogel to the tumor microenvironment and are reduced to Fe^{2+} to promote the breakage of the endoperoxide bridge in the pre-injected DHA. This results in the release of free radicals for a potent anticancer effect. To our best knowledge, this is the first report of a hydrogel system for tumor therapy that creates a photo-thermal response in the NIR-II biological window. *In vivo* experiments are carried out to determine the efficiency of DHA-Fe^{2+} in chemodynamic therapy (CDT) and in photo-thermal therapy. This special hydrogel treatment way provided a great idea for synergistic tumor therapy.

RESULTS AND DISCUSSION

Synthesis and Characterization of the Hydrogel

First, the ink was diluted to a light concentration to produce a usable sample. **Figure 1A** show the various hydrogels prepared. Each hydrogel was prepared in a centrifuge tube and did not flow downwards once gelation was complete. The nanoscale morphology of the ink was determined by transmission electron microscopy (TEM) (**Figure 1B**). The ink mostly presented small aggregates. Rheology measurements on the ink@hydrogel (a mixture of agarose hydrogel and ink) with different ink concentrations showed a decrease in the storage modulus for increasing ink concentrations, as shown in **Figure 1C**. When the temperature increases, the storage modulus of the hydrogel decreases, which confirms the successful formation of the hydrogel. Representative SEM (scanning electron microscope) images of the ink@hydrogel (**Figures 1D,E**) indicated a complex pore size distribution where different concentrations and temperatures produced different pore sizes. A power density of 1 W/cm^2 at 1,064 nm irradiation was used to evaluate the temperature control ability of ink@hydrogel (**Figure 1F**). Initially, the dark colors of conglomerated ink@hydrogel were observed, but persistent laser irradiation faded the colors, indicating the degradation of the ink@hydrogel. Infrared thermal imaging (**Figure 1F**) also confirmed the increase of the temperature in the ink@hydrogel upon laser irradiation. We measured the release rate of Fe^{3+} in the hydrogel with or without laser irradiation (**Figure 1G**). The ink@hydrogel gradually dissolved and released Fe^{3+} under laser irradiation at 1,064 nm (1 W/cm^2), whereas there was no significant change in the group without laser irradiation, which showed that the hydrogel was irradiated by laser irradiation to dissolve and release iron ions.

Photo-Thermal of the ink@hydrogel for PTT

The photo-thermal performance of the ink was estimated by irradiating a centrifuge tube containing an aqueous ink dispersion at various concentrations (0, 10, 25, 50, and 100 μg/mL) with an NIR laser (1,064 nm, 1 W/cm^2) in parallel, while capturing the infrared thermal images of the ink solutions to confirm the temperature response during irradiation (**Figures 2A,B**). The photo-thermal heating effect of the ink was concentration-dependent for a fixed irradiation power. Higher ink concentrations resulted in a greater heating effect, which indicated that the ink efficiently converted light to thermal energy. Furthermore, the temperature of the ink solution at 100 μg/mL increased from the initial 35°C to nearly 60°C in 5 min. This suggests that the laser irradiation triggers a forceful hyperthermia and the elevated temperature is sufficient to damage tumor cells through the destruction of the intracellular protein and genetic materials. The ink solution was irradiated at 1,064 nm with 1 W/cm^2 for 5 min. Then, the laser was turned off to allow the initial temperature to recover. This cycle was repeated four times (**Figure 2C**) to demonstrate that the variation of the peak temperature in every cycle was negligible and that the photo-thermal performance of the ink was stable and reproducible during cycling. The photo-thermal conversion efficiency (η) of the ink was calculated from the data of **Figures 2D,F** and was as high as 35.0%, which is higher than Au nanorods (21%), graphene quantum dots (28.58%), and Ti_3C_2 nanosheets (30.6%) (Liu et al., 2015; Rasool et al., 2016; Shao et al., 2016; Deng et al., 2019). **Figure 2E** shows the UV-visible-NIR absorbance spectrum of the ink solution, revealing a broad and strong absorbance between 800 and 1,100 nm, without any

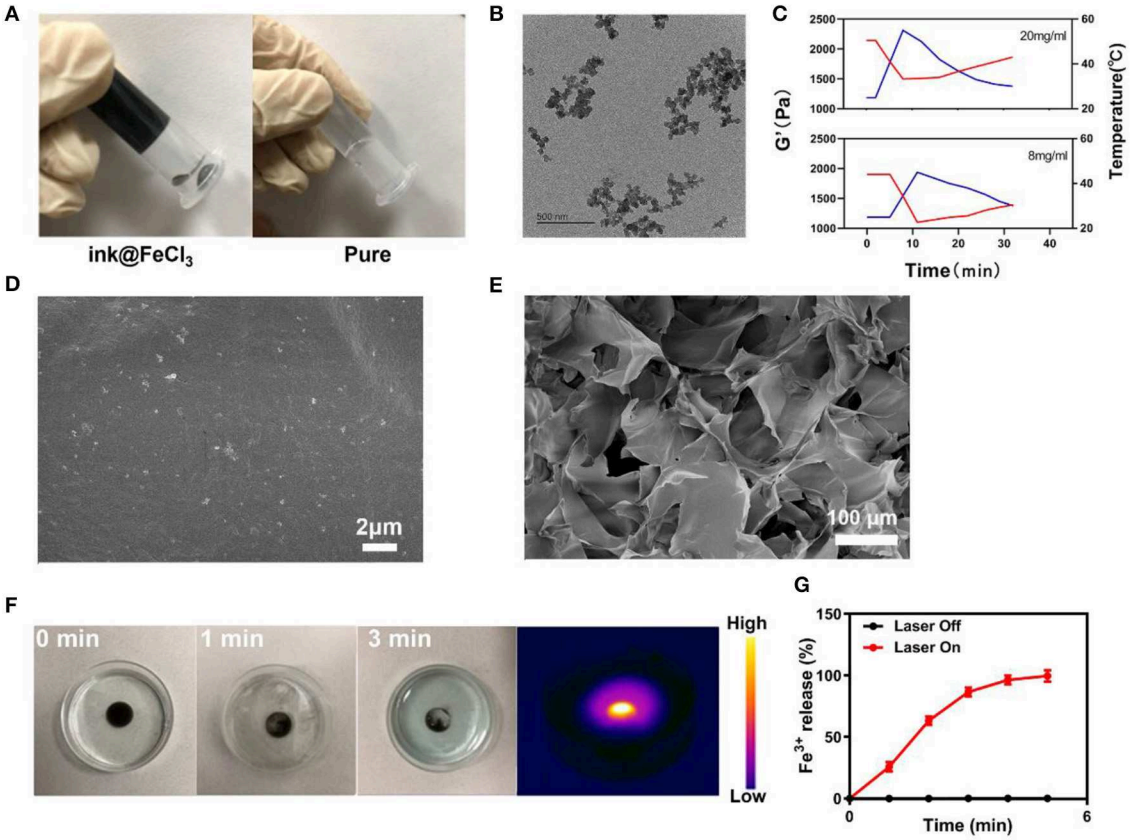

FIGURE 1 | (A) Various hydrogels prepared. **(B)** TEM image of the ink. **(C)** Rheological curve (red line) and corresponding temperature curve (blue line) of ink@hydrogel under NIR irradiation at 1 W/cm^2. **(D)** SEM image of the ink@hydrogel. **(E)** SEM image of the ink@hydrogel at a lower magnification. **(F)** Hydrogel dissolved by the 1,064-nm laser irradiation (1 W/cm^2). **(G)** Release rate of Fe^{3+} from the ink@hydrogel with (red) and without (black) laser irradiation.

obvious peak. This indicates that the hydrogel is a very suitable photo-thermal material.

In vitro Combination Therapy

We prepared appropriate amounts of ink@hydrogel to generate ROS *in vitro*. After the 4T1 cells were treated with different hydrogels for 2 h, the ROS stress level in the cells was measured by fluorescence microscope (**Figures 3A,B**). Upon laser irradiation, the ink@hydrogel samples had a high ROS level, whereas the un-irradiated hydrogel samples and irradiated PBS control had lower ROS levels. This might be attributed to the dissolution of the ink@hydrogel released Fe^{3+} ions that were then locally reduced to Fe^{2+}, which can be coupled with DHA. Next, we examined the fluorescence images of the 4T1 cells stained with FDA (Fluorescein diacetate) (live cells, green fluorescence) and PI (propidium iodide) (dead cells, red fluorescence) under different conditions (**Figure 3C**). By comparing the images of the ink@hydrogel group with or without laser irradiation, the viability of the 4T1 cells significantly decreased upon laser irradiation most likely due to the temperature increase that triggers the dissolution of the hydrogel and releases Fe^{3+} ions. The group with ink@hydrogel and DHA subjected to the laser irradiation showed a high level of apoptosis due to the generation of hydroxyl radicals from the breakage of endoperoxide bridges during the action of DHA and Fe^{2+}. **Figure 3D** later confirmed the cell toxicity of the hydrogel with DHA upon laser irradiation. The cells incubated with hydrogel were damaged and died after 5 min of laser irradiation.

In vivo Anti-tumor Study

Since the *in vitro* results were very encouraging for the ink@hydrogel combined with DHA, we studied the *in vivo* potential. Mice bearing 4T1 tumors were split into five groups when the tumor volume reached ≈200 mm^3 ($n = 5$): (1) PBS solution group, (2) laser irradiation group, (3) 5 mg/kg DHA solution group, (4) ink@hydrogel with laser irradiation, (5) ink@hydrogel and DHA with laser irradiation. The five groups significantly demonstrated the efficiency of a therapy using hydrogel combined with DHA and laser irradiation. DHA was administered by intra-peritoneal injection whereas the other solutions were administered by orthotopic injection. DHA was injected 12 h before the ink@hydrogel. **Figure 4A** shows an infrared image of the PBS group and the hydrogel with DHA group under laser irradiation. The temperature in the

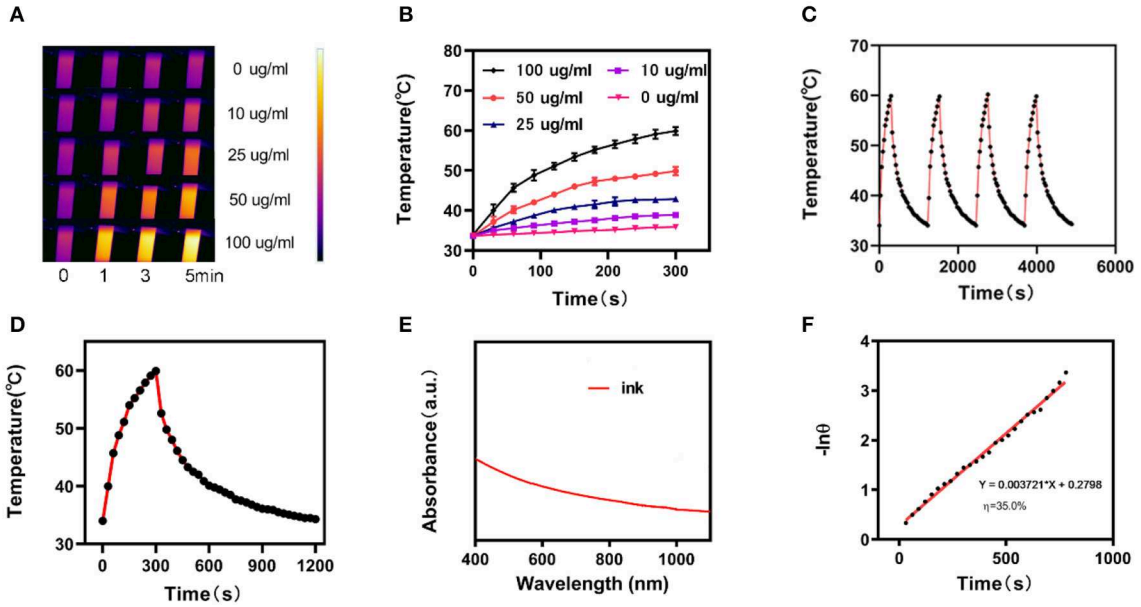

FIGURE 2 | (A) Infrared thermographic maps of ink solution in the centrifuge tube upon NIR laser irradiation for 0–5 min. **(B)** Temperature increase for the different ink concentrations upon laser irradiation at 1,064 nm and 1 W/cm^2 for 5 min. **(C)** Temperature variation of an ink solution at 100 mg/mL under cyclic laser irradiation during which the laser is on for 20 min in each cycle. **(D)** Temperature profile of an ink solution at 100 mg/mL upon heating when the laser is on and subsequent cooling once the laser is turned off. **(E)** UV-visible-NIR absorbance spectrum of an ink solution. **(F)** Calculation of the time constant for the heat transfer using a linear regression of the cooling profile.

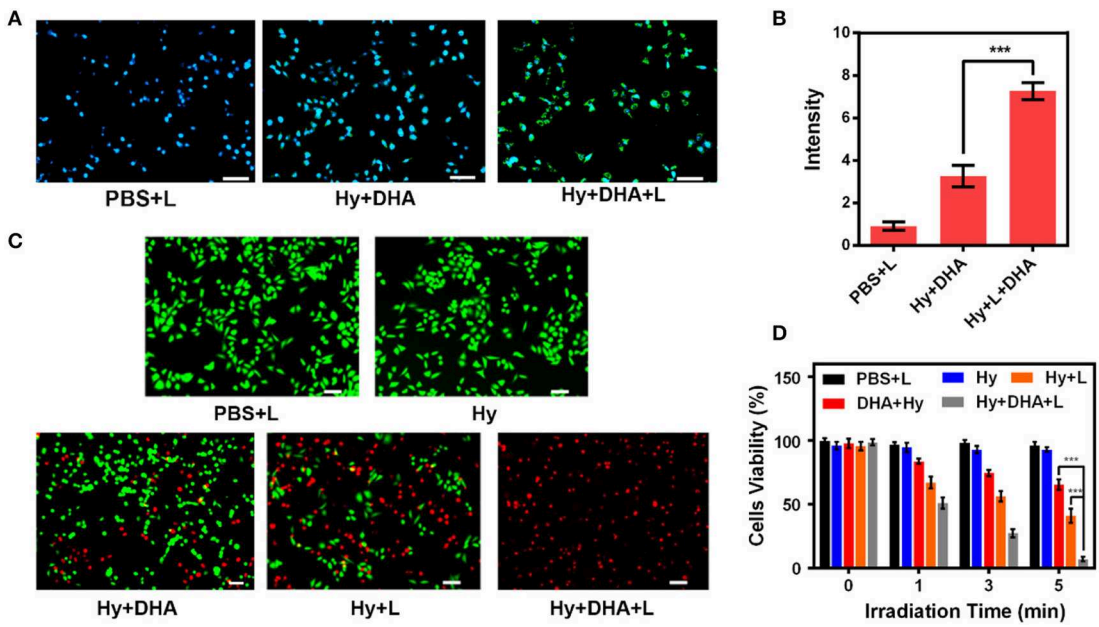

FIGURE 3 | (A) DCFH-DA (2,7-Dichlorodi-hydrofluorescein diacetate) staining in 4T1 cells upon different treatments. Scale bar: 50 μm. **(B)** Fluorescence intensity of DCFH-DA from **(A)**. **(C)** Fluorescence images of 4T1 cells stained with FDA (live cells, green fluorescence) and PI (dead cells, red fluorescence) after incubation with different formulations. **(D)** Cell viability of 4T1 cells cultured in the presence of various formulations after laser irradiation. ***$p < 0.005$.

control group barely increased, whereas the *in vivo* temperature distribution in the ink@hydrogel with DHA group was raised by about 15°C in 5 min (**Figure 4B**). The reduced heat tolerance of the tumor tissue compared to normal cells results in the selective destruction of the tumor cells at temperatures above hyperthermia (42–47°C) (Yang et al., 2017). The volume of the

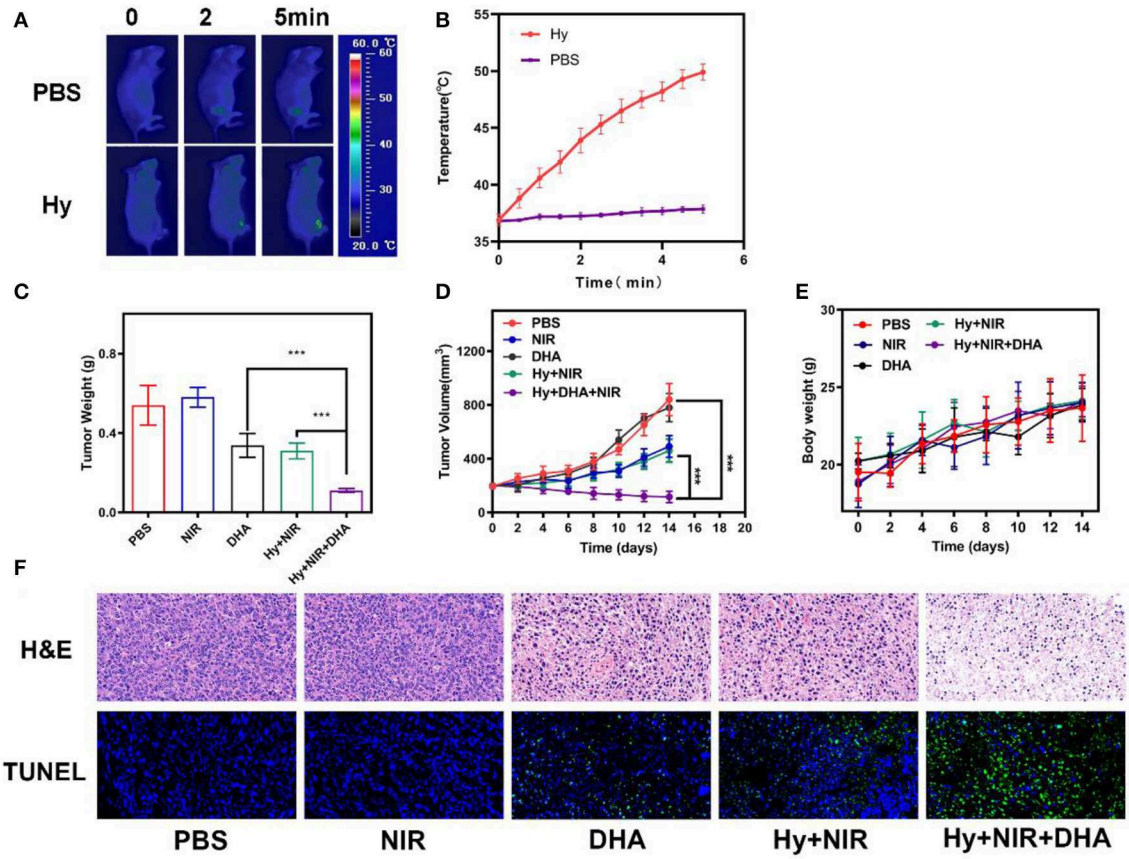

FIGURE 4 | (A) Infrared images of the mice tissue under laser irradiation after the administration of PBS and ink@hydrogel (Hy). **(B)** Temperature of the mice upon laser irradiation. The data represent mean ± standard deviation ($n = 3$). **(C)** Evolution of the tumor weight during therapy. **(D)** Evolution of the volume of 4T1 tumors bearing female BALB/C mice after various treatments. **(E)** Body weight of nude mice recorded every other day for various treatments. **(F)** H&E and TUNEL staining of tumor sections from the 4T1 tumor-bearing mice. ***$p < 0.005$.

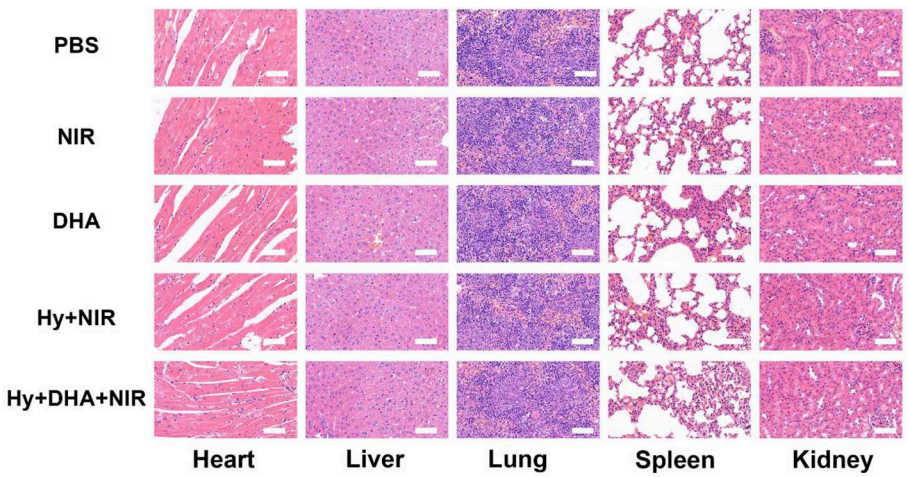

FIGURE 5 | Evaluation of the toxicity *in vivo*. Histological data (H&E staining) obtained in the major organs (heart, liver, spleen, lung, and kidney) of the mice 14 days after injection under various conditions. Scale bar: 100 μm.

tumors in each of the five groups was measured every other day using a digital caliper and the tumor weight was calculated, as shown in **Figures 4C,D**. Compared with the PBS and NIR irradiation group, the tumor grew slowly in the DHA group and the ink@hydrogel without DHA group under laser irradiation. The volume and the weight of the tumor in the hydrogel with DHA group were significantly lowered as the average mice weight in hydrogel with DHA group were only 0.11 g. The body-weight regularly increased in all groups during the whole therapy (**Figure 4E**), which confirmed that these treatments produced negligible adverse effects on the mice. We also examined the micrographs of tumor tissues stained with H&E and TUNEL (**Figure 4F**). The combination of the photo-thermal therapy with DHA yielded the highest apoptosis rate for the tumor cells.

Histological Analysis

We performed a histological analysis of the major organs (heart, liver, spleen, lung, and kidney) for the ink@hydrogel combined with DHA group (**Figure 5**). The results indicated that the synergistic ink@hydrogel and DHA therapy did not cause deep pathological changes in the organs, suggesting that there was no significant histological abnormality in the treatment groups.

CONCLUSION

In summary, we designed a newfangled ink@hydrogel system, which can produce a synergistic activity with DHA for the treatment of cancer. The ink in the ink@hydrogel could generate huge heat energy and hyperthermia when under 1064 nm laser irradiation as it possessed good photothermal performance and stability. Furthermore, Hu Kaiwen ink as a an NIR-II photo-thermal material has great maximum permissible exposure (MPE) and a larger penetration depth. Then, Fe^{3+} ions rapidly diffused from the hydrogel to the tumor microenvironment with dissolution of ink@hydrogel and were reduced to Fe^{2+} to promote the breakage of the endoperoxide bridges in the previously-injected DHA. This resulted in the release of free radicals for a potent anti-cancer effect. And the drug release rate can be controlled by changing different condition. *In vitro* and *in vivo* experiments illustrated the great therapeutic effect of DHA-Fe^{2+}. To our best knowledge, this is the first report of a hydrogel tumor therapy system that generates a photo-thermal response in the NIR-II window. We envisioned that this special hydrogel treatment way holds great potential in synergistic tumor therapy.

DATA AVAILABILITY STATEMENT

All datasets generated for this study are included in the article/supplementary material.

ETHICS STATEMENT

The animal study was reviewed and approved by Wuhan University Animal Care Facility.

AUTHOR CONTRIBUTIONS

DC and CC performed the experiments, analyzed all the data, drafted all the figures, and prepared the manuscript. CH performed the experiments. TC and ZL conceived, designed the experiments, and revised the manuscript.

FUNDING

This work was supported by the Independent Research Project of Wuhan University (znpy2018094) and the Fundamental Research Funds for the Central Universities (2042019kf0229).

REFERENCES

Cao, Y., Wu, T., Zhang, K., Meng, X., Dai, W., Wang, D., et al. (2019). Engineered exosome-mediated near-infrared-II region V2C quantum dot delivery for nucleus-target low-temperature photothermal therapy. *ACS Nano* 13, 1499–1510. doi: 10.1021/acsnano.8b07224

Chu, K. F., and Dupuy, D. E. (2014). Thermal ablation of tumours: biological mechanisms and advances in therapy. *Nat. Rev. Cancer* 14, 199–208 doi: 10.1038/nrc3672

Deng, X., Liang, S., Cai, X., Huang, S., Cheng, Z., Shi, Y., et al. (2019). Yolk-shell structured au nanostar@metal-organic framework for synergistic chemo-photothermal therapy in the second near-infrared window. *Nano Lett.* 19, 6772–6780. doi: 10.1021/acs.nanolett.9b01716

Hou, M., Yang, R., Zhang, L., Zhang, L., Liu, G., Xu, Z., et al. (2018). Injectable and natural humic acid/agarose hybrid hydrogel for localized light-driven photothermal ablation and chemotherapy of cancer. *ACS Biomater. Sci. Eng.* 4, 4266–4277. doi: 10.1021/acsbiomaterials.8b01147

Hu, J. J., Chen, Y., Li, Z. H., Peng, S. Y., Sun, Y., and Zhang, X. Z. (2019). Augment of oxidative damage with enhanced photodynamic process and MTH1 inhibition for tumor therapy. *Nano Lett.* 19, 5568–5576. doi: 10.1021/acs.nanolett.9b02112

Jia, H. R., Wang, H. Y., Yu, Z. W., Chen, Z., and Wu, F. G. (2016). Long-time plasma membrane imaging based on a two-step synergistic cell surface modification strategy. *Bioconjug. Chem.* 27, 782–789. doi: 10.1021/acs.bioconjchem.6b00003

Jiang, W., Zhang, H., Wu, J., Zhai, G., Li, Z., Luan, Y., et al. (2018). CuS@MOF-based well-designed quercetin delivery system for chemo-photothermal therapy. *ACS Appl. Mater. Interfaces* 10, 34513–34523. doi: 10.1021/acsami.8b13487

Li, S. Y., Cheng, H., Xie, B. R., Qiu, W. X., Zeng, J. Y., Li, C. X., et al. (2017). Cancer cell membrane camouflaged cascade bioreactor for cancer targeted starvation and photodynamic therapy. *ACS Nano* 11, 7006–7018. doi: 10.1021/acsnano.7b02533

Liang, S., Deng, X., Chang, Y., Sun, C., Shao, S., Xie, Z., et al. (2019). Intelligent hollow Pt-CuS janus architecture for synergistic catalysis-enhanced sonodynamic and photothermal cancer therapy. *Nano Lett.* 19, 4134–4145. doi: 10.1021/acs.nanolett.9b01595

Lin, H., Gao, S., Dai, C., Chen, Y., and Shi, J. (2017). A two-dimensional biodegradable niobium carbide (MXene) for photothermal tumor eradication in NIR-I and NIR-II biowindows. *J. Am. Chem. Soc.* 139, 16235–16247. doi: 10.1021/jacs.7b07818

Liu, C., Xing, J., Akakuru, O. U., Luo, L., Sun, S., Zou, R., et al. (2019). Nanozymes-engineered metal-organic frameworks for catalytic cascades-enhanced synergistic cancer therapy. *Nano Lett.* 19, 5674–5682. doi: 10.1021/acs.nanolett.9b02253

Liu, Y., Ashton, J. R., Moding, E. J., Yuan, H., Register, J. K., Fales, A. M., et al. (2015). A plasmonic gold nanostar theranostic probe for *in vivo* tumor imaging and photothermal therapy. *Theranostics* 5, 946–960. doi: 10.7150/thno.11974

Niu, X., Zhang, Z., and Zhong, Y. (2017). Hydrogel loaded with self-assembled dextran sulfate-doxorubicin complexes as a delivery system

for chemotherapy. *Mater. Sci. Eng. C Mater. Biol. Appl.* 77, 888–894. doi: 10.1016/j.msec.2017.04.013

Ouyang, B., Liu, F., Ruan, S., Liu, Y., Guo, H., Cai, Z., et al. (2019). Localized free radicals burst triggered by NIR-II light for augmented low-temperature photothermal therapy. *ACS Appl. Mater. Interfaces* 11, 38555–38567. doi: 10.1021/acsami.9b15009

Qiu, M., Wang, D., Liang, W., Liu, L., Zhang, Y., Chen, X., et al. (2018). Novel concept of the smart NIR-light-controlled drug release of black phosphorus nanostructure for cancer therapy. *Proc. Natl. Acad. Sci. U.S.A.* 115, 501–506. doi: 10.1073/pnas.1714421115

Rasool, K., Helal, M., Ali, A., Ren, C. E., Gogotsi, Y., and Mahmoud, K. A. (2016). Antibacterial activity of Ti(3)C(2)Tx MXene. *ACS Nano* 10, 3674–3684. doi: 10.1021/acsnano.6b00181

Shao, J., Xie, H., Huang, H., Li, Z., Sun, Z., Xu, Y., et al. (2016). Biodegradable black phosphorus-based nanospheres for *in vivo* photothermal cancer therapy. *Nat. Commun.* 7:12967. doi: 10.1038/ncomms12967

Song, G., Liang, C., Gong, H., Li, M., Zheng, X., Cheng, L., et al. (2015). Core-shell MnSe@Bi_2 Se_3 fabricated via a cation exchange method as novel nanotheranostics for multimodal imaging and synergistic thermoradiotherapy. *Adv. Mater.* 27, 6110–6117. doi: 10.1002/adma.201503006

Sun, H., Su, J., Meng, Q., Yin, Q., Chen, L., Gu, W., et al. (2017). Cancer cell membrane-coated gold nanocages with hyperthermia-triggered drug release and homotypic target inhibit growth and metastasis of breast cancer. *Adv. Funct. Mater.* 27:1604300. doi: 10.1002/adfm.201604300

Wang, D., Zhou, J., Chen, R., Shi, R., Xia, G., Zhou, S., et al. (2016). Magnetically guided delivery of DHA and Fe ions for enhanced cancer therapy based on pH-responsive degradation of DHA-loaded Fe_3O_4@C@MIL-100(Fe) nanoparticles. *Biomaterials* 107, 88–101. doi: 10.1016/j.biomaterials.2016.08.039

Wang, S., Cao, Y., Zhang, Q., Peng, H., Liang, L., Li, Q., et al. (2017). New application of old material: chinese traditional ink for photothermal therapy of metastatic lymph nodes. *ACS Omega* 2, 5170–5178. doi: 10.1021/acsomega.7b00993

Wu, H., Liu, L., Song, L., Ma, M., Gu, N., and Zhang, Y. (2019). Enhanced tumor synergistic therapy by injectable magnetic hydrogel mediated generation of hyperthermia and highly toxic reactive oxygen species. *ACS Nano*. 13, 14013–14023. doi: 10.1021/acsnano.9b06134

Wu, M. X., Yan, H. J., Gao, J., Cheng, Y., Yang, J., Wu, J. R., et al. (2018). Multifunctional supramolecular materials constructed from polypyrrole@UiO-66 nanohybrids and pillararene nanovalves for targeted chemophotothermal therapy. *ACS Appl. Mater. Interfaces* 10, 34655–34663. doi: 10.1021/acsami.8b13758

Xing, R., Liu, K., Jiao, T., Zhang, N., Ma, K., Zhang, R., et al. (2016). An injectable self-assembling collagen-gold hybrid hydrogel for combinatorial antitumor photothermal/photodynamic therapy. *Adv. Mater.* 28, 3669–3676. doi: 10.1002/adma.201600284

Yang, J., Xie, R., Feng, L., Liu, B., Lv, R., Li, C., et al. (2019). Hyperthermia and controllable free radical coenhanced synergistic therapy in hypoxia enabled by near-infrared-II light irradiation. *ACS Nano* 13, 13144–13160. doi: 10.1021/acsnano.9b05985

Yang, Y., Zhu, W., Dong, Z., Chao, Y., Xu, L., Chen, M., et al. (2017). 1D coordination polymer nanofibers for low-temperature photothermal therapy. *Adv. Mater.* 29:1703588. doi: 10.1002/adma.201703588

Yu, X., Li, A., Zhao, C., Yang, K., Chen, X., and Li, W. (2017). Ultrasmall semimetal nanoparticles of bismuth for dual-modal computed tomography/photoacoustic imaging and synergistic thermoradiotherapy. *ACS Nano* 11, 3990–4001. doi: 10.1021/acsnano.7b00476

Zhang, F., Liu, Y., Lei, J., Wang, S., Ji, X., Liu, H., et al. (2019). Metal–organic-framework-derived carbon nanostructures for site-specific dual-modality photothermal/photodynamic thrombus therapy. *Adv. Sci.* 6:1901378. doi: 10.1002/advs.201901378

Zhou, J., Jiang, Y., Hou, S., Upputuri, P. K., Wu, D., Li, J., et al. (2018). Compact plasmonic blackbody for cancer theranosis in the near-infrared II window. *ACS Nano* 12, 2643–2651. doi: 10.1021/acsnano.7b08725

Conflict of Interest: The authors declare that the research was conducted in the absence of any commercial or financial relationships that could be construed as a potential conflict of interest.

frontiers in Chemistry

MINI REVIEW
published: 17 June 2020
doi: 10.3389/fchem.2020.00472

Recent Progresses in Cancer Nanotherapeutics Design Using Artemisinins as Free Radical Precursors

Yalan Wu[1,2], *Qingping Zeng*[2], *Zhiwen Qi*[3], *Tao Deng*[1]* *and Fang Liu*[1]*

[1] *Institute of Tropical Medicine and Artemisinin Research Center, Guangzhou University of Chinese Medicine, Guangzhou, China,* [2] *Science and Technology Innovation Center, Guangzhou University of Chinese Medicine, Guangzhou, China,* [3] *Institute of Chemical Industry of Forest Products, Chinese Academy of Forestry (CAF), Nanjing, China*

Artemisinin and its derivatives (ARTs) are sort of important antimalarials, which exhibit a wide range of biological activities including anticancer effect. To solve the issues regarding poor solubility and limited bioavailability of ARTs, nanoformulation of ARTs has thus emerged as a promising strategy for cancer treatment. A common consideration on nanoARTs design lies on ARTs' delivery and controlled release, where ARTs are commonly regarded as hydrophobic drugs. Based on the mechanism that ARTs' activation relies on ferrous ions (Fe^{2+}) or Fe^{2+}-bonded complexes, new designs to enhance ARTs' activation have thus attracted great interests for advanced cancer nanotherapy. Among these developments, the design of a nanoparticle that can accelerate ARTs' activation has become the major consideration, where ARTs have been regarded as radical precursors. This review mainly focused on the most recent developments of ARTs nanotherapeutics on the basis of advanced drug activation. The basic principles in those designs will be summarized, and a few excellent cases will be also discussed in detail.

Keywords: artemisinins, anticancer, nanomedicine, chemodynamic therapy, free radicals

OPEN ACCESS

Edited by:
Yanyan Jiang,
Shandong University, China

Reviewed by:
Yuanzeng Min,
University of Science and Technology of China, China
Jiangwei Tian,
China Pharmaceutical University, China

***Correspondence:**
Tao Deng
dengtao@gzucm.edu.cn
Fang Liu
fangliu@gzucm.edu.cn

Specialty section:
This article was submitted to Nanoscience, a section of the journal Frontiers in Chemistry

Received: *05 March 2020*
Accepted: *06 May 2020*
Published: *17 June 2020*

Citation:
Wu Y, Zeng Q, Qi Z, Deng T and Liu F (2020) Recent Progresses in Cancer Nanotherapeutics Design Using Artemisinins as Free Radical Precursors. Front. Chem. 8:472. doi: 10.3389/fchem.2020.00472

INTRODUCTION

Artemisinin (ART) is derived from the extracts of *Artemisia annua,* a Chinese herbal plant, and it is well-established for the treatment of malaria. Up to date, several semi-synthetic derivatives of ART have been synthesized and clinically applied, including artesunate (AS), dihydroartemisinin (DHA), artemether (ARM), and arteether (ARE). Besides anti-malarial usage, the therapeutic effect of ARTs has also been extended to non-parasitic diseases, such as inflammatory disease and cancer (Krishna et al., 2008; Li, 2012). ARTs have been proved to be effective to treat a wide range of cancers both *in vitro* and *in vivo* (Wong et al., 2017). Although the anticancer mechanism of ARTs is not fully discovered yet, some investigations have pointed out that Fe^{2+} may be the natural catalyst in cells that mediates ARTs' activation. Fe^{2+}-catalyzed opening of the endoperoxide bridge is through an Fenton-like reaction, which generates alkyl radicals and reactive oxygen species (ROS) that can subsequently react with susceptible protein targets (O'neill et al., 2010; Wang et al., 2015; Deng et al., 2020). Tumor cells often have elevated iron accumulation, which has been regarded as one of the leading reasons why ARTs can kill cancer cells selectively (Pfeifhofer-Obermair et al., 2018; Zhang et al., 2018).

However, using ARTs for real cancer therapy has been limited by their poor solubility, low bioavailability, and extremely short half-life *in vivo* (De Vries and Dien, 1996; Dwivedi et al., 2015). Nanotechnology offers the possibilities to overcome those drawbacks, thus being extensively used in the delivery of drugs especially for those with difficulty in water solubility (Kalepu and Nekkanti, 2015; Patra et al., 2018). A general method for ARTs delivery is loading the drug molecules within a certain nanocarrier, which could be made from inorganic or organic substrates, or both of them (Wang et al., 2016b; Mangrio et al., 2017; Manjili et al., 2018; Xiao et al., 2020). Additional chemistry for achieving tumor targeting and controllable drug release is often considered during the design (Tran et al., 2016; Jabbarzadegan et al., 2017; Akbarian et al., 2020). Up to date, numerous nanosystems have been reported for ARTs delivery and controlled release, and those studies have been well-summarized in previous review articles (Chen et al., 2009; Aderibigbe, 2017; Charlie-Silva et al., 2018). Another much advanced strategy to improve the therapeutic effect of ARTs is the method of so-called chemodynamic therapy (CDT), which has been attracting interests for cancer treatment via localized Fenton reaction (Tang et al., 2019; Zhao et al., 2019). Therefore, the ways of the delivery and controlled release of active Fenton reagent such as Fe^{2+} to accelerate ARTs' activation are attracting the great attentions in the design of ART-CDT nanotherapeutics. The main target of those nanosystems is to cause free radical burst thus leading to cell toxicity, whereby ARTs are usually used as radical precursors. In the present review, we will focus on the recent progress mostly within the last 5 years in cancer nanotherapeutics design using ARTs as free radical precursors. The discussion will be divided into four parts according to the differences of technique aspects.

ARTS NANOTHERAPEUTICS

Iron Oxide-Based ARTs Nanotherapeutics

With the common sense that Fe^{2+} ions are the most active species that can activate ARTs, iron oxide-based inorganic and inorganic/organic hybrid nanoparticles have therefore been considered for ARTs' delivery and controlled activation. Most of these nanoparticles are made from the mixtures of Fe^{2+} and Fe^{3+}, which are potentially able to release active Fe^{2+} in mild acidic environment of tumor tissues and acidic intracellular compartments. In addition, many oxide nanoparticles are paramagnetic and serve as excellent contrast reagents for magnetic resonance imaging (MRI), which offers the possibilities for the development of advanced theranostics (Bao et al., 2018). Up to now, several iron oxide–based ART nanotherapeutics have been reported and proved to be effective *in vitro* and *in vivo* in cancer therapies. For example, Chen et al. have reported a nanoparticle Fe_3O_4@C/Ag@mSiO_2 with mesoporous properties, which can load with ART up to 484 mg/g. This nanoparticle was internalized by cancer cells mainly through endocytosis pathways, Fe_3O_4 in acidic endo/lysosome was able to release catalytic Fe^{2+} that further activated the generation of radical species from ART. The authors found elevated apoptosis to HeLa cells treated with this nanoparticle compared with ART itself (Chen et al., 2014). By following this design, the same group has presented another Fe_3O_4-based nanosystem Fe_3O_4@C@MIL-100(Fe), where dihydroartemisinin (DHA) was encapsulated as radical precursors. More interestingly, this system is able to increase the accumulation of DHA and Fe^{2+} within targeted cancer cells under the guidance of an external magnetic field. Much improved therapeutic effect has been found *in vivo* in this study (Wang et al., 2016a).

The cases above have revealed that targeting to the acidic endo/lysosome is a promising way to achieve Fe^{2+}/Fe^{3+} release from iron oxide nanoparticles. By following these studies, several ARTs nanosystems have been reported most recently (Wang D. et al., 2017; Zhang et al., 2017; Pan et al., 2018; Guo et al., 2019; Li et al., 2019; Qin et al., 2019). Generally, nanoparticles are easy to be chemically modified with additional ligands to strengthen the functionalities. For instance, Zhang et al. (2016) reported a multi-functional nanoparticle, in which hyaluronic acid (HA) was grafted on the ART doped mesoporous Fe_3O_4 core structures. Controlled release of Fe^{2+} and ART is thus achievable since tumor cells are often enriched with hyaluronidases (Mcatee et al., 2014). Such an HA-gate method has also been applied in another report by the same research group (Zhang et al., 2017). In a recent report, an additional cancer cell-targeting and membrane-penetrating RGD peptide was integrated on a Fe_3O_4@cisplatin/ART nanoparticle to form ART-loaded cRGD-AFePt@NPs for cancer targeted co-delivery of cisplatin and ART, and controlled drug activation (Gao et al., 2018). The most recently reported iron oxide nanosystems for ARTs-based cancer therapeutics have been summarized and listed in **Table 1**. We do believe that this sort of design will be continually applied in the fabrication of advanced ARTs nanodrugs in the future.

Iron-Containing Soft Matters for ARTs Delivery and Activation

Polymeric soft matters including natural proteins, polysaccharides, and synthetic polymers have gained great attentions for the fabrication of nanotherapeutics. Numerous small molecular drugs have been provided as nanoformulations in clinic applications by using polymeric soft matters as drugs' nanocarriers (Malmsten, 2006; Liechty et al., 2010). Different to other small molecular drugs, a successful delivery system for ARTs-based cancer treatment requires not only effective drug release but also efficient peroxide bridge activation. Therefore, the soft matters that can serve as the carriers for both ARTs and the catalyst Fe^{2+}/Fe^{3+} are much extensively studied.

Transferrin, a kind of iron containing proteins, has been used as nanocarriers to directly deliver ARTs for cancer therapy in several cases. One of the earliest reports presented a drug-protein complex by covalently conjugating an ART derivative with the carbohydrate chains of transferrin. *In vivo* evidence showed that linkage with transferrin can greatly enhance the therapeutic effect of ART on the mice implanted with human ovarian cancer cells, HO-8910 (Nakase et al., 2008). It has also been found that transferrin with ART tagged with lysine residues was less effective than those with ART tagged to the carbohydrate chains (Lai et al., 2005). Direct conjugation of ARTs to transferrin may lead to some drawbacks such as limited loading efficiency and

TABLE 1 | Recent developments of iron oxide nanoparticle-based ARTs nanotherapeutics.

	Nanotherapeutics	ARTs	DLC	Activator	Strategy	Evidence	References
1	Fe_3O_4@C/Ag@mSiO_2	ART	48.4%	Fe^{2+}/Fe^{3+}	ART-CDT	*in vitro*	Chen et al., 2014
2	Fe_3O_4@C@MIL-100(Fe)	DHA	80.4%	Fe^{2+}/Fe^{3+}	ART-CDT	*in vitro/in vivo*	Wang et al., 2016a
3	$Mn_3[Co(CN)_6]_2$@MIL-100 (Fe)	AS	53.1%	Fe^{2+}/Fe^{3+}	ART-CDT	*in vitro/in vivo*	Wang D. et al., 2017
4	ART@HQZFNPs	ART	23.0%	Fe^{2+}/Fe^{3+}	ART-CDT	*in vitro*	Pan et al., 2018
5	MNP-ART, MNP-DHA, MNP-AS	ART, DHA, AS	15.3%, 15.3%, 15.7%	Fe^{2+}/Fe^{3+}	ART-CDT	*in vitro*	Guo et al., 2019
6	DHA-MLPs	DHA	82.1%	Fe^{2+}/Fe^{3+}	ART-CDT	*in vitro/in vivo*	Li et al., 2019
7	Fe_3O_4@SiO_2-ART-HNPa	ART	45.2%	Fe^{2+}/Fe^{3+}	ART-CDT, PDT	*in vitro*	Qin et al., 2019
8	A-TiO_2-IONPs/ART	ART	27.5%	Fe^{2+}/Fe^{3+}	ART-CDT, PDT	*in vitro/in vivo*	Zhang et al., 2017
9	HA-mFe_3O_4/ART	ART	52.8%	Fe^{2+}/Fe^{3+}	ART-CDT, AMF	*in vitro/in vivo*	Zhang et al., 2016
10	cRGD-AFePt@NPs	ART	5.2%	Fe^{2+}/Fe^{3+}	ART-CDT Cisplatin	*in vitro*	Gao et al., 2018
11	Fe_3O_4@$MnSiO_3$-FA	ART	21.9%	Mn^{2+}, Fe^{2+}/Fe^{3+}	ART-CDT	*in vitro/in vivo*	Chen et al., 2015
12	ART-MSP loaded with ICG	ART	22.5%	Fe^{2+}/Fe^{3+}	ART-CDT, PTT	*in vitro/in vivo*	Ding et al., 2018

DLC, drug loading capacity; MNP, magnetic nanoparticle; MSP, porous magnetite supraparticles; AFM, alternating magnetic field (AMF) irradiation; ZFNPs, Zinc ferrite ($ZnFe_2O_4$) nanoparticles; HQ, 8-hydroxyquinoline; MLPs, magnetic nano-liposomes; HA, hyaluronic acid; ICG, indocyanine green; HNPa, 3-[1-hydroxyethyl]-3-devinyl-131-b,b-dicyanomethylene-131-deoxopyropheophorbide-a.

potential suppressive effect to the intrinsic biological functions of transferrin. To overcome the drawbacks, some much advanced nanosystems have been presented (Zhang et al., 2015a,b; Ji et al., 2019; Luo et al., 2019). For example, in a recent study, Xing's group reported a system for pH-triggered cancer chemotherapy by coating graphene oxide (GO) with both transferrin and DHA, where transferrin served as not only a cancer cell-targeting ligand but also an iron carrier (Liu et al., 2015). Most recently, Tian's group has presented a DHA encapsulated liposomal nanosystem functionalized with transferrin as tumor-targeting ligands. Elevated oxidative stress was observed specifically at the tumor site and enhanced tumor eradication was achieved by their nanosystem (Yu et al., 2020). Methemoglobin (MHb) is the most common iron-containing protein, which has also been utilized in ARTs' delivery and controlled activation through the similar mechanisms to transferring (Li et al., 2017). The iron ion in both transferrin and MHb exists mainly as Fe^{3+}, it will convert to Fe^{2+} under reductive intracellular microenvironment, thus mediating ARTs' activation (Liu et al., 2015). Other ARTs nanosystems based on Fe^{3+} bonded polymers may follow a similar activation mechanism as stated in **Figure 1**.

Polydopamine (PDA) is made from the polymerization of natural dopamine monomers, which shows the abilities to tightly coordinate with Fe^{2+} and Fe^{3+} ions. The release of these ions from polydopamine depends on the degradation of polymer structure as well as the pH values surrounding it. Generally, lower pH often leads to greater release. A recent study presented a hollow nanosphere DHA@HPDA-Fe, in which polydopamine vesicles were loaded with DHA and Fe^{3+}. *In vivo* evidence showed that the anticancer efficacy of DHA@HPDA-Fe was 3.05 times higher compared with free DHA (Dong et al., 2019). Besides, some other biocompatible polyphenolic compounds such as tannic acid have similar binding and releasing futures toward Fe^{2+} and Fe^{3+}(Kell, 2009; Du et al., 2019; He et al., 2019). These polymers could also be considered for construction of ART's nanotherapeutics, but the related research is still rare.

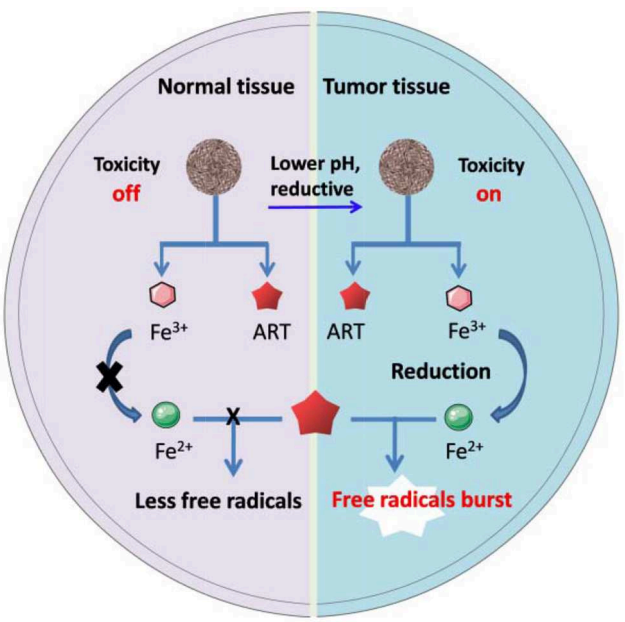

FIGURE 1 | Schematic artwork of tumor selective ART-CDT through iron-containing polymer nanoparticles.

ARTs Nanotherapeutics Activated by Other Metal Ions

In addition to Fe^{2+}, some other transition metal ions such as Zn^{2+}, Mn^{2+}, Ni^{2+}, Ti^{3+}, Cu^{2+}, and Co^{2+} ions could also be used as catalysts to catalyze Fenton reaction (Bokare and Choi, 2014). This may greatly expand the alternatives when considering a catalyst for ARTs' activation. For instance, Chen et al. have reported a Mn^{2+}-doped nanoparticle Fe_3O_4@$MnSiO_3$-FA for successful delivery of AS to tumors in mice models. It was found that both Fe^{2+} and Mn^{2+} would contribute to the catalyzed activation of AS. The authors further suggested that Mn^{2+} would be more effective to promote Fenton-like reaction and lead to more free radicals generated from AS (Chen et al., 2015). Zhou et al. presented a multifunctional nanoparticle ART-loaded mesoporous NiO (mNiO) for cancer cell targeted therapy, in which Ni^{2+} served as the catalyst for ART's activation. The authors found the evidence that mNiO can undergo degradation in acidic tumor microenvironment and release free Ni^{2+}, which benefits the tumor selectivity over normal tissues (Liu et al., 2018). Although Mn^{2+} and Ni^{2+} doped with ARTs nanocomposites have exhibited catalytic effect in ARTs' activation, and there are still many ions alternative to choose for testing, the biocompatibility issues of such nanosystems should be greatly concerned for the purpose of real use.

Nanotherapeutics With the Combination of ART-CDT and Other Therapeutic Techniques

ARTs with peroxide bridges offer excellent radical precursors for the design of ARTs-based chemodynamic therapy (ART-CDT), which often involves the dynamic activation of ARTs and the generation of toxic free radicals (Tang et al., 2019). H_2O_2, hydroxyl radicals, and alkyl radicals are considered as the major radical species from the consequences following ART activation (Deng et al., 2019). Another radical-based therapeutic strategy is photodynamic therapy (PDT), whereby photo-mediated generation of singlet oxygen ($^1O_2$) is the major scientific bases for therapy. ART-CDT and PDT are all ROS involved, and the combination therapy based on both is thus attracting increasing interests (Feng et al., 2018).

More recently, Jin et al. have developed a nanosystem Fe_3O_4@SiO_2-ART-HNPa for cancer therapy with the combination of ART-CDT and PDT. Within their core-shell nanoparticle Fe_3O_4@SiO_2, ART and a porphyrin photosensitizer HNPa were encapsulated into the mesoporous structure of SiO_2. In this system, ART was considered to generate ROS and alkyl radicals through pH-mediated Fenton-like reactions. Meanwhile, $^1O_2$ generation from HNPa and molecular oxygen was mediated by NIR light (700 nm) excitation. Enhanced anticancer effect has been observed compared with PDT or the Fenton-like reaction alone (Qin et al., 2019). Recently, a nanoscale metal organic framework (nanoMOF) doped with Fe^{3+}, ART, and a photosensitizer have been constructed by Tang's group for synergistic cancer therapy based on ART-CDT and PDT. In this study, Fe^{3+} and the photosensitizer 4,4,4,4-(Porphine-5,10,15,20-tetrayl)tetrakis(benzoic acid) (TCPP) were coordinated to form the nanoMOF core structures followed by the encapsulation of DHA. To prevent non-specific DHA release, the nanoMOF was further coated with a layer of $CaCO_3$. A 655 nm laser was applied for PDT during the combination therapy. Both the *in vitro* and *in vivo* results indicated synergistic therapy effect from this nanosystem, which could ablate the tumor completely on the breast cancer cell 4T1-bearing mice (Wan et al., 2019).

Photothermal therapy (PTT) is a therapeutic approach of heat ablation, which uses the heat converted from pathologic tissue localized light irradiation (Vines et al., 2019). It has been found that PTT is able to improve Fenton-reaction-based therapy through enhancing the generation of ROS (Hu et al., 2017; Chen et al., 2020), thus holding the great promise to be combined with ART-CDT in cancer treatment (Wang et al., 2016b; Hu et al., 2017; Ding et al., 2018; Liu et al., 2018). Most recently, Wang et al. have presented a dual functional magnetic nanoparticle MSP@ART@P for cancer treatment based on the combination of ART-CDT and NIR laser (785 nm) mediated PTT. In their design, ART was firstly loaded into a magnetic iron oxide nanoparticle. A poly (aspartic acid) polymer linked with dopamine and indocyanine green (ICG) was then coated with the ART-loaded core nanoparticle. The authors have experimentally confirmed the cancer ablation effect from ART-CDT, and that the therapeutic effect could be further promoted by photothermal effect. This research offers a way to elevate cancer tissue–localized ROS generation through photosensitizer/O_2-independent manners (Ding et al., 2018).

SUMMARY AND PERSPECTIVES

The peroxide bridges existing in ARTs make them the most attractive free radical precursors for radical-based CDT. Fe^{2+} and Fe^{2+}-containing complexes such as heme are considered as the major catalysts that can activate ARTs within cells through Fenton-like reactions. Based on these considerations, some iron oxide nanoparticle-based ARTs delivery and activation systems have been developed as discussed above. The activation relies on Fe^{2+} generation either from the direct ion release of iron oxide nanoparticles or reductive conversion of Fe^{3+}. The controlled release and activation of ARTs could also be achieved by loading ARTs with iron-containing soft matters, which include natural iron-containing proteins such as transferrin and hemoglobin, as well as polyphenols chelated with Fe^{2+}/Fe^{3+}. The recent developments in this field have been summarized, and a few excellent cases have been discussed in details. Besides Fe^{2+}, cancer cell-targeted release of Ni^{2+} and Mn^{2+} has also been proven effective in ARTs' activation, resulting in high antitumor activity *in vitro* and *in vivo*. In principle, some other metal ions that catalyze Fenton-like reaction can also serve as the activators for ART-CDT. However, in such kinds of design, the potential toxic issues due to the overloading of metal ions have to be carefully considered. An alternative way against the delivery of toxic metal ions is to enhance the catalytic effect of intrinsic Fe^{2+} by delivering a proper iron chelate into the cells. For example, heme, a protoporphyrin IX-Fe^{2+} complex, has been proven to

be more effective in catalyzing activation of ARTs. The way to improve the formation of intracellular heme would be a possible strategy to enhance the anticancer activities of ARTs, which have gained evidences in some recent studies (Wang J. et al., 2017; Chen et al., 2019).

Combination of ART-CDT and other advanced therapeutic methods will be the most promising trend in the design of ART-based nanotherapeutics. ART-CDT combined with PDT or PTT has shown synergistic effect for cancer therapy. Elevated ROS generation from ARTs is one of the major causes of synergistic effect in these combination therapies. Ultrasound irradiation mediated sonodynamic therapy (SDT) has emerged recently as a new method for cancer therapy (Canavese et al., 2018). Compared to other external stimuli such as light, ultrasound irradiation has better tissue penetrating capability. More recently, several studies have confirmed the possibilities to generate ROS in aqueous mediums through ultrasound irradiation (Gong et al., 2015; Giuntini et al., 2018). Similar to PPT, SDT is also able to release heat locally, thus making the potentials to accelerate the Fenton-like reaction on ARTs. The combination of ART-CDT and SDT, therefore, will be a promising option in the design of advanced ART nanotherapeutics in the future.

AUTHOR CONTRIBUTIONS

YW, ZQ, and TD drafted this manuscript. FL and QZ revised it. All authors contributed to the article and approved the submitted version.

FUNDING

We gratefully acknowledge the support by the projects of National Natural Science Foundation of China (21807018), the Department of Education of Guangdong Province (2018KQNCX047), and the Youth Scientific Research Training Project of GZUCM (2019QNPY06).

REFERENCES

Aderibigbe, A. B. (2017). Design of drug delivery systems containing artemisinin and its derivatives. *Molecules* 22:323. doi: 10.3390/molecules22020323

Akbarian, A., Ebtekar, M., Pakravan, N., and Hassan, Z. M. (2020). Folate receptor alpha targeted delivery of artemether to breast cancer cells with folate-decorated human serum albumin nanoparticles. *Int. J. Biol. Macromol*. 152, 90–101. doi: 10.1016/j.ijbiomac.2020.02.106

Bao, Y., Sherwood, J. A., and Sun, Z. (2018). Magnetic iron oxide nanoparticles as T1 contrast agents for magnetic resonance imaging. *J. Mater. Chem. C*. 6, 1280–1290. doi: 10.1039/C7TC05854C

Bokare, A. D., and Choi, W. (2014). Review of iron-free fenton-like systems for activating H2O2 in advanced oxidation processes. *J. Hazard. Mater*. 275, 121–135. doi: 10.1016/j.jhazmat.2014.04.054

Canavese, G., Ancona, A., Racca, L., Canta, M., Dumontel, B., Barbaresco, F., et al. (2018). Nanoparticle-assisted ultrasound: a special focus on sonodynamic therapy against cancer. *Chem. Eng. J*. 340, 155–172. doi: 10.1016/j.cej.2018.01.060

Charlie-Silva, I., Fraceto, L. F., and de Melo, N. F. S. (2018). Progress in nano-drug delivery of artemisinin and its derivatives: towards to use in immunomodulatory approaches. *Artif. Cells Nanomed. Biotechnol*. 46, S611–S620. doi: 10.1080/21691401.2018.1505739

Chen, C.-P., Chen, K., Feng, Z., Wen, X., and Sun, H. (2019). Synergistic antitumor activity of artesunate and HDAC inhibitors through elevating heme synthesis via synergistic upregulation of ALAS1 expression. *Acta Pharm. Sin. B*. 9, 937–951. doi: 10.1016/j.apsb.2019.05.001

Chen, D., Chen, C., Huang, C., Chen, T., and Liu, Z. (2020). Injectable hydrogel for NIR-II photo-thermal tumor therapy and dihydroartemisinin-mediated chemodynamic therapy. *Front. Chem.* 8:251. doi: 10.3389/fchem.2020.00251

Chen, J., Guo, Z., Wang, H.-B., Zhou, J.-J., Zhang, W.-J., and Chen, Q.-W. (2014). Multifunctional mesoporous nanoparticles as pH-responsive Fe^{2+} reservoirs and artemisinin vehicles for synergistic inhibition of tumor growth. *Biomaterials* 35, 6498–6507. doi: 10.1016/j.biomaterials.2014.04.028

Chen, J., Zhang, W., Zhang, M., Guo, Z., Wang, H., He, M., et al. (2015). Mn(ii) mediated degradation of artemisinin based on Fe_3O_4@$MnSiO_3$-FA nanospheres for cancer therapy *in vivo*. *Nanoscale* 7, 12542–12551. doi: 10.1039/C5NR02402A

Chen, Y., Lin, X., Park, H., and Greever, R. (2009). Study of artemisinin nanocapsules as anticancer drug delivery systems. *Nanomedicine* 5, 316–322. doi: 10.1016/j.nano.2008.12.005

De Vries, P. J., and Dien, T. K. (1996). Clinical pharmacology and therapeutic potential of artemisinin and its derivatives in the treatment of Malaria. *Drugs* 52, 818–836. doi: 10.2165/00003495-199652060-00004

Deng, T., Hu, S., Huang, X.-A., Song, J., Xu, Q., Wang, Y., et al. (2019). A novel strategy for colorimetric detection of hydroxyl radicals based on a modified Griess test. *Talanta* 195, 152–157. doi: 10.1016/j.talanta.2018.11.044

Deng, T., Wang, X., Wu, S., Hu, S., Liu, W., Chen, T., et al. (2020). A new FRET probe for ratiometric fluorescence detecting mitochondria-localized drug activation and imaging endogenous hydroxyl radicals in zebrafish. *Chem. Commun*. 56, 4432–4435. doi: 10.1039/D0CC00382D

Ding, Y., Wan, J., Zhang, Z., Wang, F., Guo, J., and Wang, C. (2018). Localized Fe(II)-induced cytotoxic reactive oxygen species generating nanosystem for enhanced anticancer therapy. *ACS Appl. Mater. Interfaces*. 10, 4439–4449. doi: 10.1021/acsami.7b16999

Dong, L., Wang, C., Zhen, W., Jia, X., An, S., Xu, Z., et al. (2019). Biodegradable iron-coordinated hollow polydopamine nanospheres for dihydroartemisinin delivery and selectively enhanced therapy in tumor cells. *J. Mater. Chem. B* 7, 6172–6180. doi: 10.1039/C9TB01397K

Du, K., Liu, Q., Liu, M., Lv, R., He, N., and Wang, Z. (2019). Encapsulation of glucose oxidase in Fe(III)/tannic acid nanocomposites for effective tumor ablation via Fenton reaction. *Nanotechnology* 31:015101. doi: 10.1088/1361-6528/ab44f9

Dwivedi, A., Mazumder, A., Du Plessis, L., Du Preez, J. L., Haynes, R. K., and Du Plessis, J. (2015). *In vitro* anti-cancer effects of artemisone nano-vesicular formulations on melanoma cells. *Nanomedicine* 11, 2041–2050. doi: 10.1016/j.nano.2015.07.010

Feng, G., Liu, J., Zhang, C.-J., and Liu, B. (2018). Artemisinin and AIEgen conjugate for mitochondria-targeted and image-guided chemo- and photodynamic cancer cell ablation. *ACS Appl. Mater. Interfaces* 10, 11546–11553. doi: 10.1021/acsami.8b01960

Gao, Z., Li, Y., You, C., Sun, K., An, P., Sun, C., et al. (2018). Iron oxide nanocarrier-mediated combination therapy of cisplatin and artemisinin for combating drug resistance through highly increased toxic reactive oxygen species generation. *ACS Appl. Bio Mater*. 1, 270–280. doi: 10.1021/acsabm.8b00056

Giuntini, F., Foglietta, F., Marucco, A. M., Troia, A., Dezhkunov, N. V., Pozzoli, A., et al. (2018). Insight into ultrasound-mediated reactive oxygen species generation by various metal-porphyrin complexes. *Free Radic. Biol. Med*. 121, 190–201. doi: 10.1016/j.freeradbiomed.2018.05.002

Gong, C., Jiang, J., Li, D. A., and Tian, S. (2015). Ultrasonic application to boost hydroxyl radical formation during Fenton oxidation and release organic matter from sludge. *Sci. Rep*. 5:11419. doi: 10.1038/srep11419

Guo, S., Yao, X., Jiang, Q., Wang, K., Zhang, Y., Peng, H., et al. (2019). Dihydroartemisinin-loaded magnetic nanoparticles for enhanced chemodynamic therapy. *Front. Pharmacol*. 11:226. doi: 10.3389/fphar.2020.00226

He, Z., Su, H., Shen, Y., Shi, W., Liu, X., Liu, Y., et al. (2019). Poly(norepinephrine)-coated FeOOH nanoparticles as carriers of artemisinin for cancer photothermal-chemical combination therapy. *RSC Adv*. 9, 9968–9982. doi: 10.1039/C9RA01289C

Hu, P., Wu, T., Fan, W., Chen, L., Liu, Y., Ni, D., et al. (2017). Near infrared-assisted Fenton reaction for tumor-specific and mitochondrial DNA-targeted photochemotherapy. *Biomaterials* 141, 86–95. doi: 10.1016/j.biomaterials.2017.06.035

Jabbarzadegan, M., Rajayi, H., Mofazzal Jahromi, M. A., Yeganeh, H., Yousefi, M., Muhammad Hassan, Z., et al. (2017). Application of arteether-loaded polyurethane nanomicelles to induce immune response in breast cancer model. *Artif. Cells Nanomed. Biotechnol*. 45, 808–816. doi: 10.1080/21691401.2016.1178131

Ji, P., Huang, H., Yuan, S., Wang, L., Wang, S., Chen, Y., et al. (2019). ROS-mediated apoptosis and anticancer effect achieved by artesunate and auxiliary Fe(II) released from ferriferous oxide-containing recombinant apoferritin. *Adv. Healthc. Mater*. 8:1900911. doi: 10.1002/adhm.201900911

Kalepu, S., and Nekkanti, V. (2015). Insoluble drug delivery strategies: review of recent advances and business prospects. *Acta Pharmaceutica Sinica B*. 5, 442–453. doi: 10.1016/j.apsb.2015.07.003

Kell, D. B. (2009). Iron behaving badly: inappropriate iron chelation as a major contributor to the aetiology of vascular and other progressive inflammatory and degenerative diseases. *BMC Med. Genomics* 2:2. doi: 10.1186/1755-8794-2-2

Krishna, S., Bustamante, L., Haynes, R. K., and Staines, H. M. (2008). Artemisinins: their growing importance in medicine. *Trends Pharmacol. Sci*. 29, 520–527. doi: 10.1016/j.tips.2008.07.004

Lai, H., Sasaki, T., Singh, N. P., and Messay, A. (2005). Effects of artemisinin-tagged holotransferrin on cancer cells. *Life Sci*. 76, 1267–1279. doi: 10.1016/j.lfs.2004.08.020

Li, H., Chen, Y., Chen, T., Han, H., Tong, H., Jin, Q., et al. (2017). Methemoglobin as a redox-responsive nanocarrier to trigger the *in situ* anticancer ability of artemisinin. *NPG Asia Mater*. 9:e423. doi: 10.1038/am.2017.150

Li, H., Li, X., Shi, X., Li, Z., and Sun, Y. (2019). Effects of magnetic dihydroartemisinin nano-liposome in inhibiting the proliferation of head and neck squamous cell carcinomas. *Phytomedicine* 56, 215–228. doi: 10.1016/j.phymed.2018.11.007

Li, Y. (2012). Qinghaosu (*artemisinin*): chemistry and pharmacology. *Acta Pharmacol. Sin*. 33, 1141–1146. doi: 10.1038/aps.2012.104

Liechty, W. B., Kryscio, D. R., Slaughter, B. V., and Peppas, N. A. (2010). Polymers for drug delivery systems. *Annu. Rev. Chem. Biomol. Eng*. 1, 149–173. doi: 10.1146/annurev-chembioeng-073009-100847

Liu, L., Liu, Y., Ma, L., Mao, F., Jiang, A., Liu, D., et al. (2018). Artemisinin-loaded mesoporous nanoplatform for pH-responsive radical generation synergistic tumor theranostics. *ACS Appl. Mater. Interfaces* 10, 6155–6167. doi: 10.1021/acsami.7b18320

Liu, L., Wei, Y., Zhai, S., Chen, Q., and Xing, D. (2015). Dihydroartemisinin and transferrin dual-dressed nano-graphene oxide for a pH-triggered chemotherapy. *Biomaterials* 62, 35–46. doi: 10.1016/j.biomaterials.2015.05.036

Luo, Y., Sun, X., Huang, L., Yan, J., Yu, B.-Y., and Tian, J. (2019). Artemisinin-based smart nanomedicines with self-supply of ferrous ion to enhance oxidative stress for specific and efficient cancer treatment. *ACS Appl. Mater. Interfaces* 11, 29490–29497. doi: 10.1021/acsami.9b07390

Malmsten, M. (2006). Soft drug delivery systems. *Soft Matter*. 2, 760–769. doi: 10.1039/B608348J

Mangrio, F. A., Dwivedi, P., Han, S., Zhao, G., Gao, D., Si, T., et al. (2017). Characteristics of artemether-loaded poly(lactic-co-glycolic) acid microparticles fabricated by coaxial electrospray: validation of enhanced encapsulation efficiency and bioavailability. *Mol. Pharm*. 14, 4725–4733. doi: 10.1021/acs.molpharmaceut.7b00862

Manjili, H. K., Malvandi, H., Mousavi, M. S., Attari, E., and Danafar, H. (2018). *In vitro* and *in vivo* delivery of artemisinin loaded PCL-PEG-PCL micelles and its pharmacokinetic study. *Artif. Cells Nanomed. Biotechnol*. 46, 926–936. doi: 10.1080/21691401.2017.1347880

Mcatee, C. O., Barycki, J. J., and Simpson, M. A. (2014). Emerging roles for hyaluronidase in cancer metastasis and therapy. *Adv. Cancer Res*. 123, 1–34. doi: 10.1016/B978-0-12-800092-2.00001-0

Nakase, I., Lai, H., Singh, N. P., and Sasaki, T. (2008). Anticancer properties of artemisinin derivatives and their targeted delivery by transferrin conjugation. *Int. J. Pharm*. 354, 28–33. doi: 10.1016/j.ijpharm.2007.09.003

O'neill, P. M., Barton, V. E., and Ward, S. A. (2010). The molecular mechanism of action of artemisinin–the debate continues. *Molecules* 15, 1705–1721. doi: 10.3390/molecules15031705

Pan, U. N., Sanpui, P., Paul, A., and Chattopadhyay, A. (2018). Synergistic anticancer potential of artemisinin when loaded with 8-hydroxyquinoline-surface complexed-zinc ferrite magnetofluorescent nanoparticles and albumin composite. *ACS Appl. Bio Mater*. 1, 1229–1235. doi: 10.1021/acsabm.8b00358

Patra, J. K., Das, G., Fraceto, L. F., Campos, E. V. R., Rodriguez-Torres, M. D. P., Acosta-Torres, L. S., et al. (2018). Nano based drug delivery systems: recent developments and future prospects. *J. Nanobiotechnology* 16:71. doi: 10.1186/s12951-018-0392-8

Pfeifhofer-Obermair, C., Tymoszuk, P., Petzer, V., Weiss, G., and Nairz, M. (2018). Iron in the tumor microenvironment—connecting the dots. *Front. Oncol*. 8:549. doi: 10.3389/fonc.2018.00549

Qin, X., Zhang, H., Wang, Z., and Jin, Y. (2019). Fe_3O_4@SiO_2 mesoporous spheres as Fe(ii) donors loaded with artemisinin and a photosensitizer to alleviate tumor hypoxia in PDT for enhanced anticancer therapy. *New J. Chem*. 43, 8761–8773. doi: 10.1039/C9NJ00974D

Tang, Z., Liu, Y., He, M., and Bu, W. (2019). Chemodynamic therapy: tumour microenvironment-mediated fenton and fenton-like reactions. *Angew. Chem. Int. Edit*. 58, 946–956. doi: 10.1002/anie.201805664

Tran, T., Nguyen, T., Nguyen, H., Nguyen, H. T., Kim, J., Yong, C., et al. (2016). Targeted and controlled drug delivery system loading artersunate for effective chemotherapy on CD44 overexpressing cancer cells. *Arch. Pharm. Res*. 39, 687–694. doi: 10.1007/s12272-016-0738-4

Vines, J. B., Yoon, J. H., Ryu, N. E., Lim, D. J., and Park, H. (2019). Gold nanoparticles for photothermal cancer therapy. *Front. Chem*. 7:167. doi: 10.3389/fchem.2019.00167

Wan, X., Zhong, H., Pan, W., Li, Y., Chen, Y., Li, N., et al. (2019). Programmed release of dihydroartemisinin for synergistic cancer therapy using a $CaCO_3$ mineralized metal–organic framework. *Angew. Chem. Int. Edit*. 131, 14272–14277. doi: 10.1002/ange.201907388

Wang, D., Zhou, J., Chen, R., Shi, R., Wang, C., Lu, J., et al. (2017). Core–shell metal-organic frameworks as Fe^{2+} suppliers for Fe^{2+}-mediated cancer therapy under multimodality imaging. *Chem. Mater*. 29, 3477–3489. doi: 10.1021/acs.chemmater.6b05215

Wang, D., Zhou, J., Chen, R., Shi, R., Xia, G., Zhou, S., et al. (2016a). Magnetically guided delivery of DHA and Fe ions for enhanced cancer therapy based on pH-responsive degradation of DHA-loaded Fe_3O_4@C@MIL-100(Fe) nanoparticles. *Biomaterials* 107, 88–101. doi: 10.1016/j.biomaterials.2016.08.039

Wang, D., Zhou, J., Chen, R., Shi, R., Zhao, G., Xia, G., et al. (2016b). Controllable synthesis of dual-MOFs nanostructures for pH-responsive artemisinin delivery, magnetic resonance and optical dual-model imaging-guided chemo/photothermal combinational cancer therapy. *Biomaterials* 100, 27–40. doi: 10.1016/j.biomaterials.2016.05.027

Wang, J., Zhang, C. J., Chia, W. N., Loh, C. C., Li, Z., Lee, Y. M., et al. (2015). Haem-activated promiscuous targeting of artemisinin in Plasmodium falciparum. *Nat. Commun*. 6:10111. doi: 10.1038/ncomms10111

Wang, J., Zhang, J., Shi, Y., Xu, C., Zhang, C., Wong, Y. K., et al. (2017). Mechanistic investigation of the specific anticancer property of artemisinin and its combination with aminolevulinic acid for enhanced anticolorectal cancer activity. *ACS Cent. Sci*. 3, 743–750. doi: 10.1021/acscentsci.7b00156

Wong, Y. K., Xu, C., Kalesh, K. A., He, Y., Lin, Q., Wong, W. S. F., et al. (2017). Artemisinin as an anticancer drug: Recent advances in target profiling and mechanisms of action. *Med. Res. Rev*. 37, 1492–1517. doi: 10.1002/med.21446

Xiao, Y. S., Huang, W., Zhu, D. M., Wang, Q. X., Chen, B. Y., Liu, Z. S., et al. (2020). Cancer cell membrane-camouflaged MOF nanoparticles for a potent dihydroartemisinin-based hepatocellular carcinoma therapy. *RSC Adv*. 10, 7194–7205. doi: 10.1039/C9RA09233A

Yu, X.-A., Lu, M., Luo, Y., Hu, Y., Zhang, Y., Xu, Z., et al. (2020). A cancer-specific activatable theranostic nanodrug for enhanced therapeutic efficacy via amplification of oxidative stress. *Theranostics* 10, 371–383. doi: 10.7150/thno.39412

Zhang, H., Chen, Q., Zhang, X., Zhu, X., Chen, J., Zhang, H., et al. (2016). An intelligent and tumor-responsive Fe^{2+} donor and Fe^{2+}-dependent

drugs cotransport system. *ACS Appl. Mater. Interfaces* 8, 33484–33498. doi: 10.1021/acsami.6b11839

Zhang, H., Hou, L., Jiao, X., Ji, Y., Zhu, X., and Zhang, Z. (2015a). Transferrin-mediated fullerenes nanoparticles as Fe2+-dependent drug vehicles for synergistic anti-tumor efficacy. *Biomaterials* 37, 353–366. doi: 10.1016/j.biomaterials.2014.10.031

Zhang, H., Ji, Y., Chen, Q., Jiao, X., Hou, L., Zhu, X., et al. (2015b). Enhancement of cytotoxicity of artemisinin toward cancer cells by transferrin-mediated carbon nanotubes nanoparticles. *J. Drug Target* 23, 552–567. doi: 10.3109/1061186X.2015.1016437

Zhang, H., Zhang, H., Zhu, X., Zhang, X., Chen, Q., Chen, J., et al. (2017). Visible-light-sensitive titanium dioxide nanoplatform for tumor-responsive Fe2+ liberating and artemisinin delivery. *Oncotarget* 8, 58738–58753. doi: 10.18632/oncotarget.17639

Zhang, Y., Xu, G., Zhang, S., Wang, D., Saravana Prabha, P., and Zuo, Z. (2018). Antitumor research on artemisinin and its bioactive derivatives. *Nat. Products Bioprospect.* 8, 303–319. doi: 10.1007/s13659-018-0162-1

Zhao, P., Tang, Z., Chen, X., He, Z., He, X., Zhang, M., et al. (2019). Ferrous-cysteine–phosphotungstate nanoagent with neutral pH fenton reaction activity for enhanced cancer chemodynamic therapy. *Mater. Horiz.* 6, 369–374. doi: 10.1039/C8MH01176A

Conflict of Interest: The authors declare that the research was conducted in the absence of any commercial or financial relationships that could be construed as a potential conflict of interest.

frontiers in Chemistry

ORIGINAL RESEARCH
published: 30 June 2020
doi: 10.3389/fchem.2020.00492

Obtaining and Characterization of a Polydisperse System Used as a Transmembrane Carrier for Isosorbide Derivatives

Florin Borcan[1†], *Adél Len*[2,3†], *Diana A. Bordejevic*[4], *Zoltán Dudás*[2,5*], *Mirela C. Tomescu*[4] *and Adina N. Valeanu*[6]

[1] *The 1st Department (Analytical Chemistry), Faculty of Pharmacy, "Victor Babes" University of Medicine and Pharmacy, Timisoara, Romania,* [2] *Neutron Spectroscopy Department, Centre for Energy Research, Hungarian Academy of Sciences, Budapest, Hungary,* [3] *Faculty of Engineering and Information Technology, University of Pécs, Pécs, Hungary,* [4] *The 5th Department (Internal Medicine I), Faculty of Medicine, "Victor Babes" University of Medicine and Pharmacy, Timisoara, Romania,* [5] *"Coriolan Drăgulescu" Institute of Chemistry, Romanian Academy, Timisoara, Romania,* [6] *The 2nd Department, Faculty of Dental Medicine, "Victor Babes" University of Medicine and Pharmacy, Timisoara, Romania*

OPEN ACCESS

Edited by:
Ye Tian,
Nanjing University, China

Reviewed by:
Shih-Ting Wang,
Brookhaven National Laboratory (DOE), United States
Wang Shuang,
Changchun Institute of Applied Chemistry (CAS), China

***Correspondence:**
Zoltán Dudás
dudas.zoltan@energia.mta.hu

[†] *These authors have contributed equally to this work*

Specialty section:
This article was submitted to Nanoscience, a section of the journal Frontiers in Chemistry

Received: *19 March 2020*
Accepted: *12 May 2020*
Published: *30 June 2020*

Citation:
Borcan F, Len A, Bordejevic DA, Dudás Z, Tomescu MC and Valeanu AN (2020) Obtaining and Characterization of a Polydisperse System Used as a Transmembrane Carrier for Isosorbide Derivatives. Front. Chem. 8:492. doi: 10.3389/fchem.2020.00492

Due to their effect of vasodilatation, isosorbide nitrates represent one of the most important and most used solutions for angina pectoris. Unfortunately, these compounds have multiple dose-related adverse drug reactions such as headache, weakness, mild dizziness, and occasionally heart rate changes, nausea, vomiting, and sweating. The main aims of this research were to obtain and to evaluate new polyurethane (PU) structures that can be used as a proper transmembrane carrier with an improved release kinetic. Chitosan-based PU structures were obtained by a polyaddition process between hexamethylene diisocyanate and a mixture of chitosan, butanediol, and polyethylene glycol in the presence of caffeine as a synthesis catalyst. The obtained samples (with and without isosorbide nitrates) were characterized regarding the encapsulation and release rate (UV-Vis spectra), chemical composition (FTIR), thermal stability (thermal analysis), morphology changes (SEM and SANS), and *in vivo* irritation tests. These methods revealed no significant differences between the two sample structures. Multipopulational structures with sizes between 73 and 310 nm, with an increased tendency to form clusters and a high resistance to heat (up to 280°C), were obtained. This study presents an alternative administration of isosorbide derivatives based on a PU carrier with a high biocompatibility and a prolonged release.

Keywords: chitosan, drug delivery, polyurethane, skin irritation, microstructural characterization

INTRODUCTION

Nitrate medications (nitroglycerin, sodium nitroprusside, isosorbide derivatives, etc.) are pharmaceutical agents with vasodilator effect (Polakowska et al., 2016). Thus, medication with isosorbide nitrates as active compounds is often used to prevent angina attacks and in the prophylactic treatments of angina pectoris (Yao et al., 2015). They can be also used in combination

with cardiotonic glycosides, diuretics, and ACE inhibitors as adjuvant treatment of congestive heart failure (Kocyigit et al., 2017). Isosorbide nitrates include isosorbide dinitrate (IS-DN), 2-mononitrate (IS-2-MN), and 5-mononitrate (IS-5-MN), the last two being active metabolites of IS-DN and they exert qualitatively similar effects. A comparative study on these compounds reveals that IS-2-MN induces a lower increase of cyclic guanosine monophosphate (cGMP) and less tolerance induction, and its vasodilator effect is probably due to other mechanisms than the stimulation of guanylate cyclase (Raddino et al., 2010). U. Thadani and T. Rodgers reported a series of problems due to the administration of isosorbide nitrates: 82% of patients accused headaches and ∼10% could not tolerate them due to dizziness and/or disabling headaches; severe hypotension cases accompanied by syncope were recorded; the combination of nitrates and phosphodiesterase-5 inhibitors used together for the treatment of erectile dysfunction induces a major decrease of blood tension and might lead to death (Thadani and Rodgers, 2006).

The particles used as carriers of isosorbide derivatives have a very long history: Hirayama et al. (1988) described three decades ago the obtaining and the physicochemical properties of a carrier, based on heptakis(2,6-di-O-ethyl)-beta-cyclodextrin whose dissolution and IS-DN release rates were significantly decreased after the complexation with the cyclodextrin. Microcapsules based on hydroxypropyl cellulose with three different particle populations were developed by Yang et al. (2006) in order to obtain an improved kinetic model. A possible synergistic effect of IS-5-MN liposomalization and addition of glycerol in a transdermal carrier was studied *in vitro* by Barichello et al. (2017); they have applied both liposomal and aqueous solution with and without glycerol and they have found that glycerol facilitates the skin permeation while the liposomalization process leads to the drug accumulation. Most recently, the research team of Steinbach et al. (2017) has developed microemulsions with ceramide nanoparticles containing isosorbide and they have assessed the retarder action *ex vivo* in a Franz diffusion cell. Their results proved that ceramide particles present a better penetration in the upper layers of the skin without any irritating effect.

The usual routes for drug administration (oral, inhalable, intramuscular/intravenous, topical, and rectal) are selected depending on the drug formula, its toxicity and metabolic pathway, and the part of the body that is treated (Turner et al., 2011). Unfortunately, these classical routes are not always effective to assure the optimal dose of every drug to its specific receptor; there are several important drugs (e.g., hormones) with dosage inside the body whose gradual release is often a problem. The development of drug delivery systems, based on recent nano-sciences developments and on improved knowledge about the body membranes, represents a revolutionary advantage for many medications. Nowadays, organic and inorganic carriers are synthesized to solve two main problems: to avoid the adverse events (the side effects) and to modify the physicochemical properties of drugs in order to improve their transmembrane transfer (Solano-Umana et al., 2015).

The advantage of a polydisperse system used as a drug carrier consists in the gaining of a balance between the endocytosis-dependent cellular uptake and the amount of the encapsulated therapeutic compound; different pathways such as clathrin-caveolin-independent, caveolin-dependent, and clathrin-mediated are specific to nanoparticles, while the particles over 100 nm use macro-pinocytosis and phagocytosis to transfer their load (Danaei et al., 2018). On the other hand, the degradation of particles and their release rate depend on the type of carrier, the loading capacity, and the length of polymer chains. A polydisperse system containing particles with different sizes behaves rather like a slow-release delivery system. The interest for the prolonged released formulations containing isosorbide nitrates started more than four decades ago; R. Bonn has obtained capsules with isosorbide mononitrate that ensures a long-lasting effect (Bonn, 1988). Another long-acting formulation based on a controlled membrane principle was developed after 10 years (Prakash and Markham, 1999) and a comprehensive review describing the need of a prolonged release for this class of drugs was published in the same year (Gunasekara and Noble, 1999).

Polyurethanes (PUs) appeared in the laboratory of Prof. Otto Bayer at IG. Farbenindustrie Leverkusen (Germany) almost one century ago (Gama et al., 2018). There are many types of PU-based materials that look and behave very differently from each other. The main areas of their application are as follows: buildings (thermal insulation, sandwich panels, rigid columns, and other elements of architectural design), refrigeration (thermal insulation of refrigerators and freezers), automotive industry (car dashboard and steering wheel, door panels), furniture (cabinets, elastic mattresses, and pillows), textiles (camping products, adhesives for footwear), etc. Early use of PU in medicine was reported by Boretos and Pierce; they observed its vascular acceptability in experimental heart-assist pump chambers and arterial cannulae (Hasirci and Aksoy, 2007). In the last four decades, the use of PU covers many other medical fields such as cardiovascular devices (catheters, vascular prostheses, pacemakers), reconstructive surgery materials (wound dressings, breast implants, maxillofacial prostheses), and obstetrics and gynecology (condoms, contraceptive sponges; Vermette and Griesser, 2001). Basu et al. (2016) present a series of drug carriers based on PUs: nanoparticle systems, stimulus-responsive systems, shape-memory systems, etc.

The development of a poly(tetramethylene glycol)/isosorbide-based PU elastomer has been reported by Kim et al. (2014). It was found that this highly elastic and biocompatible PU presents increased mechanical properties and it can be used for soft tissue augmentation and regeneration. A similar study describing a PU with self-healing properties (Kim et al., 2019) has revealed that the replacement of traditional chain extenders (such as 1,4-butanediol or 1,6-hexanediol) with isosorbide or isomannide leads to materials with improved mechanical properties. Our research team already synthesized PU nano- and micro-structures with low release rates used as transmembrane delivery systems for different natural extracts (Munteanu et al., 2017; Borcan et al., 2018a,b,c, 2019). The aim of this study was to obtain and to characterize a chitosan-based PU that

can assure a constant release of isosorbide derivatives for a prolonged time.

MATERIALS AND METHODS

Reagents

Chitosan-based PU structures were obtained using the following reagents: hexamethylene diisocyanate (HDI), polyethylene glycol (PEG 200), and caffeine were obtained from Merck (Darmstadt, Germany); acetic acid 96%, acetone, and HCl 1N were obtained from Chimopar SA (Bucharest, Romania); 1,4-butanediol (BD) was purchased from Carl Roth GmbH (Karlsruhe, Germany); and chitosan was from Oxford Lab. Chem. (Vasai-Virar, Maharashtra, India). These reagents were of commercial reagent grade; they were kept under the conditions indicated by the manufacturer and they were used without further purifications.

Inorganic salts such as NaCl, KCl, $NaHCO_3$, Na_2HPO_4, K_2HPO_4, KH_2PO_4, and $MgCl_2$ were purchased from Chimopar SA (Bucharest, Romania), and they were used to prepare a simulated body fluid; they were of analytical grade and they were previously heated to remove the crystallization water.

Synthesis of Chitosan-Based PU Structures

The first step was the solubilization of chitosan: 100.0 mg chitosan, 2.5 ml acetic acid, and 5 ml HCl were added to 50 ml of double deionized distilled water, and they were mixed on a Velp hot plate stirrer with 300 rpm, at 45°C for 10 min. In the second step, the aqueous phase was prepared by using the entire previously obtained chitosan solution and 2.0 ml of BD, 3.0 ml of PEG 200, and 40.0 mg of caffeine as catalyst of PU synthesis. This mixture was further sonicated with a powerful lab homogenizer (Hielscher UP200S) for another 15 min, and after that, it was split into two different 100-ml polymerization flasks in equal volumes. Ten milliliters of aqueous solution containing 3 mmol IS-2-MN, 1 mmol IS-5-MN, and 5 mmol IS-DN was added in one of the flasks, and it was labeled as PU_1 (sample containing isosorbide nitrates), while the other flask was labeled PU_0 (reference sample, empty chitosan-based PU without nitrates).

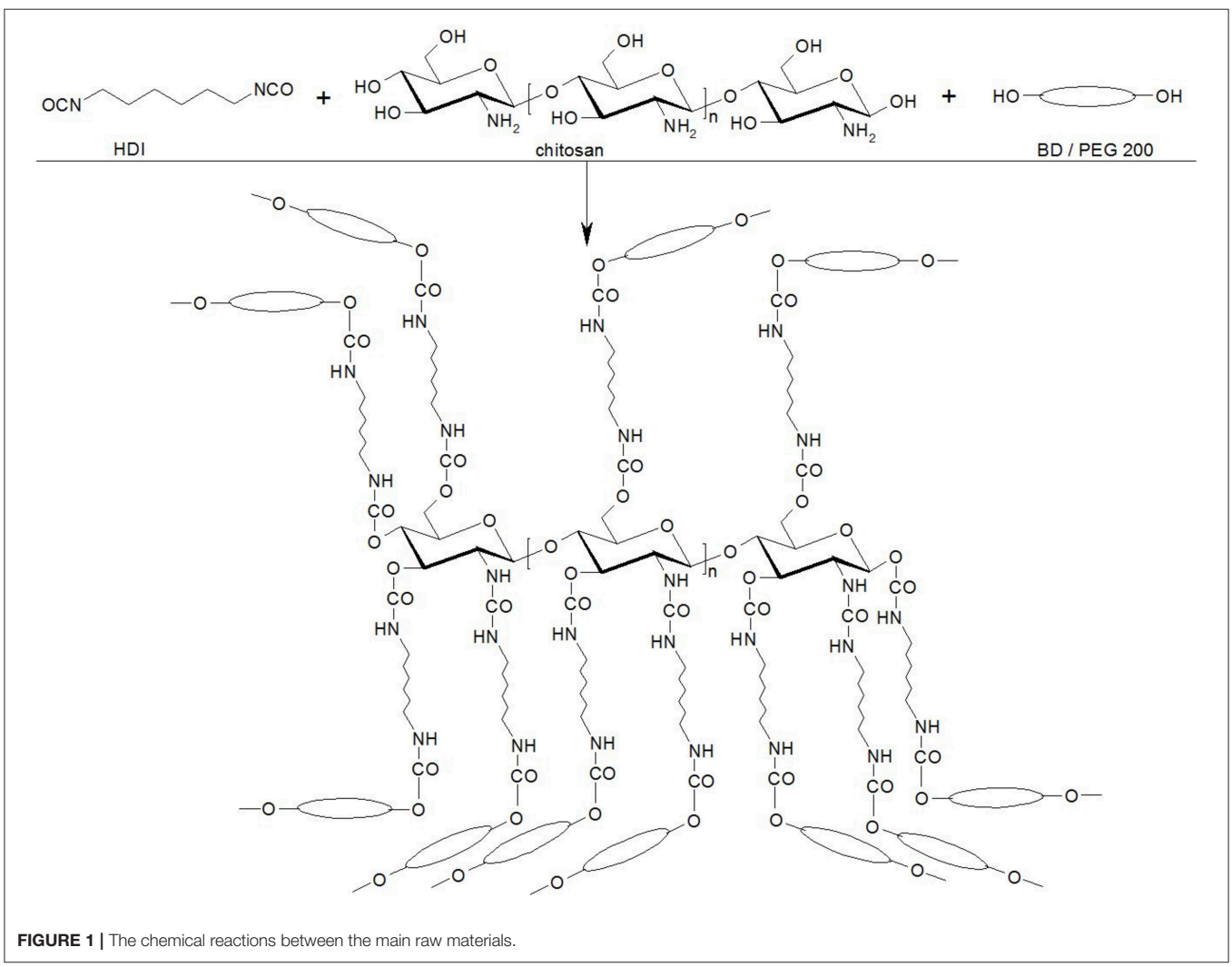

FIGURE 1 | The chemical reactions between the main raw materials.

In the third step of the synthesis, the organic phase was prepared in a 100-ml Berzelius beaker: 14.0 ml of HDI was dissolved in 50 ml of acetone, and the mixture was homogenized for 10 min and was poured in the two polymerization flasks in equal volumes.

The content of these flasks was stirred with 300 rpm, at room temperature for 90 min in order to complete all chemical reactions of macromolecular chains.

In the last step, the synthesis products were washed three times with a mixture of acetone and water (1:1, v/v) and they were slowly dried by being kept as thin layers at room temperature till no mass change was observed.

Figure 1 presents the starting chemical reactions that happen around the chitosan molecules and lead to a three-dimensional growth of chains.

Drug Encapsulation Efficiency

The percentage of drug that was successfully entrapped inside a carrier can be calculated by reporting the free/untrapped drug to the total amount of drug added (Bouchemal et al., 2004). **Figure 2** presents the UV spectra of isosorbide nitrates and of PU structures obtained on a UVi Line 9,400 Spectrophotometer (SI Analytics, Germany). It can be observed that IS-DN has no maximum peak, while the two isosorbide mononitrate isomers' (IS-MN) spectra overlap perfectly. A calibration curve, describing the dependence between the absorbance at 220 nm and the concentration of IS-2-MN standard solutions, was drawn in accordance with Tsai et al. (1994).

Drug Release Kinetics

The cumulative percentage of isosorbide derivatives that were released at a specific moment was determined by maintaining the chitosan-based PU structures with derivatives (sample PU_1) in a degradation medium (a simulated body fluid, SBF according to T. Kokubo recipe; Quan et al., 2016) for 3 weeks; the procedure is described in detail in one of our previous papers (Borcan et al., 2018c).

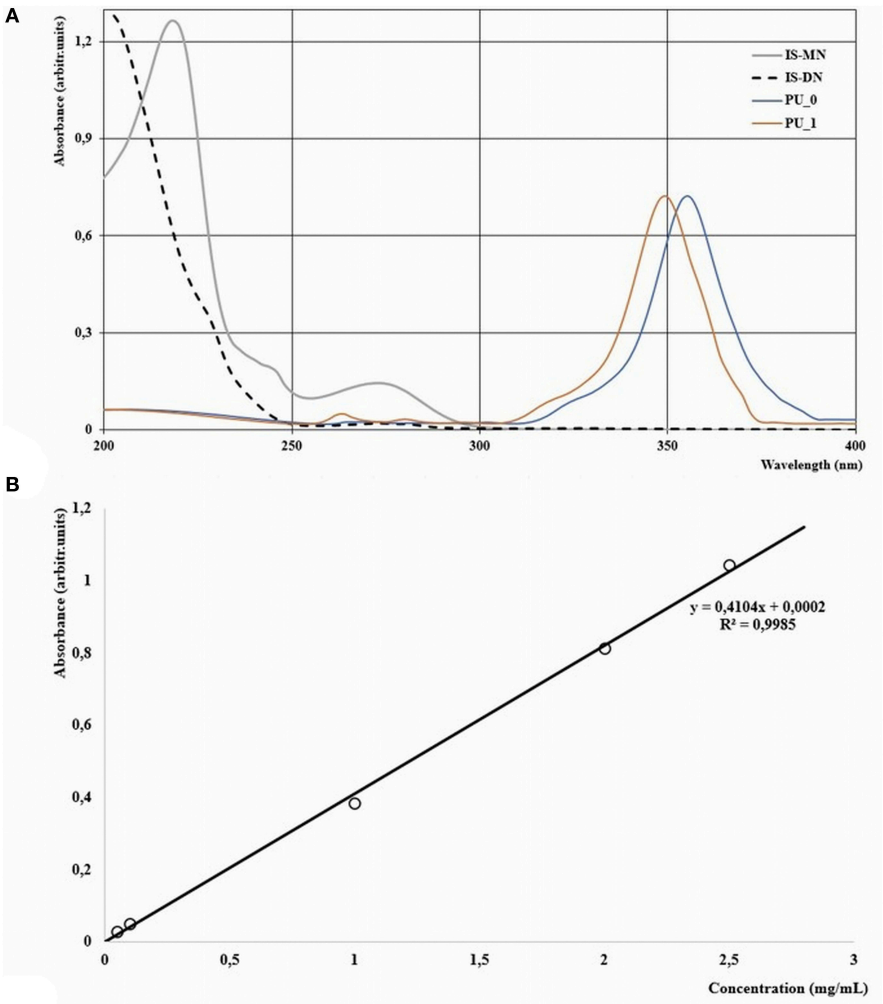

FIGURE 2 | (A) UV-Vis spectra of samples and **(B)** calibration curve of isosorbide mononitrate.

Thermal Analysis

The resistance of samples to heating and the study of thermal degradation processes were done using a DSC1 (Mettler-Toledo, Switzerland); 4 ± 0.3-mg samples were placed in aluminum crucibles with pierced lids, and they were heated in an inert atmosphere between 30 and 300°C with 5°C/min.

Zetasizer Measurements

The size and the surface charge of the chitosan-based PU structures with and without isosorbide derivatives were assessed using a Cordouan Zetasizer (Cordouan Technol., France). The following input parameters of the size module were set: evaluation temperature (25°C), time intervals (12 μs), number of channels (225), laser power (80 ± 5%), acquisition mode (statistical mode with noise limit; minimum 6 acquisitions/sample), and analysis mode (Cumulants). In the case of Zeta potential module, the parameters were quartz cuvette, temperature (25°C), laser power (75 ± 5%), applied field (automatic), medium resolution, 3 measures/sequence, and Henry function (Smoluchowski).

Scanning Electron Microscopy (SEM)

The shape and surface morphology of the PU nano-/micro-particles were determined from micrographs recorded with a TESCAN 3 VEGA scanning electron microscope secondary electron detector. The high-voltage value was set at 20 kV. The samples were tested in their natural form under vacuum.

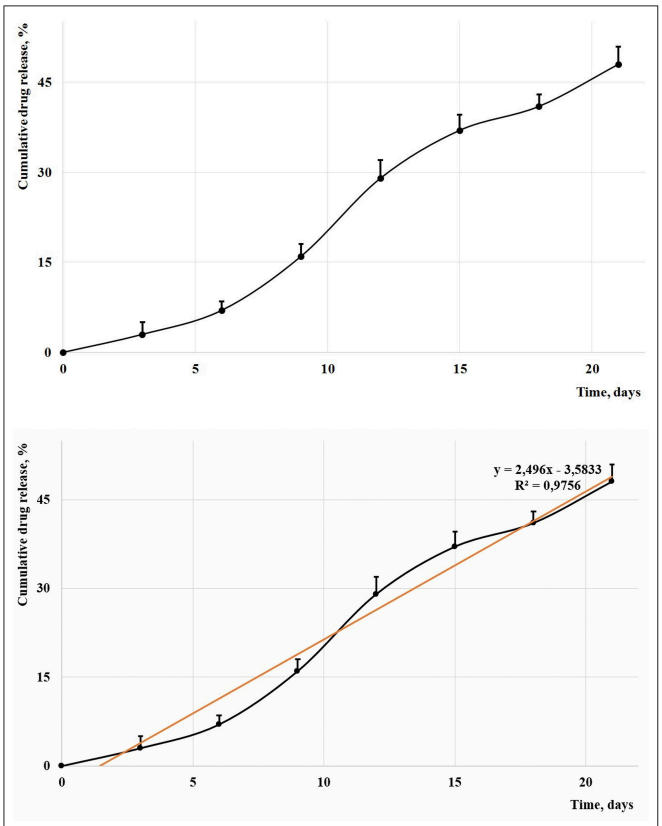

FIGURE 3 | The cumulative release of isosorbide derivatives.

Fourier Transform Infrared Spectroscopy (FTIR)

Differences on the chemical composition of the two samples' functional groups were analyzed by FTIR spectroscopy. Hereby, FTIR spectra were collected, using KBr pellets, through the use of a Cary 630 FTIR spectrophotometer (Agilent, USA), in the wavenumber ranging 400–4,000 cm^{-1}.

Small-Angle Neutron Scattering (SANS)

SANS measurements were performed on the Yellow Submarine (YS) instrument at the Budapest Neutron Centre in Hungary. Neutrons with wavelengths of 4.2 and 10.2 Å and sample-to-detector distances of 1.15 and 5.25 m were chosen. This range of wave vectors corresponds to structural sizes ranging from 1 to 100 nm. The samples were deposited in quartz cuvettes with 2-mm thickness and they were placed for 30 to 60 min in an 8-mm-diameter neutron beam.

In vivo Evaluations

Seven human volunteers (3 men and 4 women, between 25 and 37 years old) were used to evaluate the skin irritation caused by the products. The two synthesized samples (PU_0 and PU_1) and a mixture of isosorbide derivatives as reference were applied as solutions (1:20 w/v) on three areas of the left anterior forearm every third day (0.5 ml/application) and the determinations of the skin parameters were performed 25 min later on every treated area. The measurements were carried out with a MultiProbe Adapter from Courage&Khazaka Electronics (Köln, Germany), equipped with a Tewameter® TM300 probe and a Mexameter® MX18 probe, by the same operator, at the same moment of the day for 15 days. The values are expressed as differences between after and before any application due to the differences in skin types of the analyzed volunteers.

Statistics and Ethical Approval

The statistical analyses were performed using IBM SPSS v.23; the results were expressed as mean ± standard error. One-Way ANOVA and Bonferonni–Dunn tests were used to determine the statistical difference between experimental and blank values groups; ** and *** indicate $p < 0.01$ and $p < 0.001$ on **Figures 11**, **12**.

The research was done according to the principles of the Declaration of Helsinki. The authors declare that all procedures respect the specific regulations and standards: the study was first evaluated and approved by the Ethical Committee of "Victor Babes" University of Medicine and Pharmacy Timisoara, Romania. Every volunteer read and signed an informed consent and a signed informed consent for publication of the research results was also obtained.

RESULTS

Three-dimensional PU structures are often found among those materials that are preferably used in medical applications

due to their easy and cheap production as well as to their unique combination of biocompatibility, sterilizability, durability, good mechanical properties, abrasion, and chemical resistance (Kikuchi et al., 2017).

Drug Encapsulation Efficiency

The difference between the most intense absorption positions of the empty PU structures (360 nm) and isosorbide mononitrates (220 nm) represents an important advantage in the evaluation of the concentration of the active substances in the studied solutions. Encapsulation efficiency equal to 72.3% was found by reporting the quantity of free mononitrates inside the washing mixture from the last synthesis step to the total amount of isosorbide mononitrates added to synthesis.

Drug Release Kinetics

Figure 3 presents the evolution of the cumulative percentage of isosorbide mononitrates that were released inside a simulated body fluid; 5 aliquots of each 0.4 ml were replaced every third day with fresh medium, and their maximum absorption was found at 220 nm; mean concentrations and standard deviation were used to explain the release profile.

Thermal Analysis

DSC curves (**Figure 4**) indicate a mild dehydration process during the samples' heating between 50 and 100°C (a large endothermic peak) and a good thermal stability up to 260–280°C. No important difference was observed between the samples and no melting point of isosorbide derivatives was found, which indicates the absence of the isosorbide derivatives in their free form.

Zetasizer Measurements

Figures 5, **6** present the distribution of PU structure size. The complexity and multipopulation character of the samples are confirmed by their polydispersity index (PDI). Master curve, a very precious indicator for stable polydisperse samples, obtained using Pade-Laplace analysis, is defined by the averaged autocorrelation function over the whole run. PDI for sample PU_0 was found as 0.7 with five different structure populations between 73 and 408 nm. Predominant populations were 112.2 nm (76.2%) and 223.9 nm (18.6%). PDI for sample PU_1 was found as 0.6 with four main populations between 104 and 310 nm. Predominant populations were 123.1 nm (86.4%) and 309.1 nm (8.3%). Zeta potential values determined as the mobility of structures in an electric field were 10.71 mV (sample PU_0) and 9.55 mV (sample PU_1), values that are specific to colloidal systems with a high tendency to form agglomerations of structures.

Scanning Electron Microscopy (SEM)

The aspect of samples studied by SEM at different magnifications (220×, 500×, 1,000×, and 1,500×) confirms the desired heterogeneity of chitosan-based PU structures (**Figures 7**, **8**) without an explicit difference between the PU_0 and PU_1 samples.

Fourier Transform Infrared Spectroscopy

FTIR is one of the most important analysis methods in this domain. The diversity of PU functional groups justifies its use. PUs contain multiple urethane groups (-NH-CO-O-), but they are in balance with others: free hydroxyl (-OH) and amine rests (-NH_2, -NH-) or functional groups specific

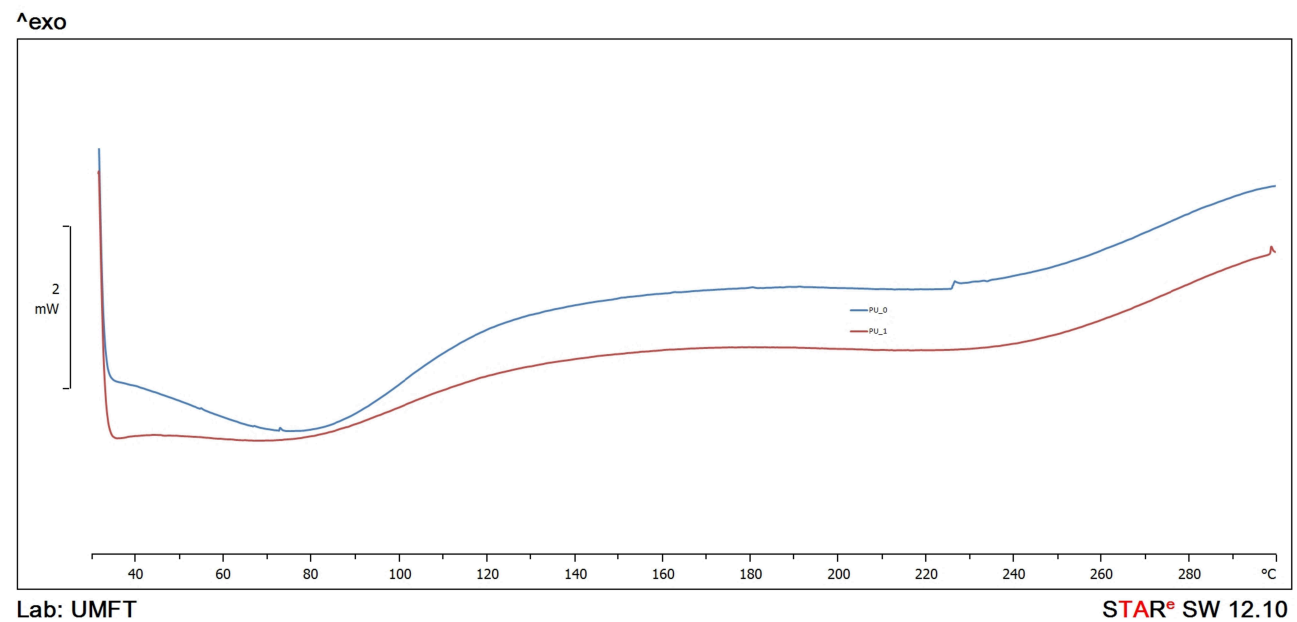

FIGURE 4 | DSC thermograms of chitosan-based PU structures.

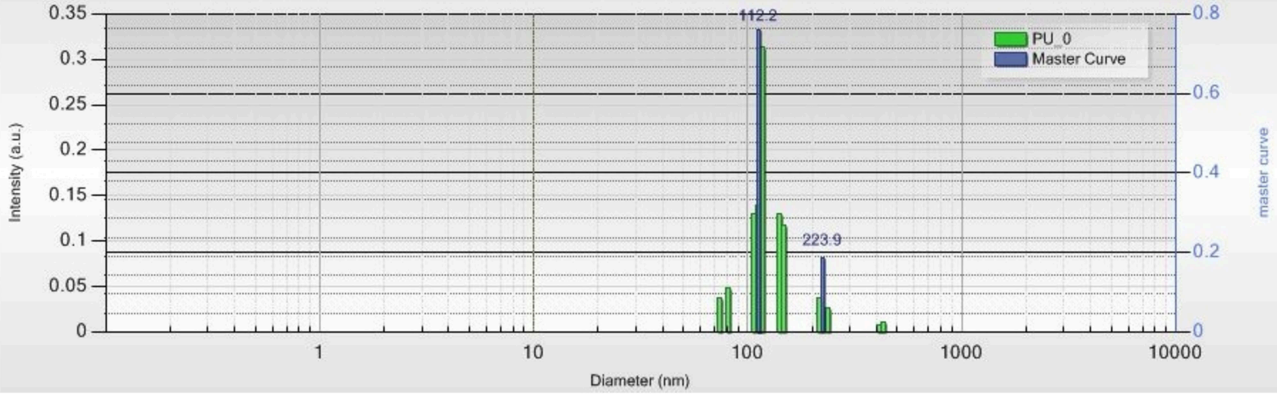

FIGURE 5 | The size distribution of structures from sample PU_0.

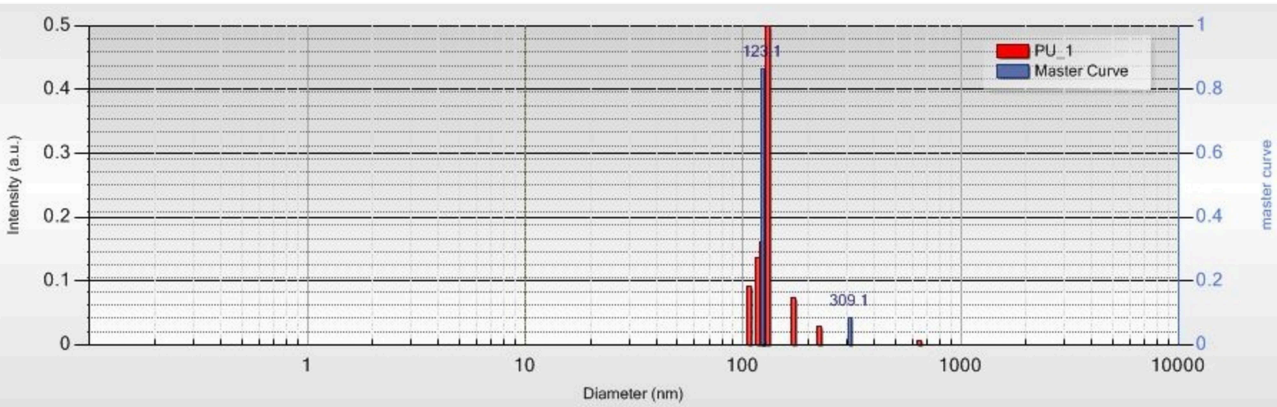

FIGURE 6 | The size distribution of structures from sample PU_1.

to secondary products as allophanate (-NH-CO-NR-CO-O-), biuret (-NH-CO-NR-CO-NH-), and urea (-NH-CO-NH-). **Figure 9** presents the overlapped IR spectra obtained for the two samples.

SANS Analysis

SANS method was used to evaluate the microtextural properties of chitosan-based PU structures. **Figure 10** presents comparative information about the synthesized samples. The calibrated SANS data curves were described with a power-law type scattering, according to the Porod approximation (see Equation 1), used for large scattering objects (where $QR >> 1$, R being a characteristic, average size of the scattering particles).

$$I(Q) = AQ^{-p} + B \quad (1)$$

A is a constant containing instrumental attributes and sample physical characteristics, and B is the incoherent background scattering. In this Q vector range, SANS did not give information about the size of the scattering particles/pores/inclusions; however, it characterized their surface. The value of the p power was characteristic to rough, fractal-like surfaces and interfaces.

In vivo Evaluations

Animal and human skin models are often used to evaluate the irritation effects of new compounds. Modern and non-invasive techniques were developed to assess the skin parameters such as skin pH, transepidermal water loss (TEWA), melanin and erythema, the level of stratum corneum hydration, sebum, etc. **Figures 11**, **12** present the changes of transepidermal water loss and erythema levels as main indicators of any irritation effect.

DISCUSSION

In the present synthesis of the PU structures, HDI was used as a diisocyanate instead of aromatic compounds often used in industrial applications for their better mechanical properties. Studies on PU materials degradation revealed that the main raw materials (polyols and isocyanates) were usually obtained during their decomposition (Bolcu and Borcan, 2005); thus, in

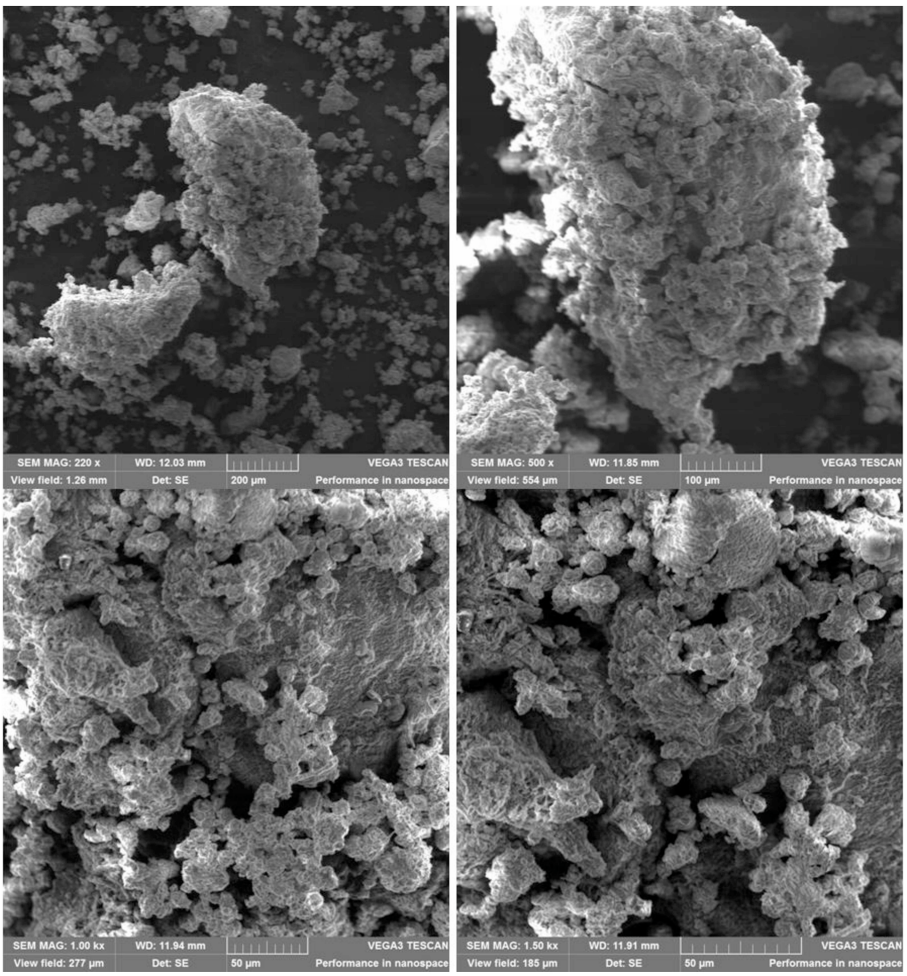

FIGURE 7 | Aspect of structures from sample PU_0 at different magnifications.

the present study, an aliphatic diisocyanate has been chosen in order to avoid the introduction of certain aromatic compounds in the human body. Caffeine was used as synthesis catalyst instead of other tertiary amines [1,4-diazabicyclo(2.2.2)octane], tin, or bismuth organic compounds (dibutyl-tin-dilaurate, bismuth neodecanoate; Guhl, 2008); this natural cardiac and central nervous system stimulant was chosen because of its low toxicity. Chitosan has been chosen as a crosslinking agent based on the information about its natural source, ability to swell, capacity to absorb water, and grafting efficiency.

The prolonged release of isosorbide derivatives was obtained by using polyethylene glycol as raw material instead of any other ester polyol that has a faster hydrolysis (Hajnal et al., 2016) and by using a mixture of mono- and di-nitrates (**Figure 13**): IS-DN does not contain any active hydrogen and it is just physically entrapped inside the polymer matrix, while IS-2-MN and IS-5-MN contain a hydroxyl group and an important part of their amount is covalently bound to the PU chains. Literature describes the extended release as a slower delivery of the entrapped drugs at therapeutic level for 8–12 h while a prolonged release indicates a delivery over a longer and delayed period; Korsmeyer–Peppas model is often used to describe the drug release from polymeric systems (Kakar et al., 2014). Mathematical models have a key role in the interpretation of release profiles; the trend of the present release can be described by the equation $y = 2.496x - 3.5833$ ($R^2 = 0.9756$), which is specific to a better release than those described in the case of three nano-fibrous scaffolds based on Nylon 6 or polycaprolactam and used as carrier for Cetirizine (Saadatmand et al., 2019).

Bolcu and Borcan (2005) have reported that PU materials are thermally stable up to 300–320°C depending on the aliphatic/aromatic character of diisocyanates. The insertion of chitosan in the synthesis and the appearance of allophanates in the reaction between PUs' -NH- and an isocyanate, substitute biuret structures in the reaction between $-NH_2$ and two isocyanate molecules, amides (carboxylic with isocyanate groups), and urea groups in the reaction between primary amines and one isocyanate group, lead to a decreased thermal stability (the degradation begins at 260–280°C, **Figure 4**).

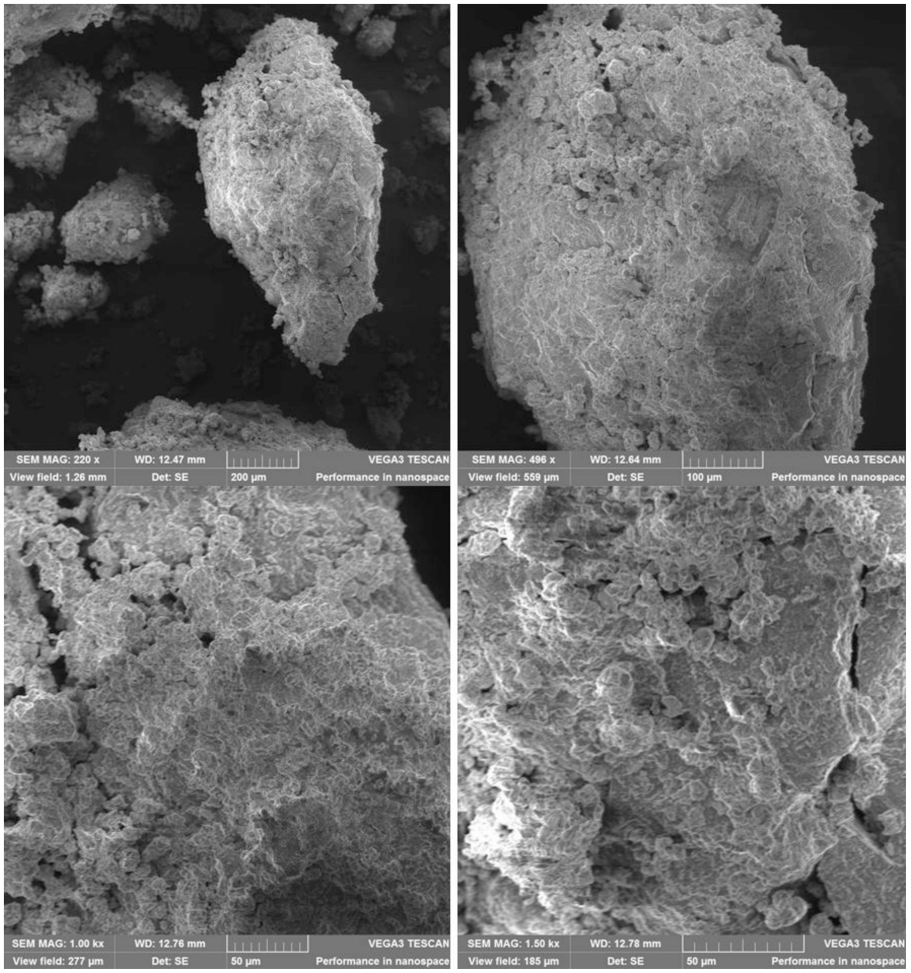

FIGURE 8 | Aspect of structures from sample PU_1 at different magnifications.

The polydispersity, or size heterogeneity of the samples, measured as PDI is a representation of the distribution of different particle populations; PDI is a number between 0.0 for perfectly homogeneous samples and 1.0 for highly heterogeneous samples with multiple particle populations. Carriers with high PDI were extensively employed to enhance the drugs' bioavailability and their release. Danaei et al. (2018) explained a few advantages of drug delivery systems with bigger PDI: the particles of a polydisperse system reach the targeted receptor at different moments and the accumulated effects specific to monodisperse carriers are thus avoided; particles with different sizes have a different capacity to entrap drugs and different degradation and release rates. The Zetasizer measurements confirm the obtaining of multipopulational PU structures that were observed in SEM images (**Figures 7**, **8**), too.

The main functional groups of PU present the following positions of their vibrations in the FTIR spectra: free hydroxyl (3,610–2,870 cm^{-1}), -NCO (2,280–2,260 cm^{-1}), urethane groups (1,715–1,650 cm^{-1}), and allophanate at 1720 cm^{-1} (Bolcu and Borcan, 2005). FTIR spectra of our samples PU_0 and PU_1 (**Figure 9**) are quite similar with a few little differences. This similarity is due to the good isolation of encapsulated isosorbide derivatives on the one hand and to a good wash of free un-encapsulated raw materials during the last step of the synthesis on the other hand. Specific signals of N-H stretching vibrations can be observed at 3,341–3,339 cm^{-1}, stretching vibrations of -CH_2- and -CH_3 at 2,932–2,862 cm^{-1}, stretching vibrations of C=O from urea and urethane groups at 1,629–1,572 cm^{-1}, -CH_2- deformations at 1,471–1,377 cm^{-1}, stretching vibrations of urethane C–O at 1,260-1,256 cm^{-1} and of ether C–O–C between 1,110 and 1,070 cm^{-1}, while the other signals correspond to deformation vibration of urethane CO–O bonds. There were no observed specific signals of free -NCO (stretching vibrations at 2,260 cm^{-1}) and C = O of isocyanurate rings (1,690 cm^{-1}).

The significant absorption bands of isosorbide nitrate FTIR spectra were already described in literature (Silvieri

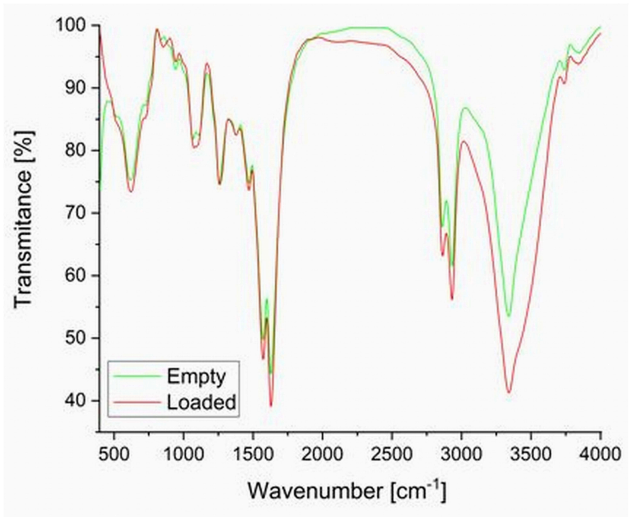

FIGURE 9 | Comparative FT-IR spectra of empty and drug-loaded PU capsules.

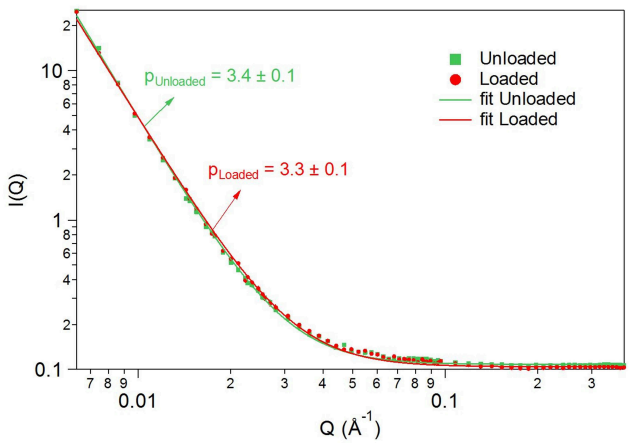

FIGURE 10 | Comparative SANS analysis.

and DeAngelis, 1975): stretching vibrations of aliphatic C–H (2,950–2,850 cm^{-1}), stretching vibrations of asymmetric NO_2 (1,665 and 1,635 cm^{-1}), scissoring vibrations of methylene (1,460 cm^{-1}), stretching vibrations of symmetric NO_2 (1,285-1,270 cm^{-1}), stretching vibrations of asymmetric C–O–C (∼1,100 cm^{-1}) and stretching vibrations of O–NO_2 (865 cm^{-1}).

The surface fractal-like character of the studied PU samples nanostructure in the available Q scattering vector [$Q = (4\pi/\lambda)\sin\Theta$; λ, neutron wavelength; 2Θ, scattering angle] range (0.006–0.300 $Å^{-1}$) has been shown by SANS. The small-angle scattering curves of both (loaded and unloaded) samples showed power exponents: $p_{loaded} = 3.3 \pm 0.1$ and $p_{unloaded} = 3.4 \pm 0.1$ (see raw data and fitted models in **Figure 10**) corresponding to a network-like three-dimensional porous PU skeleton constructed of units with sizes larger than the nanometric scale range, having a rough surface and thus a large surface area. Complementary to the results obtained by SEM, where the texture of the material has been studied on a micrometric level, SANS evidenced surface fractal-like character for both samples at a smaller size scale (size range approximately 20–1,000 Å) in the whole studied volume. This proves that the PU nanostructure was not affected by the drug encapsulation.

The evaluation of skin irritation potential represents a new alternative method to assess the hazard of a new synthesized compound. The skin sensitivity is a very good and fair parameter used in many toxicity assays on new cosmetics, but it can be generally used in the evaluation of any chemicals. The changes of skin parameters (especially the level of transepidermal water loss and erythema) are fast and directly proportional with the irritation potential of the compounds (Kose et al., 2018). The visual observations were replaced by modern, more accurate, credible and non-invasive techniques. In this 2-week experiment, TEWA differences around 6 g/h/m^2 were observed after the application of multiple samples, and according to Oestmann et al. (1993), these changes were inside a normal range. Erythema measurements indicated an increase by about 70 units after 15 days; increases of erythema levels were seen in every experiment done in our Phyto-science Research Center either in mice or in human skin experiments in the last 8 years due to the skin sensitivity.

Sodium lauryl sulfate (SLS) is often used as control sample in these irritation potential tests. V.G. Gurita (Ciobotaru) and her team have reported increases of TEWA around 11 g/h/m^2 and of erythema index approximately 90 units using the same instruments in a 25-h experiment on the skin of healthy human volunteers (Gurita (Ciobotaru) et al., 2019). In another study of our team, SLS solution was used as reference in an assessment of the toxicological profile of betulin entrapped in a PU carrier (Borcan et al., 2018c); they presented comparative values of TEWL and erythema between the PU samples and SLS at 6 days, and important increases were found in the case of the well-known irritative agent (around 4 g/h/m^2 for the transepidermal water loss and more than 175 units for erythema index).

In conclusion, PU structures were developed by using a polyaddition process between chitosan, an aliphatic isocyanate, and an ether polyol as main raw materials. The obtained polydisperse carrier, consisting of structures between 104 and 310 nm, presents good encapsulation efficiency of isosorbide derivatives (around 70%), a very slow release, and a good stability against thermal degradation. The carrier structures possess low values of their surface charge, which indicates a high tendency to form clusters, confirmed by SEM images; their maximum absorption was recorded at 345–360 nm. The skin irritation potential of samples, measured on human volunteers as transepidermal water loss and erythema level, did not show important modifications of these parameters in a 15-day experiment.

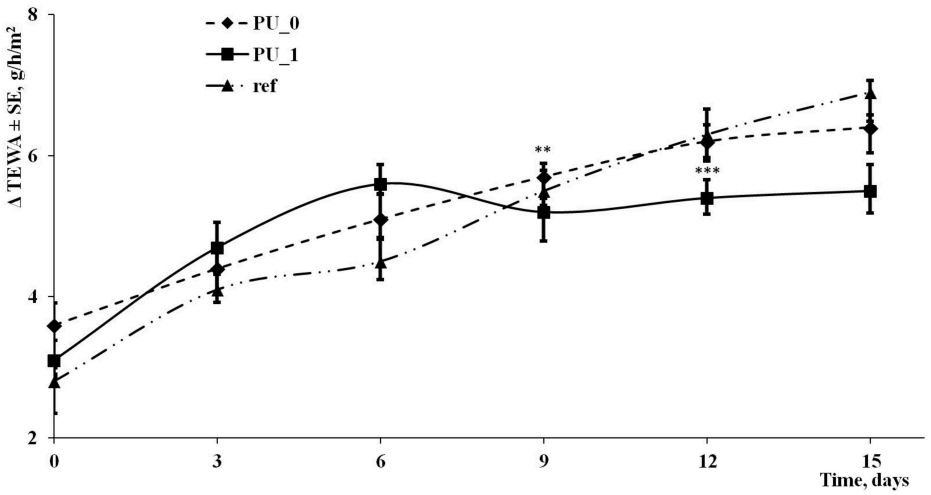

FIGURE 11 | Evolution of TEWA during the experiment.

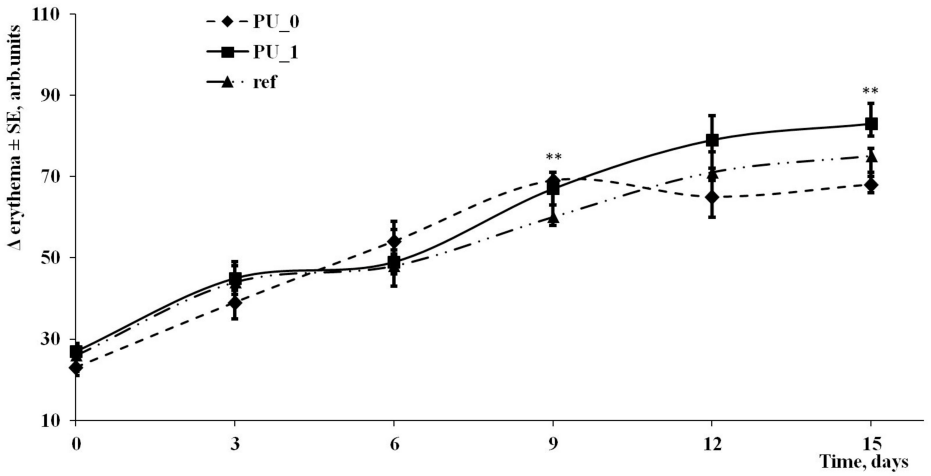

FIGURE 12 | Evolution of erythema during the experiment.

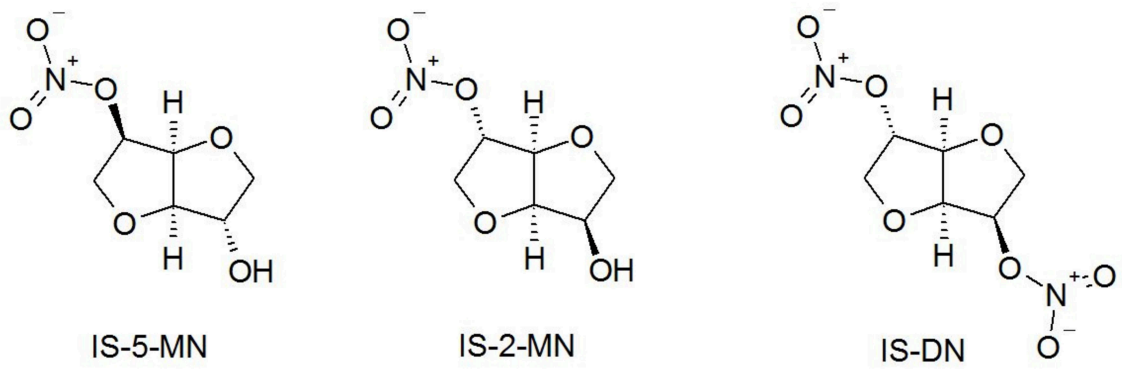

FIGURE 13 | Chemical structures of isosorbide derivatives.

DATA AVAILABILITY STATEMENT

All datasets presented in this study are included in the article/supplementary material.

ETHICS STATEMENT

The studies involving human participants were reviewed and approved by Ethical Committee of Victor Babes University of Medicine and Pharmacy Timisoara, Romania. The patients/participants provided their written informed consent to participate in this study.

AUTHOR CONTRIBUTIONS

Conceptualization: FB, ZD, and MT. Methodology and investigation: AL and DB. Software: MT. Resources: FB and AV. Writing—original draft preparation: FB and ZD. Writing—review and editing: FB, AL, and MT. Project administration: FB. All authors contributed to the article and approved the submitted version.

FUNDING

This article was supported by the grant 5EXP/1244/30.01.2020 from Victor Babes University of Medicine and Pharmacy, Timisoara, Romania.

ACKNOWLEDGMENTS

FB would like to express his special appreciation and thanks to his advisors for the great support and kind advice throughout his PhD research studies (Prof. R. Nutiu and Assoc. Prof. Ctin. Bolcu from West University Timisoara, Romania).

REFERENCES

Barichello, J. M., Yamakawa, N., Kisyuku, M., Handa, H., Shibata, T., Ishida, T., et al. (2017). Combined effect of liposomalization and addition of glycerol on the transdermal delivery of isosorbide 5-nitrate in rat skin. *Int. J. Pharm*. 357, 199–205. doi: 10.1016/j.ijpharm.2008.01.052

Basu, A., Farah, S., Kunduru, K. R., Doppalapudi, S., Khan, W., and Domb, A. J. (2016). "Polyurethanes for controlled drug delivery" in *Advances in Polyurethane Biomaterials,* eds S. L. Cooper and J. Guan (Duxford: Woodhead Publishing), 217–246.

Bolcu, C., and Borcan, F. (2005). The study of the reactions of 2,4-dihydroxy-benzophenone with mono- and diisocyanates. *Mater. Plast.* 42, 35–39.

Bonn, R. (1988). Sustained-release isosorbide mononitrate (50 mg): optimization of a once-daily dosage form for long-term treatment of angina pectoris. *Am. J. Cardiol.* 61, 12E−14E. doi: 10.1016/0002-9149(88)90082-3

Borcan, F., Chirita-Emandi, A., Andreescu, N. I., Borcan, L. C., Albulescu, R. C., Puiu, M., et al. (2019). Synthesis and preliminary characterization of polyurethane nanoparticles with ginger extract as a possible cardiovascular protector. *Int. J. Nanomed.* 14, 3691–3703. doi: 10.2147/IJN.S202049

Borcan, F., Preda, M., Borcan, L. C., Pinzaru, I., Florescu, S., Sisu, E., et al. (2018a). Comparative characterization of birch bark extracts encapsulated inside polyurethane microstructures. *Mater Plast.* 55, 385–388. doi: 10.37358/MP.18.3.5035

Borcan, F., Soica, C. M., Lazureanu, V., Pinzaru, I. A., Cheveresan, A., and Poenaru, M. (2018b). Toxicological assessment of betulin entrapped in a polyurethane carrier. *Mater. Plast.* 55, 149–151. doi: 10.37358/MP.18.2.4983

Borcan, L. C., Dudas, Z., Len, A., Fuzi, J., Borcan, F., and Tomescu, M. C. (2018c). Synthesis and characterization of a polyurethane carrier used for a prolonged transmembrane transfer of a chili pepper extract. *Int. J. Nanomed.* 13, 7155–7166. doi: 10.2147/IJN.S181667

Bouchemal, K., Briançon, S., Perrier, E., Fessi, H., Bonnet, I., and Zydowicz, N. (2004). Synthesis and characterization of polyurethane and poly(ether urethane) nanocapsules using a new technique of interfacial polycondensation combined to spontaneous emulsification. *Int. J. Pharm.* 269, 89–100. doi: 10.1016/j.ijpharm.2003.09.025

Danaei, M., Dehghankhold, M., Ataei, S., Hasanzadeh Davarani, F., Javanmard, R., Dokhani, A., et al. (2018). Impact of particle size and polydispersity index on the clinical applications of lipidic nanocarrier systems. *Pharmaceutics* 10:E57. doi: 10.3390/pharmaceutics10020057

Gama, N. V., Ferreira, A., and Barros-Timmons, A. (2018). Polyurethane foams: past, present, and future. *Materials* 11, 1–35. doi: 10.3390/ma11101841

Guhl, D. (2008). *Alternatives to DBTL Catalysts in Polyurethanes – A Comparative Study*. (Berlin: European Coatings Conference).

Gunasekara, N. S., and Noble, S. (1999). Isosorbide 5-mononitrate: a review of a sustained-release formulation (Imdur) in stable angina pectoris. *Drugs* 57, 261–277. doi: 10.2165/00003495-199957020-00016

Gurita (Ciobotaru), V.G., Pavel, I.Z., Borcan, F., Moaca, A., Danciu, C., Diaconeasa, Z., et al. (2019). Toxicological evaluation of some essential oils obtained from selected Romania Lamiaceae Species in complex with hydroxypropyl - gamma-cyclodextrin. *Rev. Chim. Bucharest* 70, 3703–3707.

Hajnal, K., Gabriel, H., Aura, R., Erzsébet, V., and Blanka, S. S. (2016). Prodrug strategy in drug development. *Acta Med. Maris.* 62, 356–362. doi: 10.1515/amma-2016-0032

Hasirci, N., and Aksoy, E. A. (2007). Synthesis and modifications of polyurethanes for biomedical purposes. *High Perform. Polym.* 19, 621–637. doi: 10.1177/0954008307081203

Hirayama, F., Hirashima, N., Abe, K., Uekama, K., Ijitsu, T., and Ueno, M. (1988). Utilization of diethyl-beta-cyclodextrin as a sustained-release carrier for isosorbide dinitrate. *J. Pharm. Sci.* 77, 233–236. doi: 10.1002/jps.2600770310

Kakar, S., Singh, R., and Semwal, A. (2014). Drug release characteristics of dosage forms: a review. *J. Coastal Life Med.* 2, 332–336.

Kikuchi, I. S., Cardoso Galante, R. S., Dua, K., Malipeddi, V. R., Awasthi, R., Ghisleni, D. D. M., et al. (2017). Hydrogel based drug delivery systems: a review with special emphasis on challenges associated with decontamination of hydrogels and biomaterials. *Curr. Drug Deliv.* 14, 917–925. doi: 10.2174/1567201813666161205130825

Kim, H. J., Kang, M. S., Knowles, J. C., and Gong, M. S. (2014). Synthesis of highly elastic biocompatible polyurethanes based on bio-based isosorbide and poly(tetramethylene glycol) and their properties. *J. Biomater. Appl.* 29, 454–464. doi: 10.1177/0885328214533737

Kim, H. N., Lee, D. W., Ryu, H., Song, G. S., and Lee, D. S. (2019). Preparation and characterization of isosorbide-based self-healable polyurethane elastomers with thermally reversible bonds. *Molecules* 24:1061. doi: 10.3390/molecules24061061

Kocyigit, D., Gurses, K. M., Yalcin, M. U., and Tokgozoglu, L. (2017). Traditional and alternative therapies for refractory angina. *Curr. Pharm. Design* 23, 1098–1111. doi: 10.2174/1381612823666161123145148

Kose, O., Erkekoglu, P., Sabuncuoglu, S., and Kocer-Gumusel, B. (2018). Evaluation of skin irritation potentials of different cosmetic products in Turkish market by reconstructed human epidermis model. *Regul. Toxicol. Pharmacol.* 98, 268–273. doi: 10.1016/j.yrtph.2018.08.010

Munteanu, M. F., Ardelean, A., Borcan, F., Trifunschi, S. I., Gligor, R., Ardelean, S. A., et al. (2017). Mistletoe and garlic extracts as polyurethane carriers—a possible remedy for *Choroidal Melanoma*. *Curr. Drug Deliv.* 14, 1178–1188. doi: 10.2174/1567201814666170126113231

Oestmann, E., Lavrijsen, A. P., Hermans, J., and Ponec, M. (1993). Skin barrier function in healthy volunteers as assessed by transepidermal water loss and

vascular response to hexyl nicotinate: intra- and inter-individual variability. *Br. J. Dermatol.* 128, 130–136. doi: 10.1111/j.1365-2133.1993.tb15141.x

Polakowska, M., Orzelska-Gorka, J., and Talarek, S. (2016). Drugs modulating the L-arginine: NO: cGMP pathway–current use in therapy. *Curr. Issues Pharm. Med. Sci.* 29, 14–20. doi: 10.1515/cipms-2016-0004

Prakash, A., and Markham, A. (1999). Long-acting isosorbide mononitrate. *Drugs* 57, 93–100. doi: 10.2165/00003495-199957010-00008

Quan, H., Park, Y. K., Kim, S. K., Heo, S. J., Koak, J. Y., Han, J. S., et al. (2016). Surface characterization and human stem cell behaviors of zirconia implant disks biomimetic-treated in simulated body fluid. *Int. J. Oral Maxillofac. Implants* 31, 928–938. doi: 10.11607/jomi.4376

Raddino, R., Caretta, G., Bonadei, I., Teli, M., Vizzardi, E., and Cas, L. D. (2010). Differences between nitrates: role of isosorbide 2-mononitrate. *J. Cardiovasc. Med. (Hagerstown)* 11, 486–492. doi: 10.2459/JCM.0b013e328335fb8c

Saadatmand, M. M., Yazdanshenas, M. E., Khajavi, R., Mighani, F., and Toliyat, T. (2019). Patterning the surface roughness of a nano fibrous scaffold for transdermal drug release. *Int. J. Nano Dimens* 10, 78–88.

Silvieri, L. A., and DeAngelis, N. J. (1975). Isosorbide dinitrate. *Anal. Profiles Drug Subst.* 4, 225–244. doi: 10.1016/S0099-5428(08)60015-5

Solano-Umana, V., Vega-Baudrit, J. R., and González-Paz, R. (2015). The new field of the nanomedicine. *Int. J. Appl. Sci. Technol.* 5, 79–88.

Steinbach, S. C., Triani, R., Bennedsen, L., Gabel, A., Haeusler, O., Wohlrab, J., et al. (2017). Retarder action of isosorbide in a microemulsion for a targeted delivery of ceramide NP into the *Stratum corneum*. *Pharmazie* 72, 440–446. doi: 10.1691/ph.2017/7004

Thadani, U., and Rodgers, T. (2006). Side effects of using nitrates to treat angina. *Expert Opin. Drug Saf.* 5, 667–674. doi: 10.1517/14740338.5.5.667

Tsai, F.-Y., Chen, C.-J., and Chien, C.-S. (1994). Determination of isosorbide nitrate and its analogues in pharmaceuticals by high-performance liquid chromatography. *J. Food Drug Anal.* 2, 271–280.

Turner, P. V., Brabb, T., Pekow, C., and Vasbinder, M. A. (2011). Administration of substances to laboratory animals: routes of administration and factors to consider. *J. Am. Assoc. Lab. Anim. Sci.* 50, 600–613.

Vermette, P., and Griesser, H. J. (2001). *Biomedical Applications of Polyurethanes*. Georgetown, DC: Eurekah.com.

Yang, G. M., Kuo, J. F., and Woo, E. M. (2006). Preparation and control-release kinetics of isosorbide dinitrate microspheres. *J. Microencapsul.* 23, 622–631. doi: 10.1080/02652040600776465

Yao, Y., Feng, Y., and Lin, W. (2015). Systematic review and meta-analysis of randomized controlled trials comparing compound danshen dripping pills and isosorbide dinitrate in treating angina pectoris. *Int. J. Cardiol.* 182, 46–47. doi: 10.1016/j.ijcard.2014.12.112

Conflict of Interest: The authors declare that the research was conducted in the absence of any commercial or financial relationships that could be construed as a potential conflict of interest.

frontiers in Chemistry

ORIGINAL RESEARCH
published: 22 July 2020
doi: 10.3389/fchem.2020.00581

Mechanisms of Macrophage Immunomodulatory Activity Induced by a New Polysaccharide Isolated From *Polyporus umbellatus* (Pers.) Fries

Chun-Ping Liu[1,2†], Xiong Li[1†], Ge-Na Lai[1], Jin-Hua Li[1], Wen-Yu Jia[1], Ying-Ying Cao[1], Wen-Xing Xu[1], Qing-Long Tan[1], Chang-Yuan Zhou[1], Min Luo[1], Xue-Ying Zhang[1], Dao-Qing Yuan[1], Jin-Ying Tian[1], Xian Zhang[1] and Xing Zeng[1*]*

[1] Department of Integrated Chinese Medicine Immunization, The Second Affiliated Hospital, Guangzhou University of Chinese Medicine, Guangzhou, China, [2] Department of Cardiovascular Medicine, Guangdong Provincial Hospital of Chinese Medicine, Guangzhou, China

OPEN ACCESS

Edited by:
Ruibing Wang,
University of Macau, China

Reviewed by:
Kuo-Feng Hua,
National Ilan University, Taiwan
Jie Zan,
Guangdong University of Technology, China
Xiaoyu Ji,
Shantou University, China

***Correspondence:**
Xiong Li
mantianxing1997@126.com
Xing Zeng
zengxing-china@163.com

†These authors have contributed equally to this work

Specialty section:
This article was submitted to Medicinal and Pharmaceutical Chemistry, a section of the journal Frontiers in Chemistry

Received: 29 February 2020
Accepted: 05 June 2020
Published: 22 July 2020

Citation:
Liu C-P, Li X, Lai G-N, Li J-H, Jia W-Y, Cao Y-Y, Xu W-X, Tan Q-L, Zhou C-Y, Luo M, Zhang X-Y, Yuan D-Q, Tian J-Y, Zhang X and Zeng X (2020) Mechanisms of Macrophage Immunomodulatory Activity Induced by a New Polysaccharide Isolated From Polyporus umbellatus (Pers.) Fries. Front. Chem. 8:581. doi: 10.3389/fchem.2020.00581

Bladder cancer is one of the most malignant tumors closely associated with macrophage immune dysfunction. The Chinese medicine polyporus has shown excellent efficacy in treating bladder cancer, with minimal side effects. However, its material basis and mechanism of action remain unclear. A new water-soluble polysaccharide (HPP) with strong immunomodulatory activity was isolated from the fungus *Polyporus umbellatus* (Pers.) Fries. HPP had an average molecular weight of 6.88 kDa and was composed mainly of an <-(1→ 4)-linked D-galactan backbone. The immunomodulatory activity of HPP was determined *in vitro*, and the results revealed that it could obviously increase the secretion of immune factors by IFN-γ-stimulated macrophages, including nitric oxide (NO), interleukin-6 (IL-6), interleukin-1β (IL-1β), RANTES and interleukin-23 (IL-23), and the expression of the cell membrane molecule CD80. In addition, HPP was recognized by Toll-like receptor 2 (TLR2) and activated the signaling pathways of NF-κB and NLRP3 in a bladder cancer microenvironment model, indicating that HPP could enhance host immune system function. These findings demonstrated that HPP may be a potential immune modulator in the treatment of immunological diseases or bladder cancer therapy.

Keywords: *Polyporus umbellatus*, polysaccharide, immunomodulatory activity, NLR P3 inflammasome, NF-κB pathway

INTRODUCTION

Bladder cancer, the most common malignancy affecting the urinary tract, is characterized by the proliferation of abnormal cells in the urothelial lining of the urinary bladder (Zhang et al., 2012; John and Said, 2017; Kolawole et al., 2017; Moschini et al., 2017). According to statistics, more than 100,000 people die from bladder cancer every year worldwide, ranking fourth in incidence among male malignant tumors (Ferlay et al., 2015; Dy et al., 2016). The traditional treatment of bladder cancer is mainly surgery combined with BCG intravesical perfusion. Although BCG has a good healing effect, it is also accompanied by serious side effects, and at the same time, since as many as 30–50% of patients' relapse within 5 years, clinical doctors have to find other auxiliary therapies (Kawai et al., 2013).

Macrophages are important immune cells with great functional diversity and a series of functions, including immunomodulation of host defense, resolution of inflammation, and maintenance of various homeostatic processes (Saha et al., 2017). To carry out these seemingly contrasting functions, macrophages need to display functional plasticity in response to micro-environmental signals (Solinas et al., 2010). Clinical and experimental data indicated that bladder tumor-related macrophages ware heterogeneous and can be induced to present tumor-associated macrophages (TAMs) that are similar to the M2 subtype in the tumor microenvironment, promoting tumor growth, invasion, invasion and angiogenesis (Suriano et al., 2013; Qi et al., 2019). Generally, TAMs promote tumor growth and angiogenesis, suppressing adaptive immunity, and play important roles in tumor cell migration, invasion, and metastasis (Wu et al., 2020). M1 subtype macrophages differentiate through mainly JAK1/2, STAT1/2, 5, TLR4/NF-κB, P38 MAPK pathway activation, excrete inflammatory cytokines and chemokines, participate in a positive immune response; as such, they are able to kill tumor cells in tumor tissue and foreign pathogens. The immune function of M1 macrophages is achieved mainly by secreting cytokines, such as IL-6, TNF-α, IL-1β, IL-23 and other inflammatory factors, as well as chemokines, such as McP-1, RANTES and CXCL10 (Gambardella et al., 2020). Interferon-γ (IFN-γ) is a major macrophage activation factor responsible for M1 macrophage activation. Compared with unstimulated RAW 264.7 cells treated with T24 cell culture supernatant, IFN-stimulated macrophages are characterized by the production of increased quantities of inflammatory cytokines in medium alone or in a co-culture microenvironment. IFN-stimulated macrophages are implicated in acute inflammation and defense against tumors. Therefore, in this study, the treatment of RAW 264.7 cells with T24 cell culture supernatant was used as a model to simulate the bladder tumor microenvironment *in vitro*, and the macrophages were activated by exposure to IFN-γ (Liu et al., 2017).

Polyporus umbellatus is a Chinese traditional herbal medicine, also known as Zhuling in China, that shows diuretic, nephron-protective, anticancer, immune-stimulating, hepatoprotective, anti-inflammatory and anti-oxidative activities (He P. F. et al., 2016). Clinical applications have confirmed its satisfactory efficacy in treating kidney diseases and bladder cancer. Additionally, no side effects or toxicity have been reported for this fungus (Zhao, 2013). Polyporus polysaccharide, which is the main ingredient in *Polyporus umbellatus*, has multiple pharmacological functions, including anticancer, immunoenhancing, radioprotective and antioxidative activities (He P. F. et al., 2016). In a previous study, we found that crude polyporus polysaccharide could suppress the growth of tumor cells via the TLR4/NF-κB pathway (Zeng et al., 2011) and greatly induce the transformation of M2 subtype macrophages to the M1 subtype *in vitro* (Jiang et al., 2015). In addition, we measured the toxicity of PPS in a rat model of bladder cancer *in vivo* and found that the mortality of the Bacillus Calmette-Guérin (BCG)-treated group was higher than that of the group treated with PPS combined with BCG (Zhang et al., 2010, 2011), indicating that PPS can reduce the toxicity of BCG.

In this study, a new polysaccharide (HPP) was first isolated from polyporus total polysaccharide, which was proven to have an α-(1→ 4)-linked D-galactan backbone. We further examined whether HPP could regulate macrophage polarization in the microenvironment of bladder cancer and thereby exert anticancer effects through the NF-κB and NLRP3 pathways.

MATERIALS AND METHODS

Antibodies and Reagents

RAW 264.7 macrophages and T24 cells were purchased from the ATCC (Rockville, MD, USA). Antibodies for western blotting were purchased from Cell Signaling Technologies (Pickering, ON, CAN), including those targeting P65, P-P65, TAK1, iKKa/b, INOS, COX2, IKB, p-IKB, NLRP3, Caspase-1, and GAPDH. Secondary antibodies for western blotting and 3-(4,5-dimethylthiazol-2-yl)-2,5- diphenyltetrazolium bromide (MTT) were purchased from Sigma (Sigma Aldrich, St. Louis, MO, USA). Transitional cell carcinoma of the bladder cells (T24 cells) and a mouse macrophage cell line (RAW 264.7 macrophages) were purchased from the American Type Culture Collection (Rockville, MD, USA). Fetal bovine serum (FBS), Dulbecco's modified Eagle's medium (DMEM) and penicillin/streptomycin solution were purchased from HyClone (Logan, UT, USA). Phycoerythrin (PE)-conjugated anti-CD80 and fluorescein isothiocyanate (FITC)-conjugated anti-mouse CD282, PE-IgG2a and FITC-IgG2a antibodies, were purchased from BD Systems (BD Biosciences, USA). ProcartaPlex™ Multiplex Immunoassay Kits were purchased from eBioscience (San Diego, CA, USA). DEAE-52 and Sephadex G-100 gel filtration medium were purchased from GE Healthcare Bio-Sciences AB (UPPPala, Sweden). SC75741 (purity, 99.79%) was purchased from Selleck (Shanghai, China).

Isolation and Purification of Polysaccharides

Total *Polyporus umbellatus* polysaccharide was purchased from Hui Zhou Xian Cao Plant Health Care SCI & THE Co., Ltd. (Huizhou, China, batch number 150780681), and the polysaccharide content determined by the phenol-sulfuric acid method was 73.5%. The polysaccharides were deproteinized using Sevag reagent (1-butanol/chloroform, v/v = 1:4), and the supernatant was lyophilized to obtain the deproteinized polysaccharides. The deproteinized polysaccharides were dissolved in deionized water, after which the solution was applied to a DEAE-52 cellulose column (3 × 35 cm) and eluted with deionized water at a flow rate of 1 mL/min. Test tubes were collected using an automated step-by-step fraction collector, after which the total carbohydrate content of each tube was measured based on the absorbance at 490 nm using the phenol-sulfuric acid colorimetric method. The main fraction containing carbohydrates from the elution step was then concentrated and lyophilized. The collected fraction was further applied to a Sephadex G-100 gel-filtration column (2.9 × 50 cm), after which it was eluted with deionized water at a flow rate of 1.0 mL/min. The neutral carbohydrate was eluted as a single

fraction according to the elution profile and lyophilized as a white powder.

High-Performance Gel-Permeation Chromatographic Analysis

The homogeneity and molecular weight of the purified polysaccharide were determined using high-performance gel-permeation chromatography (HPGPC) via an Agilent-1,200 HPLC system matched with a TSK gel G4000 PWxl column (7.8 mm × 300 mm,), column temperature 30°C, and detected using a differential refraction index detector (RID) at 35°C. The sample was dissolved in distilled water to a concentration of 0.5 mg/mL and then eluted at a flow rate of 0.6 mL/min. A calibration curve was constructed using dextrans of various molecular weights (Mw 4,300, 5,300, 7,200, 9,200, 16,230 and 17,900).

UV, ORD, IR, and NMR Analysis

UV–Vis absorption spectra were recorded using a U-2,910 spectrophotometer (Hatachi, Japan) in the wavelength range of 200–400 nm. The FT-IR spectra (KBr pellets) of the polysaccharides (2 mg) were recorded at 400–4,000 cm^{-1} using a Fourier transform infrared spectrophotometer (FT-IR, PerkinElmer, UK) at room temperature. The optical rotatory dispersion (ORD) was recorded using a Rudolph I automatic polarimeter (Rudolph Research Analytical, USA). 1D and 2D NMR spectra were recorded using a Bruker 5 mm broadband observe probe at 20°C with a Bruker Avance 600 MHz spectrometer (Germany), operating at 600 MHz for ^{1}H NMR and 150 MHz for ^{13}C NMR,™ in ppm, rel. to $SiMe_4$ as an internal standard, *J* in Hz.

Monosaccharide Composition Analysis

The monosaccharide composition of HPP was analyzed by GC-MS and PMP derivatization HPLC. For GC-MS analysis, 10 mg samples were hydrolyzed using 4 mol/L trifluoroacetic acid (TFA) at 120°C for 4 h, after which the TFA was removed using nitrogen at 25°C. Next, 10 mg of hydroxylamine hydrochloride and 0.6 mL of pyridine were added, reacted at 90°C for 0.5 h, evaporated with nitrogen and diluted in 2 mL of $CHCl_3$. The reaction products were subsequently analyzed by gas chromatography–mass spectrometry (GC–MS, QP2010, Shimadzu, Japan) using a DB-1701 silica capillary column (30 m × 0.25 mm × 0.25m). During GC–MS, the flow rate of helium was 1 mL/min, the detector and inlet temperatures were 280 and 250°C, respectively, and the oven temperature program was set to increase from 100°C (standing for 2 min) to 260°C (standing for 15 min) at a rate of 15°C/min. For PMP derivatization HPLC, five milligrams of PPS were dissolved in NaOH and precolumn derivated with 1-phenyl-3-methyl-5-pyrazolone (PMP) using the method described by Ma et al. (2017). The PMP derivatives of the seven standard sugars (Ara, Gal, Glc, Gal UA, Man, Rha) and PPS were subjected to HPLC with an Agilent 1,200 (Dionex Co., USA) fitted with a HypersiL BDS C_{18} column (250 × 4.6 mm, 5 μm).

Cell Line Culture and Tumor-Conditioned Media Preparation

RAW 264.7 macrophages and T24 cells were cultured in Dulbecco's modified Eagle's medium (DMEM) with 10% fetal bovine serum (FBS) containing 1% penicillin/streptomycin. For all experiments, cell lines were grown at 37°C in an atmosphere of 5% CO_2. The T24 supernatant was collected and filtered at 0.20 μm, after which the supernatant was stored at −80°C. Once the cells were grown to 80% confluence, 40% of the medium was discarded, and the cells were incubated with fresh DMEM or T24 supernatant for 3 h. Finally, the samples were treated with different concentrations of IFN-γ (100 ng/mL) with or without HPP for 24 h, with equal volumes of medium used as controls.

MTT Cell Viability Assay

RAW 264.7 cells (1×10^4 cells/well) were seeded into 96-well microtiter plates for 24 h at 37°C with 5% CO_2. Various concentrations of HPP (3.75–1,000 μg/mL) were then added and co-cultured for 24 h, after which 20 l of MTT solution (5 mg/mL) was added into each well, and samples were incubated at 37°C for 4 h. Following incubation, the supernatant was removed, and 200 μL of dimethyl sulfoxide was added to solubilize the formazan salt, which was then quantified based on the absorbance at 570 nm. The control wells were designated 100% viability, and the blank values, indicating the absorbance of MTT and DMSO only, were subtracted from all samples. Each experiment was repeated at least three times. The cell viability (%) after HPP treatment of RAW264.7 cells was calculated as follows: (absorbance of test sample/absorbance of control) × 100%.

Measurement of NO Production

RAW 264.7 cells (5×10^5 cells/well) were preincubated in six-well plates for 24 h at 37°C in a 5% CO_2 incubator. The cells were preincubated with 40% T24 cell culture supernatant for 3 h before being treated with IFN-γ (100 ng/mL) or HPP (1–100 μg/mL) for 24 h. After treatments, the supernatant was harvested and measured based on the Griess reaction.

Multiplex Immunoassay Analysis

RAW 264.7 cells (2.5×10^5 cells/well) were seeded in 12-well plates and cultured for 24 h at 37°C in a humidified atmosphere containing 5% CO_2. Cells were treated with 40% T24 cell culture supernatant for 3 h. Subsequently, the cells were stimulated with IFN-γ (100 ng/mL) or HPP (1–100 μg/mL) for 24 h. The supernatant was then harvested, and the levels of RANTES, IL-23, IL-1β and IL-6 in the RAW 264.7 culture supernatant were assayed using ProcartaPlex™ Multiplex Immunoassay Kits according to the manufacturer's instructions.

Flow Cytometry Analysis

The cell phenotypes were determined using a flow cytometer. RAW 264.7 macrophages (5×10^5 cells per well) were plated in 12-well culture plates. After 24 h, the culture medium was replaced with T24 cell culture supernatant for 3 h before incubating with IFN-γ or with different concentrations of HPP (1–100 μg/mL) for 24 h. Finally, we harvested the treated cells and washed them twice with cold phosphate-buffered saline

(PBS). Next, 5 μL of anti-mouse (PE)-conjugated anti-CD80, (FITC)-conjugated anti-mouse CD282, PE-IgG2a, and FITC-IgG2a antibodies, were added to the tubes and incubated for 20 min on ice. Finally, the stained cells were suspended in cold buffer, and fluorescence-activated cell sorting (FACS) was used to analyze the data.

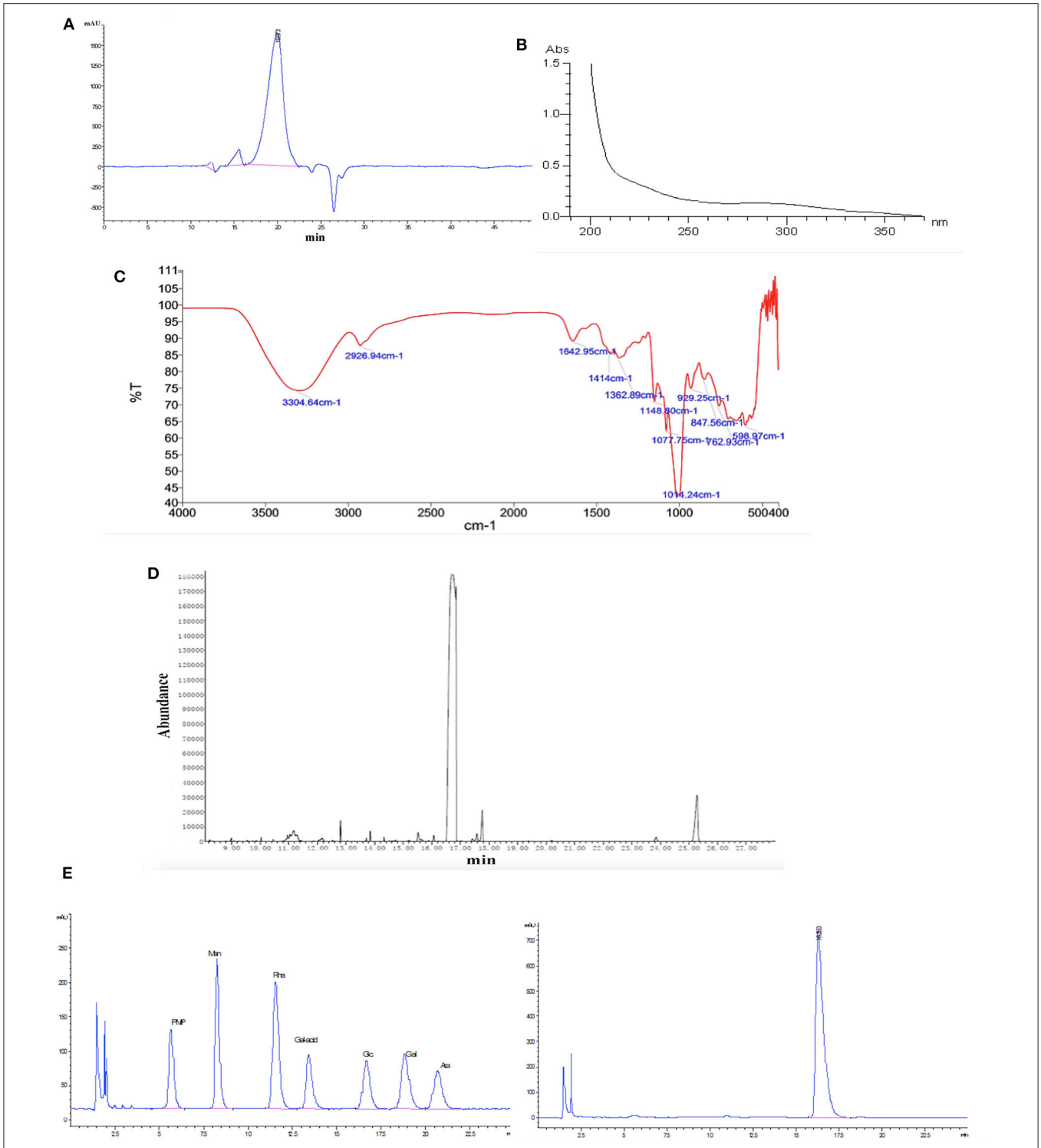

FIGURE 1 | Characterization of HPP by **(A)** high-performance gel permeation chromatography (HPGPC), **(B)** UV scanning spectrum, **(C)** infrared spectrum, **(D)** gas chromatography of the glucose standard (16.6 min), and **(E)** gas chromatography of the HPP sample (16.5 min).

Western Blot Analysis

After various treatments, cells were washed with ice-cold phosphate buffer, lysed in 1× RIPA lysis buffer and then harvested. The lysates were subsequently centrifuged at 6,000 × g for 10 min at 4°C. Before analysis, the proteins in the supernatant were measured using a Thermo protein assay kit. Protein samples were loaded, separated on 10% gels and transferred to polyvinylidene difluoride membranes (Immun-Blot PVDF membrane, 0.45 μm). The membranes were then blocked with 5% BSA in 1× Tris-buffered saline (TBS) for 2 h, after which they were incubated with primary antibodies at 4°C overnight. The membranes were subsequently washed and incubated with horseradish peroxidase-conjugated secondary antibody raised against rabbit IgG for 1.5 h at room temperature. After washing with TBST, membranes were detected using an enhanced chemiluminescence (ECL) kit.

Statistical Analysis

The experimental data were measured four times, and GraphPad Prism 6.0 was used for statistical analysis. Groups were compared using Student's *t*-test. Data are presented as the means ± SEM. $p < 0.05$ was considered statistically significant.

RESULTS AND DISCUSSION

Structural Assignment of HPP

Determination of the Molecular Weight (M_w) of HPP

The purified polysaccharide appeared as a single and symmetrical sharp peak upon HPGPC analysis (**Figure 1A**), indicating that HPP was a homogeneous polysaccharide. The average molecular weight of HPP was determined to be 6.88 kDa.

UV, FT-IR, GC, and PMP Derivatization HPLC Analysis of HPP

The UV spectra revealed that there was no absorption at 260 or 280 nm, suggesting that nucleic acids and proteins were absent (**Figure 1B**; Wang et al., 2017). FT-IR spectroscopy showed that HPP had typical features of sugars (**Figure 1C**). A strong and broad absorption peak at 3,304.6 cm^{-1} corresponded to the O-H stretching vibration, while a weak C-H stretching vibration was observed at 2,926.9 cm^{-1}. The absorption peaks between 1,400 and 1,200 cm^{-1} may be associated with O-H deformation vibration and C-O stretching vibration. The bands at 1,148.8, 1,077.8 and 1,014.2 cm^{-1} contributed to the stretching vibration of sugar structures with pyranose configurations. There was no absorption at 1,740 cm^{-1} or 890 cm^{-1} for the uronic acid and ™-type glycosidic linkages, respectively. Moreover, a characteristic absorption band at 847.6 cm^{-1} indicated the presence of <-type glycosidic linkages (Li et al., 2008). The high positive ORD values (+158.4°, c, 1.0, H_2O) further indicated that the polysaccharide is composed of <-D-glucose (Li et al., 2013). GC and PMP derivatization HPLC analysis showed that HPP was composed only of glucose (**Figures 1D,E**).

NMR Analysis of HPP

The ^1H and ^{13}C NMR spectra of HPP are shown in **Figures 2A,B**. The anomeric proton signals of residues were >5.0 (δ 5.40 ppm),

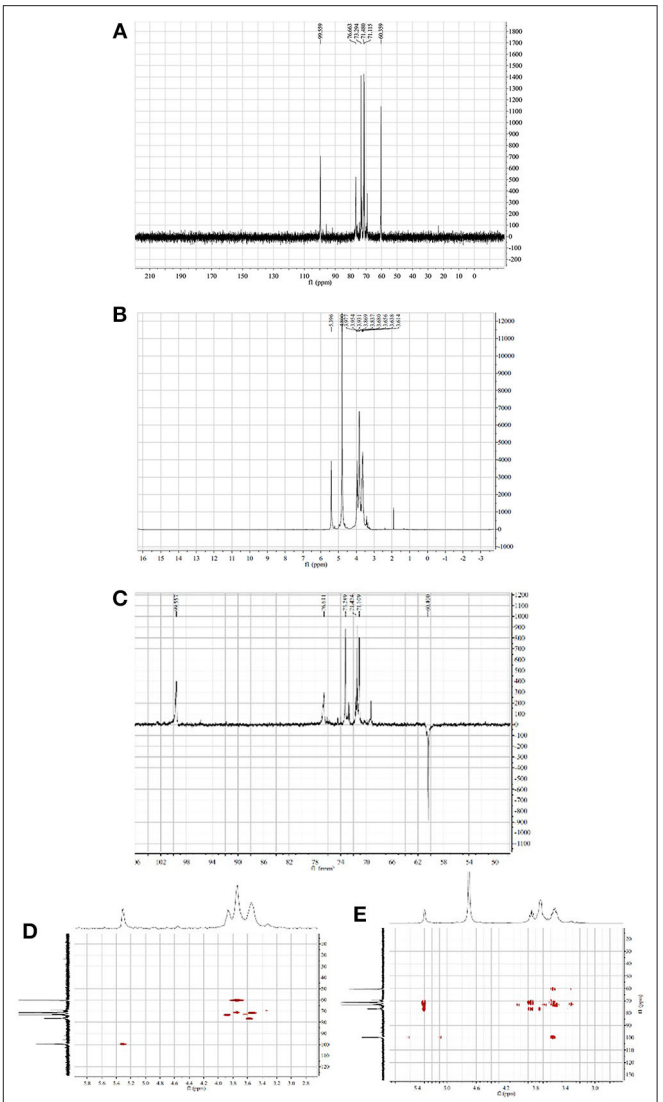

FIGURE 2 | NMR spectra of HPP (solvent: D_2O). **(A–E)** represent the ^1H NMR spectrum, ^{13}C NMR spectrum, DEPT spectrum, HSQC spectrum and HMBC spectrum at 60°C, respectively.

and the broad single peak indicated that the glucosidic bond is connected to the alpha form. The rest of the hydrogen chemical shifts were in the range of 3.61–3.98, corresponding to other proton signals on the sugar ring carbon, and the values were <4.0, indicating that the polysaccharide has no other sugar residue anomeric hydrogen signal. The ^{13}C-NMR spectrum showed six major carbon signals with chemical position values of 99.6, 76.6, 73.3, 71.5, 71.1, and 60.4. The anomeric carbon signal (δ 99.6 ppm) indicated that the sugar was in the pyranose form. The signal at δ 60.4 ppm was assigned to C-6 of (1→ 4)-α-D-glucosyl residues, which was supported by the corresponding reversed peak in the DEPT spectrum (**Figure 2C**). When combined with HSQC and HMBC correlation analysis (**Figures 2D,E**), the carbon and hydrogen signals were completely attributed

to HPP, wherein δ 99.6 reflected the anomeric carbon signal of glucose residues; δ 71.5, 71.1 and 73.3 were the C-2, C-3, and C-5 carbon signals of glucose, respectively; δ 76.6 was the substituted C-4 resonance signal; and δ 60.4 was the C-6 carbon signal, and its monosaccharide composition contained only α-D-glucopyranose, which is consistent with the above GC-MS, and IR analysis results. The chemical shifts of C-1 (δ 99.6) and C-4 (δ 76.6) move to the lower field indicates that the hydroxyl groups at C-1 and C-4 are substituted, which was further confirmed by the remote correlations of H-1 (δ 5.40) /C-4 (δ 76.6), and H-4 (δ 3.61) / C-1 (δ 99.6) in the HMBC spectrum. Other carbon signals with chemical shift values of 99.7, 76.8, 72.8, 72.6, 71.6, and 69.3 were also detected in the carbon spectrum, where δ 69.3 is the substituted C-6 signal, indicating that there is branching at the O-6 position, and δ 99.7, 76.8, 72.8, 72.6, and 71.6 are the C1-5 carbon signals of 1,4,6-α-D-glucopyranose, but these carbon signal intensities were weak. The above analysis indicated that the homogenized polysaccharide HPP contains glucose alone, having a backbone of 1,4-linked α-D-glucan with a (1 → 6)-α-D-glucopyranosyl side-branching unit. To our knowledge, the polysaccharide HPP isolated from *Polyporus* sp. have not previously been reported and was tentatively identified as novel.

Effects of HPP-Induced NO Production in IFN-γ-Stimulated Macrophages

To investigate the effects of HPP on the viability of RAW 264.7 macrophages, cells were treated with different concentrations of HPP (3.9–1,000 μg/mL) for 24 h, after which the cell viability

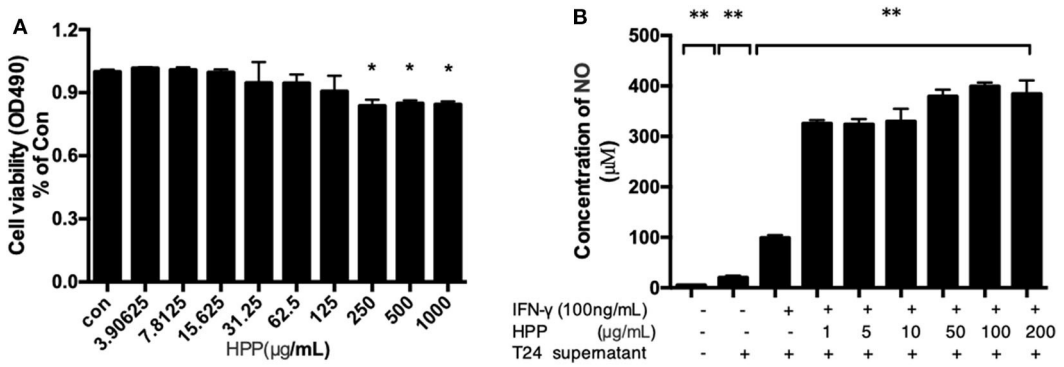

FIGURE 3 | Effect of HPP on cell viability and secretion of NO in IFN-γ-induced RAW 264.7 cells. **(A)** Effect of HPP on cell viability. **(B)** Effect of HPP on NO production. Statistical significance in comparison to the control group is designated $^{*}P < 0.05$, $^{**}P < 0.01$. Data are presented as the mean ± s.e.m.

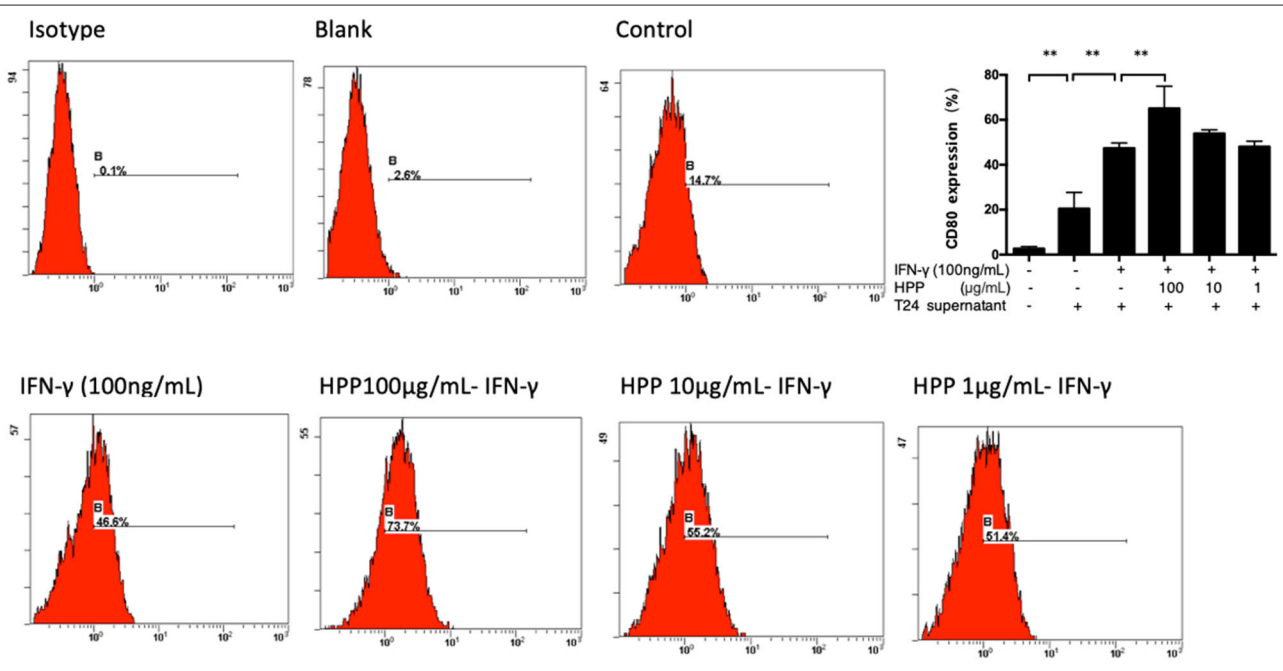

FIGURE 4 | Effect of HPP on CD80 expression of IFN-γ-induced RAW264.7 macrophages. Statistical significance in comparison to the control group is designated $^{*}P < 0.05$, $^{**}P < 0.01$. Data are presented as the mean ± s.e.m.

was determined by MTT assay. The results showed that HPP at 3.9–125 μg/mL did not affect cell viability (**Figure 3A**), which indicated that HPP at <125 μg/mL was not obviously toxic to RAW264.7 cells.

NO is an important active molecule in living organisms that plays pivotal roles in multiple pathophysiological processes, such as host defense mechanisms, inflammation, cancers and immunological diseases (Pratap et al., 2015). In this study, we found that treatment with HPP significantly induced the production of NO in IFN-γ-stimulated RAW264.7 cells in a dose-dependent manner. In particular, cells treated with HPP (1–1,000 μg/mL) showed significantly higher NO production than those in the control group (**Figure 3B**). When compared with that in the IFN-γ-stimulated RAW264.7 group, the amount of NO increased significantly after treatment with 1 μg/mL HPP ($P < 0.01$) until reaching 321 pg/mL, which is higher than that induced by rough polyporus polysaccharides (Liu et al., 2017).

Increase in IFN-γ-Stimulated CD80 Expression Induced by HPP in Macrophages

Two *in vitro* effector states (or polarization states) have been widely recognized, namely, M1 and M2 macrophages. M1 macrophages are characterized by the expression of the membrane molecule CD80. TLR-2 signaling augments the expression of the costimulatory molecule CD80 on macrophages and the production of cytokines such as IL-6, IL-12, and TNF-α (Harris et al., 1997; Vidyarthi et al., 2018). In addition, macrophages are important antigen-presenting cells, and their differentiation and activation can activate T cells. Moreover, the accessory function of macrophages depends on the presence of a number of costimulatory CD80 molecules (Meng et al., 2016; Payne et al., 2018). As shown in **Figure 4**, flow cytometry analysis demonstrated that HPP could increase the signature marker CD80 in IFN-γ-stimulated cells, suggesting that HPP enhanced the activation of RAW 264.7 macrophages.

HPP Enhanced the Secretion of Pro-inflammatory Cytokines in IFN-γ-Stimulated Macrophages

It is well known that the basic mechanisms of immunomodulators occur via the activation of macrophages, which are secreted as a series of macrophage-derived biological factors (NO, TNF-α, IL-6, IL-1β, IL-10, IL-12, etc.; Wang et al., 2017). IL-23, IL-1β, IL-6 and RANTES are important active molecules that play key roles in the immune system (Michael et al., 2015; Meurette and Mehlen, 2018). When exogenous pathogens, cancer or immunological diseases threaten the host, these molecules are produced by activated macrophages. Taken together, these results indicate that HPP displays notable immunomodulatory activities by increasing the secretion of IL-23, RANTES, IL-6 and TNF-α in RAW264.7

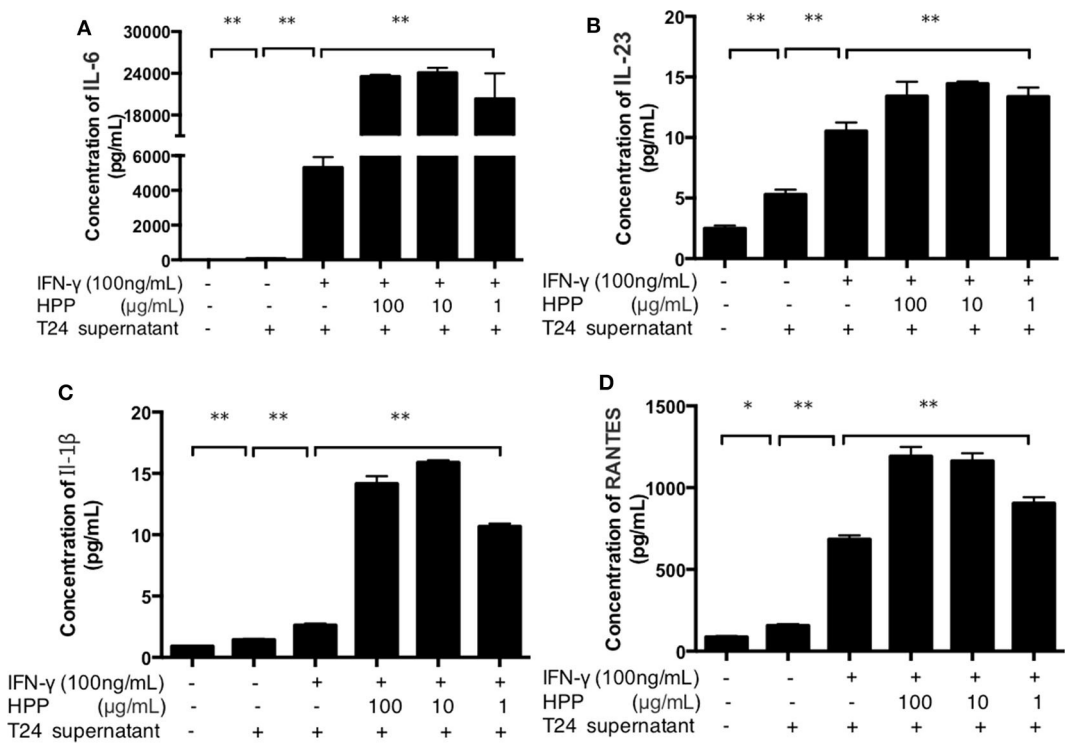

FIGURE 5 | Effect of HPP on the secretion of IL-1β, IL-23, RANTES and IL-6 in IFN-γ-induced macrophages. **(A)** Effect of HPP on IL-6 secretion. **(B)** Effect of HPP on IL-23 secretion. **(C)** Effect of HPP on IL-1β secretion. **(D)** Effect of HPP on RANTES secretion. Statistical significance in comparison to the control group is designated $^{*}P < 0.05$, $^{**}P < 0.01$. Data are presented as the mean ± s.e.m.

cells. As shown in **Figure 5**, multiplex immunoassay results showed that the secretion of IL-1β was enhanced in IFN-γ-induced cells treated with HPP (10–100 μg/mL). In addition, when compared with that in the IFN-γ group, the amount of IL-6 increased significantly after treatment with 10 μg/mL HPP (P <0.01). Moreover, HPP had similar concentration-dependent effects on the production of IL-23 and RANTES in IFN-γ-induced RAW264.7 cells. These data suggest that the enhanced inflammation in IFN-γ-stimulated RAW264.7 cells induced by HPP treatment was correlated with expression of pro-inflammatory cytokines.

The NLRP3 and NF-κB Pathways Participate in Macrophage Activation Induced by HPP

As mentioned above, the range of cytokines (NO, IL-23, IL-1β, IL-6, and RANTES) in RAW264.7 cells induced by HPP raises interesting questions regarding the signaling pathways activated. Several mechanisms involved in cytokine production have been reported, among which upregulation of the NF-κB and NLRP3 pathways has been proposed as a main mechanism (Mishra et al., 2013; Serra et al., 2018). Therefore, we investigated whether HPP could enhance immune-stimulatory activities in the tumor microenvironment through the NF-κB and NLRP3 pathways.

Pattern recognition receptors (PRRs) have been reported on macrophages that recognize polysaccharides to activate macrophages to participate in the immune regulation process. Studies have shown that polysaccharide from polyporus can bind to TLR2 and activate the downstream NF-κB signaling pathway (Wei, 2009). As shown in **Figure 6A**, HPP at concentrations of 10–100 μg/mL significantly enhanced the expression of TLR2 (p < 0.01). To investigate whether HPP is involved in the activation of macrophages, the expression of TLR2 on cells was determined by flow cytometry.

The NF-κB pathway plays central roles in regulating immune and inflammatory processes that regulate the expression of cytokines involved in immunity and inflammation (Kim et al., 2016). NF-κB complexes are normally held inactive in the cytoplasm by binding to members of the IKB family of proteins in resting cells. In addition, NF-κB can be activated in response to a large variety of stimuli, such as IFN-γ and LPS, causing the phosphorylation of IKB proteins on conserved serine residues by the IKB kinase (IKK) complex (Begalli et al., 2017). HPP was shown to increase the expression of IKKa/b, IKB, TAK1, iNOS, COX2, and NF-κB P65 in RAW264.7 macrophages. Additionally, macrophages activated through the NF-κB pathway produce cytotoxic molecules and inflammatory cytokines, such as NO, IL-6, RANTES, IL-23, and IL-1β (Afonina et al., 2017). To investigate whether the NF-κB signaling pathway participated in IFN-γ-induced macrophage activation by HPP, RAW264.7 cells were pretreated with T24 cell culture supernatant for 3 h and then stimulated with IFN-γ or HPP (1–100 μg/mL) for 3 h. Western blot analysis showed that the expression of P65-NF-κB, TAK1, IKKa/b, P-IKB, INOS, and COX2 increased vitally after treatment with HPP for 8 h (**Figure 6B**).

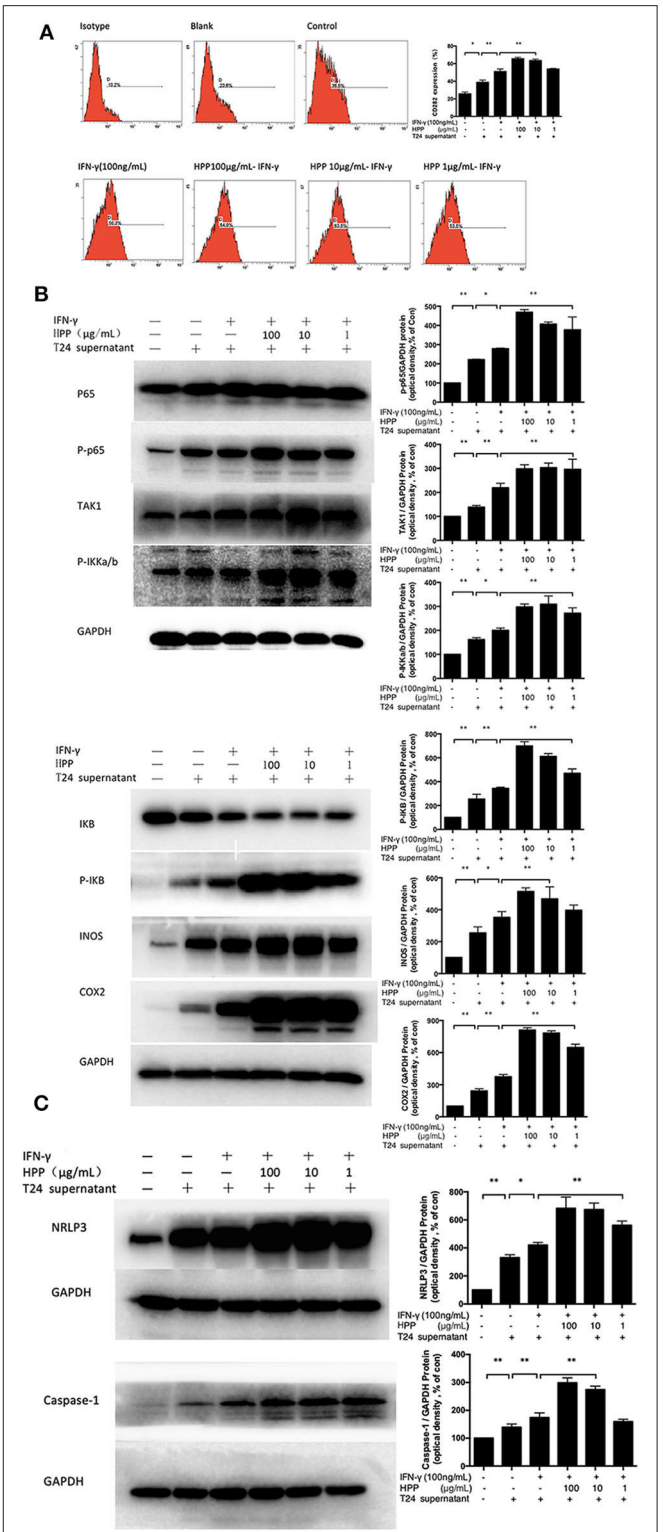

FIGURE 6 | Effect of HPP on the NF-κB/NLRP3 pathway in IFN-γ-induced RAW264.7 macrophages. **(A)** Effect of HPP on the expression of TLR2. **(B)** Effect of HPP on the phosphorylation of NF-κB. **(C)** Effect of HPP on the expression of NLRP3. Statistical significance in comparison to the control group is designated *P < 0.05, **P < 0.01. Data are presented as the mean ± s.e.m.

The NLRP3 inflammasome is a polyprotein complex of approximately 700 kDa that plays a crucial role in the inflammatory process (Zhang et al., 2012). ASC protein is important for NLRP3 activation. It has been reported that RAW264.7 cells cannot express ASC protein, so NLRP3 cannot be activated in these cells (Pelegrin, 2008). However, in recent years, a large number of literatures have reported that ingredients of Chinese medicine can regulate the ASC of RAW264.7 cells and activate NLRP3 pathway. Pinellia pedatisecta lectin was reported to bind with NLRP3 through ASC following by caspase-1 in the inflammation of RAW264.7 cells (Wang et al., 2019). And luteolin was reported to decrease production of ROS and expression of NLRP3, ASC, caspase-1, IL-18 and IL-1β proteins in RAW264.7 cells, which were incubated with LPS (Zhang et al., 2018). In addition, the Smilax glabra Roxb polysaccharide could evidently promote the phagocytosis and increase macrophage-derived biological factors, including nitric oxide (NO), interleukin-6 (IL-6), and interleukin-1 (IL-1β) secretion, via JNK and ERK signaling pathways and NLRP3 inflammasome signaling pathway (Wang et al., 2017). Our study also found that polyporus polysaccharide can activate NLRP3. This difference may be due to the differential expression of the ASC gene in the different types/sources of RAW264.7 cell lines or various culture condition. NLRP3 inflammasome assembly results in the activation of caspase-1, which in turn processes pro-IL-1β and pro-IL-18 into their mature forms, which initiate inflammation (Afonina et al., 2017; Kaufmann et al., 2017). When NLRP3 is activated, pro-caspase-1 is cleaved, resulting in caspase-1 activation (Zhang et al., 2012). Caspase-1 is essential to the production of mature interleukin-1β (IL-1β) and interleukin-18 (IL-18) in response to a variety of agonists or stimuli. Activated caspase-1 subsequently leads to the processing of the interleukin-1β (IL-1β) and interleukin-18 (IL-18) pro-inflammatory cytokines. Active mature IL-1β is formed by cleavage of the inactive pro–precursor by caspase-1 (Song et al., 2017). IL-1β has been linked to the production of a variety of inflammatory mediators, which play a critical role in the activation and regulation of immune cells and inflammatory responses (Lee et al., 2015; Kaufmann et al., 2017).

To investigate whether HPP is involved in IFN-γ-induced macrophage activation via the NLRP3 signaling pathways, RAW264.7 cells were pre-incubated with T24 cell culture supernatant for 3 h before culturing with IFN-γ for 3 h. The cells were then treated with HPP (1–100 μg/mL) for 8 h, after which western blot analysis was used to detect the expression of NLRP3 and Caspase-1. As shown in **Figure 6C**, increased NLRP3 expression was observed in cells treated with HPP. Based on the above results, we suggest that HPP-induced increases in the secretion of NO, IL-23, IL-1β, IL-6 and RANTES may have occurred via increases in the NLRP3 and NF-κB pathways.

Inhibition of the NF-κB Pathways

To further investigate whether the NF-κB signaling pathway was involved in IFN-γ-stimulated macrophage activation induced by HPP, HPP-treated macrophages were exposed to a specific P65-NF-κB inhibitor, SC75741, after which the secretion of IL-1β, IL-23, IL-6 and RANTES was measured using a Procarta PlexTM multiplex immunoassay. As shown in **Figure 7A**, the NF-κB inhibitor SC75741 attenuated the HPP-induced enhancement of the inflammatory factors IL-1β, IL-23, IL-6 and RANTES by 29, 25.2, 37.5, and 43.8%, respectively, in IFN-γ-stimulated macrophages. As shown in **Figure 7B**, our results demonstrated that HPP may first bind to the TLR2 receptor in macrophages and that the possible molecular mechanisms of HPP-stimulated macrophage immunomodulation may primarily occur via the NF-κB/NLRP3 signaling pathways, leading to the secretion of IL-1β, IL-23, IL-6, and RANTES.

Taken together, macrophages are the most dynamic and versatile cells involved in steady-state homeostasis, innate

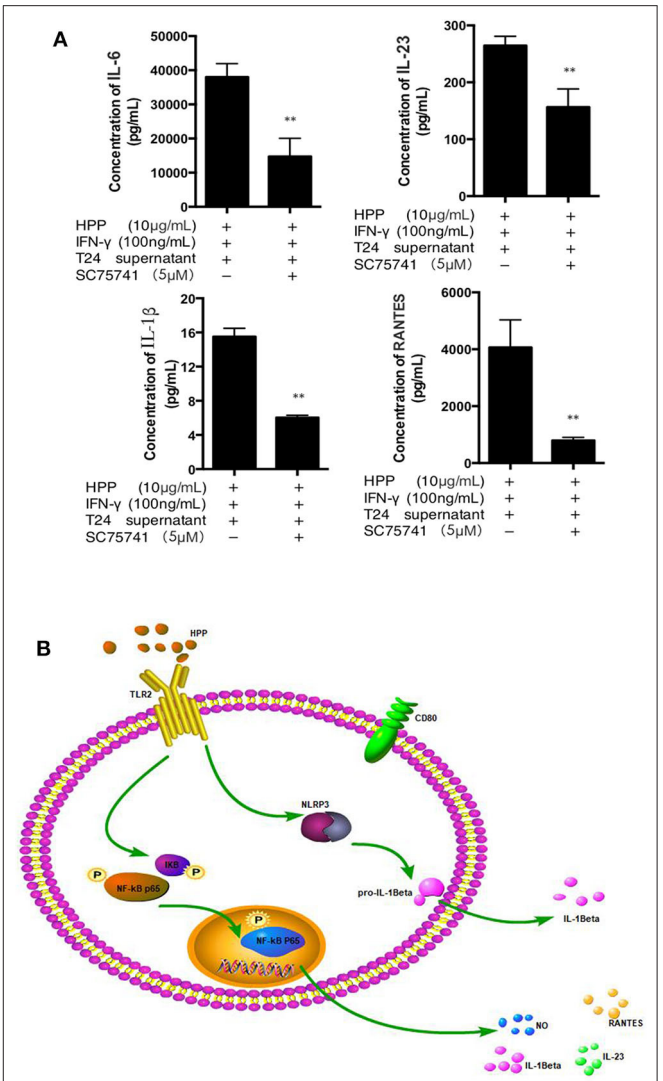

FIGURE 7 | Effect of a specific NF-κB inhibitor on IL-1β, IL-23, RANTES and IL-6 secretion in IFN-γ-stimulated RAW264.7 macrophages. **(A)** Effect of a specific NF-κB inhibitor on IFN-γ-stimulated RAW 264.7 cells treated with HPP. **(B)** Possible molecular mechanisms of HPP-induced macrophage immunomodulation. Statistical significance in comparison to the control group is designated $^{*}P < 0.05$, $^{**}P < 0.01$. Data are presented as the mean ± s.e.m.

immune surveillance, and inflammation establishment and resolution. To elucidate how HPP facilitates the suppression of bladder cancer *in vitro*, it is necessary to investigate the tumor microenvironment. Our studies have reported that RAW 264.7 cells treated with T24 cell culture supernatant may be an ideal macrophage model for vitro studies (Liu et al., 2017). In our present work, we treated RAW 264.7 cells with T24 cell culture supernatant to simulate the bladder tumor microenvironment *in vitro*. In the tumor microenvironment, macrophages that infiltrate into the tumor are generally called TAMs, which are similar to M2 macrophages. We found that HPP enhanced the activities of IFN-γ-stimulated RAW 264.7 macrophages, as shown by the release of NO, IL-6, RANTES, IL-23, and IL-1β, as well as expression of M1 phenotype indicators CD80 via the NF-κB and NLRP3 pathways in the bladder cancer microenvironment. HPP may be bound to TLR2, which is on the surface of macrophages, and a signal was transduced into the cell to participate in the process of activating macrophages. As shown in **Figure 7B**, the process in macrophages may be as follows: the NF-κB and NLRP3 proteins are stimulated by TLR2 signaling, resulting in activation of the secretion of NO, IL-6, RANTES, IL-1β, and IL-23 and thereby leading to the activation of CD 80.

CONCLUSION

In this study, our results present evidence that a new polysaccharide was separated from polyporus. Its monosaccharide composition was glucose, and the main linkage type was proven to be an α-(1→ 4)-linked D-galactan backbone. *In vitro* bioactivity tests showed that HPP has significant immune activity and may alter the tumor microenvironment by regulating the secretion of the inflammatory cytokines NO, IL-6, RANTES, IL-23, and IL-1β. The NF-κB and NLRP3 pathways are thought to be involved in immune regulation by HPP. Therefore, this homogeneous polysaccharide may be a potential candidate for application in bladder cancer therapy.

DATA AVAILABILITY STATEMENT

All datasets generated for this study are included in the article/supplementary material.

AUTHOR CONTRIBUTIONS

Corresponding authors XZe and XL designed the experimental ideas. C-PL the first author, was mainly responsible for the completion of the experiment and the analysis and interpretation of the data. G-NL, J-HL, C-YZ, and W-YJ were mainly responsible for revising the article. Other members, including ML, Q-LT, and X-YZ proofread the content. All authors contributed to the article and approved the submitted version.

FUNDING

This work was supported by the National Natural Science Foundation of China (No. 81573769), the Natural Science Foundation of Guangdong Province (No. 2014A03031345 & 2019A1515111108), and the Guangdong Provincial Hospital of Chinese Medicine (No. YN2019MJ02).

REFERENCES

Afonina, I. S., Zhong, Z., Karin, M., and Beyaert, R. (2017). Limiting inflammation-the negative regulation of NF-κB and the nlrp3 inflammasome. *Nat. Immunol.* 18, 861–869. doi: 10.1038/ni.3772

Begalli, F., Bennett, J., Capece, D., Verzella, D., D'Andrea, D., Tornatore, L., et al. (2017). Unlocking the nf-κb conundrum: embracing complexity to achieve specificity. *Biomedicines* 5, 1–35. doi: 10.3390/biomedicines5030050

Dy, G. W., Gore, J. L., Forouzanfar, M. H., Naghavi, M., and Fitzmaurice, C. (2016). Global burden of urologic cancers, 1990–2013. *Eur. Urol.* 71, 437–446. doi: 10.1016/j.eururo.2016.10.008

Ferlay, J., Soerjomataram, I., Dikshit, R., Eser, S., Mathers, C., Rebelo, M., et al. (2015). Cancer incidence and mortality worldwide: sources, methods and major patterns in globocan 2012. *Intern. J. Cancer*136, E359–E386. doi: 10.1002/ijc.29210

Gambardella, V., Castillo, J., Tarazona, N., Gimeno-Valiente, F., Martínez-Ciarpaglini, C., Cabeza-Segura, M., et al. (2020).The role of tumor-associated macrophages in gastric cancer development and their potential as a therapeutic target. *Cancer Treat. Rev.* 86:102015. doi: 10.1016/j.ctrv.2020.102015

Harris, N., Peach, R., Naemura, J., Linsley, P. S., Gros, G. L., and Ronchese, F. (1997). CD80 costimulation is essential for the induction of airway eosinophilia. *J. Exp. Med.* 185, 177–182. doi: 10.1084/jem.185.1.177

He, P. F., Zhang, A. Q., Wang, X. L., Qu, L., Li, G. L., Li, Y. P., et al. (2016). Structure elucidation and antioxidant activity of a novel polysaccharide from polyporus umbellatus sclerotia. *Int. J. Biol. Macromol.* 82, 411–417. doi: 10.1016/j.ijbiomac.2015.10.032

Jiang, Z., Zhao, J., Li, S., Hu, J., and Zeng, X. (2015). Polyporus polysaccharide induces transformation of M2 subtype macrophages to M1 macrophages 264.7. *Chin. J. Immunol.* 21, 1049–1052.

John, B. A., and Said, N. (2017). Insights from animal models of bladder cancer: recent advances, challenges, and opportunities. *Oncotarget* 8, 57766–57781. doi: 10.18632/oncotarget.17714

Kaufmann, F. N., Costa, A. P., Ghisleni, G., Diaz, A. P., Als, R., Peluffo, H., et al. (2017). Nlrp3 inflammasome-driven pathways in depression: clinical and preclinical findings. *Brain Behav. Immunity* 64:367. doi: 10.1016/j.bbi.2017.03.002

Kawai, K., Miyazaki, J., Joraku, A., Nishiyama, H., and Akaza, H. (2013). Bacillus calmette-guerin (BCG) immunotherapy for bladder cancer: current understanding and perspectives on engineered bcg vaccine. *Cancer Sci.* 104, 22–27. doi: 10.1111/cas.12075

Kim, K. N., Ko, S. C., Ye, B. R., Kim, M. S., Kim, J., Ko, E. Y., et al. (2016). 5-bromo-2-hydroxy-4-methyl-benzaldehyde inhibited lps-induced production of pro-inflammatory mediators through the inactivation of erk, p38, and nf-κb pathways in raw 264.7 macrophages. *Chem. Biol. Interact.* 258, 108–114. doi: 10.1016/j.cbi.2016.08.022

Kolawole, O. M., Lau, W. M., and Mostafid, H. (2017). Advances in intravesical drug delivery systems to treat bladder cancer. *Int. J. Pharm.* 532, 105–117. doi: 10.1016/j.ijpharm.2017.08.120

Lee, J. S., Kwon, D. S., Lee, K. R., Park, J. M., Ha, S. J., and Hong, E. K. (2015). Mechanism of macrophage activation induced by polysaccharide from cordyceps militaris culture broth. *Carbohydr. Polym.* 120, 29–37. doi: 10.1016/j.carbpol.2014.11.059

Li, H., Sun, Y., Wang, Y., and Li, X. (2008). Immunohistochemical localization of methionine-enkephalin in the body surface and digestive system of neverita didyma. *Chinese J. Zool.* 43, 72–76. doi: 10.13859/j.cjz.2008.04.010

Li, N., Yan, C., Hua, D., and Zhang, D. (2013). Isolation, purification, and structural characterization of a novel polysaccharide from ganoderma

capense. *Int. J. Biol. Macromol.* 57, 285–290. doi: 10.1016/j.ijbiomac.2013.03.030

Liu, C. P., Zhang, X., Tan, Q. L., Xu, W. X., Zhou, C. Y., Luo, M., et al. (2017). NF-κB pathways are involved in m1 polarization of raw 264.7 macrophage by polyporus polysaccharide in the tumor microenvironment. *PLoS ONE* 12:e0188317. doi: 10.1371/journal.pone.0188317

Ma, X. L., Song, F. F., Zhang, H., Huan, X., and Li, S. Y. (2017). Compositional Monosaccharide Analysis of Linn by HPLC and HPCE Quantitative Determination and Comparison of Polysaccharide from Linn by HPCE and HPLC. *Curr. Pharm. Analysis* 13, 433–437. doi: 10.2174/1573412913666170330150807

Meng, F. D., Wang, S., Jiang, Y. H., and Sui, C. G. (2016). Antitumor effect of dendritic cells transfected with prostate-specific membrane antigen recombinant adenovirus on prostate cancer: an *in vitro* study. *Mol. Med. Rep.* 13, 2124–2134. doi: 10.3892/mmr.2016.4754

Meurette, O., and Mehlen, P. (2018). Signaling in the tumor microenvironment. *Cancer Cell*. 34, 536–548. doi: 10.1016/j.ccell.2018.07.009

Michael, A., Cannarile, C.. H., Ries, S. H., and Dominik, R. (2015). Tumor-associated macrophages provide significant prognostic information in urothelial bladder cancer. *PLoS ONE* 10:e0133552. doi: 10.1371/journal.pone.0133552

Mishra, B. B., Rathinam, V. A. K., Martens, G. W., Martinot, A. J., Kornfeld, H., Fitzgerald, K. A., et al. (2013). Nitric oxide controls the immunopathology of tuberculosis by inhibiting nlrp3 inflammasome-dependent processing of IL-1β. *Nat. Immunol.* 14, 52–60. doi: 10.1038/ni.2474

Moschini, M., D'Andrea, D., Korn, S., Irmak, Y., Soria, F., Compérat, E., et al. (2017). Characteristics and clinical significance of histological variants of bladder cancer. *Nat. Rev. Urol.* 14, 651–668. doi: 10.1038/nrurol.2017.125

Payne, K. K., Aqbi, H. F., Butler, S. E., Graham, L., Keim, R. C., Wan, W., et al. (2018). $Gr1^{-}$/lowcd11b^{-}/lowmhcii^{+} myeloid cells boost t cell anti-tumor efficacy. *J. Leukoc. Biol.* 104, 1215–1228. doi: 10.1002/JLB.5A0717-276RR

Pelegrin, P. Barroso-Gutierrez, C. and Surprenant, A. (2008). P2x7 receptor differentially couples to distinct release pathways for IL-1β in mouse macrophage. *J. Immunol.* 180, 7147–7157. doi: 10.4049/jimmunol.180.11.7147

Pratap, U. P., Sharma, H. R., Mohanty, A., Kale, P., Gopinath, S., Hima, L., et al. (2015). Estrogen upregulates inflammatory signals through nf-κb, ifn-γ, and nitric oxide via akt/mtor pathway in the lymph node lymphocytes of middle-aged female rats. *Int. Immunopharmacol.* 29, 591–598. doi: 10.1016/j.intimp.2015.09.024

Qi, Y., Chang, Y., Wang, Z., et al. (2019). Tumor-associated macrophages expressing galectin-9 identify immunoevasive subtype muscle-invasive bladder cancer with poor prognosis but favorable adjuvant chemotherapeutic response. *Cancer Immunol. Immunother.* 68, 2067–2080. doi: 10.1007/s00262-019-02429-2

Saha, S., Shalova, I. N., and Biswas, S. K. (2017). Metabolic regulation of macrophage phenotype and function. *Immunol. Rev.* 280, 102–111. doi: 10.1111/imr.12603

Serra, G., Incani, A., Serreli, G., Porru, L., Melis, M. P., Tuberoso, C. I. G., et al. (2018).Olive oil polyphenols reduce oxysterols -induced redox imbalance and pro-inflammatory response in intestinal cells. *Redox Biol.* 17:354. doi: 10.1016/j.redox.2018.05.006

Solinas, G., Schiarea, S., Liguori, M., Fabbri, M., Pesce, S., Zammataro, L., et al. (2010). Tumor-conditioned macrophages secrete migration-stimulating factor: a new marker for m2-polarization, *influencing tumor cell motility. J. Immunol.* 185, 642–652. doi: 10.4049/jimmunol.1000413

Song, G., Wang, K., Zhang, H., Sun, H., Wu, B., and Ju, X. (2017). Structural characterization and immunomodulatory activity of a novel polysaccharide from pteridium aquilinum. *Int. J. Biol. Macromol.* 102, 599–604. doi: 10.1016/j.ijbiomac.2017.04.037

Suriano, F., Santini, D., Perrone, G., et al. (2013). Tumor associated macrophages polarization dictates the efficacy of BCG instillation in non-muscle invasive urothelial bladder cancer. *J. Exp. Clin. Cancer Res.* 32:87. doi: 10.1186/1756-9966-32-87

Vidyarthi, A., Khan, N., Agnihotri, T., Negi, S., Das, D. K., Aqdas, M., et al. (2018). Tlr-3 stimulation skews m2 macrophages to m1 through ifn-αβ signaling and restricts tumor progression. *Front. Immunol.* 9:1650. doi: 10.3389/fimmu.2018.01650

Wang, M., Yang, X. B., Zhao, J. W., Lu, C. J., and Zhu, W. (2017). Structural characterization and macrophage immunomodulatory activity of a novel polysaccharide from smilax glabra roxb. *Carbohydr. Polym.* 156, 390–402. doi: 10.1016/j.carbpol.2016.09.033

Wang, W., Mao, S. Yu, H. Wu, H. Shan, X., Zhang, X., et al. (2019). Pinellia pedatisecta lectin exerts a proinflammatory activity correlated with ros-mapks/nf-κb pathways and the nlrp3 inflammasome in raw264.7 cells accompanied by cell pyroptosis. *Int. Immunopharmacol.* 66, 1–12. doi: 10.1016/j.intimp.2018.11.002

Wei, J. (2009). *Effect of BCG and Polyporus Polysaccharide on TLR2/4- NF-κB Signal Pathway in Bladder Cancer Cells[D]*. Guangdong: Guangzhou University of Traditional Chinese Medicine, Guangzhou.

Wu, H., Zhang, X., Han, D., et al. (2020). Tumour-associated macrophages mediate the invasion and metastasis of bladder cancer cells through CXCL8. *PeerJ.* 8:e8721. doi: 10.7717/peerj.8721

Zeng, X., Li, C., Huang, Y., Zhang, G., Zhang, X., and Yang, M. (2011). Effects of Polyporus umbellatus and Polyporus umbellatus polysaccharide on phagocytosis and expression of surface immune related molecules in abdominal macrophages of bladder cancer model rats. *Chinese J. Immunol.* 27, 414–418

Zhang, C., Boini, K. M., Xia, M., Abais, J. M., Li, X., Liu, Q., et al. (2012). Activation of nod-like receptor protein 3 inflammasomes turns on podocyte injury and glomerular sclerosis in hyperhomocysteinemia. *Hypertension* 60, 154–162. doi: 10.1161/HYPERTENSIONAHA.111.189688

Zhang, G., Zeng, X., Han, L., Wei, J. A., and Huang, H. (2010). Diuretic activity and kidney medulla aqp1, aqp2, aqp3, v2r expression of the aqueous extract of sclerotia of polyporus umbellatus fries in normal rats. *J. Ethnopharmacol.* 128, 433–437. doi: 10.1016/j.jep.2010.01.032

Zhang, G., Zeng, X., Li, C., Li, J., Huang, Y., Han, L., et al. (2011). Inhibition of urinary bladder carcinogenesis by aqueous extract of sclerotia of polyporus umbellatus fries and polyporus polysaccharide. *Am. J. Chinese Med.* 39, 135–144. doi: 10.1142/S0192415X11008701

Zhang, B. C., Li, Z., Xu, W., Xiang, C. H., and Ma, Y. F. (2018). Luteolin alleviates nlrp3 inflammasome activation and directs macrophage polarization in lipopolysaccharide-stimulated raw264.7 cells. *Am. J. Transl. Res.* 10, 265–273. doi: 10.3969/j.issn.1000-484X.2011.05.007

Zhao, Y. Y. (2013). Traditional uses, phytochemistry, pharmacology, pharmacokinetics and quality control of polyporus umbellatus, (pers.) fries: a review. *J. Ethnopharmacol.* 149, 35–48. doi: 10.1016/j.jep.2013.06.031

Conflict of Interest: The authors declare that the research was conducted in the absence of any commercial or financial relationships that could be construed as a potential conflict of interest.

frontiers in Chemistry

REVIEW
published: 24 September 2020
doi: 10.3389/fchem.2020.00751

Rationally Designed DNA Nanostructures for Drug Delivery

Fan Xu†, *Qing Xia*† *and Pengfei Wang**

Institute of Molecular Medicine, Shanghai Key Laboratory for Nucleic Acid Chemistry and Nanomedicine, State Key Laboratory of Oncogenes and Related Genes, Department of Oncology, School of Medicine, Renji Hospital, Shanghai Jiao Tong University, Shanghai, China

DNA is an excellent biological material that has received growing attention in the field of nanotechnology due to its unique capability for precisely engineering materials via sequence specific interactions. Self-assembled DNA nanostructures of prescribed physicochemical properties have demonstrated potent drug delivery efficiency *in vitro* and *in vivo*. By using various conjugation techniques, DNA nanostructures may be precisely integrated with a large diversity of functional moieties, such as targeting ligands, proteins, and inorganic nanoparticles, to enrich their functionalities and to enhance their performance. In this review, we start with introducing strategies on constructing DNA nanostructures. We then summarize the biological barriers ahead of drug delivery using DNA nanostructures, followed by introducing existing rational solutions to overcome these biological barriers. Lastly, we discuss challenges and opportunities for DNA nanostructures toward real applications in clinical settings.

Keywords: drug deliver systems, DNA self-assembly, nanocarrier, biological barrier, rational design

OPEN ACCESS

Edited by:
Ye Tian,
Nanjing University, China

Reviewed by:
Qianhao Min,
Nanjing University, China
Baoquan Ding,
National Center for Nanoscience and Technology (CAS), China

***Correspondence:**
Pengfei Wang
pengfei.wang@sjtu.edu.cn

†*These authors have contributed equally to this work*

Specialty section:
This article was submitted to Nanoscience, a section of the journal Frontiers in Chemistry

Received: *12 June 2020*
Accepted: *21 July 2020*
Published: *24 September 2020*

Citation:
Xu F, Xia Q and Wang P (2020) Rationally Designed DNA Nanostructures for Drug Delivery. Front. Chem. 8:751. doi: 10.3389/fchem.2020.00751

INTRODUCTION

Nanocarriers capable of the potent delivery of therapeutic molecules play a pivotal role in enhancing their therapeutic efficacy in clinic, and typically aid in minimizing systemic toxicity, improving biostability/bioavailability, and strengthening delivery efficiency to targeted tissues, cells, or subcellular locations (Savjani et al., 2012; Huang et al., 2013; Din et al., 2017; Gustafson et al., 2018; Zhang R. et al., 2019). Enormous progress has been made in this area, accompanied by the evolution of a large diversity of nanomaterials. Several delivery systems, such as liposomes and cationic dendritic polymers, have been approved for clinical use (Cheng et al., 2011; Bulbake et al., 2017). Meanwhile, many other types of delivery systems, including inorganic particles and cell mimics, are under extensive study in laboratories or in clinics (Chen et al., 2016; Pang et al., 2017). Nevertheless, there are many limitations that remain to be tackled in order to fully realize the therapeutic potential of drug delivery systems, which include but are not limited to acute toxicity in the short term and unknown toxicity in the long run (Lv et al., 2006), heterogenicity of formulated delivery systems (Adjei et al., 2014), and very limited targeting delivery efficiency (Wilhelm et al., 2016).

With the substantial development of DNA molecular self-assembly in the last four decades, DNA-based nanocarriers have emerged as promising delivery systems for drug delivery. Derived from the unique Watson-Crick base pairing, it is fully possible to create a variety of DNA

nanostructures with a well-defined size and homogeneous geometry through the sequence design of DNA molecules followed by a straightforward self-assembly process, which is highly predictable, reproducible, and scalable (Seeman and Sleiman, 2017). DNA is a natural biological molecule, which is biodegradable with minimal toxicity. Furthermore, drugs like DNA intercalators (e.g., doxorubicin) and nucleic acids (e.g., siRNA, antisense oligonucleotides) can be easily integrated into DNA-based nanocarriers (Li et al., 2011; Lee H. et al., 2012; Zhao et al., 2012; Fakhoury et al., 2014; Rahman et al., 2017). Aided by well-established nucleic acid synthesis and bioconjugation techniques, DNA strands may be incorporated with various functional moieties to enrich the functionality of delivery systems, such as loading a variety of macromolecules (e.g., protein, inorganic particle) or targeting ligands (Li et al., 2019; Shin et al., 2020). These unique properties make DNA-based nanomaterials an attractive drug delivery system. After introducing responsive components, DNA nanocarriers can acquire dynamic capabilities in response to a variety of physiological or non-physiological stimuli (Zhang Y. et al., 2019). However, the high complexity of *in vivo* microenvironments poses great challenges to their proper performance in living organisms (Zhao Z. et al., 2019). Therefore, rational design strategies are essential in order to maintain their multifunctional delivery properties *in vivo*. With improved understanding of their *in vivo* fate, the drug delivery performance of DNA nanocarriers could then be highly predictable and designable (Jiang et al., 2019). In this review, we will first introduce the design methods for fabricating DNA-based nanocarriers, and then discuss strategies of tuning DNA-based nanocarriers for overcoming biological barriers to maximize their potential for efficient drug delivery.

CONSTRUCTING DNA NANOSTRUCTURES FOR DRUG DELIVERY

DNA Self-Assembly Strategies

Distinguishing from DNA vectors like plasmids, DNA nanocarriers are based on the *de novo* design of self-assembled DNA nanostructures. Invented by Seeman in the early 1980s, methods of constructing DNA nanostructures have advanced rapidly in the last four decades (Seeman, 2020). In the early stage of DNA nanotechnology, by breaking the sequence symmetry of the Holliday junction, the original slidable 4-arm branched DNA junction can be fixed and serves as a basic assembling unit to build higher-order structures (**Figure 1A**) (Seeman, 1982). Seeman's group later introduced a tile-based method for DNA assembly. They bundled DNA strands by DNA crossovers to form a variety of units called "tiles." Repeated tiles were interconnected by complementary single-stranded extensions (sticky ends) and eventually grew into large assemblies (Ding et al., 2004). Following the initial immobile 4-arm Holliday junction, junctions of a diverse number of arms were designed as DNA building blocks (Ma et al., 1986; Wang et al., 1991; Wang and Seeman, 2007). Well-designed tiles allow for the construction of highly-ordered 1D, 2D, and 3D DNA structures. Mao and Seeman later reported the successful fabrication of DNA 3D crystals by using tensegrity triangular tiles (Zheng et al., 2009). Yan and Laban first designed a point-star-like tile containing bulged T loops. These loops are located in the center of the tile linking two adjacent arms (Yan et al., 2003). Further tuning the length of the loops allows their linking arms to bend from the original geometric plane with varying degrees. For instance, 3-point star tiles with varied lengths of loops can self-assemble into a number of different polyhedra including

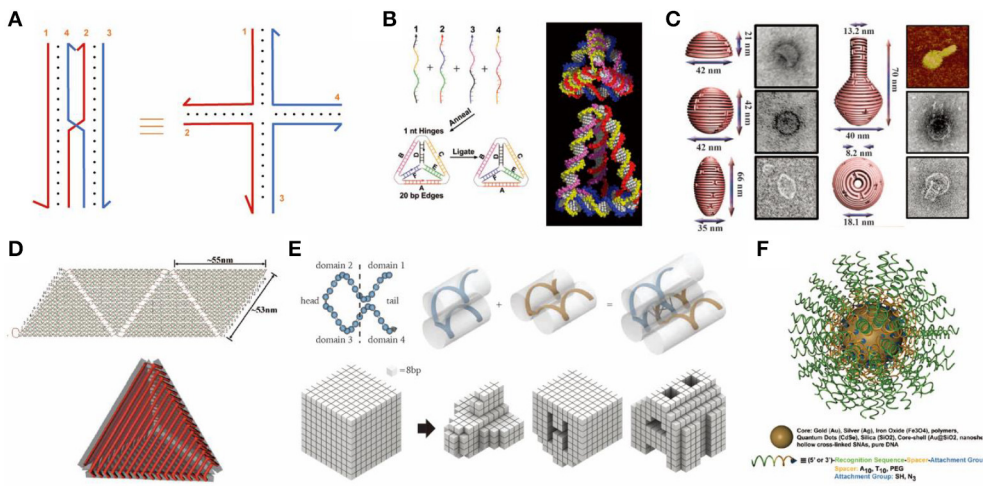

FIGURE 1 | Rationally designed DNA nanostructures. **(A)** An immobile Holliday junction. **(B)** DNA tetrahedron formed from 4 single-stranded DNAs. Adapted with permission from Goodman et al. (2005). Copyright 2005 AAAS. **(C)** 3D DNA origami structure with precisely controlled curvature. Adapted with permission from Han et al. (2011). Copyright 2011 AAAS. **(D)** DNA container constructed by folding and joining single-layered 2D origami sheets. Adapted with permission from Ke et al. (2009b). Copyright 2009 ACS. **(E)** DNA objects assembled from single-stranded tiles (or DNA bricks). Adapted with permission from Ke et al. (2012). Copyright 2012 AAAS. **(F)** Spherical nucleic acids tethered onto a gold nanoparticle core. Adapted with permission from Cutler et al. (2012). Copyright 2012 ACS.

tetrahedrons, dodecahedrons, and Buckyball structures (He et al., 2008; Wang et al., 2016).

Differing from polyhedrons assembled by point-star-tiles which contain repeated units of tiles, DNA nano-objects such as cubes, tetrahedrons, and octahedrons may also be assembled from multiple single-stranded DNAs (Chen and Seeman, 1991; Zhang and Seeman, 1994; Goodman et al., 2005). For example, in 2005, Goodman et al. reported a simple and rapid way to assemble 4 single-stranded DNAs into tetrahedrons by one annealing step with a high yield up to 95%, which has been widely used for a variety of applications (**Figure 1B**) (Goodman et al., 2005).

Another breakthrough in the field of DNA nanotechnology was the invention of the DNA origami technique by Rothemund (2006), where one long single-stranded scaffold DNA is folded by a set of complementary short strands (staples) to form various 2D objects (Rothemund, 2006; Wang et al., 2017). Further, Shih and colleagues extended this method to 3D by pleating the plane of DNA helixes and arranging them into compact lattices (Douglas et al., 2009; Ke et al., 2009a). Yan and colleagues built 3D hollow objects by programming the curvature of designated helixes via adding or deleting bases within DNA crossovers (**Figure 1C**) (Dietz et al., 2009). 3D origami structures may also be assembled by folding and joining single-layered 2D origami sheets, which resulted in the successful generation of container-like DNA boxes (**Figure 1D**) (Andersen et al., 2009; Ke et al., 2009b).

In 2012, Yin and colleagues reported a simple single-stranded tile (SST) or DNA brick method to build 2D and 3D objects of arbitrary shapes (Ke et al., 2012; Wei et al., 2012; Ong et al., 2017). SST consists of 4 domains that interact with adjacent tiles. Each SST can bind to four adjacent counterparts by complementary domains and assemble into prescribed structures (**Figure 1E**) (Ke et al., 2012).

Other Strategies to Build DNA Nanostructures

Jones et al. used inorganic nanoparticles to provide rigidity and initiated another branch of DNA nanotechnology (Jones et al., 2015). For example, single-stranded DNA oligonucleotides with thiol modified ends can tightly bind to Au nanoparticles. This type of structure was named "spherical nucleic acids" (SNA, **Figure 1F**) (Cutler et al., 2012). These DNA-particle hybrids have a variety of applications, including drug delivery. Particularly, it has been used for the combination of gene regulation and photothermal therapy (Kim J. et al., 2016).

Rolling-circle amplification (RCA) is another popular method for constructing drug delivery DNA nanostructures, which employ DNA/RNA polymerase to generate large quantities of long concatemeric DNA products from a predesigned circular DNA template (Mohsen and Kool, 2016). The products contain repeated sequences and can be cleaved to generate functional DNA fragments. Due to its high yield of products, the nucleic acids can directly condense into particles with or without the help of condensing agents (Lee J. B. et al., 2012), which offers a great advantage toward high-volume drug loading.

ENHANCING BIOSTABILITY AND EXTENDING CIRCULATION TIME

Rapid and non-specific clearance is a great challenge for nanoparticle-based drug delivery systems *in vivo*. After intravenous administration, a sufficient circulation time of nanocarriers is a prerequisite for good therapeutic efficacy (Wang et al., 2013). It is generally challenging for DNA nanocarriers to reside in physiological environments due to the following reasons. Firstly, as a biological material, DNA is prone to degradation by deoxyribonucleases (DNases) in serum. Secondly, the ionic strength of body fluids is quite different from the DNA assembly buffers. In particular, low cationic concentration may cause the disassembly of DNA nanostructures due to increased electrostatic repulsion between negatively charged DNA helices (Hahn et al., 2014). Thirdly, the opsonization effect by non-specific adsorption of serum proteins induces macrophages to engulf DNA nanocarriers for clearance (Surana et al., 2013). Lastly, DNA nanostructures have a high tendency for fast renal or hepatic clearance (Messaoudi et al., 2019).

There are numerous strategies to address the challenges that DNA nanostructures face. One is from a design point of view. For instance, it has been reported that less compact DNA structures or structures with a wireframe geometry exhibit higher resistance to nuclease degradation or cation-depletion-induced structure disassembly (Jiang et al., 2016; Kielar et al., 2018; Chandrasekaran et al., 2020). Apart from this design perspective, many other strategies are available to enhance the biostability of DNA nanostructures which will be introduced in detail in the following section.

DNA Backbone Modification

Natural DNA backbone is composed of repeated deoxyribose and phosphate groups. It is the target of DNases which catalyze the hydrolytic cleavage of phosphodiester linkages. Chemical modification of the backbone can drastically enhance its biological stability by hindering the attack of nuclease. These backbone-modified nuclei acids containing unnatural components can be called synthetic nucleic acid polymers, which includes xeno-nucleic acids (XNA), peptide nucleic acids (PNA), locked nucleic acids (LNA), threose nucleic acids (TNA), and phosphorothioate DNA (**Figure 2A**) (Burns et al., 2013; Pedersen et al., 2015). These hybrid nanostructures function no less efficiently than their natural analog counterparts. On that basis, using a series of engineered polymerases, Philipp's group synthesized nano-objects fully composed of unnatural nucleic acids, where they used 2′F-RNA, 2′-fluoroarabino nucleic acids (FANA), hexitol nucleic acids (HNA), and cyclohexene nucleic acids (CeNA) to assemble tetrahedral structures (**Figure 2B**). HNA tetrahedrons remained intact after 8 day incubation in serum-containing cell culture media, while tetrahedrons of natural DNAs were fully degraded in 2 days (Taylor et al., 2016).

Kim K. R. et al. used L-DNA, a mirror form of natural D-DNA, as building materials for DNA nanocarriers (**Figure 2B**). L-DNA has identical thermodynamic properties to D-DNA, but it has significantly higher serum stability, prolonged *in vivo* residency,

and enhanced cellular uptake. In xenograft mouse models, an L-DNA nanocarrier showed better effect on tumor inhibition than D-DNA tetrahedrons or PEGylated liposomes while loaded with doxorubicin (Kim K. R. et al., 2016).

Covalent Crosslinking

Self-assembled DNA nanostructures generally contain several to thousands of DNA single strands, which impose a high density of nicking points that render the DNA structures

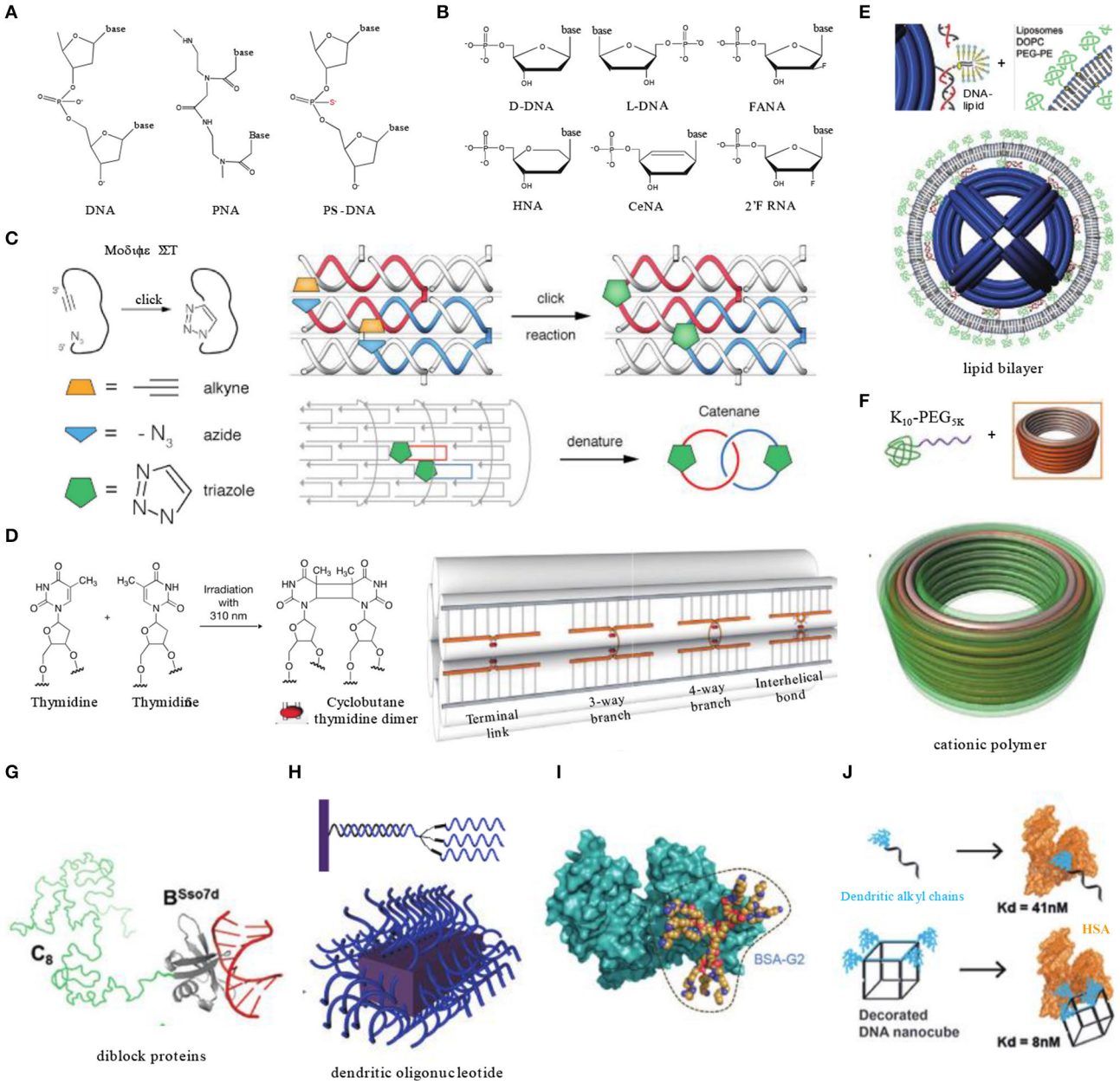

FIGURE 2 | Enhancing the biostability and extending the circulation time of DNA nanocarriers. **(A)** Natural DNA backbone and common inter-nucleotide linkage modifications involved in DNA nanotechnology. **(B)** Natural nucleosides and their analogs involved in DNA nanotechnology. **(C)** Covalent crosslinking of 6-Helix DNA structure containing strands modified with azides and alkynes by click chemistry. Adapted with permission from Cassinelli et al. (2015). Copyright 2015 Wiley. **(D)** Light triggered dimer formation of adjacent thymidine residues in DNA origami objects. Adapted with permission from Gerling et al. (2018). Copyright 2018 AAAS. **(E)** Lipid bilayer encapsulation of DNA nanocages. Adapted with permission from Perrault and Shih (2014). Copyright 2014 ACS. **(F)** Electrostatically coating DNA origami nanostructures with polyamine-PEG block copolymers. Adapted with permission from Ponnuswamy et al. (2017). Copyright 2017 Springer Nature. **(G)** A diblock protein containing a non-sequence-specific DNA binding domain (B^{Sso7d}) and an unstructured blocking domain (C_8) for DNA structure coating. Adapted with permission from Sanchez-Rueda et al. (2019). Copyright 2019 RSC Pub. **(H)** Dendritic oligonucleotides on DNA brick nanostructures. Adapted with permission from Kim and Yin (2020). Copyright 2020 Wiley. **(I)** Albumin dendron conjugates for DNA origami coating. Adapted with permission from Auvinen et al. (2017). Copyright 2017 Wiley. **(J)** Dendritic alkyl decorating DNA nanocubes with high-affinity binding to human serum albumin. Adapted with permission from Lacroix et al. (2017). Copyright 2017 ACS.

vulnerable to cationic depletion and nuclease degradation. To circumvent this instability issue induced by nicking points, covalent crosslinking of DNA strands represents one elegant solution. For instance, crosslinking of DNA was shown to be able to stabilize DNA structures in the presence of denaturing agents or at elevated temperature (Rajendran et al., 2011). In 2015, Manetto reported a 6-helix bundle DNA structure composed of terminal functionalized single stranded DNA with linear alkyne and azide moieties. A copper-catalyzed click reaction was performed after assembly to bridge nicking points, resulting in the formation of cyclized strands interlinking with each other (**Figure 2C**). After crosslinking, the 6-helix bundles were able to remain intact in buffers lacking magnesium and stay resistant to exonuclease-I (Cassinelli et al., 2015). In 2018, Gerling et al. reported another strategy to achieve crosslinking of DNA origami structures without introducing chemical moieties (**Figure 2D**). It was accomplished by light-triggered formation of pyrimidine dimers between adjacent thymine or cytosine bases. These bases are designed to be placed in adjacent terminals of nicks formed by strands, branches, or helixes. Comparing with non-crosslinked structures, crosslinked origami objects needed a significantly prolonged time (∼6-fold) to be degraded in biological media (Gerling et al., 2018).

Encapsulation

Encapsulation of DNA structures by functional agents may also enhance their stability. For instance, Shih et al. encapsulated DNA origami structures via *in-situ* formation of liposomes surrounding the structures (Perrault and Shih, 2014). The lipid bilayer envelope not only shielded DNA nanocarriers from enzymes in serum, but also changed their surface characters which is important to determine immune responses and biodistributions. After lipid bilayers' encapsulation, immune activation by DNA structures was decreased by 2 orders of magnitude, and pharmacokinetic bioavailability was improved by a factor of 17 (**Figure 2E**).

Cationic polymer is another type of material used for DNA structure encapsulation. Cationic polymers can tightly adsorb onto the negatively charged phosphate backbone of DNA through electrostatic interaction. The molecular ratio of polymers to DNA structures is critical since an improper ratio may cause unwanted aggregation or distortion (Kiviaho et al., 2016). As a widely used anti-opsonization agent, polyethylene glycol (PEG) has shown to have broad application potentials in drug delivery. Introducing PEG into coating polymers is a common strategy to alleviate non-specific adsorption of proteins (Dai et al., 2014). Shih's group enveloped DNA barrels with oligolysine-PEG copolymers, which helped the DNA barrel to avoid rapid renal clearance and extended its blood half-life from 9 to 45 min (**Figure 2F**) (Ponnuswamy et al., 2017). Similar with synthetic polymers, a series of diblock recombinant proteins were also employed, which are composed of a non-specific DNA-binding domain (e.g., Sso7d, K12) and a hydrophilic unstructured peptide segment. The diblock proteins form brush-like structures around the DNA to provide better resistance to enzyme degradation (**Figure 2G**) (Sanchez-Rueda et al., 2019).

Inspired by spherical nucleic acids, of which the densely packed nucleic acids are highly resistant to nuclease degradation, Kim and Yin coated the outer surface of DNA brick nanostructures with dendritic oligonucleotides through base paring between overhang strands and oligonucleotides (**Figure 2H**) (Kim and Yin, 2020). This method can increase the biostability of DNA brick structures in comparison to their naked counterparts.

Bound to Albumin

As the most abundant protein, albumin holds a relatively long circulation half-life in blood. Physiologically, albumin can bind with other molecules such as bilirubin, fatty acids, and metal ions to extend their circulation time and to improve their biodistribution. Albumin is also an anti-opsonization agent that can prevent phagocytosis of nanocarriers. Therefore, albumin is a promising agent to be used for drug delivery. In fact, some albumin-bound chemotherapeutics have already been approved by the FDA for clinical use, such as Abraxane, an albumin-bound form of Pacilitaxel.

However, it is generally challenging to achieve high affinity binding between albumin and DNA nanocarriers. To address this technical challenge, Kostiainen et al. engineered bovine serum albumin (BSA) into biohybrid macromolecules with cationic dendritic conjugates (polyamine analogs). The conjugate was anchored to BSA via a cysteine–maleimide bond with cysteine residues (**Figure 2I**). Thus, the engineered BSA can attach to DNA structures through electrostatic interactions between polyamine and DNA backbones (Auvinen et al., 2017). Lacroix et al. reported another method by decorating DNA structures with dendritic alkyl chains (**Figure 2J**). Tuning the number and orientation of the amphiphilic decorations enables DNA nanocubes to bind with human serum albumin (HSA) with a high affinity in low nanomolar range. Meanwhile, HSA did not hinder the activity of cargo antisense oligonucleotide *in vitro* (Lacroix et al., 2017). Since these two reports were lacking in *in vivo* experiments, the efficiency of albumin pre-binding strategy needs to be validated in animal models.

TARGETING STRATEGIES *IN VIVO*

After systemic administration, another big hurdle ahead of DNA nanostructure carriers is the targeting delivery to specific organs/tissues of interest. Enabling selective accumulation of drug molecules in targeted sites not only boosts its therapeutic efficacy but also alleviates off-target delivery-related systemic toxicity. Therefore, targeting functionality is a pivotal factor determining the therapeutic performance of drug delivery systems. In this section, *in vivo* targeting strategies that have been used on DNA nanocarriers is summarized.

In vivo Biodistribution of Pristine DNA Nanostructures

In order to investigate the *in vivo* performance of DNA nanocarriers, numerous studies have firstly examined their

biodistributions in various animal models. Generally, pristine DNA nanostructures have a preferential accumulation in organs like the liver, kidneys, and lymph nodes. For instance, as one of the simplest DNA structures, DNA tetrahedrons (Tds) have been widely researched. Kim K. R. et al. reported a tendency of hepatic accumulation of Tds after intravenous injection (Kim K. R. et al., 2016). By changing DNA backbones to increase biostability, the phenomenon of hepatic accumulation can be significantly enhanced. They harnessed this property of Td for liver delivery of siRNA successfully, which targets the overexpressed ApoB1 mRNA in hypercholesterolemia. ApoB1 siRNAs were loaded on Tds through DNA linkers extending from each side. As a result, an ∼20–30% decrease in serum lipid levels was observed when compared with PBS controls (**Figure 3A**) (Kim et al., 2020). Jiang et al. studied the biodistribution of radiolabeled DNA origami nanostructures (DONs) through positron emission tomography (PET) imaging. DONs of three different geometries, including rectangle, triangle, and tube, were tested. All three exhibited predominant renal uptake, among which triangular DONs were used to effectively treat acute kidney injury in mice model (Jiang et al., 2018).

Apart from intravenous injection, subcutaneous injection is another commonly used administration route. The negative surface charge and size (6–10 nm) of Tds were found to be quite suitable for lymphatic drainage. Moreover, Tds can be easily uptake macrophages and have good intracellular stability, which extends their lymph node retention time. Taking advantages of these properties, Kim et al. labeled Tds with Cy5 fluorophore to visualize the sentinel lymph nodes of tumor (Kim et al., 2013). Compared with linear DNA probes, Tds showed enhanced translocation in lymph nodes and a prolonged retention time in mice xenograft models.

Passive Delivery to Tumors

It is generally believed that most solid tumors exhibit enhanced permeability and retention (EPR) (Fang et al., 2011; Park-Windhol and D'Amore, 2016), though this has become controversial in recent years (Sindhwani et al., 2020). For DNA nanostructures, the impact of shape diversity on EPR effect has been revealed. Zhang et al. demonstrated that triangle-shaped DNA origami exhibited optimal tumor passive targeting accumulation compared to rectangular and tubular origami structures (**Figure 3B**) (Zhang et al., 2014). They revealed that triangle-shaped origami accumulated at the tumor site and reached peak levels at 6 h and maintained high levels for 24 h after intravenous administration. Kim et al. built a library of wireframe DNA objects of various backbones for *in vivo* screening (Kim et al., 2019). According to their results, cages with backbone modifications had better tumor accumulation. In terms of shape effect, pyramid-shaped nanocages exhibited the highest tumor specific delivery efficiency.

Active Delivery to Cells

With the discovery of pathological mechanisms, disease-specific molecular markers or microenvironmental characteristics are constantly revealed. Cells harboring pathological changes, such as cancerization or infection, usually over-express certain molecular receptors or biomarkers which could well serve as targets for active delivery. In addition, microenvironmental parameters like pH or oxygen level may significantly change

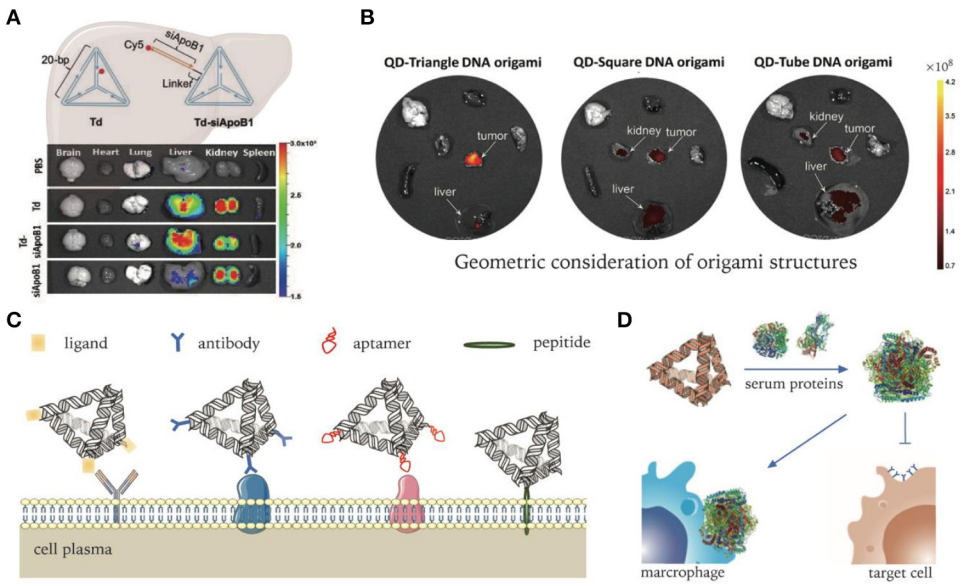

FIGURE 3 | DNA nanocarriers targeting organs, tumors, and cells. **(A)** Delivery of ApoB1 siRNA to hepatic cells by pristine DNA tetrahedrons. Adapted with permission from Kim et al. (2020). Copyright 2020 RSC Pub. **(B)** DNA origami's passive delivery to malignancy. Adapted with permission from Zhang et al. (2014). Copyright 2014 ACS. **(C)** Modifications of DNA nanocarriers for active targeting to specific cells. **(D)** Non-specific protein adsorption to DNA nanocarriers in serum environment. Adapted with permission from Oh et al. (2018). Copyright 2018 Springer Nature.

under pathological conditions that may be targeted to realize active delivery (Salahpour Anarjan, 2019).

Molecular ligands used for targeting delivery include antibodies, aptamers, receptor ligands, functional peptides, etc. They can be tethered onto DNA nanocarriers via various conjugation methods to realize targeting functionality (**Figure 3C**) (Wu et al., 2013; Setyawati et al., 2016; Xia et al., 2016; Santi et al., 2017). Active targeting functionalized DNA nanocarriers have been demonstrated to enhance brain permeability, which passive delivery fails to reach due to the existence of blood–brain barrier (BBB). Tian et al. modified framework tetrahedral DNA nanoprobes with peptides targeting both brain capillary endothelial cells and malignant glioma cells. Through receptor-mediated transcytosis, DNA nanoprobes successfully passed through the BBB model and then entered the cytoplasm of the tumor cells (Tian et al., 2018).

However, despite pronounced selectivity *in vitro*, some ligands were found to lose targeting ability *in vivo* (e.g., transferrin) (Mirshafiee et al., 2013). One important reason for the failure of the targeting capability in complex biological milieu is the occurrence of biotransformation when adsorbed by serum proteins, which not only abolishes molecular recognition capability, but also induces clearance by phagocytes (**Figure 3D**) (Oh et al., 2018). Therefore, systematic study and optimization need to be conducted to fully realize the targeting capability of various ligands for *in vivo* delivery applications.

CELL ENTRY ROUTES AND INTRACELLULAR FATE

Over billions of years of evolution, the cell membrane has become a wall to protect sophisticated cellular organelles from the extracellular environment. Only selected substances can pass through the membrane. Most nanoscale substances, including molecules and nanoparticles, enter cells through an energy consuming pathway called endocytosis, which can be categorized into several distinct subtypes (**Figure 4A**) (Lee et al., 2016). Phagocytosis primarily exists in immune cells like macrophages to engulf large particles ($>0.5\,\mu m$). Pinocytosis is widely adopted by all types of cells, which can be further subdivided into macropinocytosis, clathrin-mediated endocytosis, caveolae-mediated endocytosis, clathrin-, and caveolae-independent endocytosis. After endocytosis, nanocarriers are encapsulated and transported in membrane vesicles like endosomes (Conner and Schmid, 2003). Proteins on the endosome membranes induce the maturation of endosomes into lysosomes and then transport cargo into corresponding subcellular regions. The permeability of lysosomal membranes is complicatedly regulated and plays an important role in determining the intracellular fate of nanocarriers (Johansson et al., 2010). Thus, it is critical to tune and to optimize DNA nanocarriers in order to achieve potent intracellular delivery performance.

Enhancing Cellular Uptake Efficiency

Since DNA and RNA molecules are negatively charged due to phosphate groups on the backbone, electrostatic repulsion from cell membranes makes it difficult for them to enter cells efficiently. As mentioned earlier, encapsulating DNA nanocarriers with cationic polymers can facilitate its cell uptake. For instance, Lee J. B. et al. used polyethylenimine (PEI) to condense sponge-like structures generated from RCA reactions, which significantly enhanced the cell uptake efficiency of siRNA sponges and achieved significant knockdown of target mRNA (Lee J. B. et al., 2012).

Despite its anionic nature, DNA nanostructures of prescribed three-dimensional geometries likes cages or origami structures were found to be able to enter cells efficiently without the aid of transfection reagents. Ligand binding receptors on cell membranes are responsible for the uptake of DNA nanostructures. Liang et al. demonstrated that DNA tetrahedrons were internalized by a caveolin-dependent endocytosis pathway and transported to lysosomes in a microtubule-dependent manner (Liang et al., 2014). Vindigni et al. reported that scavenger receptor LOX-1 was responsible for mediating pristine DNA nanocages into cells. Cells overexpressing LOX-1 internalized cages 30 times higher than their low-expressing counterparts (Vindigni et al., 2016). Wang et al. reported that cancer cells can readily uptake DNA origami nanostructures (DONs) with various sizes and shapes with high efficiency. Further study revealed that DONs of a larger size and higher aspect ratio had increased uptake efficiency compared to their counterparts. Moreover, they visualized the multi-stage internalization process of DONs on a high-resolution single particle level (**Figure 4B**) (Wang et al., 2018). Lee et al. reported that the number and disposition of targeting ligands (i.e., folate) on the DNA tetrahedral nanocarriers largely affect its *in vitro* and *in vivo* delivery efficiency (Lee H. et al., 2012).

Modulating Intracellular Fate

Biomolecular drugs like ASOs and siRNAs are prone to enzymatic degradation. After entering cells through endocytosis, they need to escape from lysosomes to cytoplasm or avoid endosomal encapsulation in the first place. Strategies like membrane fusion and acid swelling have been applied in many delivery systems to circumvent this challenge (Smith et al., 2019), which, however, cannot be easily adapted by DNA nanocarriers. A more feasible strategy for DNA nanocarriers would be trying to avoid endolysosomal entrapment. It was reported that endosomes induced by certain receptors of caveolae-mediated endocytosis may transport to non-lysosome organells (Parton and Simons, 2007). Targeting these receptors is a practical method for DNA nanocarriers avoiding degradation in lysosome. Folic acid, albumin, cholesterol, and transferrin are ligands that have been proven to be able to serve this purpose (**Figure 4C**) (Mirshafiee et al., 2013). Some aptamers have also been reported to be able to guide DNA nanocarriers to avoid lysosomal degradation. For example, nucleolin-targeting aptamer AS1411 can be internalized into a wide variety of cancer cells and migrates to the nucleus. It was internalized via macropinocytosis in cancer cells, but via a non-macropinocytic pathway in normal cells (Reyes-Reyes et al., 2010). Charoenphol et al. incorporated AS1411 aptamers into DNA pyramids, which led to selective inhibition of cancer cells (Charoenphol

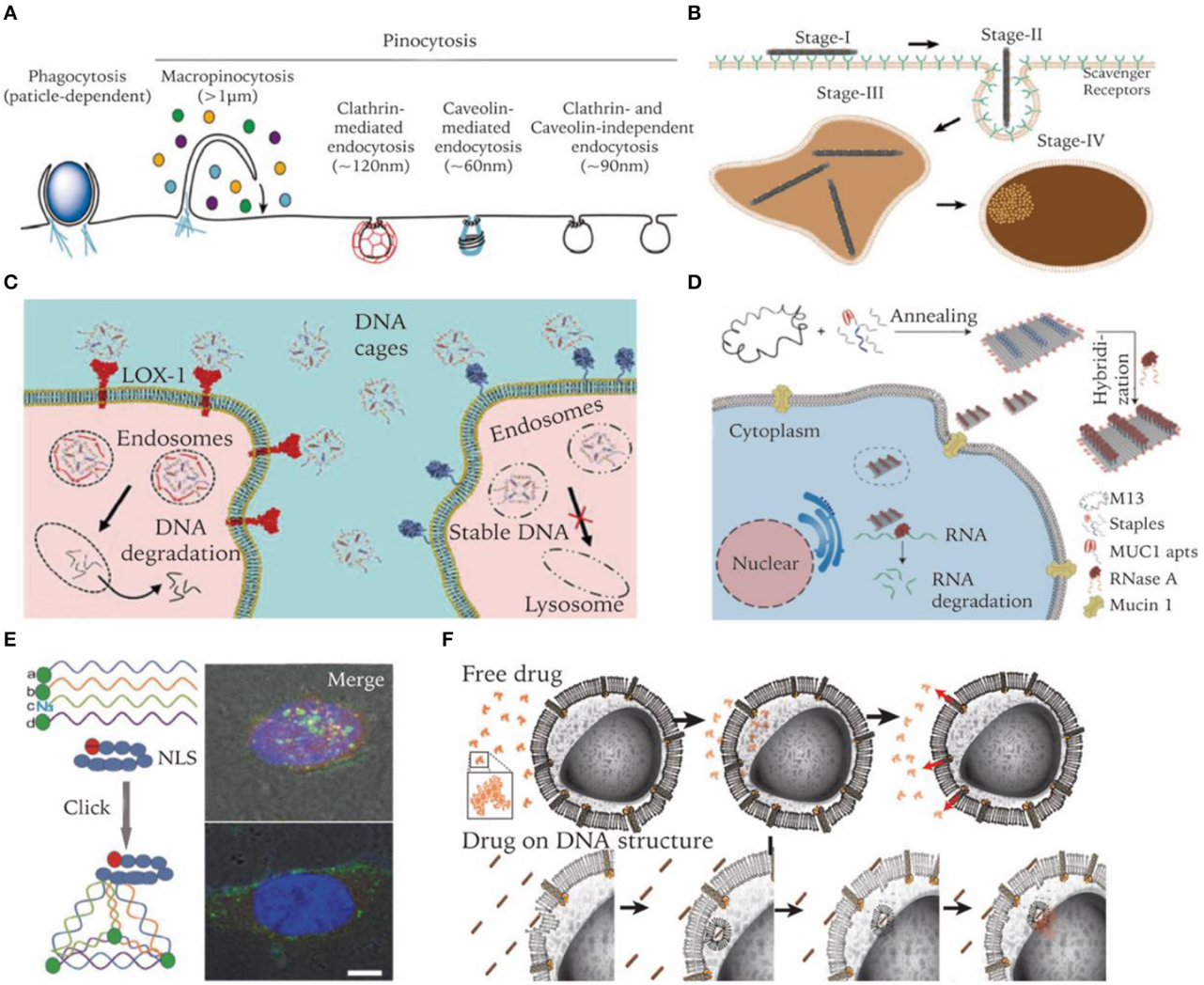

FIGURE 4 | Enhancing cell entry of DNA nanostructures and regulating their intracellular fate. **(A)** Endocytosis pathways involved in nanoparticle's cell uptake. Adapted with permission from Lee et al. (2016). Copyright 2016 RSC Pub. **(B)** Cell internalization process of a DNA origami rod structure. Adapted with permission from Wang et al. (2018). Copyright 2018 ACS. **(C)** Bypass lysosome pathway through targeting specific receptors. Adapted with permission from Raniolo et al. (2018). Copyright 2018 RSC Pub. **(D)** Lysosome escape and delivery of active enzymes by DNA origami modified with MUC1 aptamer. Adapted with permission from Zhao S. et al. (2019). Copyright 2019 ACS. **(E)** Lysosome escape of DNA tetrahedrons modified with nucleus-targeting signaling peptides. Adapted with permission from Liang et al. (2014). Copyright 2014 Wiley. **(F)** Drugs on DNA nanocarriers circumvent efflux-pump-mediated drug resistance mechanisms. Adapted with permission from Halley et al. (2016). Copyright 2016 Wiley.

and Bermudez, 2014). MUC1 aptamer is another example. In cancer cells, MUC1 protein was reported to be crucial for the stabilization of lysosome membranes (Dudeja et al., 2007). Zhao S. et al. found that MUC1 aptamer-tethered DNA origami structures can be efficiently transported to cytoplasm within 24 h. In contrast, naked DNA origami structures were trapped in lysosomes (**Figure 4D**) (Zhao S. et al., 2019). Fan et al. reported another strategy of escaping lysosomes by using peptides. They functionalized the tetrahedral DNA nanostructures with nucleus-targeting signaling (NLS) peptides through a click reaction. Though entering cells by the endocytosis route, NLS modified structures were transported to the nucleus after 16 h and remained intact (**Figure 4E**) (Liang et al., 2014).

In certain scenarios, lysosomal entrapment of nanocarriers may not necessarily be a disadvantage. For instance, in some cases, drugs need to be localized to endosomes in order to function. Castro et al. used rod-shaped DNA origami to load and deliver daunorubicin to cancer cells to circumvent efflux-pump-mediated drug resistance. Compared to free drugs entering cells via passive diffusion, delivery of daunorubicin by DNA origami carriers led to a higher amount of drug accumulation and better resistance to pump-mediated drug efflux (**Figure 4F**) (Halley et al., 2016). The endosomatic pathway also plays important roles in regulating innate immune responses. DNA structures trapped in endosomes are more accessible by specialized receptors of the innate immune system. Schüller et al. reported that DNA

origami rods decorated with CpG-containing oligonucleotides are quite efficient for cellular immunostimulation. They can trigger stronger innate immune responses than a standard carrier system such as lipofectamine (Schüller et al., 2011).

DNA NANOCARRIERS RESPONDING TO MICROENVIRONMENTS

Microenvironments of pathological sites generally exhibit distinct characteristics that are different to healthy sites, e.g., acidic and hypoxic conditions of tumor microenvironments, or overexpression of certain molecular biomarkers. Such differences in environmental characteristics could serve as another type of target for nanocarriers to aim for. In order to arm pristine DNA nanostructures with stimuli responsive capability, dynamic elements need to be integrated into the designed nanocarrier (**Figure 5A**) (Harroun et al., 2018; Zhang Y. et al., 2019). In the following section, we discuss some mechanisms that may be incorporated into DNA nanocarriers to realize environmental responsive cargo delivery.

Aptamer-Enabled Robotic Systems

Aptamers are single-stranded nucleic acids of a specific sequence that can selectively recognize and bind to a target (e.g., ions, molecules, proteins), which are generally acquired from multiple rounds of *in vitro* selection (Shangguan et al., 2006). To enable target-binding induced conformational change, a duplexed aptamer is designed by using a complementary strand to hybridize to a specific portion of the aptamer sequence, which may be released from the aptamer once the target of high affinity is present (Munzar et al., 2019). This element has been used as a key to unlock DNA origami containers to realize cell specific cargo transportation (Douglas et al., 2012). Recently, Li et al. reported the successful *in vivo* application of an autonomous DNA robot as an responsive drug delivery system (Li et al., 2018). This robotic container was fastened by aptamer AS1411, which can bind to nucleolin that overexpressed on tumor-associated vascular endothelial cells in a tumor microenvironment. Upon binding to nucleolin, the DNA robot opens up to unload its cargo thrombin to induce thrombosis in tumor-associated blood vessels to starve and eventually kill tumor cells.

Enzyme Mediated Cargo Release

Nuclease degradation of DNA nanocarriers might represent the simplest way to induce cargo release (Sun et al., 2014). Nevertheless, it is limited to the delivery of nuclease-resistant chemical drugs. Different to nuclease, enzymes like telomerase can recognize specific DNA sequences. Integrating these sequences into DNA nanostructures enables them to selectively interact with enzymes (Yin et al., 2004). Ma et al. reported a telomerase-responsive DNA-icosahedron nanocarrier that can selectively release caged platinum-nanodrugs into cisplatin resistance cancer cells. Telomerase primer sequences were incorporated into the edges of DNA icosahedrons, serving as a recognition element of telomerase. After binding with DNA icosahedrons, telomerase was activated and started to generate telomeric repeats, which hybridize with downstream toehold sequence, resulting in the detaching of drugs (Ma et al., 2018). (**Figure 5B**).

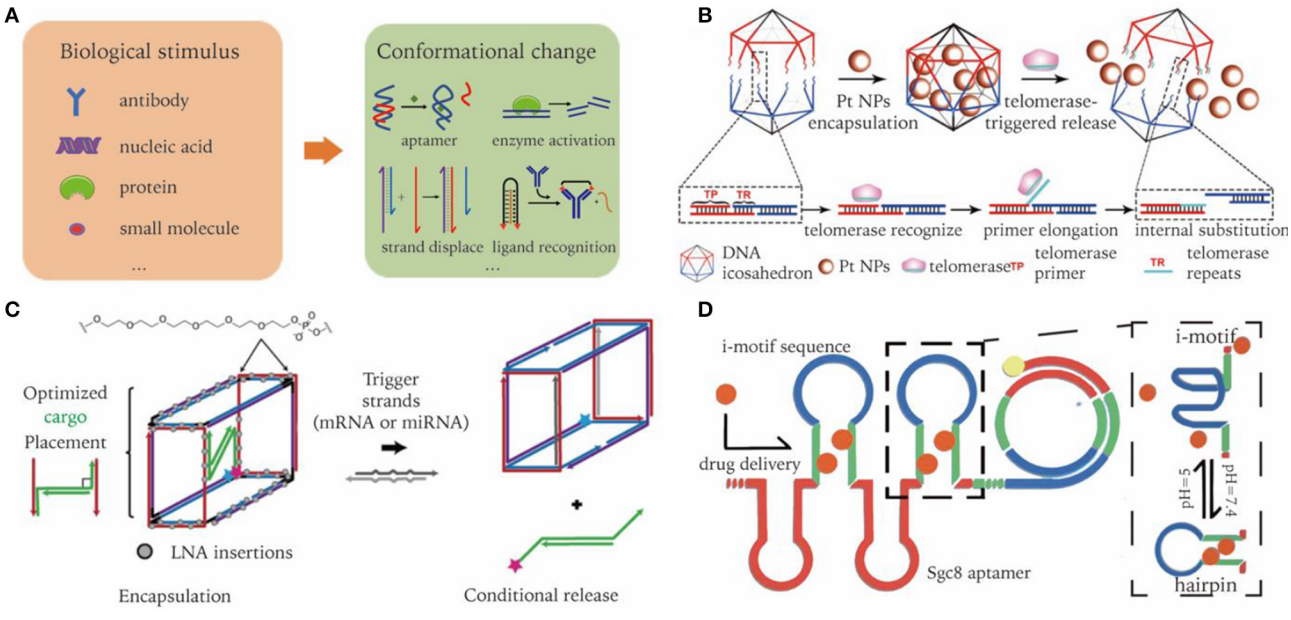

FIGURE 5 | Dynamic DNA nanocarriers for conditional triggered release of cargos in biological environment. **(A)** Biological inputs and reconfigurable elements to achieve stimuli responsive cargo release. **(B)** Active telomerase triggers detachment of DNA icosahedron nanocages resulting in targeted release of drugs. Adapted with permission from Ma et al. (2018). Copyright 2018 Wiley. **(C)** DNA nano-suitcases conditionally release siRNA cargos in the presence of oligonucleotide triggers. Adapted with permission from Bujold et al. (2016). Copyright 2016 ACS. **(D)** RCA products incorporated with pH responsive i-motif sequences. Adapted with permission from Zhao et al. (2018). Copyright 2018 ACS.

Strand Displacement Induced Cargo Unloading

Strand displacement is widely used for constructing dynamic structures, in which one strand in a DNA duplex can be released and replaced by another strand through a toehold design (Yurke et al., 2000). The invader strand can be mRNA, miRNA, etc. The released strand may then serve as a trigger of subsequent cascade reactions. In terms of drug delivery, released strands typically have a therapeutic effect, such as the delivery of siRNA or ASOs. For instance, Katherine et al. designed a DNA nano-suitcase that encapsulated a siRNA cargo, which can be specifically released upon recognition of an oligonucleotide trigger. The siRNA cargos partially bind to the edge of DNA cages, with the leftover sequence serving as a toehold for strand displacement. They showed that the whole construct was assembled in high yield, with cargo released on demand, and remained intact in biological conditions for a long period of time (**Figure 5C**) (Bujold et al., 2016).

pH Responsive Cargo Release

DNA triplex and i-motif are two commonly used pH-responsive structures. They follow strict sequence requirements, which takes advantage of binding equilibrium shifts according to the A^+-C base pair formation in acidic solution (Fu et al., 2019). An acidic extracellular microenvironment is well-recognized in the process of oncogenesis. Zhao et al. incorporated i-motif into RCA products with bilateral complementary sequences. In an acidic tumor environment, the i-motif sequences at the loop region fold, resulting in the opening of the stem region. Thus, previous intercalated drugs are released in response to environmental pH. Functionalized with aptamers, the resultant drug-carrier system accomplishes *in vivo* targeted delivery, and pH-stimulated sustained release of Dox (**Figure 5D**) (Zhao et al., 2018).

CHALLENGES AND OPPORTUNITIES FOR CLINICAL APPLICATIONS

The unique advantages of using DNA nanocarriers as drug delivery systems is quite obvious. First, the size and shape of DNA nanocarriers can be finely tuned. And the robust assembly of DNA can greatly alleviate batch-to-batch variations. Second, the numbers and positions of ligand modifications or drug loadings on DNA nanocarriers may be precisely programmed. Third, although the biological environment is quite different from where DNA nanocarriers are originally assembled, optimizing their biostability, circulation time, biodistribution, cell entry routes, and intracellular fate enable DNA nanocarriers to perform well *in vivo*. Finally, various practicable modifications on DNA allow the integration of DNA nanostructures with other materials, such as AuNPs and liposomes (Sun and Gang, 2011; Yang et al., 2016), making DNA nanocarriers a robust system with a large potential of holding multiple functionalities.

In laboratory settings, DNA nanocarriers have demonstrated the capability to conquer drug resistance of cancer cells, serve as an efficient non-viral vector for gene therapy, induce target thrombosis in tumor vessels, improve the restoration of kidney functions, and visualize sentinel lymph nodes. These problems center around demanding better solutions within real clinical settings. However, there is still a long way to go to translate their good performance in cells or in mice to clinical application in patients. More studies need to be conducted to better understand the determining factors of *in vivo* performance. It remains unclear how the physical and chemical properties, such as surface charges, oligonucleotide modifications, or protein adhesions of DNA nanostructures, affect the pharmacokinetic bioavailability. The preference of hepatic and renal uptake of DNA nanocarriers limits their applications in other organs. At a cellular level, cell entry through the endocytosis pathway is far from highly efficient and selective. Production cost is another concern, especially when chemical modifications are in high demand. At last, although DNA material is biodegradable, comprehensive assessments of their biosafety in humans are essential prior to real clinical applications. With these issues appropriately addressed, we believe DNA-based nanocarriers hold a bright future toward serving as potent drug delivery systems for treating many diseases in clinic.

AUTHOR CONTRIBUTIONS

All authors listed have made a substantial, direct and intellectual contribution to the work, and approved it for publication.

REFERENCES

Adjei, I. M., Peetla, C., and Labhasetwar, V. (2014). Heterogeneity in nanoparticles influences biodistribution and targeting. *Nanomedicine* 9, 267–278. doi: 10.2217/nnm.13.70

Andersen, E. S., Dong, M., Nielsen, M. M., Jahn, K., Subramani, R., Mamdouh, W., et al. (2009). Self-assembly of a nanoscale DNA box with a controllable lid. *Nature* 459, 73–76. doi: 10.1038/nature07971

Auvinen, H., Zhang, H., Nonappa, Kopilow, A., Niemela, E. H., Nummelin, S., Correia, A., et al. (2017). Protein coating of DNA nanostructures for enhanced stability and immunocompatibility. *Adv. Healthc. Mater.* 6:1700692. doi: 10.1002/adhm.201700692

Bujold, K. E., Hsu, J. C. C., and Sleiman, H. F. (2016). Optimized DNA "nanosuitcases" for encapsulation and conditional release of siRNA. *J. Am. Chem. Soc.* 138, 14030–14038. doi: 10.1021/jacs.6b08369

Bulbake, U., Doppalapudi, S., Kommineni, N., and Khan, W. (2017). Liposomal formulations in clinical use: an updated review. *Pharmaceutics* 9:12. doi: 10.3390/pharmaceutics9020012

Burns, J. R., Stulz, E., and Howorka, S. (2013). Self-assembled DNA nanopores that span lipid bilayers. *Nano Lett.* 13, 2351–2356. doi: 10.1021/nl304147f

Cassinelli, V., Oberleitner, B., Sobotta, J., Nickels, P., Grossi, G., Kempter, S., et al. (2015). One-step formation of "chain-armor"-stabilized DNA nanostructures. *Angew. Chem. Int. Ed Engl.* 54, 7795–7798. doi: 10.1002/anie.201500561

Chandrasekaran, A. R., Vilcapoma, J., Dey, P., Wong-Deyrup, S. W., Dey, B. K., and Halvorsen, K. (2020). Exceptional nuclease resistance of paranemic crossover (PX) DNA and crossover-dependent biostability of DNA motifs. *J. Am. Chem. Soc.* 142:14. doi: 10.1021/jacs.0c02211

Charoenphol, P., and Bermudez, H. (2014). Aptamer-targeted DNA nanostructures for therapeutic delivery. *Mol. Pharm.* 11, 1721–1725. doi: 10.1021/mp500047b

Chen, J. H., and Seeman, N. C. (1991). Synthesis from DNA of a molecule with the connectivity of a cube. *Nature* 350, 631–633. doi: 10.1038/350631a0

Chen, S., Hao, X., Liang, X., Zhang, Q., Zhang, C., Zhou, G., et al. (2016). Inorganic nanomaterials as carriers for drug delivery. *J. Biomed. Nanotechnol.* 12, 1–27. doi: 10.1166/jbn.2016.2122

Cheng, Y., Zhao, L., Li, Y., and Xu, T. (2011). Design of biocompatible dendrimers for cancer diagnosis and therapy: current status and future perspectives. *Chem. Soc. Rev.* 40, 2673–2703. doi: 10.1039/c0cs00097c

Conner, S. D., and Schmid, S. L. (2003). Regulated portals of entry into the cell. *Nature* 422, 37–44. doi: 10.1038/nature01451

Cutler, J. I., Auyeung, E., and Mirkin, C. A. (2012). Spherical nucleic acids. *J. Am. Chem. Soc.* 134, 1376–1391. doi: 10.1021/ja209351u

Dai, Q., Walkey, C., and Chan, W. C. W. (2014). Polyethylene glycol backfilling mitigates the negative impact of the protein corona on nanoparticle cell targeting. *Angew Chem Int Ed* 53, 5093–5096. doi: 10.1002/anie.201309464

Dietz, H., Douglas, S. M., and Shih, W. M. (2009). Folding DNA into twisted and curved nanoscale shapes. *Science* 325, 725–730. doi: 10.1126/science.1174251

Din, F. U., Aman, W., Ullah, I., Qureshi, O. S., Mustapha, O., Shafique, S., et al. (2017). Effective use of nanocarriers as drug delivery systems for the treatment of selected tumors. *Int. J. Nanomed.* 12, 7291–7309. doi: 10.2147/IJN.S146315

Ding, B., Sha, R., and Seeman, N. C. (2004). Pseudohexagonal 2D DNA crystals from double crossover cohesion. *J. Am. Chem. Soc.* 126, 10230–10231. doi: 10.1021/ja047486u

Douglas, S. M., Bachelet, I., and Church, G. M. (2012). A logic-gated nanorobot for targeted transport of molecular payloads. *Science* 335:831. doi: 10.1126/science.1214081

Douglas, S. M., Dietz, H., Liedl, T., Hogberg, B., Graf, F., and Shih, W. M. (2009). Self-assembly of DNA into nanoscale three-dimensional shapes. *Nature* 459, 414–418. doi: 10.1038/nature08016

Dudeja, V., Chugh, R., Yokoyama, Y., Talukdar, R., Borja-Cacho, D., Zwolak, P., et al. (2007). HSP70 stabilizes the lysosomes by transporting MUC1 to the lysosomes. *Pancreas* 35, 399–400. doi: 10.1097/01.mpa.0000297692.76686.c2

Fakhoury, J. J., McLaughlin, C. K., Edwardson, T. W., Conway, J. W., and Sleiman, H. F. (2014). Development and characterization of gene silencing DNA cages. *Biomacromolecules* 15, 276–282. doi: 10.1021/bm401532n

Fang, J., Nakamura, H., and Maeda, H. (2011). The EPR effect: unique features of tumor blood vessels for drug delivery, factors involved, and limitations and augmentation of the effect. *Adv. Drug Deliv. Rev.* 63, 136–151. doi: 10.1016/j.addr.2010.04.009

Fu, W., Tang, L., Wei, G., Fang, L., Zeng, J., Zhan, R., et al. (2019). Rational design of pH-responsive DNA motifs with general sequence compatibility. *Angew Chem. Int. Ed.* 58, 16405–16410. doi: 10.1002/anie.201906972

Gerling, T., Kube, M., Kick, B., and Dietz, H. (2018). Sequence-programmable covalent bonding of designed DNA assemblies. *Sci Adv* 4:eaau1157. doi: 10.1126/sciadv.aau1157

Goodman, R. P., Schaap, I. A., Tardin, C. F., Erben, C. M., Berry, R. M., Schmidt, C. F., et al. (2005). Rapid chiral assembly of rigid DNA building blocks for molecular nanofabrication. *Science* 310, 1661–1665. doi: 10.1126/science.1120367

Gustafson, H. H., Olshefsky, A., Sylvestre, M., Sellers, D. L., and Pun, S. H. (2018). Current state of *in vivo* panning technologies. Designing specificity and affinity into the future of drug targeting. *Adv. Drug Deliv. Rev.* 130, 39–49. doi: 10.1016/j.addr.2018.06.015

Hahn, J., Wickham, S. F., Shih, W. M., and Perrault, S. D. (2014). Addressing the instability of DNA nanostructures in tissue culture. *ACS Nano* 8, 8765–8775. doi: 10.1021/nn503513p

Halley, P. D., Lucas, C. R., McWilliams, E. M., Webber, M. J., Patton, R. A., Kural, C., et al. (2016). Daunorubicin-loaded DNA origami nanostructures circumvent drug-resistance mechanisms in a leukemia model. *Small* 12, 308–320. doi: 10.1002/smll.201502118

Han, D., Pal, S., Nangreave, J., Deng, Z., Liu, Y., and Yan, H. (2011). DNA origami with complex curvatures in three-dimensional space. *Science* 332, 342–346. doi: 10.1126/science.1202998

Harroun, S. G., Prévost-Tremblay, C., Lauzon, D., Desrosiers, A., Wang, X., Pedro, L., et al. (2018). Programmable DNA switches and their applications. *Nanoscale* 10, 4607–4641. doi: 10.1039/C7NR07348H

He, Y., Ye, T., Su, M., Zhang, C., Ribbe, A. E., Jiang, W., et al. (2008). Hierarchical self-assembly of DNA into symmetric supramolecular polyhedra. *Nature* 452, 198–201. doi: 10.1038/nature06597

Huang, C. L., Steele, T. W. J., Widjaja, E., Boey, F. Y. C., Venkatraman, S. S., and Loo, J. S. C. (2013). The influence of additives in modulating drug delivery and degradation of PLGA thin films. *NPG Asia Mater.* 5:e54. doi: 10.1038/am.2013.26

Jiang, D., England, C. G., and Cai, W. (2016). DNA nanomaterials for preclinical imaging and drug delivery. *J. Control. Release* 239, 27–38. doi: 10.1016/j.jconrel.2016.08.013

Jiang, D., Ge, Z., Im, H.-J., England, C. G., Ni, D., Hou, J., et al. (2018). DNA origami nanostructures can exhibit preferential renal uptake and alleviate acute kidney injury. *Nat. Biomed. Eng.* 2, 865–877. doi: 10.1038/s41551-018-0317-8

Jiang, Q., Zhao, S., Liu, J., Song, L., Wang, Z.-G., and Ding, B. (2019). Rationally designed DNA-based nanocarriers. *Adv. Drug Deliv. Rev.* 147, 2–21. doi: 10.1016/j.addr.2019.02.003

Johansson, A.-C., Appelqvist, H., Nilsson, C., Kågedal, K., Roberg, K., and Öllinger, K. (2010). Regulation of apoptosis-associated lysosomal membrane permeabilization. *Apoptosis* 15, 527–540. doi: 10.1007/s10495-009-0452-5

Jones, M. R., Seeman, N. C., and Mirkin, C. A. (2015). Nanomaterials. Programmable materials and the nature of the DNA bond. *Science* 347:1260901. doi: 10.1126/science.1260901

Ke, Y., Douglas, S. M., Liu, M., Sharma, J., Cheng, A., Leung, A., et al. (2009a). Multilayer DNA origami packed on a square lattice. *J. Am. Chem. Soc.* 131, 15903–15908. doi: 10.1021/ja906381y

Ke, Y., Ong, L. L., Shih, W. M., and Yin, P. (2012). Three-dimensional structures self-assembled from DNA bricks. *Science* 338, 1177–1183. doi: 10.1126/science.1227268

Ke, Y., Sharma, J., Liu, M., Jahn, K., Liu, Y., and Yan, H. (2009b). Scaffolded DNA origami of a DNA tetrahedron molecular container. *Nano Lett.* 9, 2445–2447. doi: 10.1021/nl901165f

Kielar, C., Xin, Y., Shen, B., Kostiainen, M. A., Grundmeier, G., Linko, V., et al. (2018). On the stability of DNA origami nanostructures in low-magnesium buffers. *Angew Chem. Int. Ed.* 130, 9614–9618. doi: 10.1002/ange.201802890

Kim, J., Kim, J., Jeong, C., and Kim, W. J. (2016). Synergistic nanomedicine by combined gene and photothermal therapy. *Adv. Drug Deliv. Rev.* 98, 99–112. doi: 10.1016/j.addr.2015.12.018

Kim, K.-R., Jegal, H., Kim, J., and Ahn, D.-R. (2020). A self-assembled DNA tetrahedron as a carrier for *in vivo* liver-specific delivery of siRNA. *Biomater. Sci.* 8, 586–590. doi: 10.1039/C9BM01769K

Kim, K.-R., Kang, S. J., Lee, A. Y., Hwang, D., Park, M., Park, H., et al. (2019). Highly tumor-specific DNA nanostructures discovered by *in vivo* screening of a nucleic acid cage library and their applications in tumor-targeted drug delivery. *Biomaterials* 195, 1–12. doi: 10.1016/j.biomaterials.2018.12.026

Kim, K.-R., Lee, Y.-D., Lee, T., Kim, B.-S., Kim, S., and Ahn, D.-R. (2013). Sentinel lymph node imaging by a fluorescently labeled DNA tetrahedron. *Biomaterials* 34, 5226–5235. doi: 10.1016/j.biomaterials.2013.03.074

Kim, K. R., Kim, H. Y., Lee, Y.-D., Ha, J. S., Kang, J. H., Jeong, H., et al. (2016). Self-assembled mirror DNA nanostructures for tumor-specific delivery of anticancer drugs. *J. Control. Release* 243, 121–131. doi: 10.1016/j.jconrel.2016.10.015

Kim, Y., and Yin, P. (2020). Enhancing biocompatible stability of DNA nanostructures using dendritic oligonucleotides and brick motifs. *Angew Chem. Int. Ed.* 59, 700–703. doi: 10.1002/anie.201911664

Kiviaho, J. K., Linko, V., Ora, A., Tiainen, T., Järvihaavisto, E., Mikkilä, J., et al. (2016). Cationic polymers for DNA origami coating – examining their binding efficiency and tuning the enzymatic reaction rates. *Nanoscale* 8, 11674–11680. doi: 10.1039/C5NR08355A

Lacroix, A., Edwardson, T. G. W., Hancock, M. A., Dore, M. D., and Sleiman, H. F. (2017). Development of DNA nanostructures for high-affinity binding to human serum albumin. *J. Am. Chem. Soc.* 139, 7355–7362. doi: 10.1021/jacs.7b02917

Lee, D. S., Qian, H., Tay, C. Y., and Leong, D. T. (2016). Cellular processing and destinies of artificial DNA nanostructures. *Chem. Soc. Rev.* 45, 4199–4225. doi: 10.1039/C5CS00700C

Lee, H., Lytton-Jean, A. K. R., Chen, Y., Love, K. T., Park, A. I., Karagiannis, E. D., et al. (2012). Molecularly self-assembled nucleic acid nanoparticles for targeted *in vivo* siRNA delivery. *Nat. Nanotechnol.* 7, 389–393. doi: 10.1038/nnano.2012.73

Lee, J. B., Hong, J., Bonner, D. K., Poon, Z., and Hammond, P. T. (2012). Self-assembled RNA interference microsponges for efficient siRNA delivery. *Nat. Mater.* 11, 316–322. doi: 10.1038/nmat3253

Li, J., Pei, H., Zhu, B., Liang, L., Wei, M., He, Y., et al. (2011). Self-assembled multivalent DNA nanostructures for noninvasive intracellular delivery of immunostimulatory CpG oligonucleotides. *ACS Nano* 5, 8783–8789. doi: 10.1021/nn202774x

Li, S., Jiang, Q., Liu, S., Zhang, Y., Tian, Y., Song, C., et al. (2018). A DNA nanorobot functions as a cancer therapeutic in response to a molecular trigger *in vivo*. *Nat. Biotechnol.* 36, 258–264. doi: 10.1038/nbt.4071

Li, X., Yang, D., Shen, L., Xu, F., and Wang, P. (2019). Programmable assembly of DNA-protein hybrid structures. *Chem. Res. Chin. Univ.* 36, 211−218. doi: 10.1007/s40242-019-0038-x

Liang, L., Li, J., Li, Q., Huang, Q., Shi, J., Yan, H., et al. (2014). Single-particle tracking and modulation of cell entry pathways of a tetrahedral DNA nanostructure in live cells. *Angew Chem. Int. Ed.* 53, 7745–7750. doi: 10.1002/anie.201403236

Lv, H., Zhang, S., Wang, B., Cui, S., and Yan, J. (2006). Toxicity of cationic lipids and cationic polymers in gene delivery. *J. Control. Release* 114, 100–109. doi: 10.1016/j.jconrel.2006.04.014

Ma, R. I., Kallenbach, N. R., Sheardy, R. D., Petrillo, M. L., and Seeman, N. C. (1986). Three-arm nucleic acid junctions are flexible. *Nucleic Acids Res.* 14, 9745–9753. doi: 10.1093/nar/14.24.9745

Ma, Y., Wang, Z., Ma, Y., Han, Z., Zhang, M., Chen, H., et al. (2018). A telomerase-responsive DNA icosahedron for precise delivery of platinum nanodrugs to cisplatin-resistant cancer. *Angew Chem. Int. Ed.* 130, 5487–5491. doi: 10.1002/ange.201801195

Messaoudi, S., Greschner, A. A., and Gauthier, M. A. (2019). Progress toward absorption, distribution, metabolism, elimination, and toxicity of DNA nanostructures. *Adv. Ther.* 2:1900144. doi: 10.1002/adtp.201900144

Mirshafiee, V., Mahmoudi, M., Lou, K., Cheng, J., and Kraft, M. L. (2013). Protein corona significantly reduces active targeting yield. *ChemComm* 49, 2557–2559. doi: 10.1039/c3cc37307j

Mohsen, M. G., and Kool, E. T. (2016). The discovery of rolling circle amplification and rolling circle transcription. *Acc. Chem. Res.* 49, 2540–2550. doi: 10.1021/acs.accounts.6b00417

Munzar, J. D., Ng, A., and Juncker, D. (2019). Duplexed aptamers: history, design, theory, and application to biosensing. *Chem. Soc. Rev.* 48, 1390–1419. doi: 10.1039/C8CS00880A

Oh, J. Y., Kim, H. S., Palanikumar, L., Go, E. M., Jana, B., Park, S. A., et al. (2018). Cloaking nanoparticles with protein corona shield for targeted drug delivery. *Nat. Commun.* 9:4548. doi: 10.1038/s41467-018-06979-4

Ong, L. L., Hanikel, N., Yaghi, O. K., Grun, C., Strauss, M. T., Bron, P., et al. (2017). Programmable self-assembly of three-dimensional nanostructures from 10,000 unique components. *Nature* 552, 72–77. doi: 10.1038/nature24648

Pang, L., Zhang, C., Qin, J., Han, L., Li, R., Hong, C., et al. (2017). A novel strategy to achieve effective drug delivery: exploit cells as carrier combined with nanoparticles. *Drug Deliv.* 24, 83–91. doi: 10.1080/10717544.2016.1230903

Park-Windhol, C., and D'Amore, P. A. (2016). Disorders of vascular permeability. *Annu. Rev. Pathol.* 11, 251–281. doi: 10.1146/annurev-pathol-012615-044506

Parton, R. G., and Simons, K. (2007). The multiple faces of caveolae. *Nat. Rev. Mol.* 8, 185–194. doi: 10.1038/nrm2122

Pedersen, R. O., Kong, J., Achim, C., and LaBean, T. H. (2015). Comparative incorporation of PNA into DNA nanostructures. *Molecules* 20, 17645–17658. doi: 10.3390/molecules200917645

Perrault, S. D., and Shih, W. M. (2014). Virus-inspired membrane encapsulation of DNA nanostructures to achieve *in vivo* stability. *ACS Nano* 8, 5132–5140. doi: 10.1021/nn5011914

Ponnuswamy, N., Bastings, M. M. C., Nathwani, B., Ryu, J. H., Chou, L. Y. T., Vinther, M., et al. (2017). Oligolysine-based coating protects DNA nanostructures from low-salt denaturation and nuclease degradation. *Nat. Commun.* 8:15654. doi: 10.1038/ncomms15654

Rahman, M. A., Wang, P., Zhao, Z., Wang, D., Nannapaneni, S., Zhang, C., et al. (2017). Systemic delivery of Bc12-targeting siRNA by DNA nanoparticles suppresses cancer cell growth. *Angew Chem. Int. Ed.* 56, 16023–16027. doi: 10.1002/anie.201709485

Rajendran, A., Endo, M., Katsuda, Y., Hidaka, K., and Sugiyama, H. (2011). Photo-cross-linking-assisted thermal stability of DNA origami structures and its application for higher-temperature self-assembly. *J. Am. Chem. Soc.* 133, 14488–14491. doi: 10.1021/ja204546h

Raniolo, S., Vindigni, G., Unida, V., Ottaviani, A., Romano, E., Desideri, A., et al. (2018). Entry, fate and degradation of DNA nanocages in mammalian cells: a matter of receptors. *Nanoscale* 10, 12078–12086. doi: 10.1039/C8NR02411A

Reyes-Reyes, E. M., Teng, Y., and Bates, P. J. (2010). A new paradigm for aptamer therapeutic AS1411 action: uptake by macropinocytosis and its stimulation by a nucleolin-dependent mechanism. *Cancer Res.* 70, 8617–8629. doi: 10.1158/0008-5472.CAN-10-0920

Rothemund, P. W. (2006). Folding DNA to create nanoscale shapes and patterns. *Nature* 440, 297–302. doi: 10.1038/nature04586

Salahpour Anarjan, F. (2019). Active targeting drug delivery nanocarriers: ligands. *Nano Struct. Nano Obj.* 19:100370. doi: 10.1016/j.nanoso.2019.100370

Sanchez-Rueda, E. G., Rodriguez-Cristobal, E., Moctezuma González, C. L., and Hernandez-Garcia, A. (2019). Protein-coated dsDNA nanostars with high structural rigidity and high enzymatic and thermal stability. *Nanoscale* 11, 18604–18611. doi: 10.1039/C9NR05225A

Santi, M., Maccari, G., Mereghetti, P., Voliani, V., Rocchiccioli, S., Ucciferri, N., et al. (2017). Rational design of a transferrin-binding peptide sequence tailored to targeted nanoparticle internalization. *Bioconjug. Chem.* 28, 471–480. doi: 10.1021/acs.bioconjchem.6b00611

Savjani, K. T., Gajjar, A. K., and Savjani, J. K. (2012). Drug solubility: importance and enhancement techniques. *ISRN Pharmacol.* 2012, 195727–195727. doi: 10.5402/2012/195727

Schüller, V. J., Heidegger, S., Sandholzer, N., Nickels, P. C., Suhartha, N. A., Endres, S., et al. (2011). Cellular immunostimulation by CpG-sequence-Coated DNA origami structures. *ACS Nano* 5, 9696–9702. doi: 10.1021/nn203161y

Seeman, N. C. (1982). Nucleic acid junctions and lattices. *J. Theor. Biol.* 99, 237–247. doi: 10.1016/0022-5193(82)90002-9

Seeman, N. C. (2020). DNA nanotechnology at 40. *Nano Lett.* 20, 1477–1478. doi: 10.1021/acs.nanolett.0c00325

Seeman, N. C., and Sleiman, H. F. (2017). DNA nanotechnology. *Nat. Rev. Mater.* 3:17068. doi: 10.1038/natrevmats.2017.68

Setyawati, M. I., Kutty, R. V., and Leong, D. T. (2016). DNA nanostructures carrying stoichiometrically definable antibodies. *Small* 12, 5601–5611. doi: 10.1002/smll.201601669

Shangguan, D., Li, Y., Tang, Z. W., Cao, Z. H. C., Chen, H. W., Mallikaratchy, P., et al. (2006). Aptamers evolved from live cells as effective molecular probes for cancer study. *PNAS* 103, 11838–11843. doi: 10.1073/pnas.0602615103

Shin, S. W., Yuk, J. S., Chun, S. H., Lim, Y. T., and Um, S. H. (2020). Hybrid material of structural DNA with inorganic compound: synthesis, applications, and perspective. *Nano Converg* 7:2. doi: 10.1186/s40580-019-0211-4

Sindhwani, S., Syed, A. M., Ngai, J., Kingston, B. R., Maiorino, L., Rothschild, J., et al. (2020). The entry of nanoparticles into solid tumours. *Nat. Mater.* 19:566. doi: 10.1038/s41563-019-0566-2

Smith, S. A., Selby, L. I., Johnston, A. P. R., and Such, G. K. (2019). The endosomal escape of nanoparticles: toward more efficient cellular delivery. *Bioconjug. Chem.* 30, 263–272. doi: 10.1021/acs.bioconjchem.8b00732

Sun, D., and Gang, O. (2011). Binary heterogeneous superlattices assembled from quantum dots and gold nanoparticles with DNA. *J. Am. Chem. Soc.* 133, 5252–5254. doi: 10.1021/ja111542t

Sun, W., Jiang, T., Lu, Y., Reiff, M., Mo, R., and Gu, Z. (2014). Cocoon-like self-degradable DNA nanoclew for anticancer drug delivery. *J. Am. Chem. Soc.* 136, 14722–14725. doi: 10.1021/ja5088024

Surana, S., Bhatia, D., and Krishnan, Y. (2013). A method to study *in vivo* stability of DNA nanostructures. *Methods* 64, 94–100. doi: 10.1016/j.ymeth.2013.04.002

Taylor, A. I., Beuron, F., Peak-Chew, S.-Y., Morris, E. P., Herdewijn, P., and Holliger, P. (2016). Nanostructures from synthetic genetic polymers. *Chembiochem* 17, 1107–1110. doi: 10.1002/cbic.201600136

Tian, T., Li, J., Xie, C., Sun, Y., Lei, H., Liu, X., et al. (2018). Targeted imaging of brain tumors with a framework nucleic acid probe. *ACS Appl. Mater. Interfaces* 10, 3414–3420. doi: 10.1021/acsami.7b17927

Vindigni, G., Raniolo, S., Ottaviani, A., Falconi, M., Franch, O., Knudsen, B. R., et al. (2016). Receptor-mediated entry of pristine octahedral DNA nanocages

in mammalian cells. *ACS Nano* 10, 5971–5979. doi: 10.1021/acsnano.6b01402

Wang, B., He, X., Zhang, Z., Zhao, Y., and Feng, W. (2013). Metabolism of nanomaterials *in vivo*: blood circulation and organ clearance. *Acc. Chem. Res.* 46, 761–769. doi: 10.1021/ar2003336

Wang, P., Rahman, M. A., Zhao, Z., Weiss, K., Zhang, C., Chen, Z., et al. (2018). Visualization of the cellular uptake and trafficking of DNA origami nanostructures in cancer cells. *J. Am. Chem. Soc.* 140, 2478–2484. doi: 10.1021/jacs.7b09024

Wang, P., Wu, S., Tian, C., Yu, G., Jiang, W., Wang, G., et al. (2016). Retrosynthetic analysis-guided breaking tile symmetry for the assembly of complex DNA nanostructures. *J. Am. Chem. Soc.* 138, 13579–13585. doi: 10.1021/jacs.6b06074

Wang, P. F., Meyer, T. A., Pan, V., Dutta, P. K., and Ke, Y. G. (2017). The beauty and utility of DNA origami. *Chem* 2, 359–382. doi: 10.1016/j.chempr.2017.02.009

Wang, X., and Seeman, N. C. (2007). Assembly and characterization of 8-arm and 12-arm DNA branched junctions. *J. Am. Chem. Soc.* 129, 8169–8176. doi: 10.1021/ja0693441

Wang, Y. L., Mueller, J. E., Kemper, B., and Seeman, N. C. (1991). Assembly and characterization of five-arm and six-arm DNA branched junctions. *Biochemistry* 30, 5667–5674. doi: 10.1021/bi00237a005

Wei, B., Dai, M., and Yin, P. (2012). Complex shapes self-assembled from single-stranded DNA tiles. *Nature* 485, 623–626. doi: 10.1038/nature11075

Wilhelm, S., Tavares, A. J., Dai, Q., Ohta, S., Audet, J., Dvorak, H. F., et al. (2016). Analysis of nanoparticle delivery to tumours. *Nat. Rev. Mater.* 1:16014. doi: 10.1038/natrevmats.2016.14

Wu, C., Han, D., Chen, T., Peng, L., Zhu, G., You, M., et al. (2013). Building a multifunctional aptamer-based DNA nanoassembly for targeted cancer therapy. *J. Am. Chem. Soc.* 135, 18644–18650. doi: 10.1021/ja4094617

Xia, Z., Wang, P., Liu, X., Liu, T., Yan, Y., Yan, J., et al. (2016). Tumor-penetrating peptide-modified DNA tetrahedron for targeting drug delivery. *Biochemistry* 55, 1326–1331. doi: 10.1021/acs.biochem.5b01181

Yan, H., Park, S. H., Finkelstein, G., Reif, J. H., and LaBean, T. H. (2003). DNA-templated self-assembly of protein arrays and highly conductive nanowires. *Science* 301, 1882–1884. doi: 10.1126/science.1089389

Yang, Y., Wang, J., Shigematsu, H., Xu, W., Shih, W. M., Rothman, J. E., et al. (2016). Self-assembly of size-controlled liposomes on DNA nanotemplates. *Nat. Chem.* 8, 476–483. doi: 10.1038/nchem.2472

Yin, P., Yan, H., Daniell, X. G., Turberfield, A. J., and Reif, J. H. (2004). A Unidirectional DNA walker that moves autonomously along a track. *Angew Chem. Int. Ed.* 43, 4906–4911. doi: 10.1002/anie.200460522

Yurke, B., Turberfield, A. J., Mills, A. P., Simmel, F. C., and Neumann, J. L. (2000). A DNA-fuelled molecular machine made of DNA. *Nature* 406, 605–608. doi: 10.1038/35020524

Zhang, Q., Jiang, Q., Li, N., Dai, L., Liu, Q., Song, L., et al. (2014). DNA origami as an *in vivo* drug delivery vehicle for cancer therapy. *ACS Nano* 8, 6633–6643. doi: 10.1021/nn502058j

Zhang, R., Qin, X., Kong, F., Chen, P., and Pan, G. (2019). Improving cellular uptake of therapeutic entities through interaction with components of cell membrane. *Drug Deliv.* 26, 328–342. doi: 10.1080/10717544.2019.1582730

Zhang, Y., Pan, V., Li, X., Yang, X., Li, H., Wang, P., et al. (2019). Dynamic DNA structures. *Small* 15:1900228. doi: 10.1002/smll.201900228

Zhang, Y., and Seeman, N. C. (1994). Construction of a DNA-truncated octahedron. *J. Am. Chem. Soc.* 116, 1661–1669. doi: 10.1021/ja00084a006

Zhao, H., Yuan, X., Yu, J., Huang, Y., Shao, C., Xiao, F., et al. (2018). Magnesium-stabilized multifunctional DNA nanoparticles for tumor-targeted and pH-responsive drug delivery. *ACS Appl. Mater. Interfaces* 10, 15418–15427. doi: 10.1021/acsami.8b01932

Zhao, S., Duan, F., Liu, S., Wu, T., Shang, Y., Tian, R., et al. (2019). Efficient intracellular delivery of RNase A using DNA origami carriers. *ACS Appl. Mater. Interfaces* 11, 11112–11118. doi: 10.1021/acsami.8b21724

Zhao, Y.-X., Shaw, A., Zeng, X., Benson, E., Nyström, A. M., and Högberg, B. (2012). DNA origami delivery system for cancer therapy with tunable release properties. *ACS Nano* 6, 8684–8691. doi: 10.1021/nn3022662

Zhao, Z., Ukidve, A., Krishnan, V., and Mitragotri, S. (2019). Effect of physicochemical and surface properties on *in vivo* fate of drug nanocarriers. *Adv. Drug Deliv. Rev.* 143, 3–21. doi: 10.1016/j.addr.2019.01.002

Zheng, J., Birktoft, J. J., Chen, Y., Wang, T., Sha, R., Constantinou, P. E., et al. (2009). From molecular to macroscopic via the rational design of a self-assembled 3D DNA crystal. *Nature* 461, 74–77. doi: 10.1038/nature08274

Conflict of Interest: The authors declare that the research was conducted in the absence of any commercial or financial relationships that could be construed as a potential conflict of interest.

frontiers in Chemistry

MINI REVIEW
published: 23 October 2020
doi: 10.3389/fchem.2020.573297

Advanced Nanovehicles-Enabled Delivery Systems of Epigallocatechin Gallate for Cancer Therapy

Kai Li[1,2], *Chao Teng*[1]* *and Qianhao Min*[2]*

[1] Shenzhen Polytechnic, Institute of Marine Biomedicine, Shenzhen, China, [2] State Key Laboratory of Analytical Chemistry for Life Science, School of Chemistry and Chemical Engineering, Nanjing University, Nanjing, China

Epigallocatechin gallate (EGCG) is the most abundant polyphenolic constituent derived from green tea extract, which has demonstrated versatile bioactivities in combating cardiovascular diseases, neurodegenerative diseases, diabetes, and cancer. In light of its anticancer activity, increasing attention has been paid to developing potent strategies involving EGCG in cancer chemotherapy. However, the poor bioavailability and stability of EGCG limits its effectiveness and practicality in real biomedical applications. To overcome this drawback, nanotechnology-facilitated drug delivery systems have been introduced and intensively explored to enhance the bioavailability and therapeutic efficacy of EGCG in cancer treatments and interventions. This review briefly discusses the anticancer mechanisms of EGCG, and then summarizes recent advances in engineering nanovehicles for encapsulating and delivering EGCG toward cancer therapy. In addition, we also highlight successful integrations of EGCG delivery with other chemotherapies, gene therapies, and phototherapies in one nanostructured entity for a combination therapy of cancers. To conclude, the current challenges and future prospects of the nanovehicle-based transportation systems of EGCG for cancer therapy are also discussed.

Keywords: EGCG, cancer, nanovehicles, drug delivery systems, combination therapy

OPEN ACCESS

Edited by:
Fang Liu,
Guangzhou University of Chinese Medicine, China

Reviewed by:
Hang Xing,
Hunan University, China
Jinping Wang,
University of Jinan, China

***Correspondence:**
Chao Teng
tengchao@szpt.edu.cn
Qianhao Min
minqianhao@nju.edu.cn

Specialty section:
This article was submitted to Nanoscience, a section of the journal Frontiers in Chemistry

Received: *16 June 2020*
Accepted: *24 August 2020*
Published: *23 October 2020*

Citation:
Li K, Teng C and Min Q (2020) Advanced Nanovehicles-Enabled Delivery Systems of Epigallocatechin Gallate for Cancer Therapy. Front. Chem. 8:573297. doi: 10.3389/fchem.2020.573297

INTRODUCTION

Natural products hold great potential in the fields of biomedical research, drug development, and clinical application, as they can serve as medicinal sources for the treatment of cancer, bacterial and fungal infections, inflammation, and other diseases (Mignani et al., 2018). Particularly, the superior biocompatibility, broad spectrum of biological activity, and specifically targeted effects of these compounds make them potent cancer chemoprevention and chemotherapy agents with minimal side effects (Cragg et al., 2009; Spradlin et al., 2019). Moreover, these abundant and widely varied sources can reduce the cost of cancer treatment. Epigallocatechin gallate (EGCG) is known as the most biologically active catechin derived from green tea extracts. Benefiting from the eight free hydroxyl groups in its flavone-3-ol phenolic structure (**Figure 1**), EGCG demonstrates unique merits in free radical scavenging, accounting for its biological functions in biomedicine (antioxidation, anti-inflammatory, reduction of blood lipids, and sugar, etc.) (Cai et al., 2006; Chakrawarti et al., 2016). Since the recognition of its anticancer effects, EGCG has in recent years been intensively investigated as a star phytochemical for regulating or inhibiting the physiological changes during canceration (Singh et al., 2011; Granja et al., 2016; Gan et al., 2017).

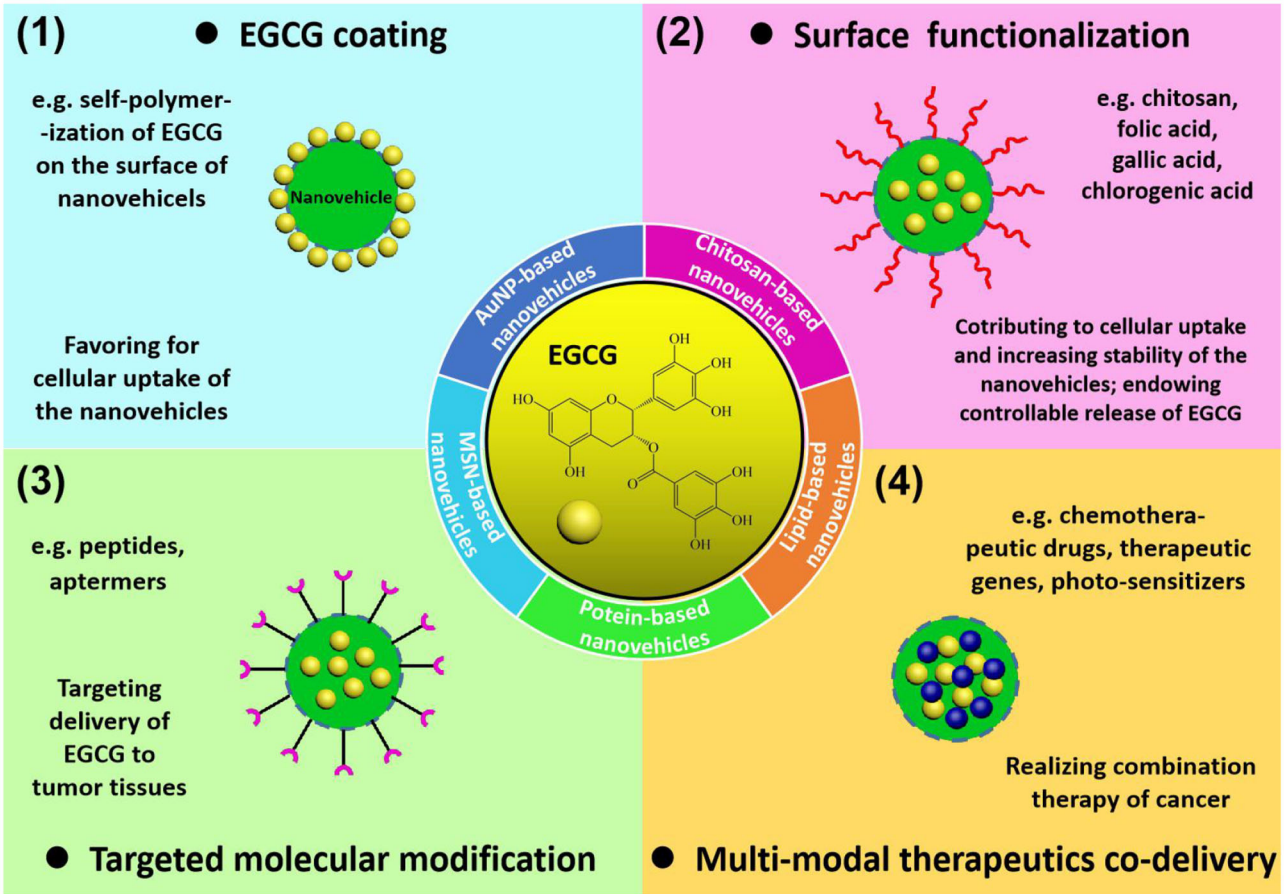

FIGURE 1 | Summary of EGCG delivery systems: (1) grafting EGCG on the surface of the nanoparticles to enhance cellular uptake of as-obtained nanovehicles; (2) surface functionalization with specific molecules (chitosan, folic acid, gallic acid, and chlorogenic acid) to enhance stability, cellular uptake, and drug release properties of the nanovehicles; (3) targeted molecular modification by peptides or aptamers to target specific cancer cell receptors; (4) construction of multi-modal therapeutics co-delivery systems to realize EGCG-involved cancer combination therapy.

According to previous literature, the anticancer mechanism of EGCG involves many pathways. Specifically, the tumor suppressive behavior of EGCG through pro-oxidative effects is based on covalent binding of EGCG with antioxidants such as glutathione (GS), then producing a certain amount of reactive oxygen species (ROS) to activate the pro-oxidative signaling pathways (Shankar et al., 2012) and induce apoptosis of tumor cells (Li et al., 2010). EGCG can also target a variety of cancer-related membrane receptors (Singh and Katiyar, 2013) or nucleus signaling receptors (Shankar et al., 2012) and down regulate or inhibit their abnormal expression, therefore inhibiting the proliferation and metastasis of tumor cells. Evidence also shows that EGCG modulates signaling cascades to induce programmed cell death through activating protein kinases (Zhu et al., 2017). Additionally, suppression of vascular endothelial growth factor (VEGF) (Wang J. et al., 2018), eliminations of cancer stem cell (CSC)-characteristics (Xia and Xu, 2015), and down-regulation of telomerase (Sadava et al., 2007; Berletch et al., 2008) have been proposed to be involved in the curative mechanisms of EGCG.

In view of its anticancer activity, EGCG has been exploited as a potent chemotherapeutic agent for various cancers. However, the poor bioavailability and stability of EGCG restricts its clinical applications. As shown by Nakagawa and Miyazawa (1997) the maximum concentration of EGCG is calculated as 0.32% of ingested EGCG in human plasma through oral administration, which is too low to exhibit ideal efficacy. The methylation, glucuronidation, sulfation, and oxidative degradation of EGCG during its metabolic process further weakened its efficacy. Therefore, it is essential to develop novel drug delivery systems that enhance the stability and bioavailability of EGCG, thus ensuring the effective concentration and bioactivity *in vivo* (Yang et al., 2019). As the use of nanotechnology-facilitated biomedicine in the past decades has flourished, encapsulating EGCG within nanovehicles has been adopted by many researchers (Granja et al., 2016; Ye and Augustin, 2018). The protection imparted by nanovehicles allowed the isolation of entrapped EGCG from the outer physiological conditions, thus avoiding the probable compositional and structural change

TABLE 1 | Summary of gold-, mesoporous silica-, lipid-, chitosan-, and protein-based EGCG delivery systems.

EGCG nano- delivery system	Synthetic method	Particle size (nm)	Encapsulation efficiency (%)	Release of EGCG	Cell lines/animal models	Achievement	References
Gold nanoparticles-based EGCG delivery systems							
EGCG-AuNPs	Reduction of sodium tetrachloro aurate by EGCG	20–40	—	—	PC-3 cells	EGCG-AuNPs internalize selectively within PC3 cells providing threshold concentrations required for photoacoustic signals.	Viator et al., 2010
EGCG-gold nanoparticles (E-GNPs)	Reduction of $HAuCl_4 \cdot 3H_2O$ by EGCG	25	0.235 (w/w)	42.9% (37°C, 48 h)	A375SM, MDA-MB-231, MIA PaCa, and PC-3 cells	E-GNPs can effectively inhibit the nuclear translocation and transcriptional activity of nuclear factor-kappaB (NF-κB) and induce apoptosis in cancer cells.	Chavva et al., 2019
EGCG-radioactive gold (^{198}AuNPs) nanoparticles	Reduction of $H^{198}AuCl_4 \cdot 3H_2O$ by EGCG	15–40	—	—	PC-3 xenograft SCID mice	The ability of EGCG to target laminin receptor (67LR) leads to the internalization of EGCG-^{198}AuNPs into prostate tumor cells, increasing the radiotherapeutic effect of ^{198}AuNPs in reducing tumor volumes.	Shukla et al., 2012
EGCG-pNG particles	EGCG and pNG were physically mixed via ultrasonication	50	27	36.2% (36°C, pH 1.2, 0.5 h)	MBT-2 tumor cells and female C3H/He mice	EGCG-pNG mediated tumor apoptosis was demonstrated to involve activation of the caspase cascade, via the Bcl-family proteins, of the mitochondrial pathway.	Hsieh et al., 2012
EGCG-physical nanogold (pNG) particles	EGCG and pNG were physically mixed via ultrasonication	64.7–127.4	29	—	murine B16F10 melanoma cells and C57/BL6 mouse model	The combined EGCG-pNG exerts an improved effect in inhibiting the growth of B16F10 melanoma cells through cell apoptosis.	Chen C. C. et al., 2014
Mesoporous silica-based EGCG delivery systems							
Colloidal mesoporous silica (CMS)- EGCG	CMS was dipped in EGCG solution for loading EGCG	50	66	—	HeLa cells	CMS inhibited the collision of EGCG radicals, prolonged the half-life of EGCG, and improved the therapeutic effect of EGCG via inducing cell apoptosis by increasing H_2O_2 production.	Ding et al., 2012
CMS@PEGA- pVEC peptide@ EGCG	CMS@peptide was dipped in EGCG solution for loading EGCG	100	—	23% (pH 7.4, 20 h, room temperature	MCF-7 cells and MCF-7 tumor-bearing mice	EGCG induces apoptosis of MCF-7 cancer cells and reduces the change of apoptosis-related proteins with no damage to normal tissue.	Ding et al., 2015
Lipid-based EGCG delivery systems							
EGCG loaded solid lipid nanoparticles (EGCG-SLN)	Emulsion-solvent evaporation method	157	67.2	83.9% (37°C, pH 5, 12 h)	MDA-MB 231 and DU-145 cells	EGCG-SLN caused an 8.1-fold increase in cytotoxicity of EGCG against MDA-MB-231 and 3.8 times increase against DU-145.	Radhakrishnan et al., 2016
EGCG-SLN;	High shear homogenization and ultrasonication technique	364 ± 11	83	40% (37°C, pH 1.2, 24 h)	Caco-2 cells	Both SLN and NLC were successfully developed for EGCG protection and stabilization and can be a useful platform for the enhancement of EGCG bioavailability.	Frias et al., 2016
Folic acid-functionalized EGCG-loaded NLC	High shear homogenization and ultrasonication technique	300	90	—	Caco-2 cells	Folic acid functionalization of EGCG-loaded lipid NPs can successfully increase its transport across the intestinal Barrier.	Granja et al., 2019
Chitosan-based EGCG delivery systems							
EGCG-loaded chitosan-gellan gum bipolymeric nanohydrogels	Ionotropic gelation and polyelectrolyte complexation technique	250	91.85	53.4% (pH 7.4, 24 h)	P. aeruginosa, *E. coli*, B. subtilis and *S. aureus*	EGCG-loaded nanohydrogels displayed sustained drug release and better antibacterial, antioxidant activity.	Dahiya et al., 2017

(Continued)

TABLE 1 | Continued

EGCG nano- delivery system	Synthetic method	Particle size (nm)	Encapsulation efficiency (%)	Release of EGCG	Cell lines/animal models	Achievement	References
Chitosan nanoparticles encapsulating EGCG (Chit-nanoEGCG)	Sonication and dialysis method	150–200	—	10% (simulated gastric juice, 24 h); 50% (simulated intestinal fluid, 24 h)	22Rv1 cells and ahymic nude mice	Chit-nanoEGCG led to sustained release of EGCG, inducing poly (ADP-ribose) polymerases cleavage; increasing protein expression of Bax with concomitant decrease in Bcl-2; activating caspases, reducing Ki-67 and proliferating cell 150 nuclear antigen.	Khan et al., 2013
Folate conjugated chitosan coated EGCG nanoparticles (FCS-EGCG-NPs)	Ionic cross-linking method	400	75	—	HeLa, H1299 and Capan-1 cells	FCS-EGCG-NPs had a greater tumor inhibition effect on cancer cells having a large expression of folic acid receptors on the surface.	Liang et al., 2014
Protein-based EGCG delivery systems							
β-lactoglobulin (β-Lg)-EGCG nanoparticles	Thermally-induced protein-EGCG co-assemblies	—	58.6 ± 6.8	25% (37°C, 180 min)	—	The very limited release from β-Lg-EGCG nanoparticles during simulated gastric digestion made it a potential enteric carrier for polyphenols.	Shpigelman et al., 2012
EGCG-β-Lg nanoparticles (Eβ-NPs)	Thermally-induced protein-EGCG co-assemblies	31.3 ± 0.62	59.2	—	FACS. A375 and TE-1 cells	The Eβ-NPs possessed better bioactivity than native EGCG with respect to the proliferative inhibition of cancer cells.	Wu et al., 2017
β-Lg, 3-mercapto-1-hexanol (3MH) and EGCG co-assembled nanocomplexes (MEβ-NPs)	Thermally-Induced protein-EGCG co-assemblies	28.4–32.3	50.2–60.8	62.0% (37°C, 24 h)	A375, Hep G2 and TE-1 cells	Antioxidant capacity, absorbability and bioavailability of EGCG in MEβ-NPs was improved, exhibiting greater stability, sustained release and anticancer effects *in vitro* and *in vivo* than free EGCG.	Yang Y. et al., 2017
EGCG-loaded β-lactoglobulin (BLG)–chlorogenic acid (CA) conjugates	Free radical method	105–110	71.8% [BLG-CA (low)]; 73.5% [BLG-CA (high)]	34.5% (pH 7.4, 6 h)	—	BLG-CA (high) showed higher inhibition of EGCG release than BLG-CA (low), suggesting that CA exhibited inhibition for digestive enzymes in intestinal stage.	Fan et al., 2017
Ferritin-chitosan Maillard reaction products (FCMPs)-EGCG complexes	EGCG solution was dripped into FCMPs solution for EGCG encapsulating	7.5	12.87 (w/w)	75.6% (simulated gastric fluid, 160 min)	Caco-2 monolayer model	The glycosylated ferritin retained its shell-like structure and can protect the encapsulated EGCG in simulated gastrointestinal tract. The ferritin-chitosan double shells can improve the absorption of encapsulated EGCG in Caco-2 monolayer model.	Yang R. et al., 2017

of the bioactive chemical cargo. Further, nanovehicles featuring high drug loading, targeted drug transportation, and site-specific drug release significantly improved the bioavailability of EGCG with sufficient concentrations in the lesions, making the precise treatment of cancer possible. To further augment the therapeutic outcomes, the combination of EGCG-dominated chemotherapy with other chemicals (Hu et al., 2015; Zhou et al., 2016), therapeutic genes (Ding et al., 2018; Liang et al., 2018), and photothermal agents or photosensitizers (Mun et al., 2014; Qi et al., 2014) has received numerous successes in boosting efficacy and minimizing drawbacks in cancer treatments. This article mainly focuses on recent advances in engineering nanovehicles for EGCG encapsulation and delivery for precise and efficient cancer therapy. Moreover, endeavors devoted to integrating EGCG-involved chemotherapy with other chemical curative agents, therapeutic genes, and phototherapeutic components in a single nanovehicle for elevating the overall potency are also overviewed.

EGCG DELIVERY SYSTEMS ENABLED BY NANOVEHICLES FOR CANCER THERAPY

The construction of EGCG-loaded nanovehicles has been generally recognized to enhance the stability and bioavailability of EGCG, exhibiting great potential for practical applications in cancer chemoprevention and chemotherapy. Numerous nanomaterials, including gold nanoparticles, mesoporous silica

nanostructures, chitosan nanoparticles, lipid nanoparticles, and protein nanoassemblies, can serve as carriers for delivering EGCG to tumor tissues, while the delivery efficiency is highly dependent on the morphological and surface characteristics of nanovehicles (**Figure 1**). The physiological stability and cellular uptake of nanovehicles in tumor sites relies on the composition, dimension, outer surface chemistry, and electrostatics of the drug-loaded nanoparticles. In addition, targeted delivery and controllable release of the entrapped therapeutic agents is determined by engineering of nanovehicles with recognition ligands and bioresponsive species. In this section, the nanovehicles for EGCG transportation differing in building components, surface functionalities, drug release mechanisms, and biomedical uses are elucidated in detail. The main characteristics of nanostructure-based EGCG delivery systems for cancer treatments are summarized in **Table 1**.

Gold Nanoparticles-Based EGCG Delivery Systems

AuNPs-enabled drug delivery systems for cancer chemotherapy have been intensively studied due to their high surface to volume ratio and controllable functionalized surface, which are favorable properties in drug loading and delivery. To date, AuNPs-based EGCG delivery systems have been substantially explored in cancer diagnosis and therapy. Previous research revealed that reduction of Au^{3+} by EGCG offered a promising synthetic route of Au nanoparticles with an EGCG-grafted surface (Viator et al., 2010; Shukla et al., 2012; Chavva et al., 2019), which is contributive to improving uptake by tumor cells. Moreover, the radioactive gold source ($H^{198}AuCl_4$) enables a radiotherapeutic effect of EGCG-^{198}AuNPs in killing prostate tumor cells (Shukla et al., 2012). The mixing of EGCG and physical nanogold (pNG) particles is also an effective method for coating EGCG on AuNPs with a prolonged half-life (110 days) (Hsieh et al., 2012). The anti-tumor mechanism of EGCG-pNG is attributed to the mitochondrial pathway-mediated apoptosis, demonstrating a 1.66-fold higher inhibition ratio than free EGCG (Chen C. C. et al., 2014).

Mesoporous Silica-Based EGCG Delivery Systems

Mesoporous silica nanoparticles (MSNs), with controllable size, ordered porosity, high internal surface area, and easily modified surfaces, have been widely applied for the construction of drug delivery systems. The high corrosion resistance of MSN under physiological conditions provides protection for the encapsulated drugs from degradation before reaching the tumor sites. The high biocompatibility of MSN with negligible cytotoxicity also makes it a safe drug carrier that can be eliminated through renal clearance (Chen et al., 2013; Li et al., 2017). According to a previous study (Ding et al., 2012), MSN can adsorb EGCG through electrostatic attraction and inhibit the collision of EGCG radicals, thus prolonging the half-life of EGCG. Our group further introduced a breast-tumor-homing cell-penetrating peptide onto the EGCG-loaded MSN for the targeted accumulation and release of EGCG in MCF-7 cells (Ding et al., 2015).

Lipid-Based EGCG Delivery Systems

Nanocapsules with lipids in the matrix could improve their biocompatibility. The high encapsulation efficiency and controlled-release from lipid-based nanovehicles maintain the prolonged efficacy of entrapped drugs. Solid lipid nanoparticles (SLN) consisting of glycerol monostearate, stearic acid, and soya lecithin were used as stealth vehicles for efficient EGCG delivery due to their high biocompatibility, while the erosion or metabolization of lipids led to the sustained release of EGCG (Radhakrishnan et al., 2016). In comparison with SLN, nanostructured lipid carriers (NLC) that consisted of both solid (Precirol® ATO) and liquid (miglyol-812) lipids showed higher encapsulation efficiency (90%) and stability during long-term storage (Frias et al., 2016). Moreover, more than 60% of encapsulated EGCG remains in the nanovehicles after contact with simulated gastric and intestinal fluids for 4 h, indicating the feasibility of EGCG-NLC for oral administration. On this basis, folic acid is introduced to make it easier for NLC-based nanovehicles to transport across the intestinal barrier (Granja et al., 2019).

Chitosan-Based EGCG Delivery Systems

As mentioned above, chitosan can serve as a surface modification agent to increase cellular uptake and conduct on-demand drug release, due to its biocompatibility and biodegradability. In addition, cross-linking agents or other structural promoters were combined in these dose forms to prevent chitosan capsules from burst breaking in acidic medium and ensure its applicability as drug carriers in oral administration. Gellan gum with high resistance to heat and acidic media was employed to construct chitosan-gellan gum bipolymeric nanohydrogels for oral EGCG delivery (Dahiya et al., 2017). The interaction between $-NH_2$ in chitosan and phosphate in pentasodium tripolyphosphate hexahydrate can also enhance the stability of EGCG-entrapped chitosan nanoparticles (Khan et al., 2013). Moreover, folic acid is introduced via the ionic gelation method for targeted EGCG delivery toward cancer cells with overexpressed folic acid receptors (Liang et al., 2014).

Protein-Based EGCG Delivery Systems

Proteins are effective nanocarriers for drug delivery systems since these renewable biomacromolecules exhibit a high drug-binding capacity with low cytotoxicity, which can also target tumor cells effectively due to the specific recognition of the receptors on tumor cell membranes. Moreover, proteins with a unique structure provide specific binding sites for EGCG, thus further enhancing the stability of encapsulated EGCG in comparison with other nanovehicles (Yang R. et al., 2017). Thermally-induced protein-EGCG co-assembly is a widely used strategy for constructing β-lactoglobulin (β-Lg)-based EGCG delivery systems with encapsulation efficiencies between 50 and 60% (Shpigelman et al., 2012; Wu et al., 2017; Yang Y. et al., 2017). The limited release (25%) of EGCG in acidic medium (pH 2, 37°C, 3 h) demonstrates the protection of β-Lg nanocapsules

for EGCG from gastric digestion and oxidative degradation (Shpigelman et al., 2012). Moreover, the intestinal absorption of β-Lg-EGCG nanoparticles (< 50 nm), followed by the sustained release of EGCG in neutral physiological conditions, ensures the high bioavailability of EGCG for cancer therapy. Conjugation of β-Lg with chlorogenic acid (CA) is another route to isolate the protein-based nanovehicles from enzymatic digestion, resulting in the limited premature release of EGCG during the delivery process (Fan et al., 2017).

In comparison with inorganic nanovehicles (Au NPs and MSN, etc.), organic nanocarriers based on nanolipids, chitosan, and proteins possess a higher encapsulation efficiency and exhibit the controllable release of EGCG. The superior biocompatibility with an easier-to-functionalize surface also makes it possible for targeted delivery and enhanced intercellular accumulation of EGCG. However, the relatively low stability restricts their application for EGCG delivery through oral administration where burst breaking or biodegradation can occur in digestive fluids, resulting in the pre-release and structural change of entrapped EGCG. Therefore, recent research is mainly focused on exploring biomolecule-based nanoplatforms with well-defined nanostructures and sufficient stability for EGCG delivery.

COMBINATION THERAPY BY EGCG-LOADED NANOVEHICLES

Although a range of EGCG-nanovehicles have contributed to the success in maintaining chemical structure integrity and increasing delivery efficiency, nanovehicle-enabled EGCG delivery for single-drug therapy is still suboptimal due to its inherent defects in pharmacological activities. To upgrade the curative effects of EGCG-involved therapy, it is of great importance to integrate multiple therapeutic approaches actuated by diverse rationales. On the other hand, considering side effects or drug resistance in the medication by conventional chemotherapeutics, gene therapeutics, and photosensitizers, introducing EGCG in the formulation would offer the possibility of boosting the therapeutic efficacy. Nanostructured drug carriers offer a versatile scaffold for the integration of EGCG with other therapeutic agents featuring chemotherapy, gene therapy, and phototherapy in a collaborative manner, rendering combination treatment more effective in curing various cancers. Here, we reviewed the recent progresses made in cancer combination therapy that encompass EGCG and therapeutic agents with different functions, and highlighted the advantages of EGCG-involved co-delivery nanovehicles.

Combination With Other Chemical Drugs

Multidrug resistance (MDR) is one of the major problems facing cancer chemotherapy due to the expression of energy-dependent drug efflux pumps on the plasma membrane. Moreover, side effects induced by anticancer drugs are another formidable factor that cause damage to normal tissues during cancer treatment. As is already known, EGCG is a promising candidate that can overcome the drawbacks of conventional chemotherapeutic agents and enhance their anticancer capabilities. The integration of EGCG and DOX is currently the most in-depth studied EGCG-involved binary therapeutic system. As reported by Yao et al. (2017), DOX-induced cardiotoxicity can be suppressed by EGCG via upregulating the expression of mitochondrial membrane potential and manganese superoxide dismutase. Moreover, EGCG can also ameliorate DOX-evoked oxidative stress injury and activate the ErbB2-involved pro-survival pathway (Saeed et al., 2015). Remarkably, the efficient interaction between EGCG and DOX leads to the high encapsulation efficiency of DOX (88%) within PEG-EGCG micellar nanocomplexes, improving blood circulation stability and tumor targeting ability of DOX while minimizing its dose-dependent side effects (Liang et al., 2018). In the orchestration of EGCG and DOX, EGCG was reported to inhibit the activity of MMP-2 and MMP-9 that are increased in MCF7/DOX cells, thus sensitizing them to DOX and reducing their metastatic potential (Stearns et al., 2010; Nowakowska and Tarasiuk, 2016). Moreover, the pro-survival autophagy of tumor cells can also be reduced by EGCG through targeting and decreasing autophagy signaling induced by DOX treatment, therefore improving the efficacy of DOX (Chen L. et al., 2014; Wang W. et al., 2018).

Combination With Gene Therapy

Gene therapy is achieved by counteracting or replacing a malfunctioning gene within the cells, and exhibits great potential to treat various cancers at their genetic roots (Naldini, 2015). In particular, the sequence-specific gene silencing induced by RNA interference (RNAi) can modulate the immune response, regulate the cell cycle, inhibit the overexpressed oncogenes, induce apoptosis of tumor cells, and has anti-angiogenesis effect, which can also amplify the efficacy of chemotherapeutic agents. Recently, the enhanced therapeutic efficacy derived from the integration of EGCG and therapeutic genes has caught great attention. It has been confirmed that 28 genes related to the pro-apoptotic (activate) and pro-survival (inhibit) of Hs578T cells are altered by the combination treatment of EGCG and p53siRNA (Braicu et al., 2015). The integration of specific siRNA and EGCG can also reverse the drug resistance of tumor cells to conventional chemotherapy agents such as tamoxifen (Esmaeili, 2015). Based on investigations at the cellular level, nanovehicles were developed for co-delivering therapeutic genes and EGCG to realize the combined treatment of cancer *in vivo*. As reported by Ding et al. (2018), siRNA and EGCG are self-assembled to form a stealth nanovehicle using protamine as the assembly skeleton, which can accommodate the two therapeutic agents and minimize side effects. In addition, the as-obtained nanovehicles modified with hyaluronic acid and tumor-homing cell-penetrating peptide demonstrated superior selectivity toward drug-resistant MDA-MB-231 cell lines with marked enhancement in cytotoxicity, which is 15 times greater than free EGCG.

Combination With Phototherapy

Photodynamic therapy (PDT) is an emerging cancer treatment strategy based on the photochemical reactions aroused by photosensitizers, which can produce ROS with high cytotoxicity under irradiation at specific wavelengths, thereby inducing

apoptosis of tumor cells and causing damage to tumor tissues. The superposition of EGCG-dominated chemotherapy and PDT in a single nanostructured entity provides a practical approach to enhance cancer therapeutic efficacy. The synergism of PDT (Radachlorin, 662 nm laser) and EGCG via intratumoral injection leads to the increased expression of primary antibodies, such as p21, p53, Bax, and PARP, causing significant enhancement in TC-1 tumor cell growth inhibition compared to PDT or EGCG-involved therapy alone (Mun et al., 2014). In addition, the irradiation of pulsed laser light can in turn contribute to transmembrane convection of EGCG by modulating the nanostructure of water layers in tumor cells (Sommer et al., 2011). In view of the synergism between EGCG and PDT, the photoreponsive nanovehicles are in great demand for EGCG delivery and release. However, related research is still rare. Notably, DOX-loaded EGCG-Fe(III) networks have been demonstrated to realize chemo- and photothermal therapy (PTT) simultaneously (Chen et al., 2019). Specifically, the photothermal capability of EGCG-Fe(III) networks under near-infrared irradiation cause damage to HT-29 cells through hyperthermia, thus reinforcing the chemotherapy efficacy of DOX in inducing tumor cell apoptosis and eventually ablating the solid tumor completely. Anisotropic gold nanostructures with fascinating photothermal properties can act as nanocarriers for delivering therapeutic molecules, but their uses in EGCG loading for chemo-photothermal combination therapy are still seldom reported. The recruitment of anisotropic gold nanostructures is a promising complement to EGCG for improving cancer therapy efficacy.

CONCLUSIONS

This review summarizes the achievements of various popular nanovehicles for EGCG delivery *in vitro* and *in vivo*. The recent progresses showed that nanovehicles designed with structural characteristics and surface functionalities allowed targeted delivery and controllable release of EGCG with enhanced stability and bioavailability. However, clinical applications of these EGCG-containing nanoplatforms are still limited. The chemically stable AuNPs and MSNs suffered severe accumulation in the liver and spleen, potentially causing toxicity to the human body. Meanwhile, the biodegradation of organic nanoparticles (e.g., nanolipid-based, chitosan-based, and protein-based nanoparticles) in digestive fluids may restrict their application for EGCG delivery through oral administration. Therefore, it is essential and urgent to develop nanocarriers with considerable stability, biocompatibility, efficiency, and safety, which would be adaptive to clinical practices of EGCG-involved therapy in the future. To this end, more attention should be paid to non-toxic and biodegradable nanomaterials with high internal surface areas, such as layered double hydroxides (LDHs), blank phosphorus (BP), and metal organic frameworks (MOFs), although studies on them for EGCG delivery are still lacking.

In comparison with the single-drug delivery systems, integration of EGCG with other therapeutic agents enabling chemotherapy, gene therapy, or phototherapy to form multifunctional nanoplatforms appears to be an ideal strategy in enhancing the efficacy of cancer treatment. Moreover, fully understanding the working principles of EGCG and other chemo-, gene, and phototherapeutic agents in cancer cells offer theoretical evidence supporting combination therapy, according to which arrangement and gathering of therapeutic agents in one nanostructure can be rationalized to maximize the potency and minimize the undesired effects. Guided by the mechanisms of synergistic action in combination therapy, we can envision that interfaces between EGCG chemotherapy and other emerging therapeutic modalities including starvation therapy, gas therapy, chemodynamic therapy, and immunity therapy would be further explored and engineered to formulate comprehensive and effective combination treatments of cancer.

AUTHOR CONTRIBUTIONS

KL designed and wrote the review with input from CT and QM for conceiving, writing, and editing the manuscript. All authors contributed to the article and approved the submitted version.

FUNDING

This study was supported by Shenzhen Science and Technology Innovation Committee (GJHZ20190819151807167), Post-doctoral Foundation Project of Shenzhen Polytechnic, and the Fundamental Research Funds for the Central Universities (020514380141), and Chinese Postdoctoral Science Foundation (2020M671437).

REFERENCES

Berletch, J. B., Liu, C., Love, W. K., Andrews, L. G., Katiyar, S. K., and Tollefsbol, T. O. (2008). Epigenetic and genetic mechanisms contribute to telomerase inhibition by EGCG. *J. Cell. Biochem.* 103, 509–519. doi: 10.1002/jcb.21417

Braicu, C., Pileczki, V., Pop, L., Petric, R. C., Chira, S., and Pointiere, E. (2015). Dual targeted therapy with p53 siRNA and epigallocatechingallate in a triple negative breast cancer cell model. *PLoS ONE* 10:e0120936. doi: 10.1371/journal.pone.0120936

Cai, Y. Z., Mei, S., Jie, X., Luo, Q., and Corke, H. (2006). Structure-radical scavenging activity relationships of phenolic compounds from traditional ChinesChakrabartie medicinal plants. *Life Sci.* 78, 2872–2888. doi: 10.1016/j.lfs.2005.11.004

Chakrawarti, L., Agrawal, R., Dang, S., Gupta, S., and Gabrani, R. (2016). Therapeutic effects of EGCG: a patent review. *Expert Opin. Ther. Pat.* 26, 907–916. doi: 10.1080/13543776.2016.1203419

Chavva, S., Deshmukh, S., Kanchanapally, R., Tyagi, N., Coym, J., Singh, A., et al. (2019). Epigallocatechin gallate-gold nanoparticles exhibit superior antitumor activity compared to conventional gold nanoparticles: potential synergistic interactions. *Nanomaterials* 9:396. doi: 10.3390/nano9030396

Chen, C. C., Hsieh, D. S., Huang, K. J., Chan, Y. L., Hong, P. D., Yeh, M. K., et al. (2014). Improving anticancer efficacy of (–)-epigallocatechin-3-gallate gold nanoparticles in murine B16F10 melanoma cells. *Drug Des. Dev. Ther.* 8, 459–474. doi: 10.2147/DDDT.S58414

Chen, L., Ye, H. L., Zhang, G., Yao, W. M., Chen, X. Z., Zhang, F. C., et al. (2014). Autophagy inhibition contributes to the synergistic interaction between EGCG and Doxorubicin to kill the hepatoma Hep3B cells. *PLoS ONE* 9:e85771. doi: 10.1371/journal.pone.0085771

Chen, X., Yi, Z., Chen, G., Ma, X., Su, W., Cui, X., et al. (2019). DOX-assisted functionalization of green tea polyphenol nanoparticles for effective chemo-photothermal cancer therapy. *J. Mater. Chem. B* 7, 4066–4078. doi: 10.1039/C9TB00751B

Chen, Y., Chen, H., and Shi, J. (2013). *In vivo* bio-safety evaluations and diagnostic/therapeutic applications of chemically designed mesoporous silica nanoparticles. *Adv. Mater.* 25, 3144–3176. doi: 10.1002/adma.201205292

Cragg, G. M., Grothaus, P. G., and Newman, D. J. (2009). Impact of natural products on developing new anti-cancer agents. *Chem. Rev.* 109, 3012–3043. doi: 10.1021/cr900019j

Dahiya, S., Rani, R., Kumar, S., Dhingra, D., and Dilbaghi, N. (2017). Chitosan-gellan gum bipolymeric nanohydrogels-a potential nanocarrier for the delivery of epigallocatechin gallate. *BioNanoSci* 7, 508–520. doi: 10.1007/s12668-017-0416-0

Ding, J., Kong, X., Yao, J., Wang, J., Cheng, X., Tang, B., et al. (2012). Core-shell mesoporous silica nanoparticles improve HeLa cell growth and proliferation inhibition by (−)-epigallocatechin-3-gallate by prolonging the half-life. *J. Mater. Chem.* 22, 19926–19931. doi: 10.1039/c2jm32271d

Ding, J., Liang, T., Min, Q., Jiang, L., and Zhu, J. J. (2018). "Stealth and fully-laden" drug carriers: Self-assembled nanogels encapsulated with epigallocatechin gallate and siRNA for drug-resistant breast cancer therapy. *ACS Appl. Mater. Interfaces* 10, 9938–9948. doi: 10.1021/acsami.7b19577

Ding, J., Yao, J., Xue, J., Li, R., Bao, B., Jiang, L., et al. (2015). Tumor-homing cell-penetrating peptide linked to colloidal mesoporous silica encapsulated (−)-epigallocatechin-3-gallate as drug delivery system for breast cancer therapy *in vivo*. *ACS Appl. Mater. Interfaces* 7, 18145–18155. doi: 10.1021/acsami.5b05618

Esmaeili, M. A. (2015). Combination of siRNA-directed gene silencing with epigallocatechin-3-gallate (EGCG) reverses drug resistance in human breast cancer cells. *J. Chem. Biol.* 9, 41–52. doi: 10.1007/s12154-015-0144-2

Fan, Y., Zhang, Y., Yokoyama, W., and Yi, J. (2017). β-Lactoglobulin–chlorogenic acid conjugate-based nanoparticles for delivery of (−)-epigallocatechin-3-gallate. *RSC Adv.* 7, 21366–21374. doi: 10.1039/C6RA28462K

Frias, I., Neves, A., Pinheiro, M., and Reis, S. (2016). Design, development, and characterization of lipid nanocarriers-based epigallocatechin gallate delivery system for preventive and therapeutic supplementation. *Drug Des. Dev. Ther.* 10, 3519–3528. doi: 10.2147/DDDT.S109589

Gan, R. Y., Li, H. B., Sui, Z. Q., and Corke, H. (2017). Absorption, metabolism, anti-cancer effect and molecular targets of epigallocatechin gallate (EGCG): an updated review. *Crit. Rev. Food Sci. Nutr.* 58, 924–941. doi: 10.1080/10408398.2016.1231168

Granja, A., Neves, A. R., Sousa, C. T., Pinheiro, M., and Reis, S. (2019). EGCG intestinal absorption and oral bioavailability enhancement using folic acid-functionalized nanostructured lipid carriers. *Heliyon* 5:e02020. doi: 10.1016/j.heliyon.2019.e02020

Granja, A., Pinheiro, M., and Reis, S. (2016). Epigallocatechin gallate nanodelivery systems for cancer therapy. *Nutrients* 8:307. doi: 10.3390/nu8050307

Hsieh, D. S., Lu, H. C., Chen, C. C., Wu, C. J., and Yeh, M. K. (2012). The preparation and characterization of gold-conjugated polyphenol nanoparticles as a novel delivery system. *Int. J. Nanomed.* 7, 1623–1633. doi: 10.2147/IJN.S30060

Hu, F., Wei, F., Wang, Y., Wu, B., Fang, Y., and Xiong, B. (2015). EGCG synergizes the therapeutic effect of cisplatin and oxaliplatin through autophagic pathway in human colorectal cancer cells. *J. Pharmacol. Sci.* 128, 27–34. doi: 10.1016/j.jphs.2015.04.003

Khan, N., Bharali, D. J., Adhami, V. M., Siddiqui, I. A., Cui, H., Shabana, S. M., et al. (2013). Oral administration of naturally occurring chitosan-based nanoformulated green tea polyphenol EGCG effectively inhibits prostate cancer cell growth in a xenograft model. *Carcinogenesis* 35, 415–423. doi: 10.1093/carcin/bgt321

Li, G. X., Chen, Y. K., Hou, Z., Xiao, H., Jin, H., Lu, G., et al. (2010). Pro-oxidative activities and dose-response relationship of (−)-epigallocatechin-3-gallate in the inhibition of lung cancer cell growth: a comparative study *in vivo* and *in vitro*. *Carcinogenesis* 31, 902–910. doi: 10.1093/carcin/bgq039

Li, Y., Li, N., Pan, W., Yu, Z., Yang, L., and Tang, B. (2017). Hollow mesoporous silica nanoparticles with tunable structures for controlled drug delivery. *ACS Appl. Mater. Interfaces* 9, 2123–2129. doi: 10.1021/acsami.6b13876

Liang, J., Cao, L., Zhang, L., and Wan, X. C. (2014). Preparation, characterization, and *in vitro* antitumor activity of folate conjugated chitosan coated EGCG nanoparticles. *Food Sci. Biotechnol.* 23, 569–575. doi: 10.1007/s10068-014-0078-4

Liang, T., Yao, Z., Ding, J., Min, Q., Jiang, L. P., and Zhu, J. J. (2018). Cascaded aptamers-governed multistage drug delivery system based on biodegradable envelope type nanovehicle for targeted therapy of HER2-overexpressing breast cancer. *ACS Appl. Mater. Interfaces.* 10, 34050–9. doi: 10.1021/acsami.8b14009

Mignani, S., Rodrigues, J., Tomas, H., Zablocka, M., Shi, X., Caminade, A. M., et al. (2018). Dendrimers in combination with natural products and analogues as anti-cancer agents. *Chem. Soc. Rev.* 47, 514–532. doi: 10.1039/C7CS00550D

Mun, S. T., Bae, D. H., and Ahn, W. S. (2014). Epigallocatechin gallate with photodynamic therapy enhances anti-tumor effects *in vivo* and *in vitro*. *Photodiagn. Photodyn. Ther.* 11, 141–147. doi: 10.1016/j.pdpdt.2014.03.003

Nakagawa, K., and Miyazawa, T. (1997). Chemiluminescence-high-performance liquid chromatographic determination of tea catechin, (−)-epigallocatechin 3-gallate, at picomole levels in rat and human plasma. *Anal. Biochem.* 248, 41–49. doi: 10.1006/abio.1997.2098

Naldini, L. (2015). Gene therapy returns to centre stage. *Nature* 526, 351–360. doi: 10.1038/nature15818

Nowakowska, A., and Tarasiuk, J. (2016). Comparative effects of selected plant polyphenols, gallic acid and epigallocatechin gallate, on matrix metalloproteinases activity in multidrug resistant MCF7/DOX breast cancer cells. *Acta Biochim. Pol.* 63, 571–575. doi: 10.18388/abp.2016_1256

Qi, H., Abe, N., Zhu, B., Murata, Y., and Nakamura, Y. (2014). (−)-Epigallocatechin-3-gallate ameliorates photodynamic therapy responses in an *in vitro* T lymphocyte model. *Phytother. Res.* 28, 1486–1491. doi: 10.1002/ptr.5152

Radhakrishnan, R., Kulhari, H., Pooja, D., Gudem, S., Bhargava, S., Shukla, R., et al. (2016). Encapsulation of biophenolic phytochemical EGCG within lipid nanoparticles enhances its stability and cytotoxicity against cancer. *Chem. Phys. Lipids* 198, 51–60. doi: 10.1016/j.chemphyslip.2016.05.006

Sadava, D., Whitlock, E., and Kane, S. E. (2007). The green tea polyphenol, epigallocatechin-3-gallate inhibits telomerase and induces apoptosis in drug-resistant lung cancer cells. *Biochem. Biophys. Res. Commun.* 360, 233–237. doi: 10.1016/j.bbrc.2007.06.030

Saeed, N. M., El-Naga, R. N., El-Bakly, W. M., Abdel-Rahman, H. M., and El-Demerdash, E. (2015). Epigallocatechin-3-gallate pretreatment attenuates doxorubicin-induced cardiotoxicity in rats: a mechanistic study. *Biochem. Pharmacol.* 95, 145–155. doi: 10.1016/j.bcp.2015.02.006

Shankar, S., Marsh, L., and Srivastava, R. K. (2012). EGCG inhibits growth of human pancreatic tumors orthotopically implanted in Balb C nude mice through modulation of FKHRL1/FOXO3a and neuropilin. *Mol. Cell. Biochem.* 372, 83–94. doi: 10.1007/s11010-012-1448-y

Shpigelman, A., Cohen, Y., and Livney, Y. D. (2012). Thermally-induced β-lactoglobuline-EGCG nanovehicles: loading, stability, sensory and digestive-release study. *Food Hydrocolloids* 29, 57–67. doi: 10.1016/j.foodhyd.2012.01.016

Shukla, R., Chanda, N., Zambre, A., Upendran, A., Katti, K., Kulkarni, R. R., et al. (2012). Laminin receptor specific therapeutic gold nanoparticles (^{198}AuNP-EGCg) show efficacy in treating prostate cancer. *Proc. Natl. Acad. Sci. U.S.A.* 109, 12426–12431. doi: 10.1073/pnas.1121174109

Singh, B. N., Shankar, S., and Srivastava, R. K. (2011). Green tea catechin, epigallocatechin-3-gallate (EGCG): Mechanisms, perspectives and clinical applications. *Biochem. Pharmacol.* 82, 1807–1821. doi: 10.1016/j.bcp.2011.07.093

Singh, T., and Katiyar, S. K. (2013). Green tea polyphenol, (−)-epigallocatechin-3-gallate, induces toxicity in human skin cancer cells by targeting beta-catenin signaling. *Toxicol. Appl. Pharmacol.* 273, 418–424. doi: 10.1016/j.taap.2013.09.021

Sommer, A. P., Zhu, D., Mester, A. R., and Försterling, H. D. (2011). Pulsed laser light forces cancer cells to absorb anticancer drugs-The role of water in nanomedicine. *Artif. Cells Blood Substit. Biotechnol.* 39, 169–173. doi: 10.3109/10731199.2010.516262

Spradlin, J. N., Hu, X., Ward, C. C., Brittain, S. M., Jones, M. D., Ou, L., et al. (2019). Harnessing the anti-cancer natural product nimbolide for targeted

protein degradation. *Nat. Chem. Biol.* 15, 747–755. doi: 10.1038/s41589-019-0304-8

Stearns, M. E., Amatangelo, M. D., Varma, D., Sell, C., and Goodyear, S. M. (2010). Combination therapy with epigallocatechin-3-gallate and Doxorubicin in human prostate tumor modeling studies. *Am. J. Pathol.* 177, 3169–3179. doi: 10.2353/ajpath.2010.100330

Viator, J. A., Gupta, S., Goldschmidt, B. S., Bhattacharyya, K., Kannan, R., Shukla, R., et al. (2010). Gold nanoparticle mediated detection of prostate cancer cells using photoacoustic flowmetry with optical reflectance. *J. Biomed. Nanotechnol.* 6, 187–191. doi: 10.1166/jbn.2010.1105

Wang, J., Man, G. C. W., Chan, T. H., Kwong, J., and Wang, C. C. (2018). A prodrug of green tea polyphenol (–)-epigallocatechin-3-gallate (Pro-EGCG) serves as a novel angiogenesis inhibitor in endometrial cancer. *Cancer Lett.* 412, 10–20. doi: 10.1016/j.canlet.2017.09.054

Wang, W., Chen, D., and Zhu, K. (2018). SOX2OT variant 7 contributes to the synergistic interaction between EGCG and Doxorubicin to kill osteosarcoma via autophagy and stemness inhibition. *J. Exp. Clin. Cancer Res.* 37:37. doi: 10.1186/s13046-018-0689-3

Wu, M., Jin, J., Jin, P., Xu, Y., Yin, J., Qin, D., et al. (2017). Epigallocatechin gallate-β-lactoglobulin nanoparticles improve the antitumor activity of EGCG for inducing cancer cell apoptosis. *J. Funct. Foods* 39, 257–263. doi: 10.1016/j.jff.2017.10.038

Xia, P., and Xu, X. Y. (2015). PI3K/Akt/mTOR signaling pathway in cancer stem cells: From basic research to clinical application. *Am. J. Cancer Res.* 5, 1602–1609.

Yang, Q. Q., Wei, X. L., Fang, Y. P., Gan, R. Y., Wang, M., Ge, Y. Y., et al. (2019). Nanochemoprevention with therapeutic benefits: an updated review focused on epigallocatechin gallate delivery. *Crit. Rev. Food Sci. Nutr.* 60, 1243–1264. doi: 10.1080/10408398.2019.1565490

Yang, R., Liu, Y., Gao, Y., Wang, Y., Blanchard, C., and Zhou, Z. (2017). Ferritin glycosylated by chitosan as a novel EGCG nano-carrier: structure, stability, and absorption analysis. *Int. J. Biol. Macromol.* 105, 252–261. doi: 10.1016/j.ijbiomac.2017.07.040

Yang, Y., Jin, P., Zhang, X., Ravichandran, N., Ying, H., Yu, C., et al. (2017). New epigallocatechin gallate (EGCG) nanocomplexes co-assembled with 3-mercapto-1-hexanol and β-lactoglobulin for improvement of antitumor activity. *J. Biomed. Nanotechnol.* 13, 805–814. doi: 10.1166/jbn.2017.2400

Yao, Y. F., Liu, X., Li, W. J., Shi, Z. W., Yan, Y. X., Wang, L. F., et al. (2017). (–)-Epigallocatechin-3-gallate alleviates doxorubicin-induced cardiotoxicity in sarcoma 180 tumor-bearing mice. *Life Sci.* 180, 151–159. doi: 10.1016/j.lfs.2016.12.004

Ye, J. H., and Augustin, M. A. (2018). Nano- and micro-particles for delivery of catechins: Physical and biological performance. *Crit. Rev. Food Sci. Nutr.* 59, 1563–1579. doi: 10.1080/10408398.2017.1422110

Zhou, Y., Tang, J., Du, Y., Ding, J., and Liu, J. Y. (2016). The green tea polyphenol EGCG potentiates the antiproliferative activity of sunitinib in human cancer cells. *Tumor Biol.* 37, 8555–8566. doi: 10.1007/s13277-015-4719-x

Zhu, J., Jiang, Y., Yang, X., Wang, S., Xie, C., Li, X., et al. (2017). Wnt/β-catenin pathway mediates (–)-Epigallocatechin-3-gallate (EGCG) inhibition of lung cancer stem cells. *Biochem. Biophys. Res. Commun.* 482, 15–21. doi: 10.1016/j.bbrc.2016.11.038

Conflict of Interest: The authors declare that the research was conducted in the absence of any commercial or financial relationships that could be construed as a potential conflict of interest.

frontiers in Chemistry

REVIEW
published: 29 October 2020
doi: 10.3389/fchem.2020.00799

Green Synthesis of Metallic Nanoparticles and Their Potential Applications to Treat Cancer

*Dan Zhang†, Xin-lei Ma†, Yan Gu, He Huang and Guang-wei Zhang**

Department of Cardiology, First Hospital of Jilin University, Changchun, China

Nanoparticle synthesis using microorganisms and plants by green synthesis technology is biologically safe, cost-effective, and environment-friendly. Plants and microorganisms have established the power to devour and accumulate inorganic metal ions from their neighboring niche. The biological entities are known to synthesize nanoparticles both extra and intracellularly. The capability of a living system to utilize its intrinsic organic chemistry processes in remodeling inorganic metal ions into nanoparticles has opened up an undiscovered area of biochemical analysis. Nanotechnology in conjunction with biology gives rise to an advanced area of nanobiotechnology that involves living entities of both prokaryotic and eukaryotic origin, such as algae, cyanobacteria, actinomycetes, bacteria, viruses, yeasts, fungi, and plants. Every biological system varies in its capabilities to supply metallic nanoparticles. However, not all biological organisms can produce nanoparticles due to their enzymatic activities and intrinsic metabolic processes. Therefore, biological entities or their extracts are used for the green synthesis of metallic nanoparticles through bio-reduction of metallic particles leading to the synthesis of nanoparticles. These biosynthesized metallic nanoparticles have a range of unlimited pharmaceutical applications including delivery of drugs or genes, detection of pathogens or proteins, and tissue engineering. The effective delivery of drugs and tissue engineering through the use of nanotechnology exhibited vital contributions in translational research related to the pharmaceutical products and their applications. Collectively, this review covers the green synthesis of nanoparticles by using various biological systems as well as their applications.

Keywords: metallic nanoparticles, green synthesis, extracellular, intracellular, tissue engineering, bio-detection

OPEN ACCESS

Edited by:
Fang Liu,
Guangzhou University of Chinese Medicine, China

Reviewed by:
Zhiqiang Pei,
Northwestern University, United States
Wang Shuang,
Chinese Academy of Sciences, China

***Correspondence:**
Guang-wei Zhang
zguangw543@aliyun.com

†These authors have contributed equally to this work

Specialty section:
This article was submitted to Nanoscience, a section of the journal Frontiers in Chemistry

Received: *20 May 2020*
Accepted: *30 July 2020*
Published: *29 October 2020*

Citation:
Zhang D, Ma X-l, Gu Y, Huang H and Zhang G-w (2020) Green Synthesis of Metallic Nanoparticles and Their Potential Applications to Treat Cancer. Front. Chem. 8:799. doi: 10.3389/fchem.2020.00799

INTRODUCTION

Nanotechnology is amongst the most widely used technologies in translational research. The development of metallic nanoparticles employing biological materials by an eco-friendly approach has attracted significant attention. Nanotechnology deals with particles of a size ranging from 1 to 100 nm, their synthesis strategy, and manipulation. This knowledge domain naturally commingles all the fields of natural sciences together with chemistry, physics, biological sciences, engineering, materials science, and computational sciences for the formulation of nanostructures (Shenton et al., 1999; Medvedeva et al., 2007). The nanostructures have different applications attributable to their new or increased properties (Tang et al., 2007; Thakkar et al., 2009) depending upon their size, distribution, and morphology. It has applications in various fields including biomedical, catalysis,

chemical industries, cosmetics, drug delivery, electronics, environment, energy science, food and feed, health care, mechanics, optics, space industries, non-linear optical devices, single-electron transistors, and photo-electrochemical applications. The metallic nanoparticles are considered one of the most promising systems for all the aforementioned functions (Wang et al., 2005; You et al., 2013; Singh et al., 2016).

A nanoscale drug carrier acts as a single unit with respect to its properties and transport. These nanoclusters have narrow size distribution and a minimum of one dimension between 1 and 10 nanometers. The agglomerates of ultrafine particles, nanoclusters or nanoparticles, are nanopowders whereas nanocrystals are the crystals of nanoparticle size

There are two general strategies for the synthesis of nanomaterials: the top-down approach, wherein a larger structure is broken down into smaller pieces using chemical, physical, and biological energy; and the bottom-up approach, in which material is synthesized from the atomic level using various chemical, physical, or biological reactions to make a large nanostructure (Das et al., 2017). The chemical and biological methods are primarily accustomed to build nanostructured carriers (NC) employing this approach (**Figure 1**).

The physical and chemical strategies are in-use for the synthesis of nanoparticles. The utilization of toxic chemicals could exert potential hazards like carcinogenicity, toxicity, and environmental toxicity (Gupta and Xie, 2018). The toxicity problems are quite prominent due to the use of hazardous substances such as reducing agents, organic solvents, and stabilizers. These chemicals prevent the agglomeration of colloids. The use of toxic solvents and chemical contaminations limits the use of nanoparticles in various clinical and biomedical applications (Hua et al., 2018). Therefore, a reliable, clean, biologically appropriate, and environmental-friendly techniques is indeed required to synthesize nanoparticles (Jain et al., 2010; Thakkar et al., 2010; Kulkarni and Muddapur, 2014). The biological synthesis of nanoparticles may prove to be an attractive alternative. It includes adoption of multicellular and unicellular biological entities- bacteria (Roh et al., 2001; Nair and Thalappil, 2002; Lengke et al., 2006; Husseiny et al., 2007; Joglekar et al., 2011), actinomycetes (Ahmad et al., 2003a,b; Sastry et al., 2005), fungi Mukherjee et al., 2001, 2002; Ahmad et al., 2002, 2005; Bhainsa and D'Souza, 2006, plants Philip, 2010; Kumar et al., 2011, viruses (Lee et al., 2002; Merzlyak and Lee, 2006; Khan et al., 2013), and yeasts (Dameron et al., 1989; Kowshik et al., 2003; Gericke and Pinches, 2006a,b). The biologically synthesized nanoparticles have a broad area to study with respect to their shape, size, composition, and physicochemical properties (Mohanpuria et al., 2008). Further, biological entities may operate as a pattern for the assembly, synthesis, and organization of the nanometer scale. The present review covers the use of biological routes for the synthesis of metal oxide and metal

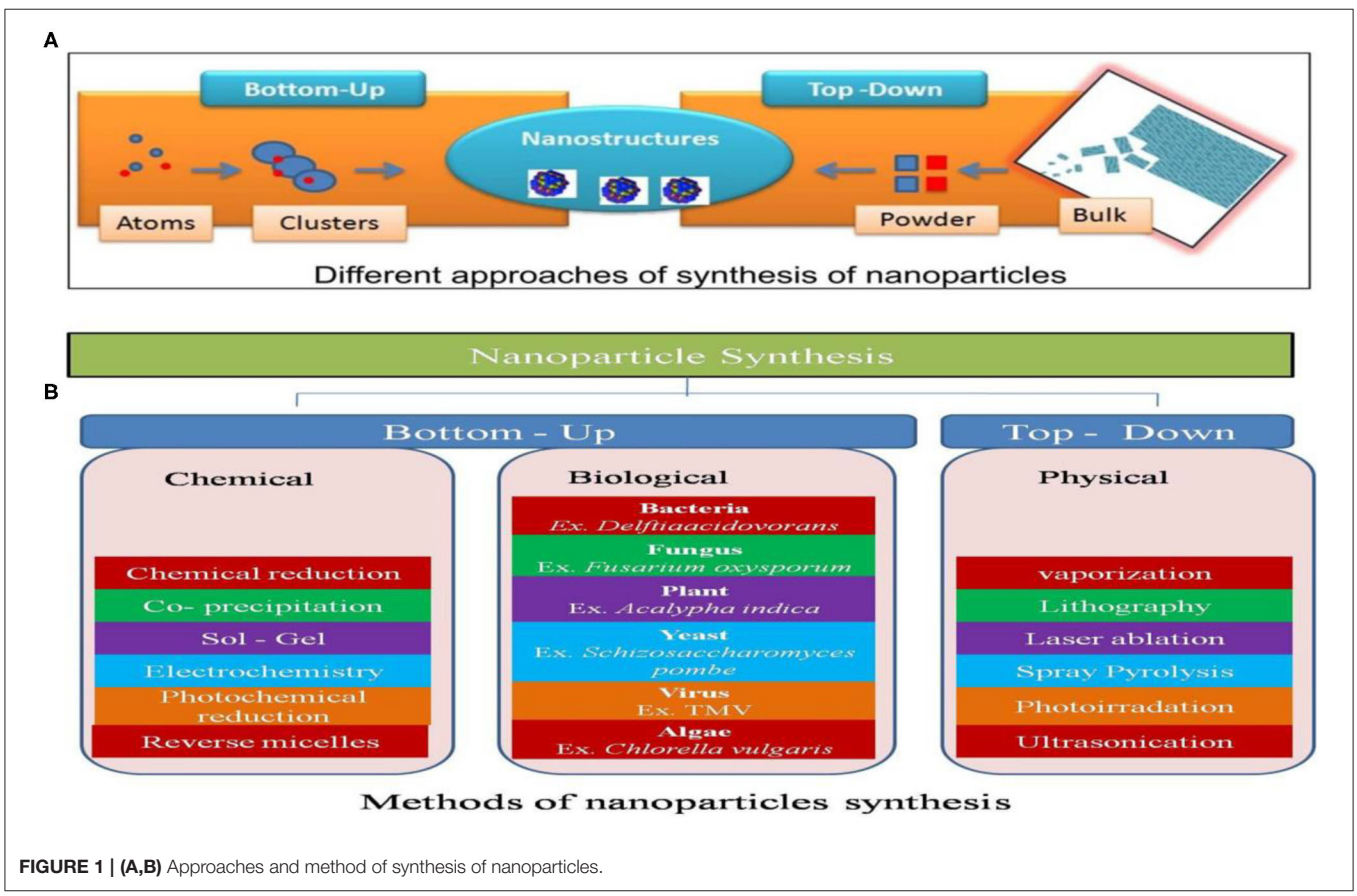

FIGURE 1 | (A,B) Approaches and method of synthesis of nanoparticles.

nanoparticles, and various factors affecting their synthesis, and possible mechanisms employed along with likely applications of nanoparticles formed using biological factories.

BIOLOGICAL SYNTHESIS OF NANOPARTICLES

Organisms have advanced to endure in environments of high concentrations of metals (Bisen et al., 1987, 1996; Khare and Bisen, 1991). These organisms may alter the chemical nature of the toxic metals by lowering their toxicity or making them non-toxic (Singh et al., 1989, 1993; Sharma and Bisen, 1992; Sharma et al., 2001). The formation of nanoparticles is the "consequence" of the resistance mechanism of an organism in contrast to a specific metal (**Figure 2**). The synthesis of "Natural" biogenic metallic nanoparticle synthesis is split into two categories:

(a) **Bioreduction**: More stable forms of metal ions may be achieved by chemical reduction using biological means and is achieved by dissimilatory metal reduction. The metal ion is reduced and the enzyme is oxidized (Deplanche et al., 2010). This concludes in the production of impotent metallic nanoparticles which may be harmlessly recovered from a contaminated sample.

(b) **Biosorption**: The metal ions bind to the organism itself from an aqueous sample or soil sample. Either the metal ions are bonded to the cell wall or peptides are synthesized by some plants, bacteria, and fungi, and these synthesized peptides assembles into stable nanoparticulate structures (Yong et al., 2002).

The selection of biological methods for synthesis and engineering of nanoparticles is dependent upon several variables. The form of the metal nanoparticle to be synthesized is the most important variable. Resistance developed against a small number of metals by the organisms limit the choice of organisms. Following are a number of the microbial resources (algae, fungi, bacteria, viruses, and yeast) used for most of the frequently studied metal and metal salts nanoparticles consisting of copper, silver, gold, cadmium, platinum, palladium, cadmium sulfide, titanium dioxide, and zinc oxide (Mousavi et al., 2018; Gahlawat and Roy Choudhury, 2019).

Bacteria Mediated Synthesis of Nanoparticles

Pure gold nanoparticles were synthesized by bacterium, *Delftia acidovorans* (Johnston et al., 2013). Delftibactin is a small non-ribosomal peptide and is considered liable for the synthesis of gold nanoparticles as it is known to induce resistance against toxic gold ions. The transition metal, gold, did not exert toxicity toward bacterium due to the formation of inert gold nanoparticles (AuNPs) bound to delftibactin (Pantidos and Horsfall, 2014). A substitutive method for gold nanoparticle synthesis by the bacterium *Rhodopseudomonas capsulata* was shown to produce extracellular gold nanoparticles ranging in size from 10 to 20 nm via NADH-Dependant Reductase (He et al., 2007). Green products may act as a stabilizing and reducing agent for AuNPs synthesis and these preparations exhibit medicinal applications (Lee et al., 2020).

Palladium (Pd), one of the members of the Platinum Group Metals (PGM) has a compilation of highly catalytically active metals, and is being employed as a catalyst for hydrogenation and dehalogenation reactions. The heavy contamination of those bacteria that had been isolated from Alpine sites with

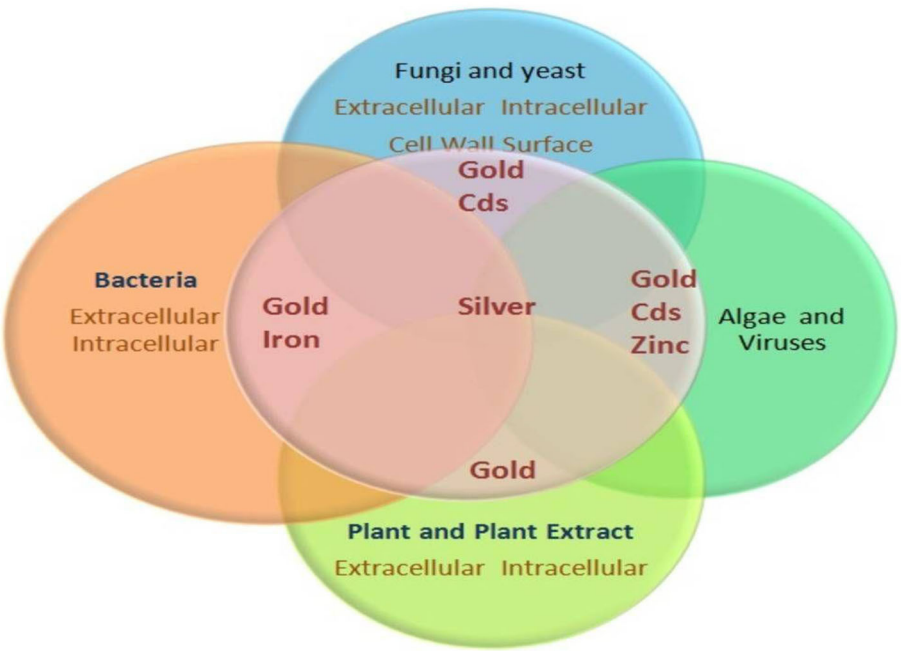

FIGURE 2 | Various biological synthesis of nanoparticles.

that of heavy metals led to the synthesis of zero-valent Palladium (Pd^0) nanoparticles (Schlüter et al., 2014). Amongst various bacteria isolated from the site, only Pseudomonas cells exhibited the potential to produce catalytically active Pd nanoparticles. Furthermore, they were able to carry out the reductive dehalogenation of congeners like tri and tetra-chlorinated dioxin. *Escherichia coli* synthesized Pd^0 nanoparticles using hydrogenases present in the cells (Lloyd et al., 1998). Pd nanoparticles were synthesized on the bacterial cell envelope and may be separated easily.

The bacterium, *Bacillus licheniform,* reportedly produced silver nanoparticles (AgNPs) intracellularly (Kalimuthu et al., 2008). The production/synthesis of nanoparticles required 24 h and was demonstrated by the color modification of culture into dark brown after the augmentation of silver ions. However, as the nanoparticles were synthesized intracellularly an additional extraction step was required. Intracellular AgNPs were synthesized by the members of the *Bacillus* spp. subcultured in $AgNO_3$ containing media and the reaction was completed in 7 days (Pugazhenthiran et al., 2009). The culture supernatant was tested for its capability to form metallic nanoparticles (Shahverdi et al., 2007) in 5 min. The extracellular production of nanoparticles is recommended compared to the intracellular synthesis due to the simple purification process with the increased production rate (Das et al., 2014).

Green synthesis of AgNPs using lactic acid bacteria was demonstrated by Sintubin et al. (2009). *Lactobacillus* spp., *Pediococcus pentosaceus*, *Enterococcus faecium*, and *Lactococcus garvieae* was shown to synthesize the nanoparticles by many bacteria. The procedure of AgNP formation was proposed to be a two-step method. The biosorption of Ag ions on the cell wall was followed by a reduction of these ions resulting in AgNPs formation (Sintubin et al., 2009). Additionally, the cell wall could be thought to be a capping agent, maintaining their stability by stopping their aggregation.

The biosynthesis of Ag and AuNPs has been a focal point of research because of their antimicrobial attributes. The extensive studies were conducted to synthesize the metallic nanoparticles using Bacillus species due to their metal accumulating abilities (Pollmann et al., 2006; Kalimuthu et al., 2008; Pugazhenthiran et al., 2009). *Bacillus sphaericus* JG-A12 can collect excessive concentrations of Al, Cd, Cu, Pb, and U (**Figure 3**). The Uranium bioremediation from the aqueous environment was attributed to the S-layer proteins of *B. sphaericus*. It is a porous layer surrounding the bacterial cell and is made up of identical proteins, ∼5–15 nm thick, with the pores ranging in size from 2 to 6 nm. The S-layer contributes up to 15% of the total proteins of the cell. The S-layer has been stated to be liable for the binding of heavy metals from the aqueous environments (Pollmann et al., 2006) with a capability to bind up to 20 mg U/g of protein, and the U binds to the phosphate and carboxyl and groups of the S-layer protein (Pollmann et al., 2006).

Copper (Cu) is not reportedly stable and is oxidized rapidly to copper oxide (CuO) (Baco-Carles et al., 2011). Therefore,

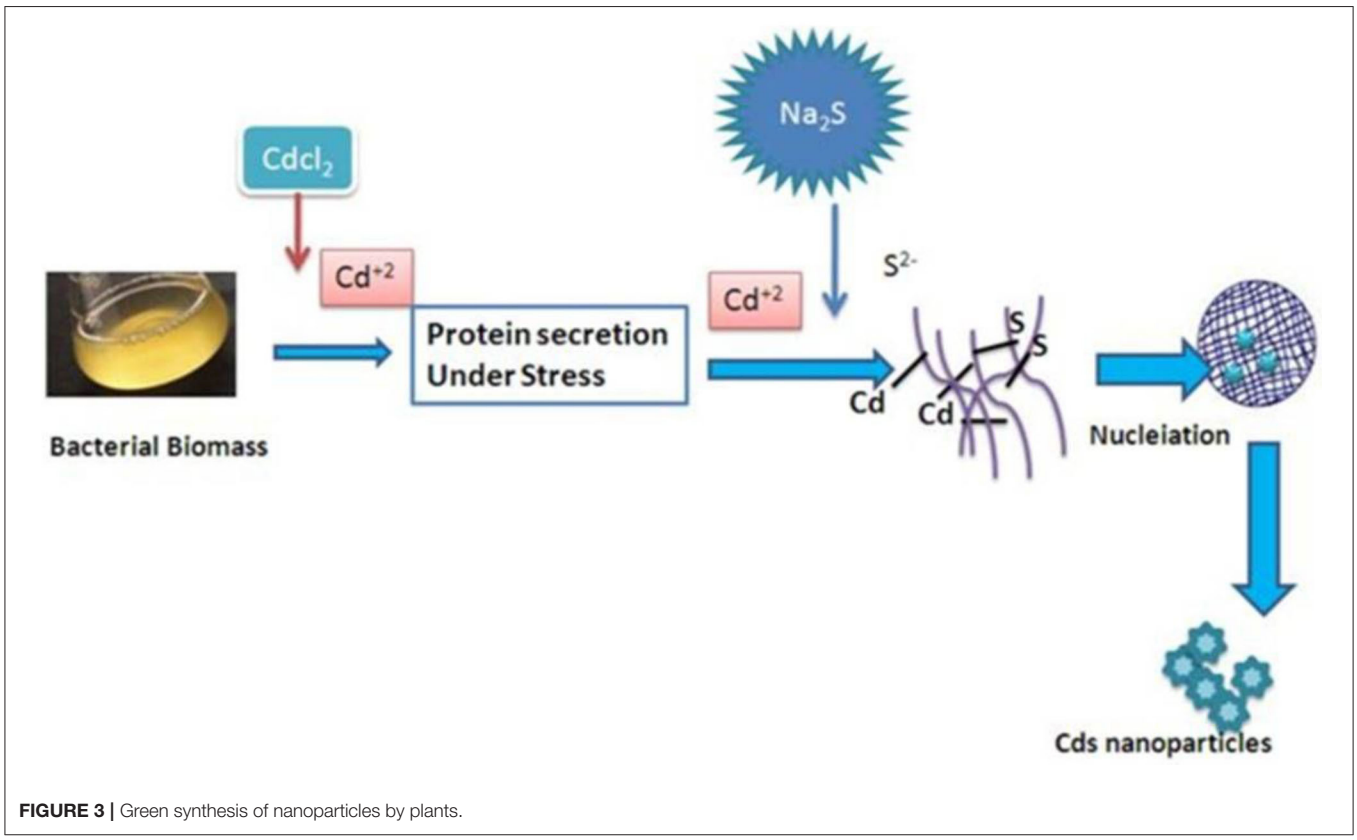

FIGURE 3 | Green synthesis of nanoparticles by plants.

Cu nanoparticles need to be stabilized as soon as they are formulated. The synthesis of Cu nanoparticles using *Morganella morganii* is proved with the help of intracellular uptake of Cu ions accompanied by the means of binding of ions to a metallic ion reductase or a comparable protein ensuring in the reduction of the ion to metallic Cu^0 (Baco-Carles et al., 2011). The metallic Cu nanoparticles then accumulate extracellularly since they are effluxed out of the cell. *Morganella* sp. additionally extracellularly synthesized AgNPs (Parikh et al., 2008). The Cu nanoparticles synthesis using *M. morganii* may be due to an Ag resistance mechanism to provide elemental Cu nanoparticles through silE homolog to copper-binding protein from different microorganisms (Ramanathan et al., 2013).

Nanoparticle Synthesis Using Fungi

The production of AgNPs using fungi has been the focal point of investigation because of their applications in numerous industries such as antimicrobials and electronics (Rai et al., 2008; Ummartyotin et al., 2012). The capability of the fungus *Fusarium oxysporum* to synthesize AgNPs has been verified with sizes ranging from 5 to 15 nm which had been capped through fungal proteins to lead them to becoming stable. *Fusarium oxysporum* could also synthesize nanoparticles extracellularly (Rai et al., 2008; Ummartyotin et al., 2012) as compared to earlier studies in which intracellular production of Ag and AuNPs, lead sulfide (PbS), cadmium sulfide (Cds), molybdenum sulfide (MoS), and zinc sulfide (ZnS) nanoparticles intracellular production of Ag and AuNPs, cadmium sulfide (Cds), lead sulfide (PbS), zinc sulfide (ZnS), and molybdenum sulfide (MoS) had been reported (Ahmad et al., 2002, 2003a).

Aspergillus fumigatus is used to synthesize extracellular silver nanoparticles of larger sizes ranging from 5 to 25 nm as compared to *Fusarium oxysporum,* with the disadvantage of difficulty in anticipating the catalytic activity with the size difference in every batch (Bhainsa and D'Souza, 2006). However, the bio-production of AgNPs using *A. fumigatus* is an attractive prospect as organism reduces Ag ions into nanoparticles within 10 min of contact (Bhainsa and D'Souza, 2006). Fungus *Trichoderma reesei* could also be used for extracellular production of AgNPs with a size range of 5–50 nm nanoparticles. It took 72 h to synthesize AgNPs which was appreciably slower than *A. fumigatus* and *Fusarium oxysporum* (Ahmad et al., 2002, 2005; Bhainsa and D'Souza, 2006). Furthermore, the use of *T. reesei* has an advantage over the use of other fungi since it has been an extensively-studied organism which may be manipulated for the production of an excessive quantity of enzymes (Roy et al., 2008; Vahabi et al., 2011) and may help increase the rate of production of nanoparticles. However, the nanoparticles were not as homogenous as those which were produced by *A. Fumigates* (Bhainsa and D'Souza, 2006) and *F. oxysporum* (Ahmad et al., 2002). The fungal attribute to produce intracellular nanoparticles is helpful in getting rid of the fungus and its gathered metallic contaminant. A white-rot fungus (*Coriolus versicolor*) is suggested to provide and accumulate AgNPs extra and intracellularly by manipulating reaction conditions (Sanghi and Verma, 2008). Only a few fungi are considered to have the potential to synthesize gold nanoparticles despite the increasing demand in various fields. The small size of gold nanoparticles causes them to become more reactive and appropriate as compared to the bulk form to be used as precursors for electronics applications and catalysts (Mukherjee et al., 2001; Eustis and El-Sayed, 2006). The synthesis of AuNPs using *Verticillium* sp. by the biological reduction of $AuCl_4$ localized on the surface of the mycelia (Mukherjee et al., 2001).

Biological synthesis of Platinum nanoparticles (PtNPs) was carried out by the use of fungus *Neurospora crassa*. It produced single PtNPs (Platinum nanoparticles) intracellularly ranging in size from 4 to 35 nm in diameter. They may additionally synthesize spherical nano-agglomerates in the range of 20–110 nm diameter (Castro et al., 2013). Both biomass and extract of *N. crassa* were used to synthesize PtNPs. The PtNPs synthesized using the *N. Crassa* extract contains single-crystal nano agglomerates (Castro et al., 2011, 2013). PtNPs were also reportedly synthesized extra and intracellularly by *F. oxysporum* but with sub-optimal quantity when synthesized intracellularly (Riddin et al., 2006). The phytopathogenic fungus *F. oxysporum* and the endophytic fungus *Verticillium* sp. had been reported to synthesize magnetite (a common iron oxide) nanoparticles (MaNPs) intracellularly (Bharde et al., 2006).

The use of fungi for nanoparticles synthesis has some benefits over the use of bacteria namely; scaling up and easy downstream processing, the economic status, and an increased surface area provided by the fungal mycelia (Mukherjee et al., 2001). The higher amount of proteins secreted by using fungi should likely increase the productivity of nanoparticle synthesis but safety is compromised since a number of fungi are phytopathogenic and may pose a safety risk (Spadaro and Gullino, 2005). *Trichoderma asperellum* and *Trichoder mareesei* are non-pathogenic making them ideal for commercial applications (Nevalainen et al., 1994; Roy et al., 2008; Vahabi et al., 2011). *T. reesei* is broadly used in animal feed, food, paper, pharmaceuticals, and textile industries (Nevalainen et al., 1994).

Nanoparticle Synthesis Using Yeast

Yeasts can absorb and accumulate a good quantity of lethal metals from their adjacent areas due to their large surfaces (Bhattacharya and Gupta, 2005; Mandal et al., 2006). Yeast uses a range of detoxification mechanisms to adapt to toxic metals such as bio-precipitation, chelation, extracellular sequestration and bio-sorption. These mechanisms adapted through yeast cells are used during nanoparticle synthesis to form and increase the durability of nanoparticles, giving rise to variation in particle size, particle properties, and location (Hulkoti and Taranath, 2014). The intracellular synthesis of CdS quantum dots turned into confirmed via *Candida glabrata* when exposed to cadmium salts (Dameron et al., 1989). The growth phase of yeast *Schizosaccharomyces pombe* cells and the formation of CdS quantum dots are linked together (Kowshik et al., 2002a,b). *Torulopsis* sp. synthesizes PbS quantum dots when exposed to Pb^2 ions and *Pichia jadinii* synthesizes Au nanoparticles intracellularly. The size range of these nanoparticles is from a few nanometers to around 100 nm. The morphological characteristics of these nanoparticles were easily conducted by monitoring the cellular activities and growth of *P. jadinii* during the synthesis

of the nanoparticle (Gericke and Pinches, 2006a,b). The use of metallic nanoparticles has become vital due to their safety and prospective applications.

Nanoparticles Synthesis Using Cyanobacteria (Blue Green Algae)

Green and valuable synthetic techniques have attracted great interest in the synthesis of nanoparticles (Sundrarajan and Gowri, 2011). Cyanobacteria strains are an inexpensive eco-friendly tool for nanometal formation. Cyanobacterial technology offers the merits of eco-friendly methods, such as timesaving for large-scale production at ambient temperatures. They grow much faster compared to the plants and could easily be manipulated as needed. Studies on molecular biology and ecology regarding synthesis of nanoparticles offer a great opportunity for efficient development of application-oriented nanoparticles. The common cyanobacterial strains used in nanoparticle biosynthesis vary from unicellular and colonial species. Colonies might form sheets, filamentous, or even hollow balls. They may fix atmospheric nitrogen besides fixing the atmospheric carbon dioxide during photosynthesis. Some strains grow in dark under organotrophic/chemotrophic/lithotrophic conditions offering a wide range of modes of nutrition with normal plants-like photosynthesis. Few strains exhibit symbiotic conditions with lichen (Fungi), bryophytes (Liverworts), gymnosperms (Cycas), and with higher plants (Macrozamia). They require a lesser quantity of chemicals as they are all photoautotrophic and may also grow under the chemo-autotrophic condition in light and dark.

Out of the 30 different strains of cyanobacteria (unicellular, colonial, undifferentiated and differentiated filamentous) studied for the silver nanoparticles biosynthesis, the filamentous heterocystous strain *Cylindrospermum stagnale* was the best organism synthesizing nanoparticles of 38–40 nm (Husain et al., 2015). In general, the time frame varied from 30 to 360 h, and the size varied from 38 to 88 nm (Husain et al., 2015). The techniques of synthesis of AgNPs using cyanobacteria *Spirulina platensis* and *Nostoclinckia* have been studied (Cepoi et al., 2014). There is a need to understand the optical conditions of the interaction among the biomass and solution containing Ag ions that may allow nanoparticles without biomass degradation at the time of Ag nanoparticle formation (Cepoi et al., 2014; Hamouda et al., 2019). The green synthesized silver nanoparticles via simple biological protocol using *Oscillatoria limnetica* aqueous extract that had provided both a decreasing and stabilizing agent for the biosynthesis of nanoparticles by suspending the live and washed biomass into the $AgNO_3$ solution and by adding $AgNO_3$ into a cell-free culture liquid (Patel et al., 2015) assessed the selected strains of cyanobacteria for the ability to synthesize AgNPs. Around 14 out of 16 tested strains have been utilized for the AgNPs biosynthesis. Mostly, AgNPs have been formed in the presence of biomass in addition to the cell-free culture media indicating that the Ag-NPs formation technique engages an extracellular compound inclusive of polysaccharide. TEM evaluation revealed that nanoparticles were set in an organic matrix. AgNPs varied in shape and sizes that ranged between 13 and 31 nm, depending upon the organism used (Patel et al., 2015). With the exception of one strain of Cyanobacterium *Limnothrix* sp., all strains confirmed the antibacterial activity of Ag-NPs (Patel et al., 2015). For the gold nanoparticles green synthesis, *Lyngbya majuscula* and *Spirulina subsalsa* were investigated as bioreagents. The cyanobacterial biomass turned purple within 72 h of incubation at 15 mg L-1 Au^{3+} solution, indicating an intracellular reduction of Au^{3+} to Au^0 and subsequent formation of gold nanoparticles. *Spirulina subsalsa* showed the synthesis of spherical nanoparticles of ∼5 to ∼30 nm in diameter along with very few nanorods. *Lyngbya majuscule* showed the presence of spherical and hexagonal nanoparticles of ∼2 to ∼25 nm in diameter. The reduction of Au^{3+} to Au^0 was proved by the XRD study. FTIR analysis indicated the presence of protein shells around the gold nanoparticles (Parial and Pal, 2011). The biosynthesis of AgNPs and their antimicrobial property and photocatalytic activity for photodegradation of organic dye were studied by San Keskin et al. (2016). The characterization of synthesized Ag nanoparticles was carried out by UV–Vis spectrophotometer (surface plasmon resonance band at 430–450 nm). The Attenuated Total Reflection Fourier Transform Infrared Spectroscopy (ATR-FTIR) study confirmed the reducing nature of proteins. The Scanning electron microscopy (SEM) and Transmission electron microscopy (TEM) were used to determine the structure of AgNPs and was found to be spherical. The AgNPs showed photocatalytic activity that is photodegradation of organic dye i.e., methylene blue. It was shown that methylene blue was degraded by ∼18% within 4 h with biosynthesized AgNPs (San Keskin et al., 2016). The biosynthesis of AgNPs has been efficaciously performed with the use of bloom-forming filamentous undifferentiated cyanobacterium *Plectonema boryanum* which reacted with solution of $AgNO_3$ (∼560 mg/L Ag) for up to 28 days at 25–100°C. The precipitation of spherical AgNPs and octahedral silver platelets (of up to 200 nm) in solutions is promoted by interaction of cyanobacteria with $AgNO_3$ Solution. The mechanism of formation of AgNPs via cyanobacteria may involve the metabolic processes in which nitrate is used at 25°C, and organics are released from the lifeless cyanobacteria at 25–100°C (Lengke et al., 2006, 2007). The cyanobacterium *Gloeocapsa* sp. was an effective strain for nanosilver production (Al-Katib et al., 2015). The extracellular synthesis of AgNPs was initially detected by visual inspection for color changing of the cultured flasks solutions from transparent to brown then black, as well as nanoparticles characterization through UV-Vis spectrophotometer and Fourier Transform Infrared spectroscopy (FTIR) with characteristic surface Plasmon absorption peaks at range 400–450 nm. The FTIR spectrum data in addition confirmed the presence of specific functional groups such as proteins and does have an important role as a capping and stabilizing agent in the biosynthesis of AgNPs (Al-Katib et al., 2015). Cyanobacteria could play an instrumental role as an excellent candidate for nanoparticle biosynthesis.

Nanoparticle Synthesis Using Algae

Algae are regarded to accumulate heavy metals and may be utilized for the biogenic synthesis of metallic nanoparticles.

Dried unicellular alga *Chlorella vulgaris* could synthesize nanoparticles of diverse shapes—tetrahedral, decahedral, and icosahedral accumulated near the surface (Luangpipat et al., 2011). The extract of *Chlorella vulgaris* produced Ag nanometer scale plates at room temperature. Biosynthesis of $CuFe_2O_4$@Agnano composite from *Chlorella vulgaris* combined with ciprofloxacin confirmed promising bactericidal activity toward multidrug resistant *Staphylococcus aureus* which is a rising global risk (Kahzad and Salehzadeh, 2020). The proteins present in the algal extract perform a primary function as a stabilizing agent, reducing agent, and shape-control modifier (Xie et al., 2007). *Sargassum wightii*, a marine alga, could also synthesize extracellular Ag, Au, and Au/Ag bimetallic nanoparticles (Govindaraju et al., 2009). Rapid synthesis of extracellular Au nanoparticles with a size from 8 to 12 nm via *S. wightii* has been demonstrated by Singaravelu et al. (2007). Several other algae *Kappaphycu salvarezii* (Rajasulochana et al., 2011), *Fucus vesiculosus* (Mata et al., 2008), *Tetraselmisko chinensis* (Senapati et al., 2012), *Chondrus crispus*, and *Spirogyra insignis* (Castro et al., 2013) have been reported to synthesize Au and Ag nanoparticles (Rajasulochana et al., 2011). By using the living cells of *Euglena gracilis* microalga which have been grown under either mixotropic (exposed to light and grown in an organic carbon-enriched culture medium) or autotropic condition, the gold nanoparticles synthesized were of true yield, kinetics and colloidal stability (Dahoumane et al., 2016).

Nanoparticle Synthesis Using Plants

The plants are considered to be more suitable compared to microbes for green synthesis of nanoparticles as they are non-pathogenic and various pathways are thoroughly researched (**Figure 4**). A wide spectrum of metal nanoparticles has been produced using different plants (Narayanan and Sakthivel, 2011; Iravani and Zolfaghari, 2013; Mittal et al., 2013; Das et al., 2017). These nanoparticles have unique optical, thermal, magnetic, physical, chemical, and electrical properties in comparison to their counterpart bulk material with numerous applications in numerous fields of human interest (Husseiny et al., 2007; Duran and Seabra, 2012). There are various biological entities which are used for AgNPs synthesis (Keat et al., 2015). *Jatroa curcas* extract results in the production of homogenous (10–20 nm) AgNPs from $AgNO_3$ salt in 4 h (Bar et al., 2009). The leaf extracts of *Acalypha indica* have exhibited the capability to synthesize AgNPs. The size of the AgNPs obtained became extensively homogeneous and ranged from 20 to 30 nm (Krishnaraj et al., 2009). In another study, *Medicago sativa* seed exudates were used for the synthesis of AgNPs. The reduction of Ag^+ happened almost immediately as nanoparticles had been reported within a minute of metal salt exposure and 90% of Ag^+ was reduced at 30°C in <50 min. The resulting nanoparticles were flower-like and/or triangular and spherical with a size range of 5–108 nm and had a heterogeneous size distribution (Lukman et al., 2010). The leaf extract of *Ocimum sanctum* can also reduce Ag^+ resulting in the AgNPs of 3–20 nm in size

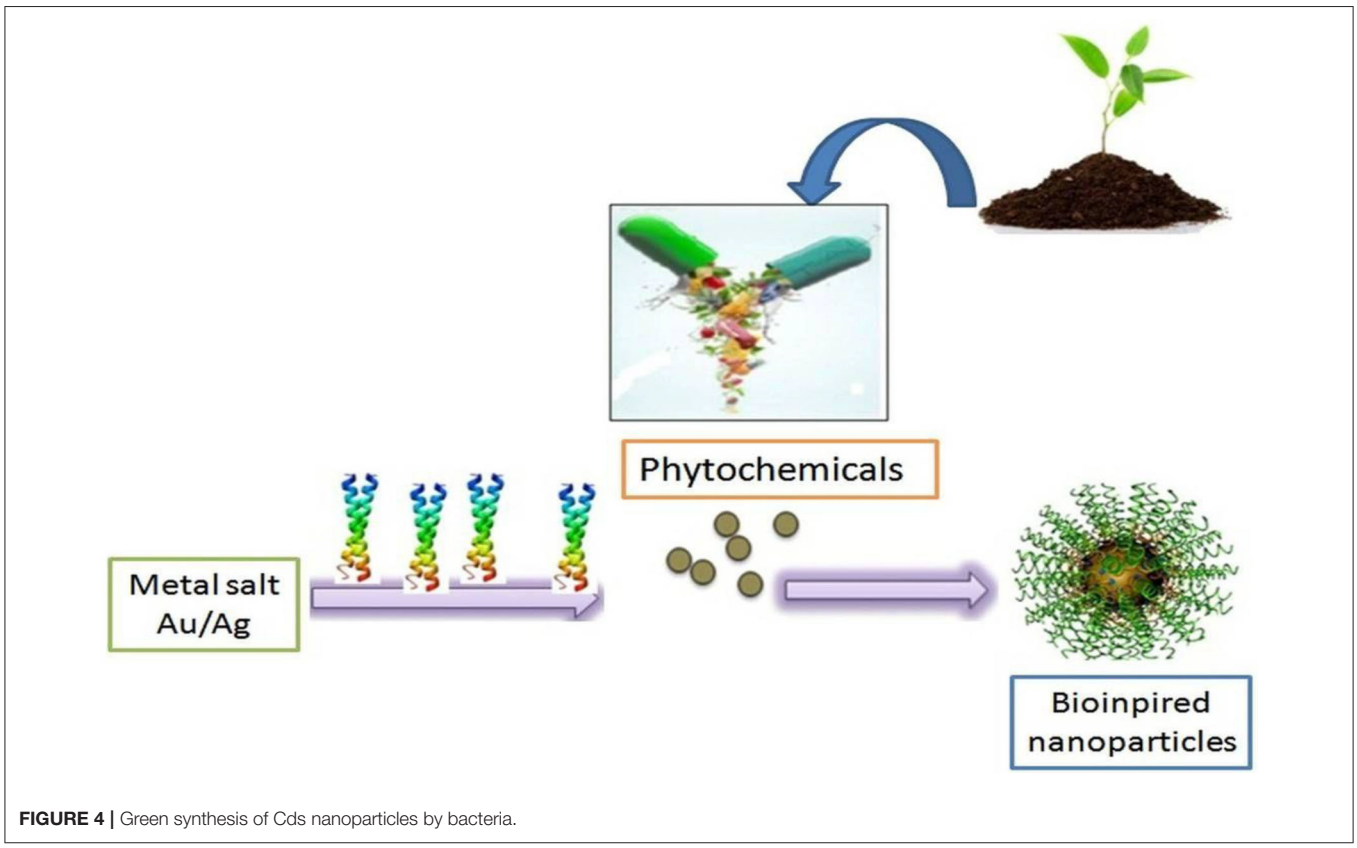

FIGURE 4 | Green synthesis of Cds nanoparticles by bacteria.

production The particles were spherical and stabilized by the way of a component of the leaf broth (Koduru et al., 2011). *Terminalia chebula* fruit extract has been used to promptly produce Ag nanoparticles (Jebakumar Immanuel Edison and Sethuraman, 2012). *Eucalyptus macrocarpa* leaf extract produced Ag nanoparticles of cubic shape ranging in size from 50 to 200 nm (Poinern et al., 2013); spherical gold nanoparticles of around 20 nm by *Nyctanthes arbor tristis* (night jasmine) flower extract (Das et al., 2011); leaf extract from *Coriandrum sativum* (coriander) leaf extract produce Ag and Au nanoparticles of 7–58 nm (Mittal et al., 2013). Phyllanthin extracted from the plant *Phyllanthus amarus* may be used to produce both gold and silver nanoparticles. This study is unique for the use of single constituent of a plant extract to synthesize metallic nanoparticles in comparison to different investigations wherein the whole plant was used (Kasthuri et al., 2008). The shape and size of nanoparticles produced had been affected by the concentration of phyllanthin used. Low concentrations of phyllanthin resulted in the triangular and hexagonal AuNPs formation, whereas higher concentrations produced increased spherical NPs (Kasthuri et al., 2008). Plant derived polysaccharides and phytochemicals nanoparticle (Park et al., 2011), soluble starch (Raveendran et al., 2003), cellulose (Cai et al., 2009), dextran (Ma et al., 2005), chitosan (Laudenslager et al., 2008), alginic acid (Saha et al., 2009), and hyaluronic acid (Kemp et al., 2009) may be harnessed and studied for the synthesis of silver and gold nanoparticles successfully. These compounds offer benefits of using less toxic chemical compounds and render capability to create nanocomposites with different metals. The incubation of the extract from lemon-grass plant, *Cymbopogon flexuosus,* with gold tetrachloride solution resulted in the formation of a unique type of liquid-like nanotriangles by the aggregation of spherical AuNPs, the surface of which forms a complex with the aldehydes and/or ketones present in the plant extract, contributing to the fluidity (Sangaru et al., 2004). The leaf broth of *Azadirachta indica,* forms a complex when dealing with the salts of silver, gold, and then both metallic ions concurrently produced silver, gold, and bimetallic silver-gold NPs. The rate of formation of nanoparticles became faster having attained the plateau in 2 h. The stability of NPs was attributed to the terpenoid and flavanone components of the leaf (Sangaru et al., 2004). Phytochemically reduced NiO NPs with garlic and ginger add on to the increased bactericidal activity toward multiple drug resistant *Staphylococcus aureus* which may address drug resistance issues to an extent (Haider et al., 2020).

Alloying Ag and Au has brought about the formation of bimetallic nanoparticles. Their production entails the competitive reduction between two aqueous solutions having one of a kind of metallic ion precursor used together with a plant extract. The Ag-Au nanoparticle, the core-shell structure is manufactured from Au due to its larger reduction potential, and Ag ions are reduced and form a shell with Ag coalescing on the core. Few plants have been efficiently used to synthesize Ag-Au bimetallic nanoparticles like *Azadirachta indica* (Sangaru et al., 2004), *Anacardium occidentale* (Sheny et al., 2011), *Swieteni amahagony* (Mondal et al., 2010), and cruciferous vegetable extracts (Jacob et al., 2012).

Extracts from various plants have been used to synthesize nanoparticles of copper (Cu) and copper oxide (CuO). Cu nanoparticles varying from 40 to 100 nm in size were synthesized from *Magnolia kobus* leaf extract (Lee et al., 2013) and from *Syzygium aromaticum* (Clove) (Subhankari and Nayak, 2013) showing spherical to granular shape with 40 nm of an average particle size. The Latex from the stem of *Euphorbia nivulia* (Common milk hedge) was used to synthesize an important class of Cu nanoparticles stabilized and coated through terpenoids and peptides of the latex (Valodkar et al., 2011a) and synthesis of a notably stable spherical nanoparticles of CuO was confirmed from *Sterculia urens* (Karaya gum) with a particle size of 4.8 nm (Padil and Cernik, 2013).

The synthesis of the first platinum nanoparticles was demonstrated with the help of Song et al. (2009b) *Diospyros kaki* (Persimmon) leaf extract and carboxylic acids, amines, alcohols. Ketones present in the leaf extract act as a functional group for the reduction of Pt ions. There was 90% reduction of Pt ions into nanoparticles in ∼2.5 h. The possibility of an enzyme mediated process was ruled out due to the temperature of execution of the experiment (95°C) which is high enough to denature proteins. Palladium nanoparticles were synthesized using the extract of *Cinnamon zeylanicum* bark (Sathishkumar et al., 2009a,b) and *Annona squamosa* (custard apple) peel extract for the synthesis of Pd nanoparticles of size 75–85 nm (Roopan et al., 2012). Nanoparticles with a mean size of 15 nm had been synthesized from the leaf extract of soybean (*Glycine max*) (Petla et al., 2012). The extracts from commonly available *Camellia sinensis* (Tea) and *Coffe aarabica* (Coffee) have been utilized to produce nanoparticles of palladium of sizes ranging from 20 to 60 nm with faced centered cubic crystal symmetry (Petla et al., 2012). Furthermore, when an extract of *Gardenia jasminoides* (Cape jasmine) is used to synthesize nanoparticles of palladium the antioxidants (geniposide, chlorogenic acid, crocins, and crocetin) present in the extracts acts as stabilizing and reducing agents (Jia et al., 2009). Other plants like *Ocimum sanctum* leaf extract (Holy basil) (Soundarrajan et al., 2011), plant wood nanomaterials (Lin et al., 2011) and lignin from red pine (*Pinus resinosa*) were used for the synthesis of nanoparticles of platinum and palladium (Coccia et al., 2012).

Nanoparticles of spherical size and ranging in size from 100 to 150 nm from metal oxide which includes titanium dioxide (TiO_2) were synthesized efficaciously using numerous plant extracts *viz. Annona squamosa* peel (Roopan et al., 2012), *Cocos nucifera* coir (Roopan et al., 2013), *Nyctanthes arbor-tristis* leaf extracts (Sundrarajan and Gowri, 2011), *Psidium guajava* (Thirunavukkarasu et al., 2013), *Eclipta prostrata* (Rajakumar et al., 2011; Zahir et al., 2015), and *Catharanthus roseus* (Kanayairam et al., 2011). Spherical shaped zinc oxide (ZnO) nanoparticles were obtained using the latex of *Calotropis procera* (Singh, 2011), *Aloe vera* (Duran and Seabra, 2012), *Physalisalke kengi* (Sangeetha et al., 2011), and *Sedum alfredii* (Qu et al., 2011a,b). Biogenic Indium oxide (In_2O_3) spherical nanoparticles were synthesized with a variable size range from 5 to 50 nm by using leaf extracts from *Aloe vera* (*Aloe barbadensis*) (Laokula et al., 2008).

Iron (Fe) nanoparticles were synthesized by the use of green chemistry methods including the aqueous *Sorghum bicolor* bran extracts (Njagi et al., 2011) and leaf extracts of *Azadirachta indica* (Pattanayak and Nayak, 2013), *Euphorbia milii, Tridax procumbens, Tinospora cordifolia, Datura innoxia, Calotropis procera,* and *Cymbopogon citratus* (Shah et al., 2014). The latex from *Jatropha curcas* has been used to synthesize spherical Pb nanoparticles of sizes from 10 to 12.5 nm (Joglekar et al., 2011). Synthesis of metallic nanoparticles includes the use of the extracts of plant parts or whole plant extracts. Also, metallic nanoparticles may be synthesized inside living plants and a novel approach for the synthesis of PdNPs by the use of *Arabidopsis thaliana* was reportedly developed (Parker et al., 2014) by growing the plant in the usual growth medium, and medium was then replaced with potassium tetrachloropalladate (K_2PdCl_4) followed by the incubation for 24 h in the salt solution. PdNPs of 2–4 nm were produced as visualized by transmission electron microscope. These biologically synthesized PdNPs had been utilized in Suzuki-Miyaura coupling reactions with better catalytic activity as compared to the commercially available PdNPs (Parker et al., 2014). The Alfalfa plant seeds were grown with various concentrations of $K(AuCl_4)$ for 2 weeks for the formation of AuNP nanoparticles (Gardea-Torresdey et al., 2002). The time taken for the synthesis of nanoparticles via this method exceeds 2 weeks, limiting its commercial feasibility. However, if production time is reduced, it might be a great strategy for creating a cheap green method for synthesizing nanoparticles.

Nanoparticle Synthesis Using Viruses

Quantum dots were synthesized by using viruses over the last decade (Dameron et al., 1989; Lee et al., 2002; Mao et al., 2003) for the synthesis of nanomaterials. The outer capsid protein present on the virus offers an attractive function in the synthesis of nanoparticles by supplying a highly reactive surface interacting with metallic ions (Makarov et al., 2014). Tobacco mosaic virus (TMV) has ∼2,130 capsid proteins masking its surface. These proteins act as notch attachments for the material to deposit (Royston et al., 2008; Aljabali et al., 2010; Górzny et al., 2010; Kobayashi et al., 2012) or may be used to synthesize the three-dimensional vessels for multiple applications in the pharmaceutical industry. The addition of Ag or Au salts to low concentrations of TMV prior to including plant extracts of *Nicotiana benthamiana* (Round-leaved native tobacco) or *Hordeum vulgare* (Barley) showed a decrease in the size of the synthesized nanoparticles. Additionally it accelerated their numbers as compared to those having no viral supplement (Love et al., 2014) showing relatively small free nanoparticles formation at higher TMV concentrations. TMV also served as a bio-template to form nanowires by using metallization. The unexplored potential of viruses in the manufacture of nanometer scale structures of different varieties have been reported elsewhere (Shenton et al., 1999; Merzlyak and Lee, 2006). They deliver inorganic substances such as cadmium sulfide (CdS), silicon dioxide (SiO_2), zinc sulfide (ZnS), and iron oxide (Fe_2O_3). Semiconductor substances such as CdS and ZnS are utilized in electronic goods and therefore hold importance in the electronics industry.

TABLE 1 | Factors affecting biological synthesis of metal nanoparticles.

S. No	Factors	Influence on biological synthesis of metal nanoparticles	References
1.	pH	Size and shape of the synthesized nanoparticle	Dubey et al., 2010; Sathishkumar et al., 2010
2.	Reactant concentration	Shape of the synthesized nanoparticles	Chandran et al., 2006
3.	Reaction time	Size and shape of the synthesized nanoparticle	Tc et al., 2011
4.	Reaction temperature	Size, shape, yield and stability of the synthesized nanoparticle	Song et al., 2009a; Sathishkumar et al., 2010

FACTORS AFFECTING BIOLOGICAL SYNTHESIS OF METAL NANOPARTICLES

The morphological characteristics of nanoparticles can be manipulated by means of various parameters *viz*. reaction time, reactant concentrations, pH, and temperature (**Table 1**). Such parameters are crucial to understand the effect of environmental factors for the synthesis of NP as they may play an important role during the optimization of metallic NPs synthesis by biological means.

pH

The reaction medium pH plays an critical role in the formation of nanoparticles (Gardea-Torresdey et al., 1999). Size and shape of nanoparticles vary with the pH of the medium, and large sized nanoparticles are produced in acidic pH (Dubey et al., 2010; Sathishkumar et al., 2010). The rod-shaped gold nanoparticles were synthesized by using biomass of *Avena sativa* (Oat) resulting in the size range from 25 to 85 nm at pH 2 which was comparatively smaller (5–20 nm) at pH 3 and 4 (Armendariz et al., 2004). Further, accessibility of functional groups for particle nucleation in the extract was better at pH 3 or 4 as compared to the pH 2 as fewer functional groups were available prompting particle aggregation to form larger Au nanoparticles. An increased number of spherical Ag nanoparticles were synthesized in *Cinnamon zeylanicum* bark extract at higher pH (pH >5) (Kumar and Yadav, 2009). A slight increase was observed in particle size at higher pH when *Cinnamon zeylanicum* bark extract was used for the synthesis of palladium (Pd) nanoparticles, and particle size was estimated from 15 to 20 nm at pH <5, and 20–25 nm at the higher pH (Kumar and Yadav, 2009).

Reactant Concentration

The formation of metallic nanoparticles is affected by the concentration of biomolecules present in the extract. The shape of the biosynthesized Au and Ag nanoparticles by using the sun-dried *Cinnamomum camphora* (camphor) leaf extract affected by the amount of biomass in the reaction medium (Huang et al., 2007). Exposure of the precursor chloroauric acid to

growing concentrations of the extract resulted in the synthesis of spherical nanoparticles instead of triangular. A change in the ratio of spherical nanoparticles to triangular plates in the reaction medium having chloroaurate ions due to the presence of carbonyl compounds in the extract was observed when treated with varying concentrations of *Aloe vera* leaf extract (Chandran et al., 2006). Nanoparticle size can be modulated between 50 and 350 nm by using different extract concentrations (Chandran et al., 2006). Spherical, triangular, hexagonal, and decahedral shapes of AgNPs were produced by varying the concentration of *Plectranthu samboinicus* leaf extract in the reaction medium (Narayanan and Sakthivel, 2010). An increase in the variety of Ag nanoparticles was observed with increasing concentration of *Cinnamon zeylanicum* bark extract (Kumar and Yadav, 2009). The extracellular (Agnihotri et al., 2009) and intracellular synthesis (Pimprikar et al., 2009) of Au nanoparticles was affected by biomass and Au salt concentration using marine yeast, *Yarrowia lipolytica*. An increased Au salt concentration produced both nanoscale spheres and plates. In another study, a silver-tolerant yeast strain MKY3 synthesized spherical Ag nanoparticles extra-cellularly with the size ranging from 2 to 5 nm (Kowshik et al., 2003).

Reaction Time

The reaction time plays an important role for synthesizing nanoparticles (Ahmad, 2012). A rapid color change was observed within 2 min when *Anana scomosus* (Pineapple) extract was used for AgNPs synthesis, and aqueous $AgNO_3$ solution was rapidly decreased, forming nanoparticles within 2 min. The reaction continued for up to 5 min and then there was a slight color change. The shape of synthesized nanoparticles was spherical with a mean size of 12 nm (Ahmad, 2012). *Chenopodium album* leaf extract was used for the biogenic production of Ag and Au nanoparticles. The nanoparticles were formed within 15 min of the reaction and the reaction continued over a period of 2 h and very few nanoparticles with larger size were synthesized (Dwivedi and Gopal, 2010). Change in the particle size (ranging 10–35 nm) was observed when reaction time was increased from 30 min to 4 h using *Azadirachta indica* leaf extract and $AgNO_3$ (Tc et al., 2011).

Reaction Temperature

The reaction temperature is a critical component which plays a key role in determining the shape, size, and yield of synthesized nanoparticles using plants (Song et al., 2009a; Sathishkumar et al., 2010). The peel extract of *Citrus sinensis* (sweet orange) produced particles with an average size of around 35 nm at 25°C. The average size of the nanoparticles decreased to 10 nm with the rise in the reaction temperature to 60°C (Kaviya et al., 2011). The stable Ag nanoparticles were synthesized by *Diospyros kaki* (persimmon) leaf extract at the reaction temperature varying from 25 to 95°C (Song et al., 2009b). The variation in the temperature of reaction conditions for the synthesis of Au nanoparticles using *Avena sativa* (oat) biomass ended in modifications in the shape and size of the nanoparticles produced (Armendariz et al., 2004). A higher temperature supports an increased rate of formation of Au nanoparticles. The spherical Au nanoparticles were predominantly formed at the lower temperature whereas at higher temperatures rod-like and plate-like nanoparticles were formed (Gericke and Pinches, 2006a,b). The reaction rate and particle formation rate increased with the increase in the reaction temperature. The particle conversion rate steadily increased and average particle size saw a decrease with the rise in the reaction temperature to 60°C.

The extracellularly produced PtNPs amount was reported to be 5.66 mg l^{-1} (Riddin et al., 2006), with the variation in the temperature that affects production rates of the PtNPs. The slight change in pH from the standard inhibits the PtNPs formation (Riddin et al., 2006).

APPLICATIONS OF METALLIC NANOPARTICLES SYNTHESIZED BY GREEN TECHNOLOGY

Nanoparticles have wide applications in both biomedical and physicochemical fields. They may be used for drug delivery, biosensing, bio-imaging, and biomolecular recognition (**Figure 5**) in bio-medical research. Such nanoparticles are integrated in various materials of everyday use which includes cosmetics, toothpaste, deodorants, water purification systems, and humidifiers due to their anti-microbial properties (Baker et al., 2005). They have an important role to play in agriculture technology such as detection and abatement of plant diseases and minimizing nutrient leaching to increase the crop yield. They are also used in solar and oxide batteries for energy storage.

Gold and Silver Nanoparticles

The variation in shape, size, and surface properties of Au nanoparticles (Wang et al., 2005; Ghosh and Pal, 2007; Cai et al., 2008; Alexandridis, 2011; Shivaji et al., 2014) makes them very beneficial for their potential applications within the area of biosensors (Chan and Nie, 1998; Kreibig and Vollmer, 2013), hyperthermia therapy (Huang et al., 2006), delivery systems for therapeutic drugs and genetic materials (Paciotti et al., 2004), as well as anti-bacterial drugs (Sondi and Salopek-Sondi, 2004; Hsiao et al., 2006). Gold nanoparticles from *Sesbaniadrum mondii* (rattlebush) have shown the catalytic activity that may be beneficial in the reduction of aromatic nitro compounds in waste decontamination.

The rise in antibiotic resistance among pathogenic bacteria has highlighted the antibacterial properties of nanoparticles and their ability to be used as new medical tools. The antimicrobial activity of Ag is widely known and is used in multiple medical preparations against pathogens (Sondi and Salopek-Sondi, 2004; Kumar and Yadav, 2009; Sotiriou and Pratsinis, 2011). The anti-bacterial properties of AbNPs have allowed for their extensive use in food storage, the health industry, textile coatings and several environmental applications. Silver nanoparticles synthesized by the use of *Tridax procumbens* (tridax daisy) extract have robust antibacterial activity toward *Escherichia coli*, *Shigella dysenteriae*, and *Vibrio cholera* (Dhanalakshmi and Rajendran, 2012). Silver nanoparticles obtained by using *Pinusthun bergii* (Japaneseblack pine) cone extracts exhibit antibacterial activity

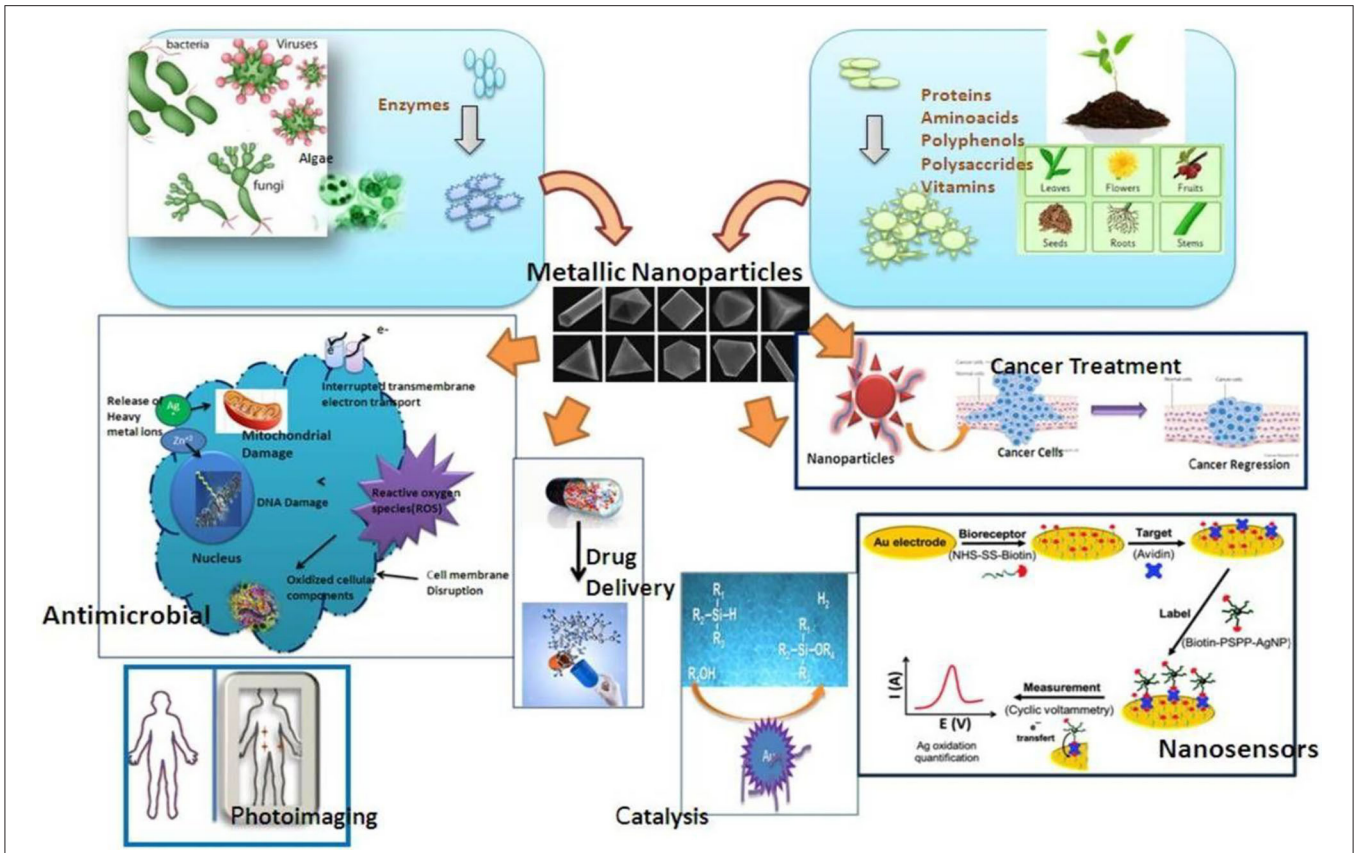

FIGURE 5 | Application of Green synthesis of metallic nanoparticles.

against diverse Gram-negative and Gram-positive agricultural pathogens (Velmurugan et al., 2012), and the antifungal effect of Ag nanoparticles has been confirmed (Vivek et al., 2011). Their utility as antifungal agents is found to be safer as compared to the conventional fungicides (Park et al., 2011). Ag nanoparticles interact closely with the bacterial cell membrane due to their high surface area to volume ratio as well as size (Chen and Schluesener, 2008). Recent antimicrobial studies of Ag nanoparticles have shown that they can cause significant membrane damage and DNA toxicity via bio-sorption and cellular uptake (Brayner et al., 2006; Simon-Deckers et al., 2009). AgNPs are already in-use as antimicrobial agents in many commercially available medical and consumer goods. Despite decades of its use, it is important to note that the evidence of the silver toxicity is not yet fully explored. Their applications have been discovered both in the field of medicine and home remedies. Silver sulfadiazine creams are often used to prevent burn site infection and some companies have also built silver into their washing machines. Presently, silver seems be a part of many consumer products such as computer keyboards, acne creams, and clothing (e.g., socks and athletic wear) that protects the wearer from emitting body odor further to deodorizing sprays. A range of organizations that offer accreditation like US-FDA, US-EPA, Korea's Testing, SIAA of Japan and Research Institute for Chemical Industry and FITI Testing and Research Institute have approved products containing silver nanoparticles (Veeraputhiran, 2013). The silver nanoparticles also display an anti-tumorigenic ability due to their cytotoxic activity against various tumor cells. The growth and survival of HeLa cells were inhibited by the silver nanoparticles synthesized from *Iresine herbstii* (Herbst's bloodleaf). AgNPs produced by latex extracts of *Euphorbia nivulia* (leafy milk hedge) exhibited toxicity toward the human lung cancer cells (A549) (Valodkar et al., 2011b). *Nerium oleander* (oleander) extracted silver nanoparticle displayed robust larvicidal activity against malaria vector larvae (Suganya et al., 2013), as optical sensors that form small molecule adsorbates (McFarland and Duyne, 2003), as selective and sensitive nanoscale affinity biosensors to investigate the transport across the membrane of living microbial cells (*P. aeruginosa*) in real time (Xu et al., 2004). Silver nanoparticles and their composites demonstrate better catalytic activities in dye reduction and their elimination (Kundu et al., 2002; Mallick et al., 2006).

Copper and Copper Oxide Nanoparticles

The nanoparticles of CuO display anti-oxidant, anti-bacterial, and antimicrobial activity against common pathogenic strains such as *Escherichia coli* and *Staphylococcus aureus* and are shown to have tremendous application potential (Heinlaan et al., 2008;

Das et al., 2012; Padil and Cernik, 2013). Cu nanoparticles have antibacterial potential against common pathogenic bacteria *Escherichia coli* (Lee et al., 2011). They have functional decontaminating properties against several infectious micro-organisms with the potential to be used as bactericidal material (Akhavan and Ghaderi, 2010; Hassan et al., 2012; Subhankari and Nayak, 2013). The Cu nanoparticles synthesized by stem latex of *Euphorbia nivulia* were seen toxic to human lung cancer cells (A549) (Valodkar et al., 2011c) surfacing the their potential application in the field of cancer therapy.

Palladium and Platinum Nanoparticles

The catalytic activity of platinum nanoparticles extracted from *Ocimum sanctum* (Holy basil) for the electrolysis of water to produce hydrogen fuel elements has been studied (Soundarrajan et al., 2011). A few Pt nanoparticle based catalysts show elevated activity for the electro-oxidation of formic acid used for the cleaning of surroundings (Waszczuk et al., 2002).

Titanium Dioxide and Zinc Oxide Nanoparticles

TiO_2 suspensions have been explored successfully for both adulticidal and larvicidal properties against *Hippobosca maculate* (hematophagous fly) and *Bovicolaovis* (sheep louse) (Kanayairam et al., 2011). TiO_2 nanoparticles synthesized from the extract of *Psidium guajava* confirmed the effective antibacterial activity against *Aeromona shydrophila, Escherichia coli, Proteus mirabilis, Pseudomonas aeruginosa*, and *Staphylococcus aureus,* pathogens with strong antioxidant behaviors (Heinlaan et al., 2008; Thirunavukkarasu et al., 2013). TiO_2 oxide nanoparticles have shown applications in the biomedical industry, disinfection of waste water, and beauty products. ZnO nanoparticles additionally possess antibacterial activity that was used in waste water treatments and food packaging (Espitia et al., 2012). Biogenic ZnO nanoparticles can be used as a drug delivery vehicle for doxorubicin (Vimala et al., 2013). The nanoparticles of magnetite were used in biomedical applications such as magnetic resonance imaging (Sun and Zeng, 2002; You et al., 2013) and oscillation damping and position sensing (Thapa et al., 2004). Furthermore, afore-mentioned NPs have many non-medical applications that include magnetic recording devices.

CONCLUSION AND FUTURE PERSPECTIVE

Green synthesis technology presents a clean, non-toxic and eco-friendly technique for the synthesis of metallic nanoparticles and is of enormous interest due to economic prospects and feasibility. However, protocols need to be modified further for making these methods cost-effective and comparable with traditional methods for the large-scale production of nanoparticles. Improvement of reliable and eco-friendly processes for the synthesis of metallic nanoparticles is a significant step in the field of applied nanotechnology. Further, most of these strategies are still under the developmental stage and challenges need to be taken care of. These encompass stability and aggregation of nanoparticles, managing the crystal growth, morphology and size. The separation and purification of nanoparticles is another vital parameter which needs to be explored further. Metal nanoparticles produced by the plants and/or plant extracts are more stable as compared to those produced through different organisms. Genetically modified organisms (GMO) have tremendous capability to optimize for generating a greater quantity of proteins, enzymes, and biomolecules required for the biosynthesis and stabilization of nanoparticles. We believe genetic change to enhance the metal tolerance and accumulation capacity is the future approach to enhance the production of metal nanoparticles by adopting the "green synthesis" approach.

AUTHOR CONTRIBUTIONS

DZ and G-wZ conceived the idea, designed study, executed, and wrote the paper. X-lM, YG, HH, and G-wZ helped during formulation of this article and approved. All authors contributed to the article and approved the submitted version.

REFERENCES

Agnihotri, M., Joshi, S., Kumar, A., Zinjarde, S., and Kulkarni, S. (2009). Biosynthesis of gold nanoparticles by the tropical marine yeast *Yarrowia lipolytica* NCIM 3589. *Mater. Lett.* 63, 1231–1234. doi: 10.1016/j.matlet.2009.02.042

Ahmad, A., Mukherjee, P., Mandal, D., Senapati, S., Khan, M. I., Kumar, R., et al. (2002). Enzyme mediated extracellular synthesis of CdS nanoparticles by the fungus, *Fusarium oxysporum*. *J. Am. Chem. Soc.* 124, 12108–12109. doi: 10.1021/ja027296o

Ahmad, A., Senapati, S., Islam Khan, M., Kumar, R., Ramani, R., Srinivas, V., et al. (2003b). Intracellular synthesis of gold nanoparticles by a novel alkalotolerant actinomycete, *Rhodococcus* species. *Nanotechnology* 14:824. doi: 10.1088/0957-4484/14/7/323

Ahmad, A., Senapati, S., Khan, M., Kumar, R., and Sastry, M. (2005). Extra-/intracellular biosynthesis of gold nanoparticles by an alkalotolerant fungus, *Trichothecium* sp. *J. Biomed. Nanotechnol.* 1, 47–53. doi: 10.1166/jbn.2005.012

Ahmad, A., Senapati, S., Khan, M. I., Kumar, R., and Sastry, M. (2003a). Extracellular biosynthesis of monodisperse gold nanoparticles by a novel extremophilic actinomycete, *Thermomonospora* sp. *Langmuir* 19, 3550–3553. doi: 10.1021/la026772l

Ahmad, N. (2012). Green synthesis of silver nanoparticles using extracts of *Ananas comosus*. *Green Sustain. Chem.* 2, 141–147. doi: 10.4236/gsc.2012.24020

Akhavan, O., and Ghaderi, E. (2010). Cu and CuO nanoparticles immobilized by silica thin films as antibacterial materials and photocatalysts. *Surf. Coat. Technol.* 205, 219–223. doi: 10.1016/j.surfcoat.2010.06.036

Alexandridis, P. (2011). Gold nanoparticle synthesis, morphology control, and stabilization facilitated by functional polymers. *Chem. Eng. Technol.* 34, 15–28. doi: 10.1002/ceat.201000335

Aljabali, A., Barclay, J., Lomonossoff, G., and Evans, D. (2010). Virus templated metallic nanoparticles. *Nanoscale* 2, 2596–2600. doi: 10.1039/c0nr00525h

Al-Katib, M., Al-Shahri, Y., and Al-Niemi, A. (2015). Biosynthesis of silver nanoparticles by cyanobacterium *Gloeocapsa* sp. *Int. J. Enhanced Res. Sci. Technol. Eng.* 4, 60–73.

Armendariz, V., Herrera, I., Peralta-Videa, J., Yacaman, M., Troiani, H., Santiago, P., et al. (2004). Size controlled gold nanoparticle formation by avena sativa biomass: use of plants in nanobiotechnology. *J. Nanoparticle Res.* 6, 377–382. doi: 10.1007/s11051-004-0741-4

Baco-Carles, V., Datas, L., and Tailhades, P. (2011). Copper nanoparticles prepared from oxalic precursors. *ISRN Nanotechnol.* 2011:729594. doi: 10.5402/2011/729594

Baker, C., Pradhan, A., Pakstis, L., Pochan, D., and Shah, S. (2005). Synthesis and antibacterial properties of silver nanoparticles. *J. Nanosci. Nanotechnol.* 5, 244–249. doi: 10.1166/jnn.2005.034

Bar, H., Bhui, D., Sahoo, G., Sarkar, P., De, S., and Misra, A. (2009). Green synthesis of silver nanoparticles using latex of *Jatropha curcas*. *Colloids Surf. A Physicochem. Eng. Asp.* 339, 134–139. doi: 10.1016/j.colsurfa.2009.02.008

Bhainsa, K., and D'Souza, S. (2006). Extracellular biosynthesis of silver nanoparticles using the fungus *Aspergillus fumigatus*. *Colloids Surf. B Biointerfaces* 47, 160–164. doi: 10.1016/j.colsurfb.2005.11.026

Bharde, A., Rautaray, D., Bansal, V., Ahmad, A., Sarkar, I., Yusuf, S., et al. (2006). Extracellular biosynthesis of magnetite using fungi. *Small* 2, 135–141. doi: 10.1002/smll.200500180

Bhattacharya, D., and Gupta, R. (2005). Nanotechnology and potential of microorganisms. *Crit. Rev. Biotechnol.* 25, 199–204. doi: 10.1080/07388550500361994

Bisen, P., Gour, R., Jain, R., Dev, A., and Sengupta, L. (1996). VAM colonization in tree species planted in Cu, Al, and coal mines of Madhya Pradesh with special reference to glomus mosseae. *Mycorrhiza News* 8, 9–11.

Bisen, P. S., Shukla, H. D., Gupta, A., and Bagchi, S. N. (1987). Preliminary characterization of a novel synechococcus isolate showing mercury, cadmium and lead tolerance. *Environ. Technol. Lett.* 8, 427–432. doi: 10.1080/09593338709384501

Brayner, R., Ferrari-Iliou, R., Brivois, N., Djediat, S., Benedetti, M. F., and Fiévet, F. (2006). Toxicological impact studies based on *Escherichia coli* bacteria in ultrafine ZnO nanoparticles colloidal medium. *Nano Lett.* 6, 66–870. doi: 10.1021/nl052326h

Cai, J., Kimura, S., Wada, M., and Kuga, S. (2009). Nanoporous cellulose as metal nanoparticles support. *Biomacromolecules* 10, 87–94. doi: 10.1021/bm800919e

Cai, W., Gao, T., Hong, H., and Sun, J. (2008). Applications of gold nanoparticles in cancer nanotechnology. *Nanotechnol. Sci. Appl.* 1, 17–32. doi: 10.2147/NSA.S3788

Castro, L., Blázquez, M. L., Muñoz, J., González, F., and Ballester, A. (2013). Biological synthesis of metallic nanoparticles using algae. *IET Nanobiotechnol.* 7, 109–116. doi: 10.1049/iet-nbt.2012.0041

Castro, L., Blázquez, M. L., Muñoz, J., González, F., García-Balboa, C., and Ballester, A. (2011). Biosynthesis of gold nanowires using sugar beet pulp. *Process Biochem.* 46, 1076–1082. doi: 10.1016/j.procbio.2011.01.025

Cepoi, L., Ludmila, R., Chiriac, T., Valuta, A., Zinicovscaia, I., Duca, G., et al. (2014). Biochemical changes in cyanobacteria during the synthesis of silver nanoparticles. *Can. J. Microbiol.* 61, 1–9. doi: 10.1139/cjm-2014-0450

Chan, W. C. W., and Nie, S. (1998). Quantum dot bioconjugates for ultrasensitive nonisotopic detection. *Science* 281, 2016–2018. doi: 10.1126/science.281.5385.2016

Chandran, S., Chaudhary, M., Pasricha, R., Ahmad, A., and Sastry, M. (2006). Synthesis of gold nanotriangles and silver nanoparticles using *Aloe vera* plant extract. *Biotechnol. Prog.* 22, 577–583. doi: 10.1021/bp0501423

Chen, X., and Schluesener, H. (2008). Nanosilver: a nanoproduct in medical application. *Toxicol. Lett.* 176, 1–12. doi: 10.1016/j.toxlet.2007.10.004

Coccia, F., Tonucci, L., Bosco, D., Bressan, M., and d'Alessandro, N. (2012). One-pot synthesis of lignin-stabilised platinum and palladium nanoparticles and their catalytic behaviour in oxidation and reduction reactions. *Green Chem.* 14, 1073–1078. doi: 10.1039/c2gc16524d

Dahoumane, S. A., Yepremian, C., Djediat, C., Couté A., Fiévet, F., Coradin, T., et al. (2016). Improvement of kinetics, yield, and colloidal stability of biogenic gold nanoparticles using living cells of *Euglena gracilis* microalga. *J. Nanoparticle Res.* 18:79. doi: 10.1007/s11051-016-3378-1

Dameron, C. T., Reese, R. N., Mehra, R. K., Kortan, A. R., Carroll, P. J., Steigerwald, M. L., et al. (1989). Biosynthesis of cadmium sulphide quantum semiconductor crystallites. *Nature* 338, 596–597. doi: 10.1038/338596a0

Das, D., Nath, B., Phukon, P., and Dolui, S. (2012). Synthesis and evaluation of antioxidant and antibacterial behavior of CuO nanoparticles. *Colloids Surf. B Biointerfaces* 101C, 430–433. doi: 10.1016/j.colsurfb.2012.07.002

Das, D. R. K., Gogoi, N., and Bora, U. (2011). Green synthesis of gold nanoparticles using *Nyctanthes arbortristis* flower extract. *Bioprocess Biosyst. Eng.* 34, 615–619. doi: 10.1007/s00449-010-0510-y

Das, R. K., Pachapur, V. L., Lonappan, L., Naghdi, M., Pulicharla, R., Maiti, S., et al. (2017). Biological synthesis of metallic nanoparticles: plants, animals and microbial aspects. *Nanotechnol. Environ. Eng.* 2:18. doi: 10.1007/s41204-017-0029-4

Das, V. L., Thomas, R., Varghese, R. T., Soniya, E. V., Mathew, J., and Radhakrishnan, E. K. (2014). Extracellular synthesis of silver nanoparticles by the bacillus strain CS 11 isolated from industrialized area. *3 Biotech* 4, 121–126. doi: 10.1007/s13205-013-0130-8

Deplanche, K., Caldelari, I., Mikheenko, I., Sargent, F., and Macaskie, L. (2010). Involvement of hydrogenases in the formation of highly catalytic Pd(0) nanoparticles by bioreduction of Pd(II) using *Escherichia coli* strains. *Microbiology* 156, 2630–2640. doi: 10.1099/mic.0.036681-0

Dhanalakshmi, T., and Rajendran, S. (2012). Synthesis of silver nanoparticles using *Tridax procumbens* and its antimicrobial activity. *Arch. Appl. Sci. Res.* 4, 1289–1293. Available online at: https://www.scholarsresearchlibrary.com/articles/synthesis-of-silver-nanoparticles-using-tridax-procumbens-and-its-antimicrobial-activity.pdf

Dubey, S., Lahtinen, M., and Sillanpää M. (2010). Tansy fruit mediated greener synthesis of silver and gold nanoparticles. *Process Biochem.* 45, 1065–1071. doi: 10.1016/j.procbio.2010.03.024

Duran, N., and Seabra, A. (2012). Metallic oxide nanoparticles: state of the art in biogenic syntheses and their mechanisms. *Appl. Microbiol. Biotechnol.* 95, 275–288. doi: 10.1007/s00253-012-4118-9

Dwivedi, A., and Gopal, K. (2010). Biosynthesis of silver and gold nanoparticles using *Chenopodium album* leaf extract. *Colloids Surf. A Physicochem. Eng. Asp.* 369, 27–33. doi: 10.1016/j.colsurfa.2010.07.020

Espitia, P., Soares, N., Coimbra, J., Andrade, N., Cruz, R., and Medeiros, E. (2012). Zinc oxide nanoparticles: synthesis, antimicrobial activity and food packaging applications. *Food Bioprocess Technol.* 5, 1447–1464. doi: 10.1007/s11947-012-0797-6

Eustis, S., and El-Sayed, M. (2006). Why gold nanoparticles are more precious than pretty gold: noble metal surface plasmon resonance and its enhancement of the radiative and nonradiative properties of nanocrystals of different shapes. *Chem. Soc. Rev.* 35, 209–217. doi: 10.1039/B514191E

Gahlawat, G., and Roy Choudhury, A. (2019). A review on the biosynthesis of metal and metal salt nanoparticles by microbes. *RSC Adv.* 9, 12944–12967. doi: 10.1039/C8RA10483B

Gardea-Torresdey, J., Parsons, J., Gomez, E., Peralta-Videa, J., Troiani, H., Santiago, P., et al. (2002). Formation and growth of Au nanoparticles inside live alfalfa plants. *Nano Lett.* 2:397. doi: 10.1021/nl015673+

Gardea-Torresdey, J. L., Tiemann, K. J., Gamez, G., Dokken, K., Tehuacanero, S., and José-Yacamán, M. (1999). Gold nanoparticles obtained by bio-precipitation from gold(III) solutions. *J. Nanoparticle Res.* 1, 397–404. doi: 10.1023/A:1010008915465

Gericke, M., and Pinches, A. (2006a). Microbial production of gold nanoparticles. *Gold Bull.* 39, 22–28. doi: 10.1007/BF03215529

Gericke, M., and Pinches, A. (2006b). Biological synthesis of metal nanoparticles. *Hydrometallurgy* 83, 132–140. doi: 10.1016/j.hydromet.2006.03.019

Ghosh, S., and Pal, T. (2007). Interparticle coupling effect on the surface plasmon resonance of gold nanoparticles: from theory to applications. *Chem. Rev.* 107, 4797–4862. doi: 10.1021/cr0680282

Górzny, M., Walton, A., and Evans, S. (2010). Catalysis: synthesis of high-surface-area platinum nanotubes using a viral template. *Adv. Funct. Mater.* 20. doi: 10.1002/adfm.201090031

Govindaraju, K., Kiruthiga, V., Kumar, G., and Singaravelu, G. (2009). Extracellular synthesis of silver nanoparticles by a marine alga, *Sargassum wightii* grevilli and their antibacterial effects. *J. Nanosci. Nanotechnol.* 9, 5497–5501. doi: 10.1166/jnn.2009.1199

Gupta, R., and Xie, H. (2018). Nanoparticles in daily life: applications, toxicity and regulations. *J. Environ. Pathol. Toxicol. Oncol.* 37, 209–230. doi: 10.1615/JEnvironPatholToxicolOncol.2018026009

Haider, A., Ijaz, M., Ali, S., Haider, J., Imran, M., Majeed, H., et al. (2020). Green synthesized phytochemically (*Zingiber officinale* and *Allium sativum*) reduced nickel oxide nanoparticles confirmed bactericidal and catalytic potential. *Nanoscale Res. Lett.* 15:50. doi: 10.1186/s11671-020-3283-5

Hamouda, R., Hussein, M., Abo-elmagd, R., and Bawazir, S. (2019). Synthesis and biological characterization of silver nanoparticles derived

from the cyanobacterium *Oscillatoria limnetica*. *Sci. Rep*. 9:13071. doi: 10.1038/s41598-019-49444-y

Hassan, M. S., Amna, T., Yang, O. B., El-Newehy, M., Al-Deyab, S., and Khil, M. S. (2012). Smart copper oxide nanocrystals: synthesis, characterization, electrochemical and potent antibacterial activity. *Colloids Surf. B Biointerfaces* 97, 201–206. doi: 10.1016/j.colsurfb.2012.04.032

He, S., Guo, Z., Zhang, Y., Zhang, S., and Ning, G. (2007). Biosynthesis of gold nanoparticles using the bacteria *Rhodopseudomonas capsulata*. *Mater. Lett.* 61, 3984–3987. doi: 10.1016/j.matlet.2007.01.018

Heinlaan, M., Ivask, A., Blinova, I., Dubourguier, H.-C., and Kahru, A. (2008). Toxicity of nanosized and bulk ZnO, CuO and TiO_2 to bacteria *Vibrio fischeri* and crustaceans *Daphnia magna* and *Thamnocephalus platyurus*. *Chemosphere* 71, 1308–1316. doi: 10.1016/j.chemosphere.2007.11.047

Hsiao, M.-T., Chen, S.-F., Shieh, D.-B., and Yeh, C.-S. (2006). One-pot synthesis of hollow Au_3Cu1 spherical-like and biomineral botallackite $Cu_2(OH)_3Cl$ flowerlike architectures exhibiting antimicrobial activity. *J. Phys. Chem. B* 110, 205–210. doi: 10.1021/jp054827x

Hua, S., de Matos, M. B. C., Metselaar, J. M., Storm, G. (2018). Current trends and challenges in the clinical translation of nanoparticulate nanomedicines: pathways for translational development and commercialization. *Front. Pharmacol*. 9:790. doi: 10.3389/fphar.2018.00790

Huang, J., Li, Q., Sun, D., Lu, Y., Su, Y., Yang, X., et al. (2007). Biosynthesis of silver and gold nanoparticles by novel sundried *Cinnamomum camphora* leaf. *Nanotechnology* 18:105104. doi: 10.1088/0957-4484/18/10/105104

Huang, X., Jain, P., El-Sayed, I., and El-Sayed, M. (2006). Determination of the minimum temperature required for selective photothermal destruction of cancer cells with the use of immunotargeted gold nanoparticles. *Photochem. Photobiol.* 82, 412–417. doi: 10.1562/2005-12-14-RA-754

Hulkoti, N., and Taranath, T. (2014). Biosynthesis of nanoparticles using microbes-a review. *Colloids Surf. B Biointerfaces* 121, 474–483. doi: 10.1016/j.colsurfb.2014.05.027

Husain, S., Sardar, M., and Fatma, T. (2015). Screening of cyanobacterial extracts for synthesis of silver nanoparticles. *World J. Microbiol. Biotechnol.* 31, 1279–1283. doi: 10.1007/s11274-015-1869-3

Husseiny, M., El-Aziz, M., Badr, Y., and Mahmoud, M. (2007). Biosynthesis of gold nanoparticles using *Pseudomonas aeruginosa*. *Spectrochim. Acta A* 67, 1003–1006. doi: 10.1016/j.saa.2006.09.028

Iravani, S., and Zolfaghari, B. (2013). Green synthesis of silver nanoparticles using pinus eldarica bark extract. *Biomed Res. Int.* 2013:639725. doi: 10.1155/2013/639725

Jacob, J., Mukherjee, T., and Kapoor, S. (2012). A simple approach for facile synthesis of Ag, anisotropic Au and bimetallic (Ag/Au) nanoparticles using cruciferous vegetable extracts. *Mater. Sci. Eng. C* 32, 1827–1834. doi: 10.1016/j.msec.2012.04.072

Jain, N., Bhargava, A., Majumdar, S., Tarafdar, J., and Panwar, J. (2010). Extracellular biosynthesis and characterization of silver nanoparticles using aspergillus flavusNJP08: a mechanism perspective. *Nanoscale* 3, 635–641. doi: 10.1039/C0NR00656D

Jebakumar Immanuel Edison, T. N., and Sethuraman, M. (2012). Instant green synthesis of silver nanoparticles using *Terminalia chebula* fruit extract and evaluation of their catalytic activity on reduction of methylene blue. *Process Biochem.* 47, 1351–1357. doi: 10.1016/j.procbio.2012.04.025

Jia, L., Zhang, Q., Li, Q., and Song, H. (2009). The biosynthesis of palladium nanoparticles by antioxidants in *Gardenia jasminoides* ellis: long lifetime nanocatalysts for p-nitrotoluene hydrogenation. *Nanotechnology* 20:385601. doi: 10.1088/0957-4484/20/38/385601

Joglekar, S., Kodam, K., Dhaygude, M., and Hudlikar, M. (2011). Novel route for rapid biosynthesis of lead nanoparticles using aqueous extract of *Jatropha curcas* L. *latex. Mater. Lett.* 65, 3170–3172. doi: 10.1016/j.matlet.2011.06.075

Johnston, C. W., Wyatt, M. A., Li, X., Ibrahim, A., Shuster, J., Southam, G., et al. (2013). Gold biomineralization by a metallophore from a gold-associated microbe. *Nat. Chem. Biol.* 9, 241–243. doi: 10.1038/nchembio1179

Kahzad, N., and Salehzadeh, A. (2020). Green synthesis of $CuFe_2O_4$@Ag nanocomposite using the *Chlorella vulgaris* and evaluation of its effect on the expression of norA efflux pump gene among *Staphylococcus aureus* strains. *Biol. Trace Elem. Res* 198:359–370. doi: 10.1007/s12011-020-02055-5

Kalimuthu, K., Babu, R., Venkataraman, D., and Gurunathan, S. (2008). Biosynthesis of silver nanocrystals by *Bacillus licheniformis*. *Colloids Surf. B Biointerfaces* 65, 150–153. doi: 10.1016/j.colsurfb.2008.02.018

Kanayairam, V., Rahuman, A., Rajakumar, G., Thirunavukkarasu, S., Marimuthu, S., Chidambaram, J., et al. (2011). Evaluation of *Catharanthus roseus* leaf extract-mediated biosynthesis of titanium dioxide nanoparticles against *Hippobosca maculata* and *Bovicola ovis*. *Parasitol. Res.* 111, 2329–37. doi: 10.1007/s00436-011-2676-x

Kasthuri, J., Kathiravan, K., and Rajendiran, N. (2008). Phyllanthin-assisted biosynthesis of silver and gold nanoparticles: a novel biological approach. *J. Nanoparticle Res.* 11, 1075–1085. doi: 10.1007/s11051-008-9494-9

Kaviya, S., Santhanalakshmi, J., Viswanathan, B., Muthumary, J., and Srinivasan, K. (2011). Biosynthesis of silver nanoparticles using citrus sinensis peel extract and its antibacterial activity. *Spectrochim. Acta A Mol. Biomol. Spectrosc.* 79, 54–598. doi: 10.1016/j.saa.2011.03.040

Keat, C. L., Aziz, A., Eid, A. M., and Elmarzugi, N. A. (2015). Biosynthesis of nanoparticles and silver nanoparticles. *Bioresourc. Bioprocess.* 2:47. doi: 10.1186/s40643-015-0076-2

Kemp, M., Kumar, A., Mousa, S., Park, T.-J., Ajayan, P., Kubotera, N., et al. (2009). Synthesis of gold and silver nanoparticles stabilized with glycosaminoglycans having distinctive biological activities. *Biomacromolecules* 10, 589–595. doi: 10.1021/bm801266t

Khan, A., Fox, E., Górzny, M., Nikulina, E., Brougham, D., Wege, C., et al. (2013). pH control of the electrostatic binding of gold and iron oxide nanoparticles to tobacco mosaic virus. *Langmuir* 29, 2094–2098. doi: 10.1021/la3044126

Khare, P., and Bisen, P. S. (1991). Mitigating effect of physico-chemical factors ON Ni^{2+} Hg^{2+} and Cu^{2+} toxicity in cylindrospermum Iu 942. *Environ. Technol.* 12, 297–301. doi: 10.1080/09593339109385009

Kobayashi, M., Tomita, S., Sawada, K., Shiba, K., Yanagi, H., Yamashita, I., et al. (2012). Chiral meta-molecules consisting of gold nanoparticles and genetically engineered tobacco mosaic virusA new tobacco mosaic virus vector and its use for the systemic production of angiotensin-I-converting enzyme inhibitor in transgenic tobacco. *Opt. Express* 20, 24856–24863. doi: 10.1364/OE.20.024856

Koduru, M., Golla, N., Dillip, D. G. R., Praveen, B., Bojja, S., Ch, L., et al. (2011). Green synthesis of silver nanoparticles using ocimum leaf extract and their characterization. *Digest J. Nanomater. Biostruct.* 6, 181–186.

Kowshik, M., Ashtaputre, S., Kharrazi, S., Vogel, W., Urban, J., Kulkarni, S., et al. (2003). Extracellular synthesis of silver nanoparticles by a silver-tolerant yeast strain MKY3. *Nanotechnology* 14, 95–100. doi: 10.1088/0957-4484/14/1/321

Kowshik, M., Deshmukh, N., Vogel, W., Urban, J., Kulkarni, S., and Paknikar, K. (2002b). Microbial synthesis of semiconductor CdS nanoparticles, their characterization, and their use in the fabrication of an ideal diode. *Biotechnol. Bioeng.* 78, 583–588. doi: 10.1002/bit.10233

Kowshik, M., Vogel, W., Urban, J., Kulkarni, S., and Paknikar, K. (2002a). Microbial synthesis of semiconductor PbS nanocrystallites. *Adv. Mater.* 14, 815–818. doi: 10.1002/1521-4095(20020605)14:11<815::aid-adma815>3.0.co;2-k

Kreibig, U., and Vollmer, M. (2013). *Optical Properties of Metal Clusters.* Berlin; Heidelberg: Springer Science and Business Media.

Krishnaraj, C., Enthai Ganeshan, J., Seetharaman, R., Kumar, S., Kalaichelvan, P., and Mohan, N. (2009). Synthesis of silver nanoparticles using *Acalypha indica leaf* extracts and its antibacterial activity against water borne pathogens. *Colloids Surf. B Biointerfaces* 76, 50–56. doi: 10.1016/j.colsurfb.2009.10.008

Kulkarni, N., and Muddapur, U. (2014). Biosynthesis of metal nanoparticles: a review. *J. Nanotechnol.* 2014:510246. doi: 10.1155/2014/510246

Kumar, P., Singh, P., Kumari, K., Mozumdar, S., and Chandra, R. (2011). A green approach for the synthesis of gold nanotriangles using aqueous leaf extract of *Callistemon viminalis*. *Mater. Lett.* 65, 595–597. doi: 10.1016/j.matlet.2010.11.025

Kumar, V., and Yadav, S. (2009). Plant-mediated synthesis of silver and gold nanoparticles and their applications. *J. Chem. Technol. Biotechnol.* 84, 151–157. doi: 10.1002/jctb.2023

Kundu, S., Ghosh, S., Mandal, M., Pal, T., and Pal, A. (2002). Silver and gold nanocluster catalyzed reduction of methylene blue by arsine in a micellar medium. *Bull. Mater. Sci.* 25, 577–579. doi: 10.1021/la0201974

Laokula, P., Klinkaewnaronga, J., Phokha, S., and Seraphin, S. (2008). Indium oxide (In_2O_3) nanoparticles using *Aloe vera* plant extract: synthesis and optical properties. *Optoelectron. Adv. Mater. Rapid Commun.* 2, 161–165.

Laudenslager, M., Schiffman, J., and Schauer, C. (2008). Carboxymethyl chitosan as a matrix material for platinum, gold, and silver nanoparticles. *Biomacromolecules* 9, 2682–2685. doi: 10.1021/bm800835e

Lee, H. J., Lee, G., Jang, N. R., Yun, J. H., Song, J. Y., and Kim, B. S. (2011). "Biological synthesis of copper nanoparticles using plant extract," in *Technical Proceedings of the 2011 NSTI Nanotechnology Conference and Expo, NSTI-Nanotech 2011*, Vol. 1 (Boston; Abington, MA : CRC Press), 371–374. Available online at: https://www.tib.eu/en/search/id/BLCP%3ACN080786126/Biological-synthesis-of-copper-nanoparticles-using/

Lee, H. J., Song, J., and Kim, B. S. (2013). Biological synthesis of copper nanoparticles using *Magnolia kobus* leaf extract and their antibacterial activity. *J. Chem. Technol. Biotechnol.* 88:4052. doi: 10.1002/jctb.4052

Lee, K. X., Shameli, K., Yew, Y. P., Teow, S.-Y., Jahangirian, H., Rafiee-Moghaddam, R., et al. (2020). Recent developments in the facile bio-synthesis of gold nanoparticles (AuNPs) and their biomedical applications. *Int. J. Nanomed.* 15, 275–300. doi: 10.2147/IJN.S233789

Lee, S.-W., Mao, C., Flynn, C. E., and Belcher, A. M. (2002). Ordering of quantum dots using genetically engineered viruses. *Science* 296, 892–895. doi: 10.1126/science.1068054

Lengke, M., Fleet, M., and Southam, G. (2007). Biosynthesis of silver nanoparticles by filamentous cyanobacteria from a silver(I) nitrate complex. *Langmuir* 23, 2694–2699. doi: 10.1021/la0613124

Lengke, M. F., Ravel, B., Fleet, M. E., Wanger, G., Gordon, R. A., and Southam, G. (2006). Mechanisms of gold bioaccumulation by filamentous cyanobacteria from gold(III)–chloride complex. *Environ. Sci. Technol.* 40, 6304–6309. doi: 10.1021/es061040r

Lin, X., Wu, M., Wu, D., Kuga, S., Endo, T., and Huang, Y. (2011). Platinum nanoparticles using wood nanomaterials: eco-friendly synthesis, shape control and catalytic activity for p-nitrophenol reduction. *Green Chem*. 13, 283–287. doi: 10.1039/C0GC00513D

Lloyd, J., Yong, P., and Macaskie, L. (1998). Enzymatic recovery of elemental palladium by using sulfate-reducing bacteria. *Appl. Environ. Microbiol.* 64, 4607–4609. doi: 10.1128/AEM.64.11.4607-4609.1998

Love, A., Makarov, V., Yaminsky, I., Kalinina, N., and Taliansky, M. (2014). The use of tobacco mosaic virus and cowpea mosaic virus for the production of novel metal nanomaterials. *Virology* 449, 133–139. doi: 10.1016/j.virol.2013.11.002

Luangpipat, T., Beattie, I., Chisti, Y., and Haverkamp, R. (2011). Gold nanoparticles produced in a microalga. *J. Nanoparticle Res.* 13, 6439–6445. doi: 10.1007/s11051-011-0397-9

Lukman, A., Gong, B., Marjo, C., Roessner, U., and Harris, A. (2010). Facile synthesis, stabilization, and anti-bacterial performance of discrete Ag nanoparticles using *Medicago sativa* seed exudates. *J. Colloid Interface Sci.* 353, 433–444. doi: 10.1016/j.jcis.2010.09.088

Ma, Y., Li, N., Yang, C., and Yang, X. (2005). One-step synthesis of amino-dextran-protected gold and silver nanoparticles and its application in biosensors. *Anal. Bioanal. Chem.* 382, 1044–1048. doi: 10.1007/s00216-005-3222-4

Makarov, V., Love, A. J., Sinitsyna, O., Makarova, S., Yaminsky, I., Taliansky, M., et al. (2014). "Green" nanotechnologies: synthesis of metal nanoparticles using plants. *Acta Nat.* 6, 35–44. doi: 10.32607/20758251-2014-6-1-35-44

Mallick, K., Witcomb, M., and Scurrell, P. (2006). Silver nanoparticle catalysed redox reaction: an electron relay effect. *Mater. Chem. Phys.* 97, 283–287. doi: 10.1016/j.matchemphys.2005.08.011

Mandal, D., Bolander, M., Mukhopadhyay, D., Sarkar, G., and Mukherjee, P. (2006). The use of microorganism for the formation of metal nanoparticles and their application. *Appl. Microbiol. Biotechnol.* 69, 485–492. doi: 10.1007/s00253-005-0179-3

Mao, C., Flynn, C. E., Hayhurst, A., Sweeney, R., Qi, J., Georgiou, G., et al. (2003). Viral assembly of oriented quantum dot nanowires. *Proc. Natl. Acad. Sci. U.S.A.* 100, 6946–6951. doi: 10.1073/pnas.0832310100

Mata, Y., Torres, E., Blázquez, M. L., Ballester, A., González, F., and Muñoz, J. (2008). Gold(III) biosorption and bioreduction with the brown alga *Fucus vesiculosus*. *J. Hazard. Mater.* 166, 612–618. doi: 10.1016/j.jhazmat.2008.11.064

McFarland, A., and Duyne, R. (2003). Single silver nanoparticles as real-time optical sensors with zeptomole sensitivity. *Nano Lett.* 3, 1057–1062. doi: 10.1021/nl034372s

Medvedeva, N. V., Ipatova, O. M., Ivanov, Y. D., Drozhzhin, A. I., and Archakov, A. I. (2007). Nanobiotechnology and nanomedicine. *Biochem. (Moscow) Suppl. B Biomed. Chem.* 1, 114–124. doi: 10.1134/S1990750807020023

Merzlyak, A., and Lee, S.-W. (2006). Phage as templates for hybrid materials and mediators for nanomaterial synthesis. *Curr. Opin. Chem. Biol.* 10, 246–252. doi: 10.1016/j.cbpa.2006.04.008

Mittal, A. K., Chisti, Y., and Banerjee, U. (2013). Synthesis of metallic nanoparticles using plant extracts. *Biotechnol. Adv.* 31, 346–356. doi: 10.1016/j.biotechadv.2013.01.003

Mohanpuria, P., Rana, N. K., and Yadav, S. K. (2008). Biosynthesis of nanoparticles: technological concepts and future applications. *J. Nanoparticle Res.* 10, 507–517. doi: 10.1007/s11051-007-9275-x

Mondal, S., Laskar, R., Sk, I., Basu, S., Mandal, D., and Begum, N. A. (2010). Biogenic synthesis of Ag, Au and bimetallic Au/Ag alloy nanoparticles using aqueous extract of mahogany (*Swietenia mahogani* JACQ.) leaves. *Colloids Surf. B Biointerfaces* 82, 497–504. doi: 10.1016/j.colsurfb.2010.10.007

Mousavi, S. M., Hashemi, S. A., Younes, G., Atapour, A., Amani, A., Savardashtaki, A., et al. (2018). Green synthesis of silver nanoparticles toward bio and medical applications: review study. *Artif. Cells* 46, S855–72. doi: 10.1080/21691401.2018.1517769

Mukherjee, P., Ahmad, A., Mandal, D., Senapati, S., Sainkar, S., Khan, M., et al. (2001). Fungus-mediated synthesis of silver nanoparticles and their immobilization in the mycelial matrix: a novel biological approach to nanoparticle synthesis. *Nano Lett.* 1, 515–519. doi: 10.1021/nl0155274

Mukherjee, P., Senapati, S., Mandal, D., Ahmad, A., Khan, M., Kumar, R., et al. (2002). Extracellular synthesis of gold nanoparticles by the fungus. *Chembiochem.* 3:461–3. doi: 10.1002/1439-7633(20020503)3:5<461::aid-cbic461>3.0.co;2-x

Nair, B., and Thalappil, P. (2002). Coalescence of nanoclusters and formation of submicron crystallites assisted by lactobacillus strains. *Cryst. Growth Des.* 2, 293–298. doi: 10.1021/cg0255164

Narayanan, K., and Sakthivel, N. (2011). Green synthesis of biogenic metal nanoparticles by terrestrial and aquatic phototrophic and heterotrophic eukaryotes and biocompatible agents. *Adv. Colloid Interface Sci.* 169, 59–79. doi: 10.1016/j.cis.2011.08.004

Narayanan, K. B., and Sakthivel, N. (2010). Phytosynthesis of gold nanoparticles using leaf extract of coleus amboinicus lour. *Mater. Charact.* 61, 1232–1238. doi: 10.1016/j.matchar.2010.08.003

Nevalainen, H., Suominen, P., and Taimisto, K. (1994). On the safety of *Trichoderma reesei*. *J. Biotechnol.* 37, 193–200. doi: 10.1016/0168-1656(94)90126-0

Njagi, E., Huang, H., Stafford, L., Genuino, H., Galindo, H., Collins, J., et al. (2011). Biosynthesis of iron and silver nanoparticles at room temperature using aqueous sorghum bran extracts. *Langmuir* 27, 264–271. doi: 10.1021/la103190n

Paciotti, G., Myer, L., Weinreich, D., Goia, D., Pavel, N., McLaughlin, R., et al. (2004). Colloidal gold: a novel nanoparticle vector for tumor directed drug delivery. *Drug Deliv.* 11, 169–183. doi: 10.1080/10717540490433895

Padil, V., and Cernik, M. (2013). Green synthesis of copper oxide nanoparticles using gum karaya as a biotemplate and their antibacterial application. *Int. J. Nanomed.* 8, 889–898. doi: 10.2147/IJN.S40599

Pantidos, N., and Horsfall, L. E. (2014). Biological synthesis of metallic nanoparticles by bacteria, fungi and plants. *J. Nanomed. Nanotechnol.* 5:233. doi: 10.4172/2157-7439.1000233

Parial, D., and Pal, R. (2011). Green synthesis of gold nanoparticles using cyanobacteria and their characterization. *Indian J. Appl. Res.* 4, 69–72. doi: 10.15373/2249555X/JAN2014/22

Parikh, R., Singh, S., Blv, P., Patole, M., Sastry, M., and Shouche, Y. (2008). Extracellular synthesis of crystalline silver nanoparticles and molecular evidence of silver resistance from morganella sp.: towards understanding biochemical synthesis mechanism. *Chembiochem* 9, 1415–1422. doi: 10.1002/cbic.200700592

Park, Y., Hong, Y. N., Weyers, A., Kim, Y. S., and Linhardt, R. (2011). ChemInform abstract: polysaccharides and phytochemicals: a natural reservoir for the green synthesis of gold and silver nanoparticles. *IET Nanobiotechnol.* 5, 69–78. doi: 10.1049/iet-nbt.2010.0033

Parker, H. L., Rylott, E. L., Hunt, A. J., Dodson, J. R., Taylor, A. F., Bruce, N. C., et al. (2014). Supported palladium nanoparticles synthesized by living plants as a catalyst for suzuki-miyaura reactions. *PLoS ONE* 9:e87192. doi: 10.1371/journal.pone.0087192

Patel, V., Berthold, D., Puranik, P., and Gantar, M. (2015). Screening of cyanobacteria and microalgae for their ability to synthesize silver

nanoparticles with antibacterial activity. *Biotechnol. Rep.* 5, 112–119. doi: 10.1016/j.btre.2014.12.001

Pattanayak, M., and Nayak, P. (2013). Green synthesis and characterization of zero valent iron nanoparticles from the leaf extract of *Azadirachta indica* (Neem). *World J. Nano Sci. Technol.* 2, 6–9. Available online at: https://idosi.org/wjnst/2(1)13/2.pdf

Petla, R. K., Vivekanandhan, S., Misra, M., Mohanty, A., and Satyanarayana, N. (2012). Soybean (*Glycine max*) leaf extract based green synthesis of palladium nanoparticles. *J. Biomater. Nanobiotechnol.* 3, 14–19. doi: 10.4236/jbnb.2012.31003

Philip, D. (2010). Green synthesis of gold and silver nanoparticles using *Hibiscus rosa* sinensis. *Phys. E:Low Dimens. Syst. Nanostruct.* 42, 1417–1424. doi: 10.1016/j.physe.2009.11.081

Pimprikar, P., Joshi, S., Kumar, A. R., Zinjarde, S., and Kulkarni, S. (2009). Influence of biomass and gold salt concentration on nanoparticle synthesis by the tropical marine yeast *Yarrowia lipolytica* NCIM 3589. *Colloids Surf. B Biointerfaces* 74, 309–316. doi: 10.1016/j.colsurfb.2009.07.040

Poinern, G. E. J., Chapman, P., Shah, M., and Fawcett, D. (2013). Green biosynthesis of silver nanocubes using the leaf extracts from *Eucalyptus macrocarpa*. *Nano Bull.* 2:130101. Available online at: http://hdl.handle.net/20.500.11937/49096

Pollmann, K., Raff, J., Mohamed, M., Fahmy, K., and Selenska-Pobell, S. (2006). Metal binding by bacteria from uranium mining waste piles and its technological applications. *Biotechnol. Adv.* 24, 58–68. doi: 10.1016/j.biotechadv.2005.06.002

Pugazhenthiran, N., Anandan, S., Kathiravan, G., Udaya Prakash, N. K., Crawford, S., and Ashokkumar, M. (2009). Microbial synthesis of silver nanoparticles by *Bacillus* sp. *J. Nanoparticle Res.* 11:1811. doi: 10.1007/s11051-009-9621-2

Qu, J., Luo, C., and Hou, J. (2011a). Synthesis of ZnO nanoparticles from Zn-hyperaccumulator (*Sedum alfredii* Hance) plants. *Micro Nano Lett. IET* 6, 174–176. doi: 10.1049/mnl.2011.0004

Qu, J., Yuan, X., Wang, X., and Shao, P. (2011b). Zinc accumulation and synthesis of ZnO nanoparticles using *Physalis alkekengi* L. *Environ. Pollut.* 159, 1783–1788. doi: 10.1016/j.envpol.2011.04.016

Rai, M., Yadav, A., and Gade, A. (2008). Silver nanoparticles as a new generation of antimicrobials. *Biotechnol. Adv.* 27, 76–83. doi: 10.1016/j.biotechadv.2008.09.002

Rajakumar, G., Rahuman, A., Priyamvada, B., Khanna, G., Kumar, D., Sujin, P., et al. (2011). Author's personal copy *Eclipta prostrata* leaf aqueous extract mediated synthesis of titanium dioxide nanoparticles. *Mater. Lett.* 68, 115–117. doi: 10.1016/j.matlet.2011.10.038

Rajasulochana, P., Dhamotharan, R., Murugakoothan, P., Subbiah, M., and Krishnamoorthy, P. (2011). Biosynthesis and characterization of gold nanoparticles using the alga *Kappaphycus alvarezii*. *Int. J. Nanosci.* 9, 511–516. doi: 10.1142/S0219581X10007149

Ramanathan, R., Field, M., O'Mullane, A., Smooker, P., Bhargava, S., and Bansal, V. (2013). Aqueous phase synthesis of copper nanoparticles: a link between heavy metal resistance and nanoparticle synthesis ability in bacterial systems. *Nanoscale* 5, 2300–2306. doi: 10.1039/C2NR32887A

Raveendran, P., Fu, J., and Wallen, S. (2003). Completely "green" synthesis and stabilization of metal nanoparticles. *J. Am. Chem. Soc.* 125, 13940–13941. doi: 10.1021/ja029267j

Riddin, T. L., Gericke, M., and Whiteley, C. G. (2006). Analysis of the inter- and extracellular formation of platinum nanoparticles by *Fusarium oxysporumf.* sp.lycopersiciusing response surface methodology. *Nanotechnology* 17, 3482–3489. doi: 10.1088/0957-4484/17/14/021

Roh, Y., Lauf, R. J., McMillan, A. D., Zhang, C., Rawn, C., Bai, J., et al. (2001). Microbial synthesis and the characterization of metal-substituted magnetites. *Solid State Commun.* 118, 529–534. doi: 10.1016/S0038-1098(01)00146-6

Roopan, S., Thakur, R., Rahuman, A., Kamaraj, D. C., Annadurai, B., and Tammineni, S. (2013). Low-cost and eco-friendly bio-synthesis of silver nanoparticles using *Cocos nucifera* coir extract and its larvicidal activity. *Ind. Crops Prod.* 43, 31–635. doi: 10.1016/j.indcrop.2012.08.013

Roopan, S. M., Bharathi, A., Kumar, R., Khanna, V. G., and Prabhakarn, A. (2012). Acaricidal, insecticidal, and larvicidal efficacy of aqueous extract of *Annona squamosa* L peel as biomaterial for the reduction of palladium salts into nanoparticles. *Colloids Surf. B Biointerfaces* 92, 209–212. doi: 10.1016/j.colsurfb.2011.11.044

Roy, M., Mandal, B., Mukherjee, P., Mukherjee, P., Ghatak, J., Tyagi, A. K., et al. (2008). Green synthesis of highly stabilized nanocrystalline silver particles by a non-pathogenic and agriculturally important fungus *T. asperellum*. *Nanotechnology* 19:075103. doi: 10.1088/0957-4484/19/7/075103

Royston, E., Ghosh, A., Kofinas, P., Harris, M., and Culver, J. (2008). Self-assembly of virus-structured high surface area nanomaterials and their application as battery electrodes. *Langmuir* 24, 906–912. doi: 10.1021/la7016424

Saha, S., Pal, A., Kundu, S., Basu, S., and Pal, T. (2009). Photochemical green synthesis of calcium-alginate-stabilized Ag and Au nanoparticles and their catalytic application to 4-nitrophenol reduction. *Langmuir* 26, 2885–2893. doi: 10.1021/la902950x

San Keskin, N. O., Koçberber KiliÇ N., Dönmez, G., and Tekinay, T. (2016). Green synthesis of silver nanoparticles using cyanobacteria and evaluation of their photocatalytic and antimicrobial activity. *J. Nano Res.* 40, 120–127. doi: 10.4028/www.scientific.net/JNanoR.40.120

Sangaru, S. S., Rai, A., Ahmad, A., and Sastry, M. (2004). Rapid synthesis of Au, Ag, and bimetallic Au core-Ag shell nanoparticles using neem (*Azadirachta indica*) leaf broth. *J. Colloid Interface Sci.* 275, 496–502. doi: 10.1016/j.jcis.2004.03.003

Sangeetha, G., Rajeshwari, S., and Rajendran, V. (2011). Green synthesis of zinc oxide nanoparticles by *Aloe barbadensis* miller leaf extract: structure and optical properties. *Mater. Res. Bull.* 46, 2560–2566. doi: 10.1016/j.materresbull.2011.07.046

Sanghi, R., and Verma, P. (2008). Biomimetic synthesis and characterisation of protein capped silver nanoparticles. *Bioresour. Technol.* 100, 501–504. doi: 10.1016/j.biortech.2008.05.048

Sastry, M., Ahmad, A., Khan, M., and Kumar, R. (2005). "Microbial nanoparticle production," in *Chemosphere*. eds. C. M. Niemeyer and C. A. Mirkin, 126–135. doi: 10.1002/3527602453.ch9

Sathishkumar, M., Sneha, K., Kwak, I., Mao, J., Tripathy, S. J., and Yun, Y.-S. (2009a). Phyto-crystallization of palladium through reduction process using *Cinnamom zeylanicum* bark extract. *J. Hazard. Mater.* 171, 400–404. doi: 10.1016/j.jhazmat.2009.06.014

Sathishkumar, M., Sneha, K., Won, S. W., Cho, C.-W., Kim, S., and Yun, Y.-S. (2009b). *Cinnamon zeylanicum* bark extract and powder mediated green synthesis of nano-crystalline silver particles and its bactericidal activity. *Colloids Surf. B Biointerfaces* 73, 332–338. doi: 10.1016/j.colsurfb.2009.06.005

Sathishkumar, M., Sneha, K., and Yun, Y.-S. (2010). Immobilization of silver nanoparticles synthesized using *Curcuma loga* tuber powder and extract on cotton cloth for bactericidal activity. *Bioresour. Technol.* 101, 7958–7965. doi: 10.1016/j.biortech.2010.05.051

Schlüter, M., Hentzel, T., Suarez, C., Koch, M., Lorenz, W., Böhm, L., et al. (2014). Synthesis of novel palladium(0) nanocatalysts by microorganisms from heavy-metal-influenced high-alpine sites for dehalogenation of polychlorinated dioxins. *Chemosphere* 117C, 462–470. doi: 10.1016/j.chemosphere.2014.07.030

Senapati, S., Syed, A., Moeez, S., Kumar, A., and Ahmad, A. (2012). Intracellular synthesis of gold nanoparticles using alga *Tetraselmis kochinensis*. *Mater. Lett.* 79, 116–118. doi: 10.1016/j.matlet.2012.04.009

Shah, S., Dasgupta, S., Chakraborty, M., Vadakkekara, R., and Hajoori, M. (2014). Green synthesis of iron nanoparticles using plant extracts. *Int. J. Biol. Pharm. Res.* 5, 549–552.

Shahverdi, A. R., Minaeian, S., Shahverdi, H., Jamalifar, H., and Nohi, A.-A. (2007). Rapid synthesis of silver nanoparticles using culture supernatants of enterobacteria: a novel biological approach. *Process Biochem.* 42, 919–923. doi: 10.1016/j.procbio.2007.02.005

Sharma, S. K., and Bisen, P. S. (1992). Hg^{2+} and Cd^{2+} induced inhibition of light induced proton efflux in the cyanobacterium anabaena flos-aquae. *Biometals* 5, 163–167. doi: 10.1007/BF01061323

Sharma, S. K., Dhyani, S., Singh, D. P., Shukla, H. D., Ahmad, A., and Bisen, P. (2001). Influence of sodium ion on heavy metal-induced inhibition of light-regulatd proton efflux and active carbon uptake in the cyanobacterium anabaena flos-aquae. *World J. Microbiol. Biotechnol.* 17, 707–711. doi: 10.1023/A:1012931228452

Shenton, W., Douglas, T., Young, M., Stubbs, G., and Mann, S. (1999). Inorganic-organic nanotube composites from template mineralization of tobacco mosaic virus. *Adv. Mater.* 11, 23–256.

Sheny, D. S., Mathew, J., and Philip, D. (2011). Phytosynthesis of Au, Ag and Au-Ag bimetallic nanoparticles using aqueous extract and dried leaf of *Anacardium occidentale*. *Spectrochim. Acta A Mol. Biomol. Spectrosc.* 79, 254–262. doi: 10.1016/j.saa.2011.02.051

Shivaji, S., Deshmukh, A., and Sadowski, Z. (2014). Biosynthesis, optimization, purification and characterization of gold nanoparticles. *Afr. J. Microbiol. Res.* 8, 138–146. doi: 10.5897/AJMR10.143

Simon-Deckers, A., Loo, S., Mayne-L'hermite, M., Herlin Boime, N., Menguy, N., Reynaud, C., et al. (2009). Size-, composition- and shape-dependent toxicological impact of metal oxide nanoparticles and carbon nanotubes toward bacteria. *Environ. Sci. Technol.* 43, 8423–8429. doi: 10.1021/es90 16975

Singaravelu, G., Arockiamary, J., Kumar, G., and Govindaraju, K. (2007). A novel extracellular synthesis of monodisperse gold nanoparticles using marine alga, *Sargassum wightii* greville. *Colloids Surf. B Biointerfaces* 57, 97–101. doi: 10.1016/j.colsurfb.2007.01.010

Singh, D. P., Khare, P., and Bisen, P. (1989). Effect of Ni^{2+}, Hg^{2+} and Cu^{2+} on growth, oxygen evolution and photosynthetic electron transport in cylindrospermum IU 942. *J. Plant Physiol.* 134, 406–412. doi: 10.1016/S0176-1617(89)80003-3

Singh, D. P., Sharma, S. K., and Bisen, P. (1993). Differential action of Hg^{2+} and Cd^{2+} on the phycobilisomes and chlorophyll a fluorescence and photosystem II dependent electron trnasport in the cyanobacterium anabaena flos-aquae. *Biometals* 6, 125–132. doi: 10.1007/BF00140114

Singh, P., Kim, Y.-J., Zhang, D., and Yang, D.-C. (2016). Biological synthesis of nanoparticles from plants and microorganisms. *Trends Biotechnol.* 34, 588–599. doi: 10.1016/j.tibtech.2016.02.006

Singh, R. (2011). Biological approach of zinc oxide nanoparticles formation and its characterization. *Adv. Mater. Lett.* 2, 313–317. doi: 10.5185/amlett.indias.204

Sintubin, L., De Windt, W., Dick, J., Mast, J., Van Der Ha, D., Verstraete, W., et al. (2009). Lactic acid bacteria as reducing and capping agent for the fast and efficient production of silver nanoparticles. *Appl. Microbiol. Biotechnol.* 84, 741–749. doi: 10.1007/s00253-009-2032-6

Sondi, I., and Salopek-Sondi, B. (2004). Silver nanoparticles as antimicrobial agent: a case study on *E. coli* as a model for gram-negative bacteria. *J. Colloid Interface Sci.* 275, 177–182. doi: 10.1016/j.jcis.2004.02.012

Song, J., Jang, H.-K., and Kim, B. S. (2009a). Biological synthesis of gold nanoparticles using *Magnolia kobus* and *Diopyros kaki* leaf extracts. *Process Biochem.* 44, 1133–1138. doi: 10.1016/j.procbio.2009.06.005

Song, J., Kwon, E.-Y., and Kim, B. S. (2009b). Biological synthesis of platinum nanoparticles using *Diopyros kaki* leaf extract. *Bioprocess Biosyst. Eng.* 33, 159–164. doi: 10.1007/s00449-009-0373-2

Sotiriou, G., and Pratsinis, S. (2011). Engineering nanosilver as an antibacterial, biosensor and bioimaging material. *Curr. Opin. Chem. Eng.* 1, 3–10. doi: 10.1016/j.coche.2011.07.001

Soundarrajan, C., Sankari, A., Dhandapani, P., Maruthamuthu, S., Ravichandran, S., Sozhan, G., et al. (2011). Rapid biological synthesis of platinum nanoparticles using *Ocimum sanctum* for water electrolysis applications. *Bioprocess Biosyst. Eng.* 35, 827–833. doi: 10.1007/s00449-011-0666-0

Spadaro, D., and Gullino, M. (2005). Improving the efficacy of biocontrol agents against soilborne pathogens. *Crop Protect.* 24, 601–613. doi: 10.1016/j.cropro.2004.11.003

Subhankari, I., and Nayak, P. (2013). Synthesis of copper nanoparticles using *Syzygium aromaticum* (Cloves) aqueous extract by using green chemistry. *World J. Nano Sci. Technol.* 2, 14–17.

Suganya, A., Murugan, K., Kovendan, K., Mahesh kumar, P., and Hwang, J.-S. (2013). Green synthesis of silver nanoparticles using *Murraya koenigii* leaf extract against *Anopheles stephensi* and *Aedes aegypti*. *Parasitol. Res.* 112, 1385–97. doi: 10.1007/s00436-012-3269-z

Sun, S., and Zeng, H. (2002). Size-controlled synthesis of magnetite nanoparticles. *J. Am. Chem. Soc.* 124, 8204–8205. doi: 10.1021/ja026501x

Sundrarajan, M., and Gowri, S. (2011). Green synthesis of titanium dioxide nanoparticles by *Nyctanthes arbor-tristis* leaves extract. *Chalcogenide Lett.* 8, 447–451.

Tang, S., Mao, C., Liu, Y., Kelly, D. Q., and Banerjee, S. K. (2007). Protein-mediated nanocrystal assembly for flash memory fabrication. *IEEE Trans. Electron. Devices* 54, 433–438. doi: 10.1109/TED.2006.890234

Tc, P., Raichur, A., Chandrasekaran, N., and Mukherjee, A. (2011). Kinetic evolution studies of silver nanoparticles in a bio-based green synthesis process. *Colloids Surf. A Physicochem. Eng. Asp.* 377, 212–216. doi: 10.1016/j.colsurfa.2010.12.047

Thakkar, K., Mhatre, S., and Parikh, R. (2009). Biological synthesis of metallic nanoparticles. *Nanotechnol. Biol. Med.* 6, 257–62. doi: 10.1016/j.nano.2009.07.002

Thakkar, K. N., Mhatre, S. S., and Parikh, R. Y. (2010). Biological synthesis of metallic nanoparticles. *Nanomedicine* 6, 257–262. doi: 10.1016/j.nano.2009.07.002

Thapa, D., Palkar, V. R., Kurup, M. B., and Malik, S. K. (2004). Properties of magnetite manoparticles synthesized through a novel chemical route. *Mater. Lett.* 58, 2692–2694. doi: 10.1016/j.matlet.2004.03.045

Thirunavukkarasu, S., Rahuman, A., Chidambaram, J., Rajakumar, G., Marimuthu, S., Kirthi, V., et al. (2013). Green synthesis of titanium dioxide nanoparticles using *Psidium guajava* extract and its antibacterial and antioxidant properties. *Asian Pac. J. Trop. Med.* 7, 968–976. doi: 10.1016/S1995-7645(14) 60171-1

Ummartyotin, S., Bunnak, N., Juntaro, J., Sain, M., and Manuspiya, H. (2012). Synthesis of colloidal silver nanoparticles for printed electronics. *Comptes Rendus Chim.* 15, 539–544. doi: 10.1016/j.crci.2012.03.006

Vahabi, K., Mansoori, G. A., and Karimi Dorcheh, S. (2011). Biosynthesis of silver nanoparticles by fungus *Trichoderma reesei* (a route for large-scale production of AgNPs). *Insci. J.* 1, 65–79. doi: 10.5640/insc.010165

Valodkar, M., Jadeja, R., Thounaojam, M., Devkar, R., and Thakore, S. (2011a). Biocompatible synthesis of peptide capped copper nanoparticles and their biological effect on tumor cells. *Mater. Chem. Phys.* 128, 83–89. doi: 10.1016/j.matchemphys.2011.02.039

Valodkar, M., Nagar, P., Jadeja, R., Thounaojam, M., Devkar, R., and Thakore, S. (2011c). Euphorbiaceae latex induced green synthesis of non-cytotoxic metallic nanoparticle solutions: a rational approach to antimicrobial applications. *Colloids Surf. A Physicochem. Eng. Asp.* 384, 337–344. doi: 10.1016/j.colsurfa.2011.04.015

Valodkar, M., Rathore, P., Jadeja, R., Thounaojam, M., Devkar, R., and Thakore, S. (2011b). Cytotoxicity evaluation and antimicrobial studies of starch capped water soluble copper nanoparticles. *J. Hazard. Mater.* 20, 244–249. doi: 10.1016/j.jhazmat.2011.11.077

Veeraputhiran, V. (2013). Bio-catalytic synthesis of silver nanoparticles. *Int. J. ChemTech Res.* 5, 2555–2562.

Velmurugan, P., Lee, S.-M., Iydroose, M., Lee, K.-J., and Oh, B.-T. (2012). Pine cone-mediated green synthesis of silver nanoparticles and their antibacterial activity against agricultural pathogens. *Appl. Microbiol. Biotechnol.* 97, 361–8. doi: 10.1007/s00253-012-3892-8

Vimala, D. K., Sundarraj, S., Paulpandi, M., Srinivasan, V., and Kannan, S. (2013). Green synthesized doxorubicin loaded zinc oxide nanoparticles regulates the bax and Bcl-2 expression in breast and colon carcinoma. *Process Biochem.* 49, 160–172. doi: 10.1016/j.procbio.2013.10.007

Vivek, M., Kumar, P. S., Steffi, S., and Sudha, S. (2011). Biogenic silver nanoparticles by *Gelidiella acerosa* extract and their antifungal effects. *Avicenna J. Med. Biotechnol.* 3, 143–148.

Wang, L., Chen, X., Zhan, J., Chai, Y., Yang, C., Xu, L., et al. (2005). Synthesis of gold nano- and microplates in hexagonal liquid crystals. *J. Phys. Chem. B* 109, 3189–3194. doi: 10.1021/jp0449152

Waszczuk, P., Barnard, T., Rice, C., Masel, R., and Wieckowski, A. (2002). A nanoparticle catalyst with superior activity for electrooxidation of formic acid. *Electrochem. Commun.* 4:732. doi: 10.1016/S1388-2481(02) 00420-4

Xie, J., Lee, J. Y., Wang, D. I. C., and Ting, Y. P. (2007). Silver nanoplates: from biological to biomimetic synthesis. *ACS Nano* 1, 429–439. doi: 10.1021/nn7000883

Xu, X.-H. N., Brownlow, W. J., Kyriacou, S. V., Wan, Q., and Viola, J. J. (2004). Real-time probing of membrane transport in living microbial cells using single nanoparticle optics and living cell imaging. *Biochemistry* 43, 10400–10413. doi: 10.1021/bi036231a

Yong, P., Rowson, N. A., Farr, J. P. G., Harris, I. R., and Macaskie, L. E. (2002). Bioaccumulation of palladium by *Desulfovibrio desulfuricans*. *J. Chem. Technol. Biotechnol.* 77, 593–601. doi: 10.1002/jctb.606

You, H., Yang, S., Ding, B., and Yang, H. (2013). Synthesis of colloidal metal and metal alloy nanoparticles for electrochemical energy applications. *Chem. Soc. Rev*. 42, 2880–2904. doi: 10.1039/C2CS35319A

Zahir, A., Chauhan, I., Bagavan, A., Kamaraj, D. C., Elango, G., Shankar, J., et al. (2015). Green synthesis of silver and titanium dioxide nanoparticles using *Euphorbia prostrata* extract shows shift from apoptosis to G 0 /G 1 arrest followed by necrotic cell death in leishmania donovani. *Antimicrob. Agents Chemother*. 59, 00098–00015. doi: 10.1128/AAC.00098-15

Conflict of Interest: The authors declare that the research was conducted in the absence of any commercial or financial relationships that could be construed as a potential conflict of interest.

frontiers in Chemistry

ORIGINAL RESEARCH
published: 30 October 2020
doi: 10.3389/fchem.2020.574614

Celastrol Loaded Nanoparticles With ROS-Response and ROS-Inducer for the Treatment of Ovarian Cancer

Weina Niu[1†], *Jianguo Wang*[2†], *Qinyao Wang*[2] *and Jianjun Shen*[2*]

[1] *Department of Oncology, The First Affiliated Hospital of USTC, Division of Life Sciences and Medicine, University of Science and Technology of China, Hefei, China,* [2] *Department of Radiation Oncology, The First Affiliated Hospital of USTC, Division of Life Sciences and Medicine, University of Science and Technology of China, Hefei, China*

Ovarian cancer is a gynecological cancer from which it is difficult to be completely cured. It is common to use regimens as an effective treatment for ovarian cancer, but these inevitably bring serious side effects. New treatment strategies and special drugs are needed to improve the prognosis of patients. Celastrol is a natural product, isolated from traditional medicine, that has been proven to be curative for inflammation and cancers. However, the non-targeting and low solubility of celastrol limit its clinical application. We prepared celastrol-loaded nanoparticles for the efficient treatment of ovarian cancer via oxidative stress amplification. In this work, a tumor-targeted, ROS-sensitive nanoparticle was designed, synthesized, and assembled into a drug delivery system that used celastrol. Folic acid (FA) groups on the surface of nanoparticles guide them to actively target the surface of the tumor cell membrane. Thioketal (TK) bonds in nanoparticles can be oxidized and broken into -SH within the ROS level of tumor tissues, which causes the breaking of the PEG hydrophilic shell layer of nanoparticles and promotes the release of celastrol. The released celastrol further stimulated the production of ROS and amplified the intracellular ROS level to promote the apoptosis of tumor cells, thus achieving a therapeutic effect on the celastrol treated ovarian cancer.

Keywords: ovarian cancer, celastrol, PLGA-TK-PEG-FA, oxidative stress amplification, ROS-response, ROS-inducer

OPEN ACCESS

Edited by:
Fang Liu,
Guangzhou University of Chinese Medicine, China

Reviewed by:
Yueqin Zheng,
China Pharmaceutical University, China
Shengpeng Wang,
University of Macau, China

****Correspondence:***
Jianjun Shen
takemeparadise@163.com

†These authors have contributed equally to this work

Specialty section:
This article was submitted to Nanoscience, a section of the journal Frontiers in Chemistry

Received: *20 June 2020*
Accepted: *31 August 2020*
Published: *30 October 2020*

Citation:
Niu W, Wang J, Wang Q and Shen J (2020) Celastrol Loaded Nanoparticles With ROS-Response and ROS-Inducer for the Treatment of Ovarian Cancer. Front. Chem. 8:574614. doi: 10.3389/fchem.2020.574614

INTRODUCTION

Ovarian cancer is a fatal gynecological cancer, and aggressive surgical treatment combined with chemotherapy still cannot guarantee a good prognosis.

At present, the adjuvant treatment of ovarian cancer generally depends on the patient's condition, such as CP (cyclophosphamide + cisplatin), TP (Taxol + carboplatin), and CAP (cyclophosphamide + Adriamycin + Cisplatin). Although the mentioned therapeutic schedules are effective in the treatment of ovarian cancer, they can cause significant side effects in the patient, and new agents that are capable of improving the prognosis of ovarian cancer are urgently needed (Gallardo-Rincon et al., 2016; Chen et al., 2018).

Traditional medicine plays an important role in the treatment of diseases, and the natural products from traditional medicine feature a diversity of structures and targets that are an important source in the development of new drugs. Celastrol derives from *Tripterygium wilfordii* and has a wide range of biological and pharmacological activities.

A study by Trott et al. initially found that celastrol significantly inhibits the activity of HSP90 (Heat Shock Proteins) by promoting nuclear transport of HSF1 (Heat Shock Transcriptional Factor 1) (Trott et al., 2008). Subsequently, a large number of scientists have carried out in-depth research on celastrol. In recent years, celastrol has been found to have significant antitumor properties independent of HSP90. Celastrol has been found to induce programmed cell death by activating glycogen synthase kinase 3β (Feng et al., 2013). Treatment of celastrol inhibits cancer growth by activating the TNF- α-induced NF-κB signaling pathway (Kang et al., 2013). Moreover, it induces the apoptosis of carcinoma cells by the WNT/β-catenin pathway (Lu et al., 2012), and inhibits the proliferation and invasion of colorectal cancer by repressing the epithelial-mesenchymal transformation (EMT) (Divya et al., 2018; Wang et al., 2019). Multiple studies have shown that celastrol induces the increase of ROS levels and induces intracellular accumulation of ROS to promote cell apoptosis in a variety of tumor cells such as melanoma (Lee et al., 2012), liver cancer (Liu et al., 2016), glioma (Liu et al., 2019), and osteosarcoma (Li et al., 2015), etc.

Unfortunately, celastrol had many properties that prevented it from being used as a therapeutic agent. Celastrol had a very strong hydrophobicity, poor corresponding bioavailability, and short serum half-life (T1/2β). The clinical application of celastrol is still limited by its narrow therapeutic window and poor solubility (Wang et al., 2016; Chen et al., 2018). Celastrol also had many targets unrelated to tumor surface receptors and affected by a variety of cell types, which meant poor targeting performance to the tumor *in vivo*.

Nanomaterials have been designed to solve each of these problems. For example, the encapsulation and transport of celastrol in nanocarriers enhanced its water solubility, changed its biological distribution and serum half-life. Nanocarriers reduced off-target effects by targeting specific cells or tissues to increase the selectivity of encapsulated celastrol. These benefits were to reduce the effective dose of significant therapy, minimize toxicity, and improve safety.

In this work, a tumor-targeted, ROS-sensitive nanoparticle was designed, synthesized, and assembled into the drug delivery system of celastrol. Folic acid (FA) groups on the surface of nanoparticles were used to guide the nanoparticles to actively target the surface of the tumor cell membrane. Thioketal (TK) bonds in nanoparticles were oxidized and broken into -SH within the ROS level (20–200 μM) of tumor tissues, which caused the breaking of the PEG hydrophilic shell layer of nanoparticles and promoted the release of celastrol. The released celastrol further stimulated the production of ROS and amplified the intracellular ROS level to promote the apoptosis of tumor cells, thus achieving a therapeutic effect on the celastrol treated ovarian cancer.

EXPERIMENTAL MATERIALS

Boc-PEG_{2k}-NH_2, $PLGA_{5k}$, polyvinyl alcohol (PVA), $PLGA_{5k}$-$mPEG_{2k}$, were purchased from HWRK CHEM Co., Ltd. (Beijing, China). Acetone, 3-mercaptopropionic acid, trifluoroacetic acid (TFA), N, N-Dimethylformamide (DMF), Dichloromethane (DCM), anhydrous ether obtained from Energy chemical Inc. Celastrol, NaCl, $NaHCO_3$, 4-dimethylaminopyridine (DMAP), N, N-Dicyclohexylcarbodiimide (DCC), folic acid (FA), fluorescein isothiocyanate isomer I (FITC), rhodamine-B (RhB), penicillin, streptomycin and 4′, 6-diamidino-2-phenylindole (DAPI) were purchased from Aladdin Inc. Dulbecco's modified Eagle's medium (DMEM), 100× mycillin, and fetal bovine serum (FBS) were purchased from Gibco Inc.

Ovarian cell lines SKOV3 were purchased from BeNa culture Collection, all cell experiments complied with the ethical review of animal experiments in The First Affiliated Hospital of USTC.

METHODS

Synthesis of TK

Under the protection of nitrogen, a solution of acetone (0.50 g, 2.77 mM), 3-mercaptopropionic acid (0.36 mL, 4.16 mM), and a catalytic amount of TFA were stirred at room temperature for 12 h. A saturated $NaHCO_3$ extraction solution was used to quench the reaction. The precipitate was collected by filtration and was washed with cold water. The obtained white powder was recrystallized from hexane and dried in a vacuum oven overnight.

Synthesis of Boc-PEG_{2k}-TK

Under the protection of nitrogen, Boc-PEG_{2k} -NH_2 (2.4 g), DMAP (0.012 g, 0.1 mM) and TK (0.374 g, 1 mM) dissolved in cold DMF (25 mL) under nitrogen protection. DCC (0.412 g, 2 mM) was dissolved in cold DMF (5 mL) and added to the mixed solution drop by drop, stirring at room temperature for 48 h. The resulting white precipitate was filtered and the concentrated filtrate reprecipitated in cold anhydrous ether. The precipitation was redissolved in 1 mL DCM and precipitated in cold anhydrous ether to obtain the precipitation of the product.

Synthesis of $PLGA_{5k}$-TK-PEG_{2k}-NH_2

Boc-$mPEG_{2k}$ -TK (2.4 g), $PLGA_{5k}$ (7.5 g), and DMAP (0.012 g, 0.1 mM) were dissolved in 25 mL DMF in an ice bath under nitrogen atmosphere. DCC (0.412 g, 2 mM) was dissolved in DMF (5 ml), added drop by drop to the mixing system, and stirred at room temperature for 48 h. The resulting white precipitate was filtered and the concentrated filtrate was reprecipitated in the cold anhydrous ether. The precipitate was further redissolved in 5 mL DCM, with a 5 mL TFA drop in. It was then stirred at room temperature for 2 h, and the mixture was extracted by saturated Na_2CO_3 and NaCl in turn. The resulting solution was concentrated and reprecipitated in the cold anhydrous ether.

The obtained precipitate was further dissolved in the 5 mL DMF and extensively dialyzed (MWCO 7 kDa, Spectrum Laboratories, Laguna Hills, CA) against deionized water.

The product $PLGA_{5k}$ -TK-PEG_{2k} -NH_2 was vacuum-dried at 25°C for 6 h (yield = 79%) and characterized by 1 H NMR (**Figure 1A**).

Synthesis of $PLGA_{5k}$-TK-PEG_{2k}-FA

$PLGA_{5k}$-TK-PEG_{2k}-NH2 was further modified with FA. The specific method was to dissolve FA (0.088 g, 2 mM), DMAP

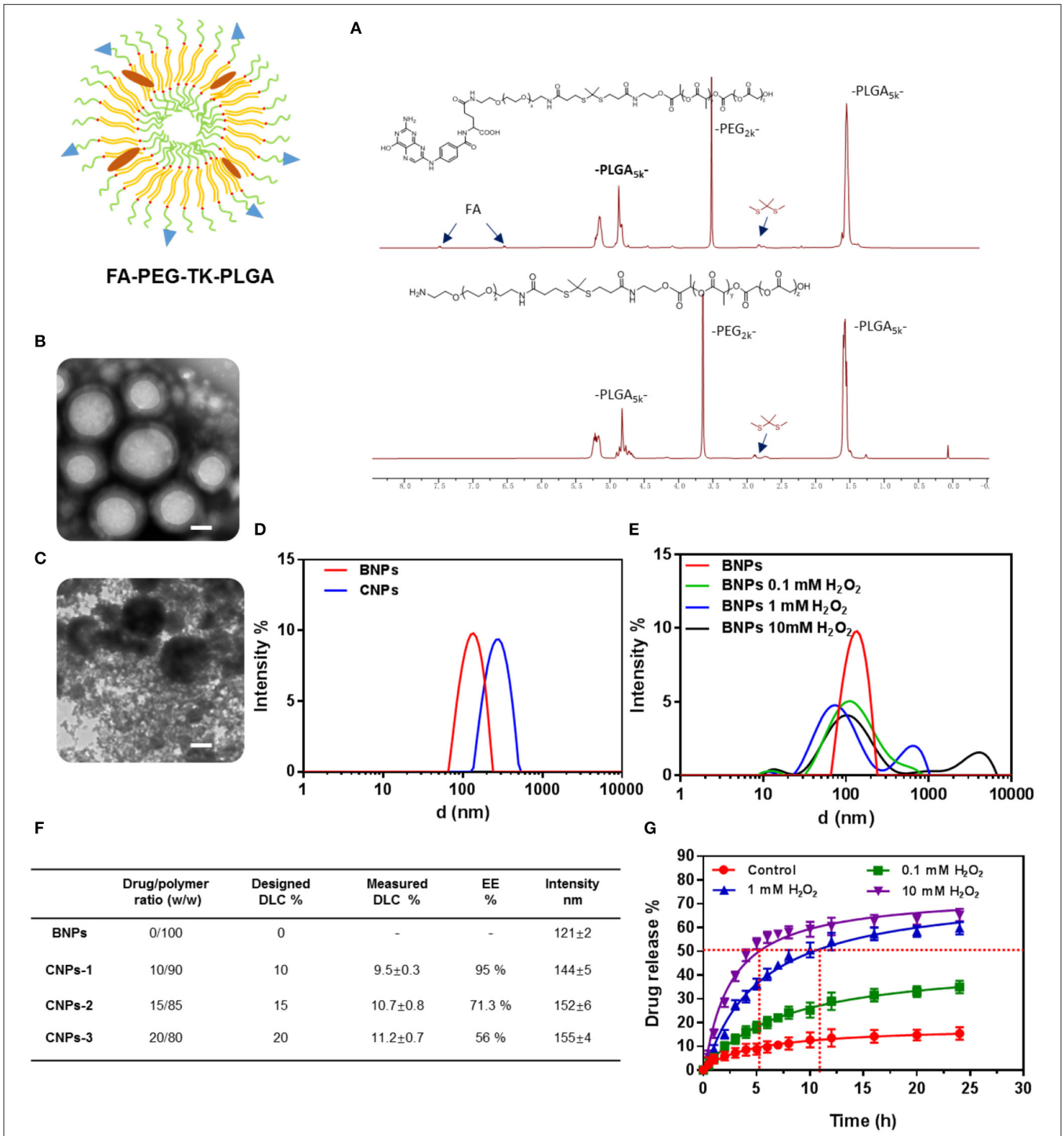

	Drug/polymer ratio (w/w)	Designed DLC %	Measured DLC %	EE %	Intensity nm
BNPs	0/100	0	-	-	121±2
CNPs-1	10/90	10	9.5±0.3	95 %	144±5
CNPs-2	15/85	15	10.7±0.8	71.3 %	152±6
CNPs-3	20/80	20	11.2±0.7	56 %	155±4

FIGURE 1 | NMR 1H of PLGA-TK-PEG-NH2 and PLGA-TK-PEG-FA **(A)**; TEM characterization of BNPs **(B)** and BNPs stimulated by ROS (1 mM H_2O_2, 20 μM $CuCl_2$) **(C)** Scale bar: 50 nm; DLS of BNPs and Cel-loaded nanoparticles **(D)** and nanoparticles stimulated by ROS (0.1, 1, 10 mM H_2O_2, 20 μM $CuCl_2$) **(E)**; DLC and EE of two amphiphiles **(F)**; drug release rate of Cel@FA-NPs **(G)**.

(0.012 g, 0.1 mM), and DCC (0.412 g, 2 mM) in 30 mL cold DMF of under the protection of nitrogen. After activation for 30 min, a 5 mL DMF solution containing 1 g $PLGA_{5k}$-TK-PEG_{2k}-NH_2 was added into the mixture drop by drop, and the reaction continued for 24 h at room temperature. After the white precipitate was filtered, the concentrated filtrate reprecipitated in the cold

n-hexane. The product $PLGA_{5k}$-TK-PEG_{2k}-FA was vacuum-dried at 25°C for 6 h (yield = 79%) and characterized by 1 H NMR (**Figure 1A**).

Preparation of BNPs and CNPs

A total of 500 μL $PLGA_{5k}$-TK-PEG_{2k}-FA solution (100 mg/mL, chloroform) was added to 6 mL of 1% PVA. In the ice bath, the ultrasonic probe was used for 5 min (80 W) to form an oil-water emulsion. The mixture was added to 30 mL 0.3% PVA and stirred overnight to volatilize chloroform and solidify the surface of the PLGA ball. The ultrafiltration concentration was cleaned with a 100 KD ultrafiltration tube. The volume was fixed to 5 mL with pure water, and the mother solution of BNPS was collected and stored at 4°C. Other different concentrations of BNPs were obtained by the dilution of the mother solution.

The celastrol was dissolved in chloroform and prepared into a solution of 20 mg/mL.

A total of 500 μL $PLGA_{5k}$-TK-PEG_{2k}-FA solutions (50 mg/mL, chloroform) and 50 μL of celastrol (20 mg/mL, chloroform) was added to 6 mL of 1% PVA ultrasonicated for 5 min by the ultrasonic probe (80 W) to form an oil-water emulsion. The mixture was added to 30 mL 0.3% PVA and stirred overnight to volatilize chloroform and solidify the surface. The ultrafiltration concentration was cleaned with 100 KD ultrafiltration tube. The volume was fixed to 5 mL with pure water, and the mother solution was collected and stored at 4°C. Other different concentrations of CNPs were obtained by the dilution of the mother solution.

TEM Characterizations

Morphology of BNPs and CNPs were examined by transmission electron microscopy. The carbon disc ultrathin grid was ionized under vacuum (0.3 Torr, 400 V, 20 s). Imaging was performed at a tension of 100 keV and a magnification at 30,000 × (Hitachi, HT7800).

DLS

The particle size of the BNPs and CNPs were determined by dynamic light scattering (DLS). Samples were measured at a polymer concentration of 5 mg/mL and were equilibrated at 25°C for 60 s before the first measurement. Particle size and distribution were obtained as triplicate and expressed as size distribution by number.

Fresh PBS solutions (pH 6.5), containing 10 mM H_2O_2 and 3.2 μM $CuCl_2$, were prepared to simulate the ROS conditions. The size changes of the nanoparticles in response to ROS conditions were measured by DLS (3000HS, Malvern Instruments Ltd.)

In brief, 1 mL of the solution of the nanoparticles (1 mg/mL) was diluted with 1 mL of PBS (pH 7.4) containing different concentrations of ROS. The solution was then incubated at 37°C in a thermostatic water bath oscillator and the size was measured at a predetermined time interval by DLS.

DLC and EE

The encapsulation efficiency (EE) and drug load capacity (DLC) of celastrol were evaluated by high performance liquid chromatography (HPLC) using Thermo Scientific C18 reversed phase column with a mobile phase of DMF at 0.5 mL/min.

The celastrol absorption curve at 280 nm was quantified and the standard curve of celastrol was established, demonstrating good linearity from 12 μg/mL to 2 mg/mL.

The lyophilized amphiphilic polymers (8.5 mg) and celastrol (1.5 mg) were dissolved in 2 mL of DMF and assembled into CNPs according to the method above. A total of 1 mg lyophilized CNPs were redissolved in 200 μL DMF, and the content of celastrol was quantitatively determined by HPLC.

The encapsulation efficiency (EE) and drug loading capacity (DLC) of celastrol were calculated by the following formula:

$$DLC(\%) = \left\{ \frac{\text{drug weight in drug-loaded micelles}}{\text{weight of drug-loaded micelles}} \right\} \times 100\%$$

$$EE(\%) = \left\{ \frac{\text{drug weight in drug-loaded micelles}}{\text{weight of drug in feeding}} \right\} \times 100\%$$

Release Profiles of Drug-Loaded NPs

One milliliter CNPs were put into a dialysis bag (3.5 kda, CA), and the drug release characteristics of CNPs were studied in PBS buffer containing H_2O_2 (0.1 mM, 1 mM, 10 mM) and $CuCl_2$ (20 μM). The content of celastrol outside the dialysis bag was concentrated and measured at a predetermined time interval by HPLC.

Cell Culture

Ovarian cancer cell (SKOV3) was purchased from the Cell Bank of the Chinese Academy of Science (Shanghai, China). 1640 medium supplemented with 10% fetal bovine serum (FBS), 1% penicillin/streptomycin, 1.5 g/L sodium carbonate, and 0.11 g/L sodium pyruvate was used to culture SKOV3 cells in a humid atmosphere with 37 °C and 5% CO_2.

Cell Viability

SKOV3 cells were inoculated into 96-well plates (20,000 cells per well). The cells were then treated with free celastrol, BNPs, and CNPs. They were then incubated with free celastrol, BNPs, and CNPs for 24 h, and the cells were washed and cell viability was measured by CCK8 assay. The absorbance at 450 nm was determined by a microplate reader (Molecular Devices, Sunnyvale, CA, USA).

Wound Healing Assay

SKOV3 cells were seeded into 6-well plates (50,000 cells per well) for 24 h. Cells were then scratched by a 200 μL pipette tip and cultured with free celastrol, BNPs, and CNPs for another 24 h. The scratch changes were photographed by an optical microscope.

Fluorescence Imaging

SKOV3 cells were seeded into 6-well plates (20,000 cells per well), incubated with PBS, free celastrol, BNPs, FL-BNPs, FL-CNPs for 24 h. NAC was added to balance intracellular ROS and to verify the effect of intracellular ROS on cell phagocytosis.

After being washed with serum-free MEM, the cells were observed by laser confocal microscopy (Leica, Wetzlar, Germany).

Reactive Oxygen Analysis

SKOV3 cells were seeded into 6-well plates (25,000 cells per well), incubated with PBS, free celastrol, BNPs, CNPs for 24 h. The cells were then incubated with 10 μM DCF-DA at 37°C for 30 min. Washed with serum-free MEM, the intracellular ROS levels were observed by fluorescence microscopy (Leica, Wetzlar, Germany) and measured by Microplate Reader (BD Biosciences, San Jose, California, USA).

Cell Apoptosis

SKOV3 cells were seeded into 6-well plates (50,000 cells per well) and incubated with different interventions for 24 h. The apoptosis effect was measured via an Annexin V-FITC/PI apoptosis detection kit (Beyotime Biotech, China) by flow cytometer.

RESULTS AND DISCUSSIONS

Characterization of Amphiphilic Polymers and Nanoparticles

Characterization of the polymer was obtained by ^{1}H NMR. The nuclear magnetic characterization of polymers after solvent peaks as shown in **Figure 1A**. The characteristic TK bond peaks of $PLGA_{5k}$-TK-PEG_{2k} were observed at 2.8 ppm. For $PLGA_{5k}$-TK-PEG_{2k}-FA, the characteristic peaks of FA at 6.7 and 7.5 ppm could be observed.

The CNPs with stable particles, uniform size, and average particle size of 120 nm were prepared by reverse evaporation. The morphology of the nanoparticles was characterized by TEM. The uniform spherical hydrophobic core of nanoparticles had a ring of faint hydrophilic shells (**Figure 1B**). A large number of PEG segments were cut off by stimulating the TK bond fracture with ROS after the hydrophilic shell layer of nanoparticles was detached. After the ROS-stimulated nanoparticles were stained with phosphotungstic acid, it was observed that a large number of PEG fragments were dispersed in the solution, while the PLGA chain segments were aggregated into black nanoparticles of different sizes due to hydrophobic action (**Figure 1C**).

The particle size of the prepared nanoparticles was further measured by the Dynamic light scattering, as shown in **Figure 1D** (DLS, Santa Barbara, Nicomp 380 ZLS).

The solution with H_2O_2 (0.1, 1, 10 mM) and catalytic $CuCl_2$ was prepared to simulate the ROS solution. BNPs were mixed with ROS solution for 2 h and measured by the Dynamic light scattering. The results were shown in **Figure 1E**. When the concentration of H_2O_2 increased from 0.1 to 10 mM, the proportion of the particle size at 100 nm gradually decreased. When the concentration of H_2O_2 reached 1 mM, a significant secondary peak appeared at 700 nm. When the concentration of H_2O_2 was further increased to 10 mM, the hydrophobic nanoparticle aggregation effect was more obvious, and the sub-peak position appeared at 3,000 nm. A large number of tiny particles appeared after ROS stimulation. This phenomenon was not presented in the DLS results, compared with TEM images (**Figure 1C**). It was ascribed to the fact that the PEG segments were hydrophilic and did not aggregate into particles in the solution.

As shown in **Figure 1F**, the average particle size of the BNPs was 121 nm. After celastrol was encapsulated into nanoparticles, the average particle size of CNPs increased to 155 nm. The entrapment efficiency (EE) and drug loading capacity (DLC) of nanoparticles were measured by HPLC, as shown in the table (**Figure 1F**). As the designed DLC gradually increased from 10 to 20%, the measured DLC increased from 9.5 to 11.2%, while the EE decreased from 95 to 56%.

The drug release characteristics of CNPs in a tumor cell microenvironment were simulated by simulating the environment with different ROS concentrations, as shown in **Figure 1G**.

9.4% celastrol was released from the CNPs in the PBS solution within 24 h. A low concentration of ROS (0.1 mM) stimulated the release of celastrol, and the release rate of celastrol increased from 9.4 to 31.7% within 24 h. Medium concentration of ROS (1 mM) further increased the release rate from 31.7 to 59.6%, while high concentration of ROS (10 mM) increased the release rate very little (59.6–62.3%).

At the same time, it can be seen from **Figure 1G** that the higher the ROS concentration was, the faster celastrol would be released. In high-concentration ROS solutions, Celastrol's release rate reached more than 50% within just 5 h. To achieve the same release rate, a medium concentration of ROS solution needed 11.5 h.

SKOV3 cells were incubated with PBS, free Celastrol, BNPs, and CNPs for 24 h to obtain the results of cell viability, as shown in **Figure 2**.

In **Figures 2C,D** the cell viability of SKOV3 was determined by CCK8 24 h after different drug treatments. The dissociated celastrol gradient concentration (0, 0.1, 0.3, 1, 3, 10 mM) was set, and the corresponding celastrol loaded NPs were configured according to the equivalent concentration, while mass concentrations such as BNPs and celastrol loaded NPs were configured.

BNPs were less toxic to SKOV3, as the concentration reached 10 μg/mL, and the cell survival rate was up to 87%. Free celastrol was highly cytotoxic to SKOV3. When the concentration of celastrol reached 1 μg/mL, the cell survival rate dropped to <80%. When the celastrol concentration reached 10 μg/mL, the cell survival rate was only 18.2%. According to the cell survival curve, the IC50 value of celastrol was estimated to be 1.4 μg/mL. The cytotoxicity of CNPs was also cytotoxic to SKOV3, but the toxicity of CNPs was slightly lower than that of free celastrol. When the concentration of CNPs reached 10 mM, the cell survival rate of SKOV3 was 48.3%. We speculated that celastrol wrapped in nanoparticles was not fully released during the 24-h cell culture process, and this feature was also combined with the drug release characteristics of CNPs.

NAC is a ROS scavenging agent and was used to balance intracellular ROS stress. NAC (10 mM) was used in combination with free celastrol and CNPs to evaluate the toxic effect of high ROS on SKOV3 cells, as shown in **Figure 2D**. Apparently,

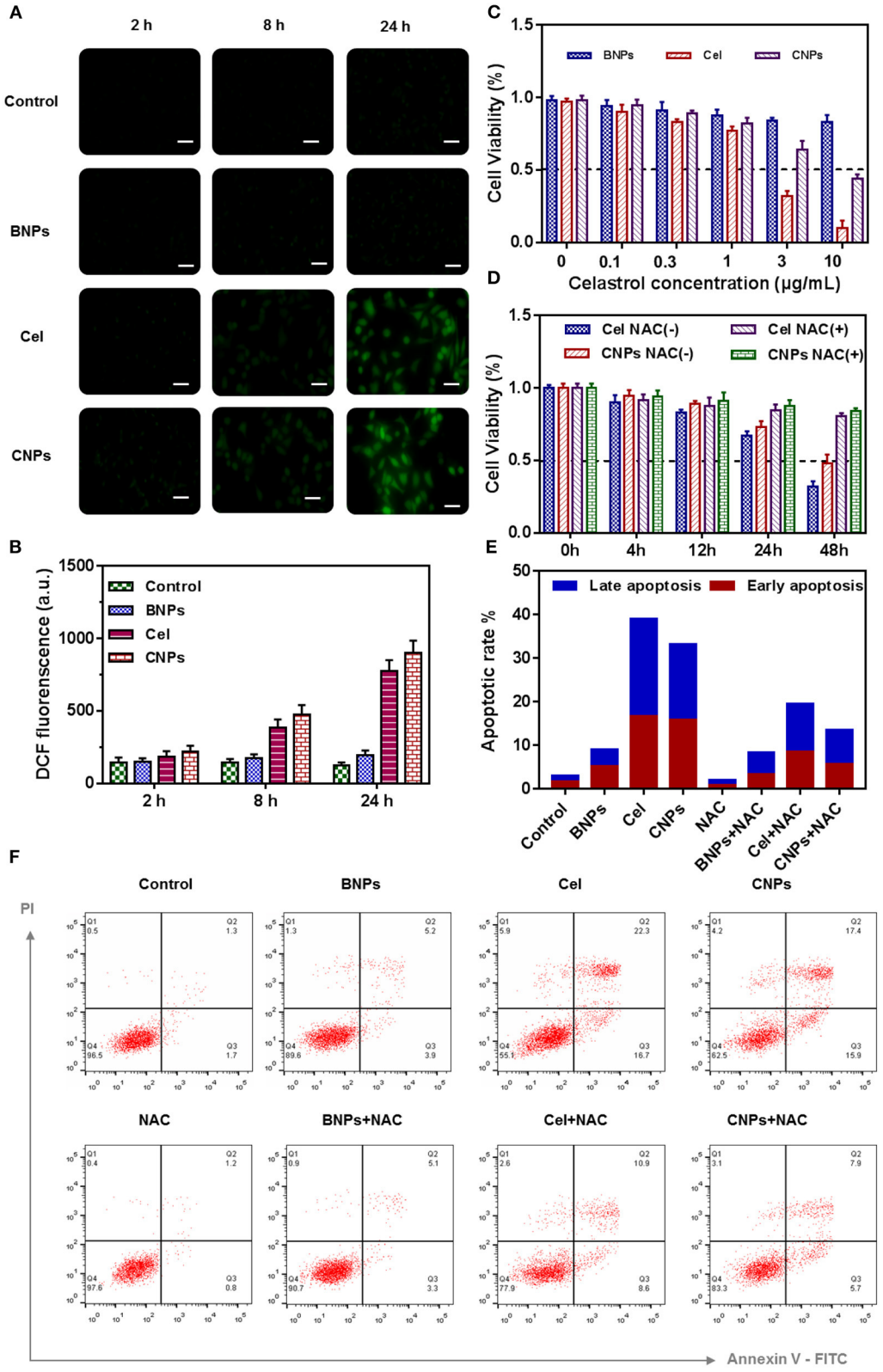

FIGURE 2 | Evaluation of the ROS regenerating ability of PBS, BNPs, celastrol, and CNPs *in vitro*. Fluorescence images of SKOV3 cells treated with different micelles for different time **(A)**. Scale bar: 20 μm. Quantitative analysis of the ROS generation in SKOV3 cells by a microplate reader **(B)**. Cell viability **(C,D)**, Apoptosis analysis **(F)**, and Quantification of apoptosis result **(E)** of SKOV3 cells induced by PBS, BNPs, celastrol, and CNPs. All error bars were presented as mean ± SD.

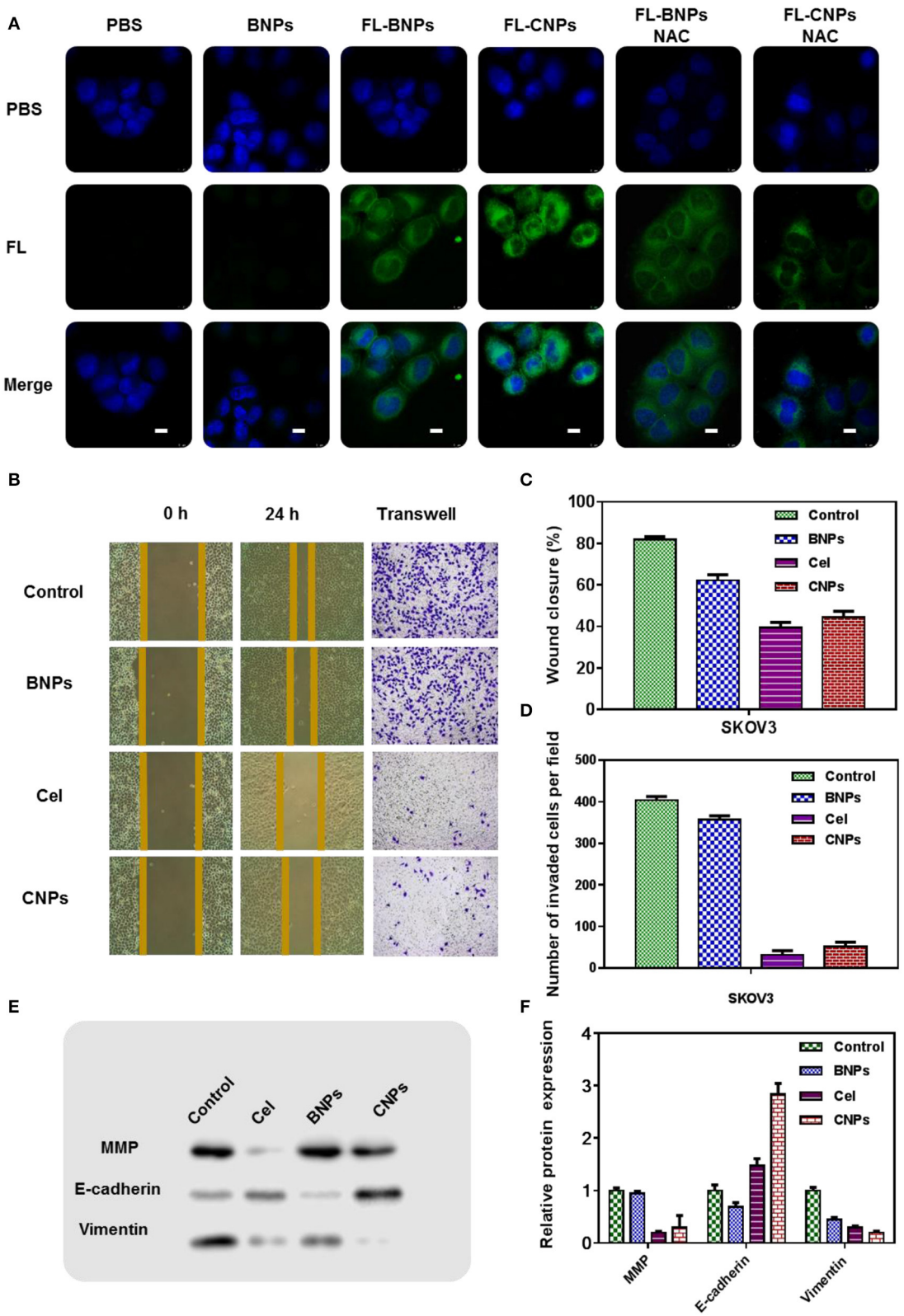

FIGURE 3 | Confocal laser scanning microscopy (CLSM) images of SKOV3 treated with PBS, BNPs, FL-BNPs, and FL-CNPs, compared with NAC intervention, Scale bar: 10 μm **(A)**; Wound healing **(B,C)**, tunnel **(B,D)**, and the protein expression **(E,F)** of SKOV3 treated with PBS, BNPs, celastrol, and CNPs.

without NAC intervention, free celastrol and CNPs significantly reduced SKOV3 cell activity within 48 h, while NAC intervention increased the cell activity to more than 80%.

SKOV3 cells were incubated with PBS, BNPs, celastrol, and CNPs for 24 h, intracellular ROS were labeled with the ROS dye DCF-DA (2 mM). By labeling with DCF-DA, the intracellular ROS level was further characterized and measured after treatment with different drugs. As shown in **Figures 2A,B** free celastrol and CNPs treatment significantly improved the level of oxidative stress in SKOV3 cells, and the longer the treatment period was, the higher the intracellular ROS level presented, which suggested that celastrol induced cells to produce high levels of ROS.

Further apoptosis experiments were conducted to verify the apoptosis-inducing effect of drugs on cells and the significant influence of NAC on drug treatment, as shown in **Figure 2F**.

After SKOV3 cells were incubated with PBS, BNPs, FL-BNPs, and FL-CNPs for 24 h, the nuclei were labeled with DAPI dye. The cell fluorescence was photographed by laser confocal imaging, as shown in **Figure 3A**.

Significant green fluorescence was observed after FL-BNPs and FL-CNPs treated cells. Notably, FL-CNPs exhibited stronger green fluorescence than FL-BNPs.

When NAC was combined with different drug treatments, significant fluorescence attenuation appeared in FL-BNPS&NAC treatment and FL-CNPS&NAC treatment, which suggested that intracellular ROS levels significantly affected the phagocytosis of nanomaterials at the cellular level.

We hypothesize that, although the TK bond in nanoparticles not only consumed intracellular ROS, it also consumed intracellular GSH, reducing GSH levels. After the cells swallowed the nanoparticles, the nanoparticles would stimulate the production of intracellular ROS. In general, the treatment of BNPs increased the intracellular ROS level.

The experimental results of scratch healing and TUNEL (**Figures 3B–D**) showed that without any intervention, the cell scratch healing was 80% 24 h later, and the wound healing of SKOV3 in the BNPs group was 65%, slightly less than that in the control group. The cell wound healing in the celastrol treatment group was 41%, while the cell scratch healing in the CNPs group was 46%. The cell healing ability in the celastrol treatment group and the CNPs group was far less than that in the control group, indicating that they could effectively inhibit the cell migration and invasion of SKOV3. The same conclusion was obtained from the TUNEL experiment results.

The expression of proteins associated with oxidative stress was further detected by WB. Specifically, SKOV3 cells were incubated with PBS, BNPs, celastrol, and CNPs for 24 h. Proteins were extracted after cell fragmentation for western blot (WB) detection to detect the contents of matrix metalloproteinases (MMP), E-calcine, and Vimentin in cells of different treatment groups (**Figures 3E,F** was the numerical statistical result of WB). The matrix metalloproteinases (MMP), E-cadherin, and vimentin EMT-related proteins determined the aggressiveness of tumor cells.

WB results showed that after celastrol and CNPs treatment, E-cadherin was significantly up-regulated, while matrix metalloproteinases and vimentin were down-regulated. This suggested that celastrol and CNPs treatments effectively inhibited epithelial mesenchymal transformation.

CONCLUSION

In this work, a tumor-targeted, ROS-sensitive nanoparticle was designed, synthesized, and assembled into the drug delivery system of celastrol. Folic acid (FA) groups on the surface of nanoparticles guide the nanoparticles to actively target the surface of the tumor cell membrane. Thioketal (TK) bonds in nanoparticles were oxidized and broken into -SH within the ROS level (20–200 μM) of tumor tissues, which caused the breaking of the PEG hydrophilic shell layer of nanoparticles and promoted the release of celastrol. The released celastrol further stimulated the production of ROS and amplified the intracellular ROS level to promote the apoptosis of tumor cells, thus achieving a therapeutic effect on the celastrol treated ovarian cancer.

Our experimental results indicate an effective strategy of inducing tumor cell apoptosis by delivering ROS sensitive nanomaterials to tumor cells and accelerating the release of natural product drugs that stimulated cells to further produce ROS, using the high ROS microenvironment in tumor cells. The results provide a theoretical basis for further animal experiments.

DATA AVAILABILITY STATEMENT

The raw data supporting the conclusions of this article will be made available by the authors, without undue reservation.

AUTHOR CONTRIBUTIONS

This project was conceptually designed by JS. The majority of the experiments were performed by WN and JW, assisted by QW. Data analysis and interpretation were carried out by WN and JS. This manuscript was prepared by JS. All authors discussed the results and commented on the manuscript. All authors contributed to the article and approved the submitted version.

FUNDING

This work was supported by the Fundamental Research Funds for the Central Universities (No. WK9110000106) and the National Natural Science Foundation of China (No. 81902761).

ACKNOWLEDGMENTS

We sincerely thank Dr. Zhaojiao Guo for insightful and helpful discussions about the celastrol-loaded nanoparticles.

REFERENCES

Chen, S. R., Dai, Y., Zhao, J., Lin, L., Wang, Y., and Wang, Y. (2018). A mechanistic overview of triptolide and celastrol, natural products from *Tripterygium wilfordii* Hook F. *Front. Pharmacol.* 9:104. doi: 10.3389/fphar.2018.00104

Divya, T., Velavan, B., and Sudhandiran, G. (2018). Regulation of transforming growth factor-beta/smad-mediated epithelial-mesenchymal transition by celastrol provides protection against bleomycin-induced pulmonary fibrosis. *Basic Clin. Pharmacol. Toxicol.* 123, 122–129. doi: 10.1111/bcpt.12975

Feng, L., Zhang, D., Fan, C., Ma, C., Yang, W., Meng, Y., et al. (2013). ER stress-mediated apoptosis induced by celastrol in cancer cells and important role of glycogen synthase kinase-3beta in the signal network. *Cell Death Dis.* 4:e715. doi: 10.1038/cddis.2013.222

Gallardo-Rincon, D., Espinosa-Romero, R., Munoz, W., R., Mendoza-Martinez, R., Villar-Alvarez, S. D., Onate-Ocana, L. D., et al. (2016). Epidemiological overview, advances in diagnosis, prevention, treatment and management of epithelial ovarian cancer in Mexico. *Salud. Publica Mex.* 58, 302–308. doi: 10.21149/spm.v58i2.7801

Kang, H., Lee, M., and Jang, S. W. (2013). Celastrol inhibits TGF-beta1-induced epithelial-mesenchymal transition by inhibiting Snail and regulating E-cadherin expression. *Biochem. Biophys. Res. Commun.* 437, 550–556. doi: 10.1016/j.bbrc.2013.06.113

Lee, J. H., Won, Y. S., Park, K. H., Lee, M. K., Tachibana, H., Yamada, K., et al. (2012). Celastrol inhibits growth and induces apoptotic cell death in melanoma cells via the activation ROS-dependent mitochondrial pathway and the suppression of PI3K/AKT signaling. *Apoptosis* 17, 1275–1286. doi: 10.1007/s10495-012-0767-5

Li, H. Y., Zhang, J., Sun, L. L., Li, B. H., Gao, H. L., Xie, T., et al. (2015). Celastrol induces apoptosis and autophagy via the ROS/JNK signaling pathway in human osteosarcoma cells: an *in vitro* and *in vivo* study. *Cell Death Dis.* 6:e1604. doi: 10.1038/cddis.2014.543

Liu, X., Gao, R. W., Li, M., Si, C. F., He, Y. P., Wang, M., et al. (2016). The ROS derived mitochondrial respirstion not from NADPH oxidase plays key role in Celastrol against angiotensin II-mediated HepG2 cell proliferation. *Apoptosis* 21, 1315–1326. doi: 10.1007/s10495-016-1294-6

Liu, X., Zhao, P., Wang, X., Wang, L., Zhu, Y., Song, Y., et al. (2019). Celastrol mediates autophagy and apoptosis via the ROS/JNK and Akt/mTOR signaling pathways in glioma cells. *J. Exp. Clin. Cancer Res.* 38:184. doi: 10.1186/s13046-019-1173-4

Lu, W., Jia, G., Meng, X., Zhao, C., Zhang, L., Ren, Y., et al. (2012). Beta-catenin mediates the apoptosis induction effect of celastrol in HT29 cells. *Life Sci.* 91, 279–283. doi: 10.1016/j.lfs.2012.07.032

Trott, A., West, J. D., Klaic, L., Westerheide, S. D., Silverman, R. B., Morimoto, R. I., et al. (2008). Activation of heat shock and antioxidant responses by the natural product celastrol: transcriptional signatures of a thiol-targeted molecule. *Mol. Biol. Cell* 19, 1104–1112. doi: 10.1091/mbc.E07-10-1004

Wang, L. P., Chen, B. X., Sun, Y., Chen, J. P., Huang, S., and Liu, Y. Z. (2019). Celastrol inhibits migration, proliferation and transforming growth factor-beta2-induced epithelial-mesenchymal transition in lens epithelial cells. *Int. J. Ophthalmol.* 12, 1517–1523. doi: 10.18240/ijo.2019.10.01

Wang, X., Zhao, F., Lv, Z. M., Shi, W. Q., Zhang, L. Y., and Yan, M. (2016). Triptolide disrupts the actin-based Sertoli-germ cells adherens junctions by inhibiting Rho GTPases expression. *Toxicol. Appl. Pharmacol.* 310, 32–40. doi: 10.1016/j.taap.2016.08.017

Conflict of Interest: The authors declare that the research was conducted in the absence of any commercial or financial relationships that could be construed as a potential conflict of interest.

frontiers in Chemistry

MINI REVIEW
published: 10 December 2020
doi: 10.3389/fchem.2020.559159

Smart Responsive Nanoformulation for Targeted Delivery of Active Compounds From Traditional Chinese Medicine

*Xuejun Jiang[1], Mei Lin[1], Jianwen Huang[1], Mulan Mo[1], Houhe Liu[1], Yuan Jiang[1], Xiaowen Cai[1], Wingnang Leung[2] and Chuanshan Xu[1]**

[1] Key Laboratory of Molecular Target and Clinical Pharmacology, State Key Laboratory of Respiratory Disease, School of Pharmaceutical Sciences & Fifth Affiliated Hospital, Guangzhou Medical University, Guangzhou, China, [2] Asia-Pacific Institute of Aging Studies, Lingnan University, Hong Kong, China

Traditional Chinese medicine (TCM) has been used to treat disorders in China for ∼1,000 years. Growing evidence has shown that the active ingredients from TCM have antibacterial, antiproliferative, antioxidant, and apoptosis-inducing features. However, poor solubility and low bioavailability limit clinical application of active compounds from TCM. "Nanoformulations" (NFs) are novel and advanced drug-delivery systems. They show promise for improving the solubility and bioavailability of drugs. In particular, "smart responsive NFs" can respond to the special external and internal stimuli in targeted sites to release loaded drugs, which enables them to control the release of drug within target tissues. Recent studies have demonstrated that smart responsive NFs can achieve targeted release of active compounds from TCM at disease sites to increase their concentrations in diseased tissues and reduce the number of adverse effects. Here, we review "internal stimulus–responsive NFs" (based on pH and redox status) and "external stimulus–responsive NFs" (based on light and magnetic fields) and focus on their application for active compounds from TCM against tumors and infectious diseases, to further boost the development of TCM in modern medicine.

Keywords: smart responsive nanoformulation, traditional Chinese medicine, targeted drug delivery, tumor, infectious disease

OPEN ACCESS

Edited by:
Fang Liu,
Guangzhou University of Chinese Medicine, China

Reviewed by:
Zhiling Yu,
Hong Kong Baptist University, Hong Kong
Yingwei Hou,
University of Illinois at Urbana-Champaign, United States

****Correspondence:***
Chuanshan Xu
xcshan@163.com

Specialty section:
This article was submitted to Nanoscience, a section of the journal Frontiers in Chemistry

Received: *05 May 2020*
Accepted: *30 October 2020*
Published: *10 December 2020*

Citation:
Jiang X, Lin M, Huang J, Mo M, Liu H, Jiang Y, Cai X, Leung W and Xu C (2020) Smart Responsive Nanoformulation for Targeted Delivery of Active Compounds From Traditional Chinese Medicine. Front. Chem. 8:559159. doi: 10.3389/fchem.2020.559159

INTRODUCTION

Traditional Chinese medicine (TCM) as an important approach to treat disorders has been used widely in China for ∼1,000 years. Accumulating evidence has shown that TCM exhibits excellent effects on tumors (Luo et al., 2019), bacteria (Kim et al., 2008; Moloney, 2016; Wang Z. et al., 2018b), and viruses (Li et al., 2018a; Yao et al., 2018; Yang et al., 2020) because of their active compounds. Some active compounds, such as artemisinin, curcumin, and epigallocatechin gallate, emodin, and celastrol, show prominent efficacy against tumors (Wang et al., 2014; Shanmugam et al., 2017). Flavonoids, polyphenols, alkaloids, and terpenoids are considered to be efficacious against antibiotic-resistant bacteria (Zhao et al., 2019b). Also, TCM shows multitarget features against viruses in direct or indirect ways (Ai et al., 2018; Li et al., 2018a).

However, the poor solubility and low bioavailability of the active compounds from TCM limit their clinical application. To address these shortcomings, novel drug-delivery nanoformulations

(NFs) are being employed to increase solubility, improve the efficiency of targeted delivery, and reduce the number of adverse effects. Recently, liposomes, nanoparticles, vesicles, mesoporous silica nanoparticles, and micelles as potential drug-delivery NFs have shown great promise in TCM (Ma et al., 2019).

"Smart responsive NFs" are new types of targeted NFs that deliver drugs specifically to target tissues or organs *via* an "intelligent response" in target sites. Usually, smart responsive NFs are classified into "internal stimuli–responsive NFs" and "external stimuli–responsive NFs" according to different stimuli conditions as shown in **Figure 1**. Internal stimuli–responsive NFs are mainly from the microenvironment of the targeted site and include pH, enzymes, redox status, and receptors. External stimuli–responsive NFs are mainly from magnets, heat, light, or ultrasound.

Here, we reviewed internal stimulus–responsive NFs and external stimulus–responsive NFs. We focused on the application of active compounds from TCM against tumors and infectious diseases, to further boost the development of TCM concepts in modern medicine.

INTERNAL STIMULUS–RESPONSIVE NFs

pH-Responsive NFs for Delivery of Active Compounds From TCM

The metabolism of tumor cells involves aerobic glycolysis to obtain energy for overgrowth and proliferation (Ganapathy-Kanniappan and Geschwind, 2013). Aerobic glycolysis is based on the conversion of glucose to pyruvate, which results in fermentation and lactate production (Shi et al., 2018), and the resulting acidosis is a ubiquitous characteristic of cancer (Tang et al., 2018). It has been demonstrated that the tumor tissues' acidic environment is about pH 6.5 (Som et al., 2016), whereas the pH of normal tissue is 7.4 (Liu et al., 2014). The microenvironment of tissues infected by bacteria is also acidic (Tao et al., 2019a). As shown in **Table 1**, based on the characteristics of an acidic microenvironment, pH-responsive NFs have been developed for targeted delivery of active compounds from TCM.

Delivery of Artemisinin and Dihydroartemisinin

Artemisinin and dihydroartemisinin are active agents from the Chinese herb *Artemisia annua*. They are used as antimalarial drugs in China (Tu, 2016). They are also potential anticancer agents when interacting with iron ions to produce reactive oxygen species (ROS), which can kill malignant cancer cells (Efferth, 2017). Chen et al. developed Fe_3O_4 nanoparticles as a pH-sensitive NF, for treating cervical cancer (Chen et al., 2014). In this NF, artemisinin was stored in the outer mesoporous shells. Fe^{2+} was liberated from the core of the Fe_3O_4 nanosphere in acidic organelles and cleaved the endoperoxide bridges of artemisinin to generate free radicals to kill HeLa cells. Artemisinin-hollow mesoporous silica-Fe_3O_4 nanoparticles have also been used to treat breast cancer *via* pH-responsive Fe_3O_4 nanoparticles (Bhaw-Luximon and Jhurry, 2017). Sustained release of artemisinin occurred in the lysosomal compartment (pH 3.8–5.0), and Fe_3O_4 was metabolized to free Fe^{2+} to generate many free radicals through reaction with the released artemisinin. In addition, an Fe_3O_4@$MnSiO_3$-folate nanosphere was developed for the treatment of lung cancer (Chen et al., 2015). Folate was introduced to increase the enhanced permeability and retention (EPR) effect. Meanwhile, Mn^{2+} was released from the silicate shells and interacted with artemisinin in an acidic tumor environment and organelles of A549 cells.

Liu et al. (2015) prepared dihydroartemisinin–graphene oxide–transferrin nanoparticles. The Fe (III) conjugated on transferrin was released in lysosomes and was reduced to Fe

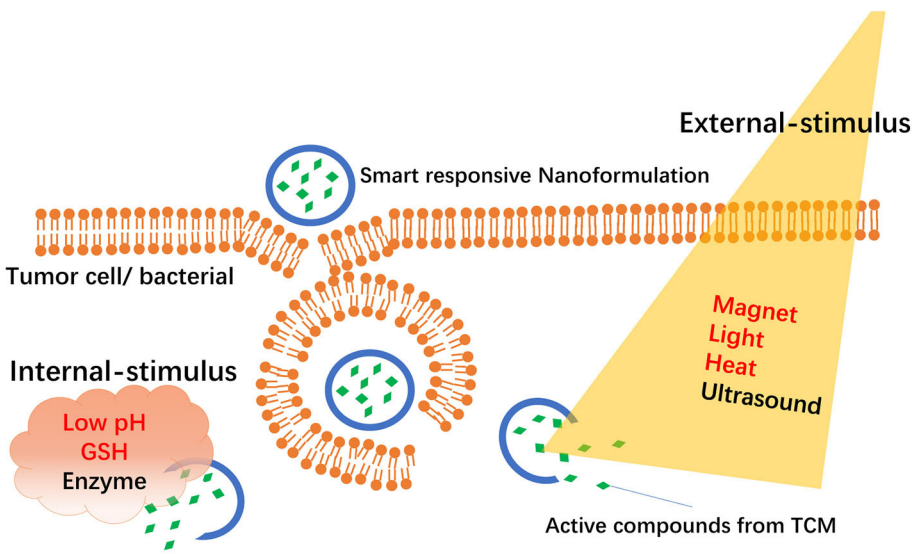

FIGURE 1 | Schematic representation of smart responsive nanoformulations-mediated delivery of active compounds from TCM.

TABLE 1 | pH-responsive nanoformulations in active compounds from TCM.

Active compounds	Response agent	Application	Cell line/animal	References
Artemisinin	Fe_3O_4 nanocrystal	Cervical cancer	HeLa	Chen et al., 2014
	Fe_3O_4@$MnSiO_3$	Lung cancer	A549 Nude mice	Chen et al., 2015
	Fe_3O_4 nanoparticles	Breast cancer	ZR75-30	Bhaw-Luximon and Jhurry, 2017
Arsenic trioxide	Polyamidoamine	Glioma	C6	Lu et al., 2018
Dihydroartemisinin	Fe (III)	Breast cancer	EMT6 EMT6 tumor-bearing nude mice	Liu et al., 2015
Baicalein	Hydrazone bond	Lung cancer	A549/DTX cell A549/DTX tumor-bearing nude mice	Li et al., 2017
Berberine	Chitosan	*H. pylori* infection		Lin et al., 2015
	Amine bond	Cervical cancer	HeLa	Pandey et al., 2013
Cinnamaldehyde	Acetal	Anticancer	DU145 SW620 RAW264.7 HEK 293 BALB/c nude mice	Yoo et al., 2018
	Acetal	*E. coli* infection *P. aeruginosa* infection	*E. coli* Drug-resistant *P. aeruginosa* DRPA-001 ICR mice	Park et al., 2016
	Acetal	Colon cancer	HCT116 BALB/cA nu/nu mice	Zhao et al., 2019a
Curcumin	PAE	Breast cancer	MCF-7 BALB/c nude mice	Yu et al., 2015
	Amine bond	Liver cancer	HepG2	Luan et al., 2017
	ZnO nanoparticle	Gastric cancer	AGS	Dhivya et al., 2018
	PAE	Hepatocellular carcinoma	SMMC 7721 HUVEC BALB/c nude mice	Zhang et al., 2017
	PAE	Anticancer	MCF-7 HepG2	Cai et al., 2016
	cis-Aconitic anhydride linker	Anticancer	A2780 SMMC 7721	Fang et al., 2016
	Poly(isoprene-b-acrylic acid) deblock copolymer	Acute myelocyte leukemia	HL-60 HL-60/Dox HL-60/CDDP	Jelezova et al., 2015
	Carboxylic groups of AGA	Colorectal cancer	HCT-116	Madhusudana Rao et al., 2015
	Menthone 1,2-glycerol ketal	Anticancer	SCC-7 tumor-bearing BALB/c mice	Chen et al., 2016a
	Hydrazone bond	Breast cancer	MCF-7 BALB/c nude mice	Cui et al., 2017
	Hydrazone bond	Breast cancer	MCF-7 Nude mice	Liu et al., 2019
	Calcium phosphate	Anticancer	MGC-803 A549	Wu et al., 2020
Eucalyptus oil	PLGA	Skin cancer	HaCaT	Sahu et al., 2017

(Continued)

TABLE 1 | Continued

Active compounds	Response agent	Application	Cell line/animal	References
Glycyrrhetinic acid	Chitosan	Liver cancer	QGY-7703 BALB/c nude mice Wistar rats	Tian et al., 2010
Glycyrrhetic acid	Hydrazone bond	Liver cancer	HepG2 HUVEC	Yan et al., 2018
Physcion	ZIF-8	Antibacteria	*Pseudomonas putida* *Escherichia coli* Engineered *Escherichia coli* *Staphylococcus aureus*	Soomro et al., 2019
Myricetin Quercetin Fisetin Luteolin	Coordination bond	Antibacteria	—	Bertleff-Zieschang et al., 2017
Quercetin	PAA	Anticancer	—	Sedghi et al., 2013
	PLGA	Skin cancer	HaCaT A431	Gupta et al., 2016
	N-acetyl-l-histidine	Anticancer	NIH/3T3 Red blood cell	Wu et al., 2016
	Boronic ester bond	Anticancer	MCF-7 A549 HepG2 IRC mice	Xing et al., 2017
	Polydopamine	Multidrug-resistant colon cancer	HCT-8 HCT-8/TAX	Shao et al., 2019
	Amide bond and ionic bond	Multidrug-resistant	MCF-7 MCF-7/DOX	Liu et al., 2017
	Chitosan	Anticancer	MCF-7	de Oliveira Pedro et al., 2018
Triptolide	Ionizable imidazole side chains	Hepatocellular carcinoma	Bel-7404 HCCLM3 Old athymic mice	Ling et al., 2014
	Tertiary amine group	Pancreatic cancer	PANC-1 MIA PaCa-2 BALB/C nude mice	Kong et al., 2019
	Silk	Pancreatic cancer	MIA PaCa-2 PANC-1	Ding et al., 2017
Ursolic acid	Chitosan	Anticancer	HeLa CD-1 female mice	Wang M. et al., 2017

(II) by ferric reductase. Fe (II) reacted with dihydroartemisinin on graphene oxide to yield ROS and oxygen/carbon-centered radicals, which then induced the death of EMT6 cells.

Delivery of Baicalein

Baicalein is a flavonoid from *Scutellaria baicalensis* Georgi. which has antioxidant, antivirus, antibacterial, anti-inflammatory, and antiallergic properties (Bie et al., 2017). Baicalein can inhibit the cell cycle; scavenge oxygen radicals; attenuate the activity of mitogen-activated protein kinase, protein kinase B, or mammalian target of rapamycin signaling pathways; and induce apoptosis by activating caspase-9/-3 (Liu et al., 2016). Recently, baicalein was delivered by a pH-responsive cleaved hydrazone bond in transferrin decorated docetaxel baicalein co-loaded solid lipid nanoparticles (Li et al., 2017). A modification based on polyethylene glycol (PEG) provided this system a long circulation in the body. Also, transferrin could guide delivery of nanoparticles into tumor cells by transferrin receptors. At an acidic condition, the hydrazone bond ruptured, resulting in shedding of the PEG layer from nanoparticles and the targeted release of baicalein.

Delivery of Cinnamaldehyde

Cinnamon is used not only as a spice, but also in TCM. Cinnamaldehyde is an active compound in cinnamon that can induce the apoptosis of tumor cells (Sadeghi et al., 2019). Yoo et al. (2018) used acetal linkages to couple cinnamaldehyde and maltodextrin to fabricate a cinnamaldehyde-maltodextrin nanoparticle. The acetal linkage dissociated in the acidic environment, and cinnamaldehyde and maltodextrin could return to their native states. Zhao et al. (2019a) also used acetal linkages to couple cinnamaldehyde

and dextran in 10-hydroxy camptothecin-cinnamaldehyde nanoparticles. The acetal linkage of cinnamaldehyde was hydrolyzed from dextran at an acidic pH, which broke the nanoparticles into water-soluble fragments, and resulted in rapid dissociation. Ferrocene-loaded poly[(3-phenylprop-2-ene-1,1-diyl)bis(oxy)bis(ethane-2,1-diyl)diacrylate]-co-4,4′(trimethylene dipiperidine)-copoly(ethylene glycol) micelles have been designed to release ferrocene and cinnamaldehyde rapidly at the site of bacterial infections (which are characterized by a low pH) (Park et al., 2016). Cinnamaldehyde induced the generation of hydrogen peroxide (H_2O_2) and iron in ferrocene and then converted H_2O_2 into highly toxic hydroxyl radicals.

Delivery of Curcumin

Curcumin is a polyphenol extracted from the herb turmeric. It has gained attention worldwide because of its antioxidant, anti-inflammatory, antimicrobial, and antiviral activities (Giordano, 2019). NF development can circumvent the poor bioavailability of curcumin to improve treatment outcome (Adiwidjaja and McLachlan, 2017).

Poly(β-amino ester) (PAE) is a typical pH-responsive biodegradable polymer. PAE has outstanding characteristics, such as positive charges, readily degradable linkages, high biodegradability, and high biocompatibility (Cordeiro et al., 2019). Yu et al. developed poly(ethylene glycol)-poly(lactide)-PAE micelles to deliver curcumin to the breast cancer cell line MCF-7. PAE is insoluble at pH 7.4 and maintains a large micelle structure with a hydrophobic PLA/PAE core (Yu and Zhang, 2014). However, PAE is soluble at pH 6.8 (thanks to protonation of tertiary amino groups) and shrinks the micelle structure to a hydrophobic PLA core. D-α-Tocopheryl PEG 1000-block-PAE (TPGSPAE) nanoparticles used in treatment of hepatocellular carcinoma have a similar mechanism of action (Zhang et al., 2017). The tertiary diamine moieties of the PAE core are protonated at low pH so that the hydrophobic curcumin is released from the hydrophilic core-shell structure. In curcumin-pluronic P123-PAE (Cai et al., 2016), P123 is constituted by poly(ethylene oxide)-poly(phenylene oxide)-poly(ethylene oxide) (PEO-PPO-PEO). The PPO/PAE core offers a local hydrophobic microenvironment for curcumin loading, and the hydrophilic PEO shell maintains a large micelle structure at pH 7.4. PAE is protonated and dissolves at weakly acidic pH, making the nanocarrier shrink to be a small micelle structure and release curcumin.

pH-sensitive linkages have also been used for curcumin delivery. At pH 4.5, chains of β-acrylic acid undergo transition to the protonated state. This action lowers their solubility abruptly and isolates them from the aqueous phase and results in rearrangements of the bilayer membrane and curcumin leakage. Fang et al. (2016) coupled a poloxamer (F68) and curcumin by a *cis*-aconitic anhydride linker. In acidic environments, the pH-sensitive *cis*-aconitic anhydride linker of F68-*cis*- curcumin conjugates were cleaved to release curcumin. Chen et al. (2016a) reported a menthone 1,2-glycerol ketal (MGK), which was used in Cur-hyaluronan-histidine-MGK. The ketal moieties of MGK could be degraded in a tumor microenvironment. Also, the imidazole group of histidine, which linked oligomeric hyaluronic acid (oHA) and MGK, could destroy lysosomal membranes to prevent the drug being degraded in cells. Luan et al. found that an acidic condition (pH < 6.5) could cause breakage of internal linkages in aliphatic amines grafted konjac glucomannan (KGM-g-AH) between a primary amine of octylamine and an aldehyde group and release curcumin. The responsive agent in KGM-g-AH8 micelles was KGM (Luan et al., 2017). Similarly, pH-sensitive hydrazone bonds have been used to deliver curcumin. Polymer oHA-hydrazone bond-folic acid biotin nanomicelles consisting of folic acid, biotin, and cluster of differentiation (CD)44 receptors can mediate the targeting of tumor tissue and cancer stem cells, from which the icariin and curcumin are released into the tumor microenvironment, depending on the pH-sensitive hydrazone bond (Liu et al., 2019).

Eucalyptus from *Eucalyptus robusta* Smith has been developed as a transdermal delivery vehicle for curcumin (Liu and Chang, 2011). Sahu et al. reported a 5-fluorouracil double-walled nanogel (FDWNL) to load eucalyptus with pH-sensitive chitosan. The hydrophilic pendant groups of chitosan (-OH and -$NHCOCH_3$) and strong ionic attraction between the ionized nanogel and hydrated counter ions caused rapid swelling of the FDWNL to release curcumin at acidic pH (Sahu et al., 2017).

Among metal nanoparticles, ZnO nanoparticles are pH-sensitive nanoplatforms used for curcumin delivery. The nontoxic ZnO nanoparticles are stable at pH ∼7, but dissolve and open up the polymer linkages of polymethyl methacrylate-acrylic acid ZnO nanoparticles to release curcumin together with toxic Zn^{2+} at a low pH (∼5.4) (Dhivya et al., 2018). Curcumin was also connected to one side of the disulfide-condensed menthone 1,2 glycerol ketal as a redox response prodrug material. The other side of menthone 1,2 glycerol ketal was connected to hyaluronic acid with an ester bond that made pH/redox response. The pH-responsive calcium phosphate shell made this NF broken at pH 5.5 to release curcumin to kill cancer (Chen et al., 2017). Wu et al. also used calcium phosphate as a pH-responsive shell to wrap the curcumin-adsorbed sodium caseinate micelles to improve the stability of curcumin. In the study, Wu et al. found that the calcium phosphate shell covering the sodium caseinate micelles was broken in the acidic stroma outside the tumor cells (Wu et al., 2020).

Delivery of Glycyrrhetinic Acid

Glycyrrhetinic acid (GA) is extracted from licorice and is modified for targeting of liver cells (Zhu et al., 2019, 2020; Li et al., 2020). In doxorubicin-loaded chitosan/poly(ethylene glycol)-GA nanoparticles, GA increases the affinity for liver cancer cells (Tian et al., 2010). Moreover, protonation of the amino groups of chitosan at an acidic condition and the acid-soluble doxorubicin hydrochloride cause the swelling of nanoparticles and release doxorubicin. In GA-modified chitosan-polyethyleneimine-4-hydrazinobenzoic acid–doxorubicin nanoparticles, GA improves the liver-targeting ability, and the hydrazone bond between doxorubicin and GA-CS-PEI-HBA is broken to release the "payload" in the intracellular environment (pH 4.5–6.5) of tumor cells (Yan et al., 2018).

Delivery of Triptolide and Celastrol

Triptolide and celastrol are contained in *Tripterygium wilfordii*. Triptolide has excellent inhibitory effects in the treatment of pancreatic cancer (Kim et al., 2018). Kong et al. (2019) enhanced the efficacy of triptolide by developing triptolide prodrug-loaded ultra–pH-sensitive micelles (T-UPSMs). After internalization by the endocytic organelles of cancer cells, the pH reached the apparent acid dissociation constant of T-UPSMs due to lysosomal acidification. The tertiary amine groups of T-UPSMs absorbed protons and induced micelle dissociation to elicit immediate drug release as a pH buffer in endosomes/lysosomes. Ding et al. (2017) found that triptolide or celastrol was weakly adsorbed or bonded to silk fibroin nanoparticles. At a low pH, silk loses its overall acidic surface properties and negative net charge, and the balance of the negative charge is shielded at an acidic pH, which destroys aggregates. Ling et al. (2014) developed nanoformulated triptolide nanoparticles for treatment of hepatocellular carcinoma. Internally packed imidazole was employed for pH-sensitive ionization and dispersion. During endosomal maturation, the decrease in pH could lead to the collapse of nanoparticles and triptolide release.

Delivery of Ursolic Acid

Ursolic acid (UA) is present in *Prunella vulgaris L*. but is also abundant in most fruits and vegetables (Yin et al., 2016). UA use has been reported in treatment of cancer (Jaman, 2018; Manayi et al., 2018; Mlala et al., 2019) and some infections (Tohmé et al., 2019). UA has been encapsulated in nanoparticles or liposomes and found to inhibit progression of cervical cancer (Wang M. et al., 2017; Wang S. et al., 2017). Jiang et al. (2017) prepared UA-loaded mesoporous silica nanoparticles and folic acid conjugated chitosan (UA@M-CS-FA) nanoparticles in which the acid-labile amide bond between CS-FA and mesoporous silica nanoparticles was broken in acidic conditions. This action made the chitosan chains swell and opened the mesopores of UA@M-CS-FA nanoparticles, resulting in UA release.

Delivery of Berberine

Berberine is isolated from *Coptis chinensis* and has antibacterial effects. Berberine was shown to markedly increase the survival rate of mice challenged with the bacterial endotoxin lipopolysaccharide (2 EU/mL) (Chu et al., 2014). Chitosan and heparin are ionized and form polyelectrolyte complexes *via* electrostatic interactions at pH 1.2–6.0 to protect berberine from destruction by gastric acids. At pH 7.0, chitosan is deprotonated, and berberine-loaded fucose-conjugated nanoparticles are broken apart to release berberine (Lin et al., 2015). Moreover, berberine as a hydrophobic part was linked to chitosan oligosaccharides with a dithiodipropionic acid linker, and 3,4-dihydroxyphenylpropionic acid as a hydrophilic part was also linked to another end of the chitosan oligosaccharides to form a polymer monomer. The positively charged 3,4-dihydroxyphenylpropionic acid attracted the negatively charged hyaluronic acid to form an oHA-3-carboxyphenylboronic acid shell and encapsulate curcumin. In the acidic microenvironment of tumor, the exposed hyaluronic acid specifically binds to the CD44 receptor, and the micelles are endocytosed by the cells and undergo charge reversal. The high concentration of glutathione (GSH) in tumor cells hydrolyzes the disulfide bonds of dithiodipropionic acid; the micelles collapse and release berberine and curcumin (Fang et al., 2019b).

Delivery of Physcion

Usually, zeolitic imidazolate framework-8 (ZIF-8) is fabricated using zinc ions and 2-methylimidazolate. ZIF-8 has high porosity, good structural regularity and tunability, adjustable surface functionality, and intrinsic pH-induced biodegradability (Gao et al., 2019b). Soomro et al. (2019) developed physcion@ZIF-8 to deliver the physcion present in rhubarb. In acidic conditions, the coordination linkage between zinc and imidazolate was broken, whereas the imidazolate was protonated, resulting in physcion release from ZIF-8.

Delivery of Quercetin

Quercetin from *Hypericum ascyron L.* has been reported to be beneficial for cardiovascular disease (Patel et al., 2018). In recent years, the nanotechnology transformation of quercetin has revealed that quercetin has considerable effects against tumors (Vinayak, 2019). Bertleff-Zieschang et al. reported quercetin/Fe (III) nanoparticles as potential antibacterial NFs. In that work, formation of a quercetin/Fe (III) network was pH-dependent based on coordination between a flavonoid ligand and Fe (III). At an acidic pH, quercetin/Fe (III) capsules were disassembled readily (Bertleff-Zieschang et al., 2017). Furthermore, amphiphilic pH-responsive 8-arm- and 12-arm-dendritic polyacrylic acid block copolymers were synthesized for quercetin loading. *In vitro* release experiments showed that both of these new materials achieved complete release faster at pH 5.0 than at pH 7.4. But the 12-arm dendritic polyacrylic acid polymer blocks copolymer release quercetin faster than the 8-arm-one (Sedghi et al., 2013). In a self-assembled micelle of *N*-acetyl-histidine-phosphocholine-chitosan conjugate, histidine was a pH-responsive molecule because of its imidazole group. At pH $\leq$6.0, the micelles swelled and ruptured to release the encaspsulated quercetin due to the protonation of the imidazole group (Wu et al., 2016).

Redox-Responsive NFs

GSH depletion promotes cancer cell death through processes such as apoptosis, necroptosis, autophagy, and ferroptosis (Lv et al., 2019). GSH deficiency, or a decrease in the ratio of GSH and glutathione disulfide (GSSG), leads to an increased susceptibility to oxidative stress implicated in the progression of cancer cells (Traverso et al., 2013). The GSH:GSSG ratio, as the major pool of thiol groups, is a key factor in the antioxidative capacity of cells. GSH is an ideal and omnipresent internal stimulus for rapid degradation of disulfide linkages (Zhang et al., 2018b). As shown in **Table 2**, there are many applications of disulfide bonds in redox-responsive delivery of TCM agents.

Wang B. et al. (2019) designed quercetin–dithiodipropionic acid–oHA–mannose–ferulic acid "nano-dandelions" for synchronous delivery of curcumin and baicalein. This was achieved by using the nano-dandelions as reduction-sensitive amphiphilic carriers. The coated oHA targeted CD44 receptors

TABLE 2 | Redox-responsive nanoformulations in active compounds from TCM.

Active compounds	Response agent	Application	Cell line/animal	References
Eucalyptus oil	Disulfide bond in 3,30-dithiodipropionic acid	Lung cancer	A549 RAW264.7 A549 bearing mice	Wang B. et al., 2019
Baicalin Curcumin Quercetin Ferulic acid	Dithiodipropionic acid–Cur	Anticancer	HepG2 A549 tumor-bearing mice	Wang K. et al., 2018
Curcumin	Cystamine	Glioma	G422	Tian et al., 2018
	Disulfide bond	Anticancer	MDA-MB-231	Dong et al., 2018
	Disulfide bond	Anticancer	HepG2 BALB/c mice	Zhang et al., 2019
Glycyrrhetic acid	PLGA	Lung cancer	Beas2B A549 NCI-H226	Zhang et al., 2020b
Homoharringtonine	PLGA	Lung cancer	Beas2B A549 NCI-H226 BALB/c-nude mice	Zhang et al., 2020
Oridonin	Oxalate ester bond	Colon carcinoma	CT26	Ou et al., 2019
Quercetin	Disulfide bond	Multidrug-resistant	4T1 L-02 BALB/C mice	Chen et al., 2018

and could facilitate uptake of nano-dandelions in tumor locations. Mannose-targeting CD206 receptors could be engulfed readily by tumor-associated macrophages. The S-S linkage in 3,30-dithiodipropionic acid connecting the hydrophobic and hydrophilic parts could be broken by the high concentration of GSH within tumor cells, which facilitated release of curcumin and baicalein.

Wang K. et al. (2018) developed distearoyl phosphatidyl ethanolamine derivatized PEG-modified nano-echinus materials. Dithiodipropionic acid–curcumin (S-S-Cur) was chemically conjugated onto the side chain of the conjugated GA-oHA (GA-HA) to generate an amphiphilic polymeric prodrug of curcumin (GA-HA-S-S-Cur). HA targeted CD44 receptors on the surface of tumor cells, and the breaking of disulfide bonds by a high concentration of GSH in a tumor environment led to disassembly of nano-echinus materials, and then released curcumin. Tian et al. (2018) developed HA-S-S-CUR micelles for glioma treatment, in which the disulfide bond of cystamine linked HA (hydrophilic group) and curcumin (hydrophobic group). Reductive cleavage of the disulfide bond by GSH in glioma cells caused instability of the hydrophobic core, resulting in micelle degradation and curcumin release.

In alendronate-oHA-S-S-curcumin micelles (Dong et al., 2018), a disulfide bond combines hydrophobic curcumin with hydrophilic oHA and alendronate to form micelles in water. These micelles fracture under a reducing environment to release curcumin. Cleavage of the disulfide bonds of PEGylated prodrug nanomicelles (Zhang et al., 2019) can transfer these nanomicelles into hydrophilic curcumin-mercapto. This action accelerates hydrolysis of the adjoining ester bond and releases curcumin from PEGylated prodrug nanomicelles.

Recently, synthetically designed polymers containing disulfide bonds have been used to deliver TCM-active compounds. Homoharringtonine (HHT)–loaded poly(lactic-co-glycolic acid)-SS-PEG (Zhang et al., 2020a) is an epidermal growth factor receptor (EGFR) aptamer-modified PLGA targeted to the EGFR (which shows high expression in lung cancer cells). The drug is delivered into the cytoplasm *via* receptor-mediated endocytosis. The disulfide bonds of PLGA are broken by GSH in lung cancer cells.

Additionally, ester bonds have also been used in the development of redox-responsive NFs. In the podophyllotoxin (POD) delivery, PODPEG nanoparticles (Ou et al., 2019) are formed by PEG and POD with oxalate ester bond bridges. The latter are cleaved in the presence of H_2O_2 to release the drug.

EXTERNAL STIMULUS–RESPONSIVE NFs

External stimuli–responsive NFs for delivery of active compounds from TCM are mainly including magnetic, light, and thermal response as shown in **Table 3**.

Magnetic-Responsive NFs for Delivery of Active Compounds From TCM

Magnetic-responsive NFs can be used to monitor tumors *in vivo* by noninvasive magnetic resonance imaging (MRI) (Kang et al., 2017). In this way, they can deliver chemotherapy drugs, small-molecule agents, photosensitizers, and small interfering

TABLE 3 | External stimulus–responsive nanoformulations in active compounds from TCM.

Response method	Active compounds	Response agent	Application	Cell line/animal	References
Magnetic	Artemisinin	Magnetic iron oxide	Breast cancer	BALB/c mice	Gharib et al., 2015
	Dihydroartemisinin	Fe_3O_4 nanoparticle	Head and neck squamous cell carcinoma	A549 HeLa HeLa tumor-bearing nude mice	Li et al., 2019a
		Fe_3O_4 nanoparticle	Myeloid leukemia	K562 HL-60 SHI-1 NB4 BALB/c male mice	Chen et al., 2016b
	Quercetin	γ-Fe_2O_3	Glioma	C6	Cruz Dos Santos et al., 2019
	Stevioside	Fe_3O_4	Lung cancer	A549	Gupta and Sharma, 2019
Thermal	Curcumin	Poly(*N*-isopropylacrylamide)	Anticancer	L929 KB MCF-7 PC3	Rejinold et al., 2011
	Honokiol	(PEG-PCL-PEG, PECE) hydrogel	Malignant pleural effusion	LL2 Red blood cell C57B/6 mice	Fang et al., 2009
Light	Artesunate	Covalent bond between carboxylic groups and amino groups of nGO-PEG	Liver cancer	HepG2 4T1 tumor-bearing mice	Pang et al., 2017
	Aloe emodin	Aloe emodin	Gastric cancer	SGC-7901	Li et al., 2016
	Hypericin	Hypericin	Glioma	U87-MG	Huntosova et al., 2012
		Hypericin	Colon carcinoma Antibacterial	Caco-2 HT-29 *E. faecalis* *E. coli* *S. aureus*	Montanha et al., 2017
		Hypericin	Ovarian cancer	A2780N A2780N tumor-bearing nude mouse	Han et al., 2020
	Quercetin	Gold nanocages	Multidrug-resistant breast cancer	MCF-7/ADR	Zhang et al., 2018c
	Tetrandrine	Fe-GA	Anticancer	4T1 U87MG	Wang K. et al., 2019

RNA molecules (Zhu et al., 2017). Iron oxide nanoparticles are essential in magnetic-responsive NFs (Vangijzegem et al., 2019).

Gharib et al. created artemisinin- and transferrin-loaded magnetic nanoliposomes coated with iron oxide. The external magnet achieved high concentrations of artemisinin and transferrin in tumors to enhance the antitumor effect of artemisinin in BALB/c mice (Gharib et al., 2015). HHT- Fe_3O_4 magnetic nanoparticles were designed to deliver the HHT to tumor sites. HHT inhibited the synthesis of the short-lived protein Mcl-1 by targeting the A-site cleft of eukaryotic ribosomes (Chen et al., 2016b).

Dihydroartemisinin-MLP nanoliposomes were created using Fe_3O_4 nanoparticles. The negative charge of dihydroartemisinin-MLPs nanoliposomes under the action of a magnetic field delivered dihydroartemisinin with nonspecific binding to plasma proteins (Li et al., 2019a). Tetrandrine–Fe_3O_4-PLGA nanoparticles were used to direct tetrandrine to specific sites upon manipulation by an external magnetic field to increase the tetrandrine concentration. Tetrandrine is derived from *Stephania tetrandra* and is an active compound of a TCM called "Fangji" (Wang K. et al., 2019).

In the design of magnetic-responsive nanoliposomes to deliver quercetin, quercetin was not only loaded as an antitumor flavonoid drug and also has strong antioxidant properties to prevent the nanomagnetic liposomes from being oxidized. However, the incorporation of quercetin might weaken the magnetic properties of the nanoliposomes, and it was necessary

to precisely control the ratio of quercetin to ensure that the superparamagnetism of the magnetic liposomes was maintained (Cruz Dos Santos et al., 2019).

Light-Responsive NFs for Delivery of Active Compounds From TCM

NFs can be activated by light (visible, ultraviolet, infrared) for using in photodynamic imaging, photodynamic therapy (PDT) or photothermal therapy (PTT) (Rkein, 2014; Chen and Zhao, 2018). Light-responsive agents ("photosensitizers") play an important part in such light-responsive NFs (Reeßing and Szymanski, 2017).

Traditional photosensitizers and TCM agents can be co-encapsulated, or a TCM agent can be encapsulated in light-responsive inorganic/organic nanoparticles. Moreover, some active compounds of TCM can be used as photosensitizers to carry out PDT or PTT after light activation.

An artesunate-modified PEGylated nanographene oxide (nGO-PEG-ARS) (Pang et al., 2017) delivered artesunate to liver cancer with the light-responsive agent. The light responsive agent was a covalent bond between carboxylic groups and amino groups of nGO-PEG. Near-infrared irradiation triggered the artesunate loaded on nGO-PEG to produce nitric oxide and peroxynitrite groups to achieve a synergistic chemophotothermal anticancer effect.

In Fe–gallic acid–PEG coordination polymer-based nanoparticles, ultrasmall (5 nm) Fe–gallic acid nanoparticles were formed by mixing $FeCl_3$ solution and gallic acid solution (Jin et al., 2017). Surface modification of PEG increased its passive accumulation in tumor cells. Also, the temperature was increased by 20°C after laser irradiation for 5 min (808-nm laser at 0.8 W cm^2).

In the treatment of gastric cancer, Li et al. (2016) used aloe emodin to fabricate aloe emodin nanoliposomes for transfection of the r-caspase-3 gene and PDT. Moreover, hypericin is an excellent photosensitizer in hypericin–low-density lipoprotein–dextran complexes for glioma treatment. In these complexes, dextran is modified on the surface of low-density lipoprotein particles, which reduces the interaction of low-density lipoprotein with other serum constituents to prevent hypericin redistribution to other free lipoproteins (Huntosova et al., 2012).

Also, single-walled carbon nanohorn-hypericin has been shown to improve the water solubility, photostability, and therapeutic effects of hypericin and to protect it from light degradation. Single-walled carbon nanohorn-hypericin can simultaneously generate sufficient ROS and hyperthermia upon light irradiation at 590 and 808 nm (Gao et al., 2019a).

Thermal-Responsive NFs for Delivery of Active Compounds From TCM

In thermal-responsive chitosan-g-poly(*N*-isopropylacrylamide) co-polymeric nanoparticles, the polymer–polymer interaction of poly(*N*-isopropylacrylamide) is greater than the polymer-curcumin interaction, whereas the hydrogen bond is weakened at a lower critical solution temperature, so curcumin molecules can escape from the entrapped polymer matrices (Rejinold et al., 2011). Honokiol hydrogel (Fang et al., 2009) loads honokiol as a free-flowing sol at room temperature or below the critical gelation temperature. Honokiol can become a gel at body temperature and remain *in situ* for a long time to reduce the burst release of honokiol.

MULTIPLE-RESPONSIVE NFs FOR DELIVERY OF ACTIVE COMPOUNDS FROM TCM

Multiple-responsive NFs usually have two or more different responsive functions and modes. The combination of multiple responsive modes can overcome the shortcomings of a single responsive mode to achieve targeted delivery of drugs. The main multiple-responsive NFs are shown in **Table 4**.

Dual Internal–Responsive NFs

For targeted delivery of cinnamaldehyde, quinone methide-cinnamaldehyde (Noh et al., 2015) was prepared as a dual-responsive NF combining a redox response and pH response. The H_2O_2-sensitive boronate linkage and acid-sensitive acetal linkage were oxidized rapidly to release quinone methide to abrogate GSH. Also, the acetal linkage degraded in acidic tumor environments to release ROS-generating cinnamaldehyde, which killed DU145 and SW620 cells efficiently *in vitro* and *in vivo*. The same type of response mode was used in tumor-specific enhanced oxidative stress polymer conjugate (Ma et al., 2020) delivery of cinnamaldehyde on CT26 and 4T1 cells. The acidic condition accelerated hydrolysis of acetal linkages in phenylboronic acid containing cinnamaldehyde derivatives, and H_2O_2 facilitated detachment of boric acid groups and intramolecular rearrangement to produce quinone methide and further accelerated the hydrolysis of acetal linkages and cinnamaldehyde release.

Celastrol was delivered to desmoplastic melanoma cells by aminoethylanisamide–polymer–disulfide bond nanoparticles (Liu et al., 2018). In an acidic tumor microenvironment, tertiary amines of mitoxantrone and celastrol copolymer were protonated and reversed the zeta potential from a negative charge to a positive charge, thereby attracting negatively charged cell membranes. Also, the disulfide bond was broken in the presence of GSH, resulting in an increased particle size.

Disulfide bonds and β-thiopropionate linkages endowed a redox response and pH response of T7-peptide-S-S-nanoparticles (Li et al., 2019b) for POD delivery. Disulfide bonds were disassociated by a high concentration of GSH, and the β-thiopropionate linkage was broken by an acidic environment, and then POD was released rapidly. Massaro et al. replaced the keto group of curcumin with a pH-responsive imine group and used a carbon chain with a disulfide bond to connect the silicon on halloysite nanotubes to prepare a pH/redox responsive curcumin prodrug. In the different pH and 10 mM GSH

TABLE 4 | Multistimulus-responsive nanoformulations in active compounds from TCM.

Response method	Active compounds	Response agent	Application	Cell line/animal	Reference
pH and redox	Berberine	pH: vitamin B_6 redox: dithiodipropionic acid	Anticancer	HepG2 HepG2 tumor-bearing nude mice	Fang et al., 2019a
	Berberine and curcumin	pH: borate ester bond redox: dithiodipropionic acid	Anticancer	PANC-1 PANC-1 tumor-bearing nude mice	Fang et al., 2019b
	Celastrol	pH: tertiary amines Redox: disulfide bond	Desmoplastic melanoma (DM)	BPD6 NIH 3T3 DM tumor-bearing mice	Liu et al., 2018
	Cinnamaldehyde	Acetal and quinone methide	Colon cancer Breast cancer	CT26 4T1 CT26 tumor-bearing mice	Ma et al., 2020
		Redox: boric acid pH: acetal linkage	Prostate cancer Colon cancer	DU145 SW620 NIH3T3 BALB/c nude mice	Noh et al., 2015
	Curcumin	Redox: dithiodipropionic acid pH: hydrazone	Multidrug-resistant	MCF-7/ADR	Wang Y. et al., 2018
		pH: imine bond Redox: disulfide bond	Anticancer	Hep3B HA22T/VGH	Massaro et al., 2016
		pH: calcium phosphate and ester bond Redox: disulfide bond	Anticancer	MCF-7 A549 MDA-MB-231 BALB/c mice	Chen et al., 2017
	Podophyllotoxin	Redox: disulfide bond pH: disulfide bond and b-thiopropionate	Breast cancer	MCF-7 MCF-7/ADR A549 A549/PTX MCF-7/ADR tumor-bearing nude mice	Li et al., 2019b
Magnetic and pH	Artemisinin	Magnetic: Fe_3O_4@C pH: MIL-100(Fe)	Anticancer	HeLa A549 BALB/c nude mice	Li et al., 2019a
	Berberine	Magnetic: Fe_3O_4 head pH: carboxylate functional group modified on the surface and pore of silica rod	Hepatocellular carcinoma	HepG2 HL-7702	Wang M. et al., 2017
	Berberine and doxorubicin	Magnetic: Janus M-MSNs pH: Janus M-MSNs	Hepatocellular carcinoma	H22 HepG2 NIH-3T3 HL-7702 H22 tumor-bearing ICR mice	Zhang et al., 2019
	Quercetin	Magnetic: Fe_3O_4@SiO_2 (FITC) pH: imine and acetal	Multidrug-resistant	A549 A549/DOX	Daglioglu, 2017
Magnetic and thermal	Stevioside	Fe_3O_4	Glioma	C6	Gupta and Sharma, 2019
Thermal and pH	Cinnamaldehyde	Thermal: glycine and Pluronicpolymer pH: Fe_3O_4 nanoparticles	Breast cancer	MCF7 MDAMB231	Wani et al., 2014
	Berberine and evodiamine	Thermo: *N*-isopropylacrylamide pH: methacrylic acid	Anticancer	HepG-2 HCT-8 HeLa HUVEC EMT-6 tumor-bearing nude mice	Feng et al., 2019

(Continued)

TABLE 4 | Continued

Response method	Active compounds	Response agent	Application	Cell line/animal	Reference
Light and redox	Curcumin	Zinc phthalocyanine and curcumin	Melanoma tumor	B16F10 mouse	Zhang et al., 2020b
Magnetic and light and thermal and pH	Artemisinin	Magnetic and photothermal: PB MOF Magnetic and PH: MIL-100(Fe) MOF	Anticancer	HeLa BALB/c nude mice	Li et al., 2019a
Magnetic and light and thermal	Gallic acid	Magnetic and thermal: SPIONs Light: ICG	Anticancer	MCF7 HT-29 4T1 tumor-bearing mice	Jin et al., 2017
Light and thermal and pH	Quercetin	pH: poly(ethylene glycol)$_{5k}$-poly(β-aminoesters)$_{10k}$ Light and thermal: Ag_2S	Anticancer	HepG-2 HL-7702 HepG-2 tumor-bearing nude mice	Zhong et al., 2020

environment, it showed a good release behavior of curcumin (Massaro et al., 2016).

External/Internal–Responsive NFs

Multiple-responsive NFs with both external and internal responses are conducive to targeted release of TCM agents at lesion sites. As stated above, often magnetically responsive delivery is combined with other responsive modes for higher efficiency of drug delivery.

A multiple-responsive NF called Prussian blue-iron carboxylate dual-metal organic frameworks [PB@MIL-100(Fe)dual-MOFs] can deliver artemisinin to HeLa cells through integrated magnetic, light and pH responses (Wang et al., 2016b). The inner Prussian blue MOFs and outer MIL-100(Fe) MOFs serve as MRI contrast agents. Under the illumination of an 808-nm near-infrared laser, the inner Prussian blue MOF induces hyperthermia by converting light energy to heat. The MIL-100(Fe) MOF can collapse in acidic environments to release artemisinin.

Dihydroartemisinin was delivered using a strategy combining a magnetic response and pH response. Fe_3O_4@C@MIL-100(Fe) nanoparticles were designed by Wang and colleagues (Wang et al., 2016a). Fe_3O_4@C nanoparticles were magnetic targeting, and carbon dots were two-photon fluorescence imaging agents. MIL-100(Fe) MOFs degraded and released dihydroartemisinin and Fe (III) ions in acidic conditions. When the pH within an endosome decreased, Fe^{3+} reduced to Fe^{2+} by ferric reductase and other reductive molecules within cells.

Magnetic field–induced endocytosis and pH-responsive drug release of berberine-loaded Fe_3O_4-$mSiO_2$ nanoparticles were exhibited in hepatocellular-carcinoma treatment because the pH-responsive carboxylate functional group was modified on the surface and pores of silica rods and the magnetic-responsive Fe_3O_4 head (Wang Z. et al., 2017). In stevioside (STE)-MNP, STE reduced the size of Fe_3O_4 nanoparticles to control magnetic properties and aligned rapidly with the external magnetic field (Gupta and Sharma, 2019). The carbohydrate nature of STE enhanced the interaction between STE-MNP and C6 cells. STE-MNP aggregated as cluster-like formations in the glioma site to enhance hyperthermia.

The magnetic-responsive agents, superparamagnetic iron oxide nanoparticles (SPIONs), and a light-responsive agent, indocyanine green (ICG), were combined in SPIONs-GA-ICG (Ghorbani et al., 2018). The SPIONs produced hyperthermia; gallic acid was oxidized and bonded to ICG by free-radical production, and gallic acid also acted as a biological coating for ICG-loaded SPIONs.

A thermal- and pH-responsive NF was used as a cinnamaldehyde-delivery platform with glycine and a pluronic polymer. Cinnamaldehyde tagged Fe_3O_4 nanoparticles capped with glycine and pluronic polymer nanoparticles increased the temperature to 41.6°C within 1 min after radiofrequency pulses of 20 MHz (Wani et al., 2014). Also, the ionic interaction between the free aldehyde group of cinnamaldehyde and the liberated protons under acidic conditions delivered cinnamaldehyde rapidly from the nanoparticles.

SUMMARY

Most of the active compounds extracted from TCM are small molecules. They have unfavorable pharmacokinetics and suboptimal biodistribution (e.g., prominent accumulation in multiple healthy organs) (Golombek et al., 2018). Through nanotechnology modification, drug molecules have a better EPR effect to increase the accumulation of drugs at lesion sites (Maeda, 2017). Thus, several types of nanodelivery system have been employed to improve the clinical outcome of the active compounds in TCM formulations: nanoparticles, liposomes, micelles, nanocapsules, and nanoemulsions (Ma et al., 2019).

Stimuli-responsive NFs can release drugs under internal and external stimuli. We reviewed the applications of stimuli-responsive NFs used commonly in the delivery of active compounds from TCM.

Four types of pH-responsive agents can be classified. The first type is inorganic material. Iron-containing nanoparticles play a key part in the pH-responsive delivery of artemisinin. The endoperoxide linkages (R-O-O-R′) in artemisinin can be cleaved with intracellular Fe^{2+} to generate toxic radicals to kill cancer cells and treat malaria (Asano and Iwahashi, 2017; Ding

et al., 2018). Fe_3O_4 dissociates rapidly at low pH in lysosomes and transforms to Fe^{2+} (Bhaw-Luximon and Jhurry, 2017). Simultaneously, Fe_3O_4 is also a magnetic agent that can induce a magnetic response. In Fe_3O_4@$MnSiO_3$-FA nanospheres, Mn^{2+} has the same function as Fe^{2+} (Chen et al., 2015). ZIF-8 is a well-known pH-sensitive imidazole derivative (Chen et al., 2018; Gao et al., 2019b) composed of Zn^{2+} coordinated by four imidazolate rings (Mateo et al., 2019). ZnO nanoparticles are also degraded readily to Zn^{2+} (Hahn and Ahmad, 2012). ZnO is stable at pH ∼7, but dissolves rapidly at pH $<$ 6 (Dhivya et al., 2018). The second type of pH-responsive material is a natural product with pH instability. Chitosan is a commonly used drug-delivery agent with special amphiphilic characteristics that enables "packaging" of a poorly soluble drug in water phases (Younes, 2015). Its pH-responsive function is attributed mainly to protonation of amino groups in acidic conditions, which make chitosan hydrogels swell rapidly and release the loaded drug. The third type of pH-responsive materials is artificial polymers such as PAE, PAGA, and PLGA. The fourth (and most common) types of pH-responsive material used in the delivery of active compounds from TCM are amine bonds and hydrazone bonds. They are linked ingeniously with the active agent from the TCM and the matrix of NFs until they encounter an acidic microenvironment. This strategy protects the drug from leaking prematurely in the circulation and promotes the targeted release of the drug at the lesion site.

Redox-responsive NFs of active compounds from TCM are dependent mainly on modification of disulfide bonds. Metabolic imbalances in tumor cells produce high levels of GSH, which can cleave disulfide bonds to release the loaded agent in target cells. In addition, pathogen infection induces an inflammatory reaction to increase H_2O_2 levels in infected tissues, which are prone to redox reactions.

In light-responsive NFs, besides the many chemical photosensitizers, several naturally active ingredients of TCM are used as photosensitizers in PDT, including curcumin (Tao et al., 2019b), hypericin (Lin et al., 2016; Li et al., 2018b; Zhang et al., 2018a), and aloe emodin. These active compounds from TCM have been shown to be useful in PDT or PTT in multiple studies.

Some active substances from TCM have been used for nanotargeted delivery. In doxorubicin-loaded CTS/PEG-GA nanoparticles (Tian et al., 2010), GA can target GA receptors on liver cancer cells. Also, GA receptors have been shown to be useful as liver-cancer targets in GA NFs (Sun et al., 2017). Similarly, in quercetin/Fe (III) (Bertleff-Zieschang et al., 2017) delivery, quercetin (as a phenolic compound) can form a complex organic–inorganic network with iron and gallic acid, and STE contributes to regulation of iron ions to form an "ideal" size of magnetic nanoparticles. Some active compounds from TCM contain both water-soluble sugar groups and water-insoluble aglycones, which form biocompatible NFs readily by self-assembly. Also, most active compounds from TCM have multiple active binding sites in biological tissues.

In stimuli-responsive NFs, internal stimulus–responsive NFs have great advantages in specifically releasing active compounds from TCM to the target site, subsequently increasing their therapeutic efficacy and decreasing the side effects. However, it is very difficult to artificially control the amounts and time of drug release from internal stimulus–responsive NFs. External stimulus–responsive NFs have advantageous properties in artificial control of drug release because they could respond to external light and magnetic energy. Therefore, we could regulate light and magnetic energy to control the release amounts and time of drugs from these NFs.

The information provided above indicates that smart responsive NFs hold great promise in targeted delivery of active compounds from TCM. However, the confirmed evidences are mainly from *in vitro* and *in vivo* experimental studies. Few clinical trials are investigated on smart responsive NFs as the targeted carriers for delivering active compounds from TCM. The main challenges are the complexity of smart responsive NFs such as tedious preparation, complicated characterization, biosafety of nanoparticle materials, and uncertainty of the *in vivo* fate of NFs. Thus, further exploring and addressing the above problem should be urgent tasks for translating smart responsive NFs as targeted delivery carriers of active compounds from TCM to clinical application.

AUTHOR CONTRIBUTIONS

All authors listed have made a substantial, direct and intellectual contribution to the work, and approved it for publication.

REFERENCES

Adiwidjaja, J., and McLachlan, A. J. (2017). Curcumin as a clinically-promising anti-cancer agent: pharmacokinetics and drug interactions. *Exp. Opin. Drug Metab. Toxicol.* 13, 953–972. doi: 10.1080/17425255.2017.1360279

Ai, H., Wu, X., Qi, M., Zhang, L., Hu, H., Zhao, Q., et al. (2018). Study on the mechanisms of active compounds in traditional chinese medicine for the treatment of influenza virus by virtual screening. *Interdiscip. Sci.* 10, 320–328. doi: 10.1007/s12539-018-0289-0

Asano, M., and Iwahashi, H. (2017). Determination of the structures of radicals formed in the reaction of antimalarial drug artemisinin with ferrous ions. *Eur. J. Med. Chem.* 127, 740–747. doi: 10.1016/j.ejmech.2016.10.053

Bertleff-Zieschang, N., Rahim, M. A., Ju, Y., Braunger, J. A., Suma, T., Dai, Y., et al. (2017). Biofunctional metal-phenolic films from dietary flavonoids. *Chem. Commun.* 53, 1068–1071. doi: 10.1039/C6CC08607A

Bhaw-Luximon, A., and Jhurry, D. (2017). Artemisinin and its derivatives in cancer therapy: status of progress, mechanism of action, and future perspectives. *Cancer Chemother. Pharmacol.* 79, 451–466. doi: 10.1007/s00280-017-3251-7

Bie, B., Sun, J., Guo, Y., Li, J., Jiang, W., Huang, C., et al. (2017). Baicalein: a review of its anti-cancer effects and mechanisms in hepatocellular carcinoma. *Biomed. Pharmacother.* 93, 1285–1291. doi: 10.1016/j.biopha.2017.07.068

Cai, X., Liu, M., Zhang, C., Sun, D., and Zhai, G. (2016). pH-responsive copolymers based on pluronic P123-poly(β-amino ester): synthesis, characterization and application of copolymer micelles. *Colloids Surf. B Biointerfaces* 142, 114–122. doi: 10.1016/j.colsurfb.2016.02.033

Chen, D., Dong, X., Qi, M., Song, X., and Sun, J. (2017). Dual pH/redox responsive and CD44 receptor targeting hybrid nano-chrysalis based on new oligosaccharides of hyaluronan conjugates. *Carbohydr. Polym.* 157, 1272–1280. doi: 10.1016/j.carbpol.2016.10.089

Chen, D., Lian, S., Sun, J., Liu, Z., Zhao, F., Jiang, Y., et al. (2016a). Design of novel multifunctional targeting nano-carrier drug delivery system based on CD44 receptor and tumor microenvironment pH condition. *Drug Deliv*. 23, 808–813. doi: 10.3109/10717544.2014.917130

Chen, H., and Zhao, Y. (2018). Applications of light-responsive systems for cancer theranostics. *ACS Appl. Mater. Interfaces* 10, 21021–21034. doi: 10.1021/acsami.8b01114

Chen, J., Guo, Z., Wang, H. B., Zhou, J. J., Zhang, W. J., and Chen, Q. W. (2014). Multifunctional mesoporous nanoparticles as pH-responsive Fe $(^{2+})$ reservoirs and artemisinin vehicles for synergistic inhibition of tumor growth. *Biomaterials* 35, 6498–6507. doi: 10.1016/j.biomaterials.2014.04.028

Chen, J., Zhang, W., Zhang, M., Guo, Z., Wang, H., He, M., et al. (2015). Mn (II) mediated degradation of artemisinin based on Fe_3O_4@$MnSiO_3$-FA nanospheres for cancer therapy *in vivo*. *Nanoscale* 7, 12542–12551. doi: 10.1039/C5NR02402A

Chen, M., Xiong, F., Ma, L., Yao, H., Wang, Q., Wen, L., et al. (2016b). Inhibitory effect of magnetic FeO nanoparticles coloaded with homoharringtonine on human leukemia cells *in vivo* and *in vitro*. *Int. J. Nanomed.* 11, 4413–4422. doi: 10.2147/IJN.S105543

Chen, X., Chen, Z., Hu, B., Cai, P., Wang, S., Xiao, S., et al. (2018). Synergistic lysosomal activatable polymeric nanoprobe encapsulating pH sensitive imidazole derivative for tumor diagnosis. *Small* 14:1703164. doi: 10.1002/smll.201703164

Chu, M., Ding, R., Chu, Z. Y., Zhang, M. B., Liu, X. Y., Xie, S. H., et al. (2014). Role of berberine in anti-bacterial as a high-affinity LPS antagonist binding to TLR4/MD-2 receptor. *BMC Comp. Altern. Med*. 14:89. doi: 10.1186/1472-6882-14-89

Cordeiro, R. A., Serra, A., and Coelho, J. F. J. (2019). Poly (β-amino ester)-based gene delivery systems: from discovery to therapeutic applications. *J. Control. Release* 310, 155–187. doi: 10.1016/j.jconrel.2019.08.024

Cruz Dos Santos, S., Osti Silva, N., Dos Santos Espinelli, J. B. Jr., Germani Marinho, M. A., Vieira Borges, Z., Bruzamarello Caon Branco, N., et al. (2019). Molecular interactions and physico-chemical characterization of quercetin-loaded magnetoliposomes. *Chem. Phys. Lipids* 218, 22–33. doi: 10.1016/j.chemphyslip.2018.11.010

Cui, T., Zhang, S., and Sun, H. (2017). Co-delivery of doxorubicin and pH-sensitive curcumin prodrug by transferrin-targeted nanoparticles for breast cancer treatment. *Oncol. Report.* 37, 1253-1260. doi: 10.3892/or.2017.5345

Daglioglu, C. (2017). Enhancing Tumor Cell Response to Multidrug Resistance with pH-Sensitive Quercetin and Doxorubicin Conjugated Multifunctional Nanoparticles. *Colloids Surf. B Biointerfaces* 156, 175–185. doi: 10.1016/j.colsurfb.2017.05.012

de Oliveira Pedro, R., Goycoolea, F. M., Pereira, S., Schmitt, C. C., and Neumann, M. G. (2018). Synergistic effect of quercetin and pH-responsive DEAE-chitosan carriers as drug delivery system for breast cancer treatment. *Int. J. Biol. Macromol*. 106, 579–586. doi: 10.1016/j.ijbiomac.2017.08.056

Dhivya, R., Ranjani, J., Rajendhran, J., Mayandi, J., and Annaraj, J. (2018). Enhancing the anti-gastric cancer activity of curcumin with biocompatible and pH sensitive PMMA-AA/ZnO nanoparticles. *Mater. Sci. Eng. C Mater. Biol. Appl*. 82, 182–189. doi: 10.1016/j.msec.2017.08.058

Ding, B., Wahid, M. A., Wang, Z., Xie, C., Thakkar, A., Prabhu, S., et al. (2017). Triptolide and celastrol loaded silk fibroin nanoparticles show synergistic effect against human pancreatic cancer cells. *Nanoscale* 9, 11739–11753. doi: 10.1039/C7NR03016A

Ding, Y., Wan, J., Zhang, Z., Wang, F., Guo, J., and Wang, C. (2018). Localized Fe(II)-induced cytotoxic reactive oxygen species generating nanosystem for enhanced anticancer therapy. *ACS Appl. Mater. Interfaces* 10, 4439–4449. doi: 10.1021/acsami.7b16999

Dong, X., Zou, S., Guo, C., Wang, K., Zhao, F., Fan, H., et al. (2018). Multifunctional redox-responsive and CD44 receptor targeting polymer-drug nanomedicine based curcumin and alendronate: synthesis, characterization and *in vitro* evaluation. *Artif. Cells Nanomed. Biotechnol*. 46, 168–177. doi: 10.1080/21691401.2017.1416390

Efferth, T. (2017). Cancer combination therapies with artemisinin-type drugs. *Biochem. Pharmacol*. 139, 56–70. doi: 10.1016/j.bcp.2017.03.019

Fang, F., Gong, C., Qian, Z., Zhang, X., Gou, M., You, C., et al. (2009). Honokiol nanoparticles in thermosensitive hydrogel: therapeutic effects on malignant pleural effusion. *ACS Nano* 3, 4080–4088. doi: 10.1021/nn900785b

Fang, L., Fan, H., Guo, C., Cui, L., Zhang, P., and Mu, H. (2019a). Novel mitochondrial targeting multifunctional surface charge-reversal polymeric nanoparticles for cancer treatment. *J Biomed Nanotechnol*. 15, 2151–2163. doi: 10.1166/jbn.2019.2854

Fang, L., Zhang, W., Wang, Z., Fan, X., Cheng, Z., Hou, X., et al. (2019b). Novel mitochondrial targeting charge-reversal polysaccharide hybrid shell/core nanoparticles for prolonged systemic circulation and antitumor drug delivery. *Drug Deliv*. 26, 1125–1139. doi: 10.1080/10717544.2019.1687614

Fang, X. B., Zhang, J. M., Xie, X., Liu, D., He, C. W., Wan, J. B., et al. (2016). pH-sensitive micelles based on acid-labile pluronic F68-curcumin conjugates for improved tumor intracellular drug delivery. *Int. J. Pharm*. 502, 28–37. doi: 10.1016/j.ijpharm.2016.01.029

Feng, Y., Li, N. X., Yin, H. L., Chen, T. Y., Yang, Q., and Wu, M. (2019). Thermo- and pH-responsive, lipid-coated, mesoporous silica nanoparticle-based dual drug delivery system to improve the antitumor effect of hydrophobic drugs. *Mol. Pharm.* 16, 422–436. doi: 10.1021/acs.molpharmaceut.8b01073

Ganapathy-Kanniappan, S., and Geschwind, J. F. (2013). Tumor glycolysis as a target for cancer therapy: progress and prospects. *Mol. Cancer* 12:152. doi: 10.1186/1476-4598-12-152

Gao, C., Jian, J., Lin, Z., Yu, Y. X., Jiang, B. P., Chen, H., et al. (2019a). Hypericin-loaded carbon nanohorn hybrid for combined photodynamic and photothermal therapy *in vivo*. *Langmuir* 35, 8228–8237. doi: 10.1021/acs.langmuir.9b00624

Gao, L., Chen, Q., Gong, T., Liu, J., and Li, C. (2019b). Recent advancement of imidazolate framework (ZIF-8) based nanoformulations for synergistic tumor therapy. *Nanoscale* 11, 21030–21045. doi: 10.1039/C9NR06558J

Gharib, A., Faezizadeh, Z., and Mesbah-Namin, S. A. (2015). Experimental treatment of breast cancer-bearing BALB/c mice by artemisinin and transferrin-loaded magnetic nanoliposomes. *Pharmacogn. Mag.* 11, S117–S122. doi: 10.4103/0973-1296.157710

Ghorbani, F., Imanparast, A., and Hataminia, F. (2018). A novel nano-superparamagnetic agent for photodynamic and photothermal therapies: an *in-vitro* study. *Photodiagn. Photodyn. Ther*. 23, 314–324. doi: 10.1016/j.pdpdt.2018.07.008

Giordano, A. (2019). Curcumin and cancer. *Nutrients* 11: E2376. doi: 10.3390/nu11102376

Golombek, S. K., May, J. N., Theek, B., Appold, L., Drude, N., Kiessling, F., et al. (2018). Tumor targeting via EPR: strategies to enhance patient responses. *Adv. Drug Deliv. Rev*. 130, 17–38. doi: 10.1016/j.addr.2018.07.007

Gupta, A., Kaur, C. D., Saraf, S., and Saraf, S. (2016). Formulation, characterization, and evaluation of ligand-conjugated biodegradable quercetin nanoparticles for active targeting. *Artif Cells Nanomed Biotechnol*. 44, 960–970. doi: 10.3109/21691401.2015.1008503

Gupta, R., and Sharma, D. (2019). Biofunctionalization of magnetite nanoparticles with stevioside: effect on the size and thermal behaviour for use in hyperthermia applications. *Int. J. Hyperthermia* 36, 302–312.doi: 10.1080/02656736.2019.1565787

Hahn, Y. B., and Ahmad, R. (2012). Chemical and biological sensors based on metal oxide nanostructures. *Chem. Commun.* 48, 10369–10385. doi: 10.1039/c2cc34706g

Han, X., Taratula, O., Taratula, O., Xu, K., St Lorenz, A., Moses, A., et al. (2020). Biodegradable hypericin-containing nanoparticles for necrosis targeting and fluorescence imaging. *Mol. Pharm.* 17, 1538–1545. doi: 10.1021/acs.molpharmaceut.9b01238

Huntosova, V., Buzova, D., Petrovajova, D., Kasak, P., Nadova, Z., Jancura, D., et al. (2012). Development of a new LDL-based transport system for hydrophobic/amphiphilic drug delivery to cancer cells. *Int. J. Pharm*. 436, 463–471. doi: 10.1016/j.ijpharm.2012.07.005

Jaman, M. S. (2018). Ellagic acid, sulforaphane, and ursolic acid in the prevention and therapy of breast cancer: current evidence and future perspectives. *Breast Cancer* 25, 517–528. doi: 10.1007/s12282-018-0866-4

Jelezova, I., Drakalska, E., Momekova, D., Shalimova, N., Momekov, G., Konstantinov, S., et al. (2015). Curcumin loaded pH-sensitive hybrid lipid/block copolymer nanosized drug delivery systems. *Eur. J. Pharm. Sci*. 78, 67–78. doi: 10.1016/j.ejps.2015.07.005

Jiang, K., Chi, T., Li, T., Zheng, G., Fan, L., Liu, Y., et al. (2017). A smart pH-responsive nano-carrier as a drug delivery system for the targeted delivery of ursolic acid: suppresses cancer growth and metastasis by modulating

P53/MMP-9/PTEN/CD44 mediated multiple signaling pathways. *Nanoscale* 9, 9428–9439. doi: 10.1039/C7NR01677H

Jin, Q., Zhu, W., Jiang, D., Zhang, R., Kutyreff, C. J., Engle, J. W., et al. (2017). Ultra-small iron-gallic acid coordination polymer nanoparticles for chelator-free labeling of Cu and multimodal imaging-guided photothermal therapy. *Nanoscale* 9, 12609–12617. doi: 10.1039/C7NR03086J

Kang, T., Li, F., Baik, S., Shao, W., Ling, D., and Hyeon, T. (2017). Surface design of magnetic nanoparticles for stimuli-responsive cancer imaging and therapy. *Biomaterials* 136, 98–114. doi: 10.1016/j.biomaterials.2017.05.013

Kim, G. S., Kim, D. H., Lim, J. J., Lee, J. J., Han, D. Y., Lee, W. M., et al. (2008). Biological and antibacterial activities of the natural herb Houttuynia cordata water extract against the intracellular bacterial pathogen salmonella within the RAW 264.7 macrophage. *Biol. Pharm. Bull.* 31, 2012–2017. doi: 10.1248/bpb.31.2012

Kim, S. T., Kim, S. Y., Lee, J., Kim, K., Park, S. H., Park, Y. S., et al. (2018). Triptolide as a novel agent in pancreatic cancer: the validation using patient derived pancreatic tumor cell line. *BMC Cancer* 18:1103. doi: 10.1186/s12885-018-4995-0

Kong, C., Li, Y., Liu, Z., Ye, J., Wang, Z., Zhang, L., et al. (2019). Targeting the oncogene KRAS mutant pancreatic cancer by synergistic blocking of lysosomal acidification and rapid drug release. *ACS Nano* 13, 4049–4063. doi: 10.1021/acsnano.8b08246

Li, H., Li, X., Shi, X., Li, Z., and Sun, Y. (2019a). Effects of magnetic dihydroartemisinin nano-liposome in inhibiting the proliferation of head and neck squamous cell carcinomas. *Phytomedicine* 56, 215–228. doi: 10.1016/j.phymed.2018.11.007

Li, K. T., Duan, Q. Q., Chen, Q., He, J. W., Tian, S., Lin, H. D., et al. (2016). The effect of aloe emodin-encapsulated nanoliposome-mediated r-caspase-3 gene transfection and photodynamic therapy on human gastric cancer cells. *Cancer Med*. 5, 361–369. doi: 10.1002/cam4.584

Li, M., Wang, Y., Jiang, S., Gao, Y., Zhang, W., Hu, S., et al. (2020). Biodistribution and biocompatibility of glycyrrhetinic acid and galactose-modified chitosan nanoparticles as a novel targeting vehicle for hepatocellular carcinoma. *Nanomedicine* 15, 145–161. doi: 10.2217/nnm-2018-0455

Li, S., Wang, L., Li, N., Liu, Y., and Su, H. (2017). Combination lung cancer chemotherapy: design of a pH-sensitive transferrin-PEG-Hz-lipid conjugate for the co-delivery of docetaxel and baicalin. *Biomed. Pharmacother*. 95, 548–555. doi: 10.1016/j.biopha.2017.08.090

Li, Y., Chen, M., Yao, B., Lu, X., Zhang, X., He, P., et al. (2019b). Transferrin receptor-targeted redox/pH-sensitive podophyllotoxin prodrug micelles for multidrug-resistant breast cancer therapy. *J. Mater. Chem. B* 7, 5814–5824. doi: 10.1039/C9TB00651F

Li, Z. H., Li, Y. Y., Hou, M., Yang, T., Lu, L. C., and Xu, X. Y. (2018b). Topically applied hypericin exhibits skin penetrability on nude mice. *Lasers Med. Sci.* 33, 1279–1286. doi: 10.1007/s10103-018-2479-8

Li, W., Wang, X. H., Luo, Z., Liu, L. F., Yan, C., Yan, C. Y., et al. (2018a). Traditional Chinese medicine as a potential source for HSV-1 therapy by acting on virus or the susceptibility of host. *Int. J. Mol. Sci.* 19:3266. doi: 10.3390/ijms19103266

Lin, S., Lei, K., Du, W., Yang, L., Shi, H., Gao, Y., et al. (2016). Enhancement of oxaliplatin sensitivity in human colorectal cancer by hypericin mediated photodynamic therapy via ROS-related mechanism. *Int. J. Biochem. Cell Biol.* 71, 24–34. doi: 10.1016/j.biocel.2015.12.003

Lin, Y. H., Lin, J. H., Chou, S. C., Chang, S. J., Chung, C. C., Chen, Y. S., et al. (2015). Berberine-loaded targeted nanoparticles as specific *Helicobacter pylori* eradication therapy: *in vitro* and *in vivo* study. *Nanomedicine* 10, 57–71. doi: 10.2217/nnm.14.76

Ling, D., Xia, H., Park, W., Hackett, M. J., Song, C., Na, K., et al. (2014). pH-sensitive nanoformulated triptolide as a targeted therapeutic strategy for hepatocellular carcinoma. *ACS Nano* 8, 8027–8039. doi: 10.1021/nn502074x

Liu, C., and Chang, F. (2011). Development and characterization of eucalyptol microemulsions for topic delivery of curcumin. *Chem. Pharm. Bull.* 59, 172–178. doi: 10.1248/cpb.59.172

Liu, H., Dong, Y., Gao, Y., Du, Z., Wang, Y., Cheng, P., et al. (2016). The fascinating effects of baicalein on cancer: a review. *Int J. Mol. Sci.* 17:1681. doi: 10.3390/ijms17101681

Liu, J., Huang, Y., Kumar, A., Tan, A., Jin, S., Mozhi, A., et al. (2014). pH-sensitive nano-systems for drug delivery in cancer therapy. *Biotechnol. Adv*. 32, 693–710. doi: 10.1016/j.biotechadv.2013.11.009

Liu, L., Wei, Y., Zhai, S., Chen, Q., and Xing, D. (2015). Dihydroartemisinin and transferrin dual-dressed nano-graphene oxide for a pH-triggered chemotherapy. *Biomaterials* 62, 35–46. doi: 10.1016/j.biomaterials.2015.05.036

Liu, M., Wang, B., Guo, C., Hou, X., Cheng, Z., and Chen, D. (2019). Novel multifunctional triple folic acid, biotin and CD44 targeting pH-sensitive nano-actiniaes for breast cancer combinational therapy. *Drug Deliv*. 26, 1002–1016. doi: 10.1080/10717544.2019.1669734

Liu, Q., Chen, F., Hou, L., Shen, L., Zhang, X., Wang, D., et al. (2018). Nanocarrier-mediated chemo-immunotherapy arrested cancer progression and induced tumor dormancy in desmoplastic melanoma. *ACS Nano* 12, 7812–7825. doi: 10.1021/acsnano.8b01890

Lu, Y., Han, S., Zheng, H., Ma, R., Ping, Y., Zou, J., et al. (2018). A novel RGDyC/PEG co-modified PAMAM dendrimer-loaded arsenic trioxide of glioma targeting delivery system. *Int. J. Nanomedicine* 13, 5937–5952. doi: 10.2147/IJN.S175418

Luan, J., Wu, K., Li, C., Liu, J., Ni, X., Xiao, M., et al. (2017). pH-Sensitive drug delivery system based on hydrophobic modified konjac glucomannan. *Carbohydr. Polym*. 171, 9–17. doi: 10.1016/j.carbpol.2017.04.094

Luo, H., Vong, C. T., Chen, H., Gao, Y., Lyu, P., Qiu, L., et al. (2019). Naturally occurring anti-cancer compounds: shining from Chinese herbal medicine. *Chin. Med*. 14:48. doi: 10.1186/s13020-019-0270-9

Lv, H., Zhen, C., Liu, J., Yang, P., Hu, L., and Shang, P. (2019). Unraveling the potential role of glutathione in multiple forms of cell death in cancer therapy. *Oxid. Med. Cell Longev*. 2019:3150145. doi: 10.1155/2019/3150145

Ma, S., Song, W., Xu, Y., Si, X., Lv, S., Zhang, Y., et al. (2020). Rationally designed polymer conjugate for tumor-specific amplification of oxidative stress and boosting antitumor immunity. *Nano Lett.* 20, 2514–2521. doi: 10.1021/acs.nanolett.9b05265

Ma, Z., Fan, Y., Wu, Y., Kebebe, D., Zhang, B., Lu, P., et al. (2019). Traditional Chinese medicine-combination therapies utilizing nanotechnology-based targeted delivery systems: a new strategy for antitumor treatment. *Int. J. Nanomed.* 14, 2029–2053. doi: 10.2147/IJN.S197889

Madhusudana Rao, K., Krishna Rao, K. S., Ramanjaneyulu, G., and Ha, C. S. (2015). Curcumin encapsulated pH sensitive gelatin based interpenetrating polymeric network nanogels for anti cancer drug delivery. *Int. J. Pharm*. 478, 788–795. doi: 10.1016/j.ijpharm.2014.12.001

Maeda, H. (2017). Polymer therapeutics and the EPR effect. *J. Drug Target* 25, 781–785. doi: 10.1080/1061186X.2017.1365878

Manayi, A., Nikan, M., Nobakht-Haghighi, N., and Abdollahi, M. (2018). Advances in the anticancer value of the ursolic acid through nanodelivery. *Curr. Med. Chem*. 25, 4866–4875. doi: 10.2174/0929867324666170713102918

Massaro, M., Amorati, R., Cavallaro, G., Guernelli, S., Lazzara, G., Milioto, S., et al. (2016). Direct chemical grafted curcumin on halloysite nanotubes as dual-responsive prodrug for pharmacological applications. *Colloids Surf. B Biointerfaces* 140, 505–513. doi: 10.1016/j.colsurfb.2016.01.025

Mateo, D., Santiago-Portillo, A., Albero, J., Navalón, S., Alvaro, M., and García, H. (2019). Long-term photostability in terephthalate metal-organic frameworks. *Angew. Chem. Int. Ed. Engl.* 58, 17843–17848. doi: 10.1002/anie.201911600

Mlala, S., Oyedeji, A. O., Gondwe, M., and Oyedeji, O. O. (2019). Ursolic acid and its derivatives as bioactive agents. *Molecules* 24:E2751. doi: 10.3390/molecules24152751

Moloney, M. G. (2016). Natural products as a source for novel antibiotics. *Trends Pharmacol. Sci*. 37, 689–701. doi: 10.1016/j.tips.2016.05.001

Montanha, M. C., Silva, L. L., Pangoni, F., Cesar, G. B., Gon?alves, R. S., Caetano, W., et al. (2017). Response surface method optimization of a novel Hypericin formulation in P123 micelles for colorectal cancer and antimicrobial photodynamic therapy. *J. Photochem. Photobiol. B Biol.* 170, 247–255. doi: 10.1016/j.jphotobiol.2017.04.008

Noh, J., Kwon, B., Han, E., Park, M., Yang, W., Cho, W., et al. (2015). Amplification of oxidative stress by a dual stimuli-responsive hybrid drug enhances cancer cell death. *Nat. Commun*. 6:6907. doi: 10.1038/ncomms7907

Ou, K., Kang, Y., Chen, L., Zhang, X., Chen, X., Zheng, Y., et al. (2019). H_2O_2-responsive nano-prodrug for podophyllotoxin delivery. *Biomater. Sci*. 7, 2491–2498. doi: 10.1039/C9BM00344D

Pandey, S., Mewada, A., Thakur, M., Shah, R., Oza, G., and Sharon, M. (2013). Biogenic gold nanoparticles as fotillas to fire berberine hydrochloride using folic acid as molecular road map. *Mater. Sci. Eng. C Mater. Biol. Appl.* 33, 3716–3722. doi: 10.1016/j.msec.2013.05.007

Pang, Y., Mai, Z., Wang, B., Wang, L., Wu, L., Wang, X., et al. (2017). Artesunate-modified nano-graphene oxide for chemo-photothermal cancer therapy. *Oncotarget* 8, 93800–93812. doi: 10.18632/oncotarget.21191

Park, S. C., Kim, N. H., Yang, W., Nah, J. W., Jang, M. K., and Lee, D. (2016). Polymeric micellar nanoplatforms for Fenton reaction as a new class of antibacterial agents. *J. Control. Release* 221, 37–47. doi: 10.1016/j.jconrel.2015.11.027

Patel, R. V., Mistry, B. M., Shinde, S. K., Syed, R., Singh, V., and Shin, H. S. (2018). Therapeutic potential of quercetin as a cardiovascular agent. *Eur. J. Med. Chem.* 155, 889–904. doi: 10.1016/j.ejmech.2018.06.053

Reeßing, F., and Szymanski, W. (2017). Beyond photodynamic therapy: light-activated cancer chemotherapy. *Curr. Med. Chem.* 24, 4905–4950. doi: 10.2174/0929867323666160906103223

Rejinold, N. S., Sreerekha, P. R., Chennazhi, K. P., Nair, S. V., and Jayakumar, R. (2011). Biocompatible, biodegradable and thermo-sensitive chitosan-g-poly (N-isopropylacrylamide) nanocarrier for curcumin drug delivery. *Int. J. Biol. Macromol.* 49, 161–172. doi: 10.1016/j.ijbiomac.2011.04.008

Rkein, A. M. (2014). Photodynamic therapy. *Dermatol. Clin.* 32, 415–425. doi: 10.1016/j.det.2014.03.009

Sadeghi, S., Davoodvandi, A., Pourhanifeh, M. H., Sharifi, N., ArefNezhad, R., Sahebnasagh, R., et al. (2019). Anti-cancer effects of cinnamon: insights into its apoptosis effects. *Eur. J. Med. Chem.* 178, 131–140. doi: 10.1016/j.ejmech.2019.05.067

Sahu, P., Kashaw, S. K., Jain, S., Sau, S., and Iyer, A. K. (2017). Assessment of penetration potential of pH responsive double walled biodegradable nanogels coated with eucalyptus oil for the controlled delivery of 5-fluorouracil: *in vitro* and *ex vivo* studies. *J. Control. Release* 253, 122–136. doi: 10.1016/j.jconrel.2017.03.023

Sedghi, R., Oskooie, H. A., Heravi, M. M., Nabid, M. R., and Zarnani, A. H. (2013). Divergent synthesis of dendrimer-like pH-responsive macromolecules through a combination of ATRP and ROP for controlled release of anti-cancer drug. *J. Mater. Chem. B* 1, 773–786. doi: 10.1039/C2TB00359G

Shanmugam, M. K., Warrier, S., Kumar, A. P., Sethi, G., and Arfuso, F. (2017). Potential role of natural compounds as anti-angiogenic agents in cancer. *Curr. Vasc. Pharmacol.* 15, 503–519. doi: 10.2174/1570161115666170713094319

Shao, M., Chang, C., Liu, Z., Chen, K., Zhou, Y., Zheng, G., et al. (2019). Polydopamine coated hollow mesoporous silica nanoparticles as pH-sensitive nanocarriers for overcoming multidrug resistance. *Colloids Surf. B Biointerfaces* 183, 110427. doi: 10.1016/j.colsurfb.2019.110427

Shi, Y., Liu, S., Ahmad, S., and Gao, Q. (2018). Targeting key transporters in tumor glycolysis as a novel anticancer strategy. *Curr. Top. Med. Chem.* 18, 454–466. doi: 10.2174/1568026618666180523105234

Som, A., Bloch, S., Ippolito, J. E., and Achilefu, S. (2016). Acidic extracellular pH of tumors induces octamer-binding transcription factor 4 expression in murine fibroblasts *in vitro* and *in vivo*. *Sci. Rep.* 6:27803. doi: 10.1038/srep27803

Soomro, N. A., Wu, Q., Amur, S. A., Liang, H., Ur Rahman, A., Yuan, Q., et al. (2019). Natural drug physcion encapsulated zeolitic imidazolate framework, and their application as antimicrobial agent. *Colloids Surf. B Biointerfaces* 182:110364. doi: 10.1016/j.colsurfb.2019.110364

Sun, Y. Q., Dai, C. M., Zheng, Y., Shi, S. D., Hu, H. Y., and Chen, D. W. (2017). Binding effect of fluorescence labeled glycyrrhetinic acid with GA receptors in hepatocellular carcinoma cells. *Life Sci.* 188, 186–191. doi: 10.1016/j.lfs.2017.07.032

Tang, H., Zhao, W., Yu, J., Li, Y., and Zhao, C. (2018). Recent development of pH-responsive polymers for cancer nanomedicine. *Molecules* 24:E4. doi: 10.3390/molecules24010004

Tao, B., Deng, Y., Song, L., Ma, W., Qian, Y., Lin, C., et al. (2019a). BMP2-loaded titania nanotubes coating with pH-responsive multilayers for bacterial infections inhibition and osteogenic activity improvement. *Colloids Surf B Biointerfaces* 177, 242–252. doi: 10.1016/j.colsurfb.2019.02.014

Tao, R., Zhang, F., Tang, Q. J., Xu, C. S., Ni, Z. J., and Meng, X. H. (2019b). Effects of curcumin-based photodynamic treatment on the storage quality of fresh-cut apples. *Food Chem.* 274, 415–421. doi: 10.1016/j.foodchem.2018.08.042

Tian, C., Asghar, S., Xu, Y., Chen, Z., Zhang, M., Huang, L., et al. (2018). The effect of the molecular weight of hyaluronic acid on the physicochemical characterization of hyaluronic acid-curcumin conjugates and *in vitro* evaluation in glioma cells. *Colloids Surf. B Biointerfaces* 165, 45–55. doi: 10.1016/j.colsurfb.2018.02.016

Tian, Q., Zhang, C. N., Wang, X. H., Wang, W., Huang, W., Cha, R. T., et al. (2010). Glycyrrhetinic acid-modified chitosan/poly (ethylene glycol) nanoparticles for liver-targeted delivery. *Biomaterials* 31, 4748–4756. doi: 10.1016/j.biomaterials.2010.02.042

Tohmé, M. J., Giménez, M. C., Peralta, A., Colombo, M. I., and Delgui, L. R. (2019). Ursolic acid: a novel antiviral compound inhibiting rotavirus infection *in vitro*. *Int. J. Antimicrob. Agents* 54, 601–609. doi: 10.1016/j.ijantimicag.2019.07.015

Traverso, N., Ricciarelli, R., Nitti, M., Marengo, B., Furfaro, A. L., Pronzato, M. A., et al. (2013). Role of glutathione in cancer progression and chemoresistance. *Oxid. Med. Cell Longev.* 2013:972913. doi: 10.1155/2013/972913

Tu, Y. (2016). Artemisinin – a gift from traditional Chinese medicine to the world (Nobel Lecture). *Angew. Chem. Int. Ed. Engl.* 55, 10210–10226. doi: 10.1002/anie.201601967

Vangijzegem, T., Stanicki, D., and Laurent, S. (2019). Magnetic iron oxide nanoparticles for drug delivery: applications and characteristics. *Exp. Opin. Drug Deliv.* 16: 69–78. doi: 10.1080/17425247.2019.1554647

Vinayak, M. (2019). Quercetin loaded nanoparticles in targeting cancer: recent development. *Anticancer Agents Med. Chem.* 19, 1560–1576. doi: 10.2174/1871520619666190705150214

Wang, B., Zhang, W., Zhou, X., Liu, M., Hou, X., Cheng, Z., et al. (2019). Development of dual-targeted nano-dandelion based on an oligomeric hyaluronic acid polymer targeting tumor-associated macrophages for combination therapy of non-small cell lung cancer. *Drug Deliv.* 26, 1265–1279. doi: 10.1080/10717544.2019.1693707

Wang, C. Y., Bai, X. Y., and Wang, C. H. (2014). Traditional Chinese medicine: a treasured natural resource of anticancer drug research and development. *Am. J. Chin. Med.* 42, 543–559. doi: 10.1142/S0192415X14500359

Wang, D., Zhou, J., Chen, R., Shi, R., Xia, G., Zhou, S., et al. (2016a). Magnetically guided delivery of DHA and Fe ions for enhanced cancer therapy based on pH-responsive degradation of DHA-loaded Fe_3O_4@C@MIL-100(Fe) nanoparticles. *Biomaterials* 107, 88–101. doi: 10.1016/j.biomaterials.2016.08.039

Wang, D., Zhou, J., Chen, R., Shi, R., Zhao, G., Xia, G., et al. (2016b). Controllable synthesis of dual-MOFs nanostructures for pH-responsive artemisinin delivery, magnetic resonance and optical dual-model imaging-guided chemo/photothermal combinational cancer therapy. *Biomaterials* 100, 27–40. doi: 10.1016/j.biomaterials.2016.05.027

Wang, K., Guo, C., Zou, S., Yu, Y., Fan, X., Wang, B., et al. (2018). Synthesis, characterization and *in vitro*/*in vivo* evaluation of novel reduction-sensitive hybrid nano-echinus-like nanomedicine. *Artif. Cells Nanomed. Biotechnol.* 46, 659–667. doi: 10.1080/21691401.2018.1466147

Wang, K., Hu, H., Zhang, Q., Zhang, Y., and Shi, C. (2019). Synthesis, purification, and anticancer effect of magnetic Fe_3O_4-loaded poly (lactic-co-glycolic) nanoparticles of the natural drug tetrandrine. *J. Microencapsul.* 36, 356–370. doi: 10.1080/02652048.2019.1631403

Wang, M., Zhao, T., Liu, Y., Wang, Q., Xing, S., Li, L., et al. (2017). Ursolic acid liposomes with chitosan modification: promising antitumor drug delivery and efficacy. *Mater. Sci. Eng. C Mater. Biol. Appl.* 71, 1231–1240. doi: 10.1016/j.msec.2016.11.014

Wang, S., Meng, X., and Dong, Y. (2017). Ursolic acid nanoparticles inhibit cervical cancer growth *in vitro* and *in vivo* via apoptosis induction. *Int. J. Oncol.* 50, 1330–1340. doi: 10.3892/ijo.2017.3890

Wang, Y., Wang, F., Liu, Y., Xu, S., Shen, Y., Feng, N., et al. (2018). Glutathione detonated and pH responsive nano-clusters of Au nanorods with a high dose of DOX for treatment of multidrug resistant cancer. *Acta Biomater.* 75, 334–345. doi: 10.1016/j.actbio.2018.06.012

Wang, Z., Chang, Z., Lu, M., Shao, D., Yue, J., Yang, D., et al. (2018a). Shape-controlled magnetic mesoporous silica nanoparticles for magnetically-mediated suicide gene therapy of hepatocellular carcinoma. *Biomaterials* 154, 147–157. doi: 10.1016/j.biomaterials.2017.10.047

Wang, Z., Wang, Y. S., Chang, Z. M., Li, L., Zhang, Y., Lu, M. M., et al. (2017). Berberine-loaded Janus nanocarriers for magnetic field-enhanced therapy against hepatocellular carcinoma. *Chem. Biol. Drug Res.* 89, 464–469. doi: 10.1111/cbdd.12866

Wang, Z., Xia, Q., Liu, X., Liu, W., Huang, W., Mei, X., et al. (2018b). Phytochemistry, pharmacology, quality control and future research of Forsythia suspensa (Thunb.) Vahl: a review. *J. Ethnopharmacol.* 210, 318–339. doi: 10.1016/j.jep.2017.08.040

Wani, K. D., Kadu, B. S., Mansara, P., Gupta, P., Deore, A. V., Chikate, R. C., et al. (2014). Synthesis, characterization and in vitro study of biocompatible cinnamaldehyde functionalized magnetite nanoparticles (CPGF Nps) for hyperthermia and drug delivery applications in breast cancer. *PLoS ONE* 9:e107315. doi: 10.1371/journal.pone.0107315

Wu, M., Cao, Z., Zhao, Y., Zeng, R., Tu, M., and Zhao, J. (2016). Novel self-assembled pH-responsive biomimetic nanocarriers for drug delivery. *Mater. Sci. Eng. C Mater. Biol. Appl.* 64, 346–353. doi: 10.1016/j.msec.2016.03.099

Wu, Q., Gao, H., Vriesekoop, F., Liu, Z., He, J., and Liang, H. (2020). Calcium phosphate coated core-shell protein nanocarriers: Robust stability, controlled release and enhanced anticancer activity for curcumin delivery. *Mater. Sci. Eng. C Mater. Biol. Appl.* 115:111094. doi: 10.1016/j.msec.2020.111094

Xing, L., Lyu, J. Y., Yang, Y., Cui, P. F., Gu, L. Q., Qiao, J. B., et al. (2017). pH-Responsive de-PEGylated nanoparticles based on triphenylphosphine-quercetin self-assemblies for mitochondria-targeted cancer therapy. *Chem. Comm.* 53, 8790–8793.doi: 10.1039/c7cc04058j

Yan, T., Cheng, J., Liu, Z., Cheng, F., Wei, X., Huang, Y., et al. (2018). Acid-sensitive polymeric vector targeting to hepatocarcinoma cells via glycyrrhetinic acid receptor-mediated endocytosis. *Mater. Sci. Eng. C Mater. Biol. Appl.* 87, 32–40. doi: 10.1016/j.msec.2018.02.013

Yang, Y., Islam, M. S., Wang, J., Li, Y., and Chen, X. (2020). Traditional Chinese medicine in the treatment of patients infected with 2019-new coronavirus (SARS-CoV-2): a review and perspective. *Int. J. Biol. Sci.* 16, 1708–1717. doi: 10.7150/ijbs.45538

Yao, J., Zhang, H., Ma, L., Mu, X., Wang, Y., Lu, Y., et al. (2018). Effect of traditional Chinese medicine Bupleurum in the treatment of influenza A (H1N1). *Pak. J. Pharm. Sci.* 31, 1713–1717.

Yin, R., Li, T., Tian, J. X., Xi, P., and Liu, R. H. (2016). Ursolic acid, a potential anticancer compound for breast cancer therapy. *Crit. Rev. Food Sci. Nutr.* 2016, 1–7. doi: 10.1080/10408398.2016.1203755

Yoo, W., Yoo, D., Hong, E., Jung, E., Go, Y., Singh, S., et al. (2018). Acid-activatable oxidative stress-inducing polysaccharide nanoparticles for anticancer therapy. *J. Control. Release* 269, 235–244. doi: 10.1016/j.jconrel.2017.11.023

Younes, I. (2015). Chitin and chitosan preparation from marine sources. Structure, properties and applications. *Mar. Drugs* 13, 1133–1174. doi: 10.3390/md13031133

Yu, D., Ruan, P., Meng, Z., and Zhou, J. (2015). The structure-dependent electric release and enhanced oxidation of drug in graphene oxide-based nanocarrier loaded with anticancer herbal drug berberine. *J. Pharm. Sci.* 104, 2489–2500. doi: 10.1002/jps.24491

Yu, Y., and Zhang, X. (2014). The anti-tumor efficacy of curcumin when delivered by size/charge-changing multistage polymeric micelles based on amphiphilic poly (β-amino ester) derivates. *Biomaterials* 35, 3467–3479. doi: 10.1016/j.biomaterials.2013.12.096

Zhang, H. Y., Sun, C. Y., Adu-Frimpong, M., Yu, J. N., and Xu, X. M. (2019). Glutathione-sensitive PEGylated curcumin prodrug nanomicelles: preparation, characterization, cellular uptake and bioavailability evaluation. *Int. J. Pharm.* 555, 270–279. doi: 10.1016/j.ijpharm.2018.11.049

Zhang, J., Li, J., Shi, Z., Yang, Y., Xie, X., Lee, S. M., et al. (2017). pH-sensitive polymeric nanoparticles for co-delivery of doxorubicin and curcumin to treat cancer via enhanced pro-apoptotic and anti-angiogenic activities. *Acta Biomater.* 58, 349–364. doi: 10.1016/j.actbio.2017.04.029

Zhang, K., Gao, S., Guo, J., Ni, G., Chen, Z., Li, F., et al. (2018a). Hypericin-photodynamic therapy inhibits proliferation and induces apoptosis in human rheumatoid arthritis fibroblast-like synoviocytes cell line MH7A. *Iran J. Basic Med. Sci.* 21, 130–137. doi: 10.22038/IJBMS.2018.23871.5991

Zhang, P., Wu, J., Xiao, F., Zhao, D., and Luan, Y. (2018b). Disulfide bond based polymeric drug carriers for cancer chemotherapy and relevant redox environments in mammals. *Med. Res. Rev.* 38, 1485–1510. doi: 10.1002/med.21485

Zhang, Z., Cheng, W., Pan, Y., and Jia, L. (2020a). An anticancer agent-loaded PLGA nanomedicine with glutathione-response and targeted delivery for the treatment of lung cancer. *J. Mater. Chem. B* 8, 655–665. doi: 10.1039/C9TB02284H

Zhang, Z., Wang, R., Huang, X., Luo, R., Xue, J., Gao, J., et al. (2020b). Self-delivered and self-monitored chemo-photodynamic nanoparticles with light-triggered synergistic antitumor therapies by downregulation of HIF-1α and depletion of GSH. *ACS App. Mater. Interfaces.* 12, 5680–5694. doi: 10.1021/acsami.9b23325

Zhang, Z., Xu, S., Wang, Y., Yu, Y., Li, F., Zhu, H., et al. (2018c). Near-infrared triggered co-delivery of doxorubicin and quercetin by using gold nanocages with tetradecanol to maximize anti-tumor effects on MCF-7/ADR cells. *J Colloid Interface Sci.* 509, 47–57. doi: 10.1016/j.jcis.2017.08.097

Zhao, C., Cao, W., Zheng, H., Xiao, Z., Hu, J., Yang, L., et al. (2019a). Acid-responsive nanoparticles as a novel oxidative stress-inducing anticancer therapeutic agent for colon cancer. *Int. J. Nanomed.* 14, 1597–1618.doi: 10.2147/IJN.S189923

Zhao, Y., Li, H., Wei, S., Zhou, X., and Xiao, X. (2019b). Antimicrobial effects of chemical compounds isolated from traditional Chinese herbal medicine (TCHM) against drug-resistant bacteria: a review paper. *Mini Rev. Med. Chem.* 19, 125–137. doi: 10.2174/1389557518666181017143141

Zhong, Y., Zou, Y., Liu, L., Li, R., Xue, F., and Yi, T. (2020). pH-responsive Ag2S nanodots loaded with heat shock protein 70 inhibitor for photoacoustic imaging-guided photothermal cancer therapy. *Acta Biomater.* 115, 358–70. doi: 10.1016/j.actbio.2020.08.007

Zhu, K., Zhou, L., Zou, M., Ning, S., Liu, S., Zhou, Y., et al. (2020). 18-GA-Suc modified liposome loading cantharidin for augmenting hepatic specificity: preparation, characterization, antitumor effects, and liver-targeting efficiency. *J. Pharm. Sci.* 109, 2038–2047. doi: 10.1016/j.xphs.2020.03.001

Zhu, L., Zhou, Z., and Mao, H. (2017). Magnetic nanoparticles for precision oncology: theranostic magnetic iron oxide nanoparticles for image-guided and targeted cancer therapy. *Nanomedicine* 12, 73–87. doi: 10.2217/nnm-2016-0316

Zhu, X. L., Wang, S. S., Li, L. H., Zhang, H. J., Xia, T., and Lyu, X. Y. (2019). Preparation and characterization of glycyrrhetinic acid-modified nano graphene oxide drug delivery system. *Zhongguo Zhong Yao Za Zhi* 44, 4621–4626. doi: 10.19540/j.cnki.cjcmm.20190804.305

Conflict of Interest: The authors declare that the research was conducted in the absence of any commercial or financial relationships that could be construed as a potential conflict of interest.

Advantages of publishing in Frontiers

OPEN ACCESS
Articles are free to read for greatest visibility and readership

FAST PUBLICATION
Around 90 days from submission to decision

HIGH QUALITY PEER-REVIEW
Rigorous, collaborative, and constructive peer-review

TRANSPARENT PEER-REVIEW
Editors and reviewers acknowledged by name on published articles

Frontiers
Avenue du Tribunal-Fédéral 34
1005 Lausanne | Switzerland

Visit us: www.frontiersin.org
Contact us: frontiersin.org/about/contact

REPRODUCIBILITY OF RESEARCH
Support open data and methods to enhance research reproducibility

DIGITAL PUBLISHING
Articles designed for optimal readership across devices

FOLLOW US
@frontiersin

IMPACT METRICS
Advanced article metrics track visibility across digital media

EXTENSIVE PROMOTION
Marketing and promotion of impactful research

LOOP RESEARCH NETWORK
Our network increases your article's readership